



# A Contribution to the Design of Long Endurance Mini Unmanned Aerial Vehicles

Murat Bronz

## ► To cite this version:

Murat Bronz. A Contribution to the Design of Long Endurance Mini Unmanned Aerial Vehicles. Automatic. Institut Supérieur de l'Aéronautique et de l'Espace - ISAE, 2012. English. NNT : 2012ESAE0025 . tel-00993465

**HAL Id: tel-00993465**

**<https://theses.hal.science/tel-00993465>**

Submitted on 20 May 2014

**HAL** is a multi-disciplinary open access archive for the deposit and dissemination of scientific research documents, whether they are published or not. The documents may come from teaching and research institutions in France or abroad, or from public or private research centers.

L'archive ouverte pluridisciplinaire **HAL**, est destinée au dépôt et à la diffusion de documents scientifiques de niveau recherche, publiés ou non, émanant des établissements d'enseignement et de recherche français ou étrangers, des laboratoires publics ou privés.



Université  
de Toulouse

# THÈSE

En vue de l'obtention du

## DOCTORAT DE L'UNIVERSITÉ DE TOULOUSE

Délivré par :

Institut Supérieur de l'Aéronautique et de l'Espace (ISAE)

---

**Présentée et soutenue par :**

**Murat BRONZ**

**le** lundi 1 octobre 2012

**Titre :**

A Contribution to the Design of Long Endurance Mini Unmanned Aerial  
Vehicles

Conception mini-drone longue endurance

---

**École doctorale et discipline ou spécialité :**

ED AA : Dynamique des fluides et Systèmes embarqués

**Unité de recherche :**

Équipe d'accueil ISAE-ONERA EDyF - ENAC

**Directeur(s) de Thèse :**

M. Jean-Marc MOSCHETTA (directeur de thèse)

M. Gautier HATTENBERGER (co-directeur de thèse)

**Jury :**

M. Christophe CROS

M. Éric FÉRON - Président, Rapporteur

M. Gautier HATTENBERGER - Co-directeur de thèse

M. Jean-Marc MOSCHETTA - Directeur de thèse

M. Joël RENEUX

M. Mehmet Fevzi ÜNAL - Rapporteur



# Declaration of Authorship

I, Murat BRONZ, declare that this thesis titled, ‘Design of A Long Endurance Mini Unmanned Aerial Vehicle’ and the work presented in it are my own. I confirm that:

- This work was done wholly or mainly while in candidature for a research degree at this University.
- Where any part of this thesis has previously been submitted for a degree or any other qualification at this University or any other institution, this has been clearly stated.
- Where I have consulted the published work of others, this is always clearly attributed.
- Where I have quoted from the work of others, the source is always given. With the exception of such quotations, this thesis is entirely my own work.
- I have acknowledged all main sources of help.
- Where the thesis is based on work done by myself jointly with others, I have made clear exactly what was done by others and what I have contributed myself.

Signed:

---

Date:

---

*“We call it theory when we know much about something but nothing works, and practice when everything works but nobody knows why.”*

Albert Einstein

# Résumé

Pour le titre de docteur

par Murat BRONZ

L'objet de cette thèse est de démontrer la faisabilité de conception d'un mini-drone longue endurance sans recourir à des véhicules de grande envergure qui nécessite des infrastructures supplémentaires, des systèmes de lancement complexes et un personnel d'exploitation important. Pour ce faire, une approche d'optimisation globale du problème a été utilisée, en s'appuyant sur les spécificités de chacun des aspects de la conception de mini-drones. Ce *concept de mini-drone longue endurance* doit repousser les limites dans plusieurs disciplines telles que l'aérodynamique, la propulsion, les structures, les sources d'énergies et le stockage, le contrôle et la navigation, ainsi que la miniaturisation de l'électronique embarquée.

Un programme de conception baptisé *Cdsgn* a été développé et prend en compte les problèmes spécifiques de chaque discipline consacrées aux mini-drones. Il permet de voir l'influence de chaque paramètre de conception sur la performance finale de la conception, menant à la sélection optimale des paramètres. *Cdsgn* génère et d'analyse rapidement de nombreuses configurations de l'avion tout en simulant la performance de chaque configuration pour un profil de mission donnée. Un outil de post-traitement a également été développé afin de filtrer et sélectionner de manière interactive les paramètres de conception parmi les nombreuses configurations pour répondre à des applications pratiques.

Le programme proposé a été utilisé dans le développement et la conception de plusieurs projets, tels que *Solar Storm*, premier mini-drone hybride au monde à énergie solaire d'une envergure de cinquante centimètre, *SPOC*, un mini-drone longue distance conçu pour voler au-dessus de la mer Méditerranée de Nice jusqu'en Corse (Calvi) et enfin *Eternity*, mini-drone de longue endurance d'une envergure d'un mètre, avec une configuration classique. Capable d'une autonomie de quatre heures avec les batteries embarquées, son temps de vol peut être amélioré jusqu'à huit heures avec l'utilisation de l'énergie solaire.

En utilisant les évaluations de chaque projet, *Cdsgn* a été amélioré à la fois pour l'exactitude des calculs et pour la performance opérationnelle afin de développer le plus petit véhicule aérien pour une mission d'endurance donnée.

# *Abstract*

Doctor of Philosophy

by Murat BRONZ

This thesis shows the feasibility of designing a long endurance mini UAV without resorting to large scale vehicles which requires additional infrastructure, complex launching systems and numerous operating crew. To do so is possible by using a global optimisation approach concentrated specifically on each aspect of the mini-UAV design with their particular challenges. So called *Long Endurance Mini UAV Concept* has to push the limits in several disciplines such as aerodynamics, propulsion, structures, energy source and storage, control and navigation, miniaturised electronics.

A conceptual design program called *Cdsgn* is developed which takes into account each discipline's specific problems devoted to mini UAVs and making it possible to see the influence of each design parameter on the final performance of the complete design leading to the optimum selection of parameters. *Cdsgn* generates and analyse numerous aircraft configurations rapidly while simulating the performance of each configuration for a given mission profile. A post processing tool is also developed in order to interactively filter and select the final design parameters among numerous analysed aircraft configurations for practical applications.

The proposed program is used in the development and design of several projects, such as *Solar Storm*, the world's first hybrid solar powered micro UAV in half a meter scale, *SPOC*, a long range mini UAV which is designed to fly across the Mediterranean sea from Nice to Corsica(Calvi) and finally the *Eternity*, the long endurance mini UAV concept which is an electrically powered, one-meter span aircraft with a conventional configuration having an endurance of four hours with the on-board batteries which can be enhanced up to eight hours with the use of solar-cells.

Using the feedback of each project, *Cdsgn* has been improved both for the accuracy and for the operational performance in order to develop the smallest aerial vehicle for a given endurance mission.



In the memory of Pascal Brisset who passed away in 2010 and left us in the absence of his great friendship...

# Acknowledgements

During my PhD, there have been a lot of people who stand beside me to help, show the correct path and encourage when I most needed. First, I would like to thank my supervisors Prof. Jean-Marc Moschetta and Gautier Hattenberger, your advice and guidance throughout my research and especially while writing this thesis is greatly appreciated. You are the kindest advisors that one can ever dream of. I would also like to thank to the "Paparazzi Team" Michel Gorraz, Catherine Ronfle-Nadaudfrom, Alexandre Bustico, Matthieu Navarro the drone laboratory of ENAC for being my second family during these years (and hopefully in the future as well) and having the patience for me to complete this thesis. It was a great pleasure to be a part of the team.

Special thanks to Antoine Drouin for initiating the opportunity of this thesis which clearly have changed my life, and to Farid Zizi for helping on financing of the thesis.

Christiane Boyer, without your endless help it would not have been possible to adapt and keep up with all difficulties that I have had during my first years. I would also like to thank to all of the DAEP department for their help and cheering.

To all of the students that I have worked together and supervised during the school projects, "Belgium Beatles", "SPOC v0", "SPOC v1.0" and "SPOC v2.0". That was completely a different experience.

Many thanks to Xavier Foulquier and Gee Mirabel, from the composite laboratory of Supaero, for their advices and all the discussions we had and especially for helping me every time without questioning whenever I came up with a new idea of manufacturing enormously complex structures. (I usually think that they are simple, which is not the case generally...)

I would also like to thank to Murat Esibatir, Philip Kolb and the Fineworx team, for giving me the opportunity to learn the techniques that lead to the successful manufacturing of my *Eternity* design. It was a pleasure to work with them and see a "German" style of organisation.

Finally, I would like to thank to my family for supporting me all the time regardless of what the situation is, it would have never been possible to achieve the things that I have without them, and to my dearest wife, Irem, for her support, love and her understanding during my hard times of writing this endless thesis.





# Contents

<b>Declaration of Authorship</b>	<b>iii</b>
<b>Résumé</b>	<b>v</b>
<b>Abstract</b>	<b>vi</b>
<b>Acknowledgements</b>	<b>viii</b>
<b>List of Figures</b>	<b>xv</b>
<b>List of Tables</b>	<b>xxi</b>
<b>Abbreviations</b>	<b>xxiii</b>
<b>Symbols</b>	<b>xxv</b>
<b>Résumé des Chapitres</b>	<b>1</b>
<b>1 Introduction</b>	<b>9</b>
1.1 Motivations . . . . .	9
1.2 Objectives . . . . .	11
1.3 Contributions . . . . .	12
1.4 Structure of the Thesis Document . . . . .	12
<b>2 Long Endurance Mini-UAV Concept</b>	<b>15</b>
2.1 Introduction . . . . .	15
2.2 Unmanned Air Vehicles . . . . .	15
2.2.1 Long Endurance Unmanned Air Vehicles . . . . .	16
2.2.2 Mini Unmanned Air Vehicles . . . . .	17
2.2.3 Potential Applications . . . . .	17
2.3 Long Endurance Flight . . . . .	18
2.3.1 Long Endurance Mini-UAV Concept . . . . .	19

2.4	State of the Art . . . . .	20
2.5	Possible Improvement Areas . . . . .	22
<b>3</b>	<b>Conceptual Design Program Devoted to Mini and Micro UAV (<i>Cdsgn</i>)</b>	<b>23</b>
3.1	Introduction . . . . .	23
3.2	Early Version of <i>Cdsgn</i> . . . . .	24
3.3	Current Version of <i>Cdsgn</i> Program . . . . .	27
3.3.1	Aircraft Configuration Selection . . . . .	28
3.3.2	Structural Mass . . . . .	31
3.3.3	System Mass . . . . .	33
3.3.4	Motor Mass . . . . .	33
3.3.5	Battery Mass . . . . .	34
3.3.6	Total Mass . . . . .	34
3.3.7	Aircraft Generation for AVL . . . . .	34
3.3.8	Performance . . . . .	35
3.4	Mission Simulation . . . . .	36
3.5	Final Selection . . . . .	37
3.6	Interactive Real-Time Filtering . . . . .	37
<b>4</b>	<b>Aerodynamics</b>	<b>39</b>
4.1	Introduction . . . . .	39
4.2	Main Aerodynamic Challenges . . . . .	40
4.3	Aerodynamic Analysis Programs . . . . .	42
4.3.1	XFOIL . . . . .	42
4.3.2	AVL Vortex-Lattice Code . . . . .	43
4.3.3	XFLR5 . . . . .	46
4.4	Program Selection . . . . .	47
4.5	Modifications . . . . .	48
4.6	Validation of the Programs . . . . .	52
4.6.1	S4 Wind-Tunnel . . . . .	52
4.6.2	Internal Balance . . . . .	54
4.6.3	Experimental Comparison . . . . .	54
4.7	Conclusion . . . . .	56
<b>5</b>	<b>Propulsion System Design</b>	<b>59</b>
5.1	Introduction . . . . .	59
5.2	Problem Definition . . . . .	60
5.2.1	Elements of Propulsion System . . . . .	60
5.2.2	Mission Definition . . . . .	61
5.3	QPOPTIMIZER Program . . . . .	62
5.3.1	QPROP and QMIL . . . . .	62
5.3.2	QPOPTIMIZER Program Flow . . . . .	64
5.4	Modelling Electric Motor and Propeller . . . . .	66
5.4.1	Electric Motor . . . . .	66

5.4.2	Propeller . . . . .	71
5.5	Motor and Propeller Matching . . . . .	75
<b>6</b>	<b>Energy</b>	<b>77</b>
6.1	Introduction . . . . .	77
6.2	Energy Storage . . . . .	77
6.2.1	Batteries . . . . .	78
6.2.2	Fuel-cells . . . . .	80
6.3	Energy Extraction . . . . .	82
6.3.1	Thermal Soaring . . . . .	83
6.3.2	Solar Energy . . . . .	83
<b>7</b>	<b>Hybrid Solar Micro Air Vehicle</b>	<b>87</b>
7.1	Introduction . . . . .	87
7.2	Design of <i>Solar Storm</i> . . . . .	87
7.3	Solar Energy Management . . . . .	90
7.3.1	Maximum Power Point Tracker <i>MPPT</i> . . . . .	90
7.4	Manufacturing and Integration . . . . .	90
7.5	Wind-tunnel Tests . . . . .	92
7.6	Flight Performance . . . . .	95
7.7	Further Improvements . . . . .	100
<b>8</b>	<b>Long Endurance Mini-UAV : Eternity</b>	<b>103</b>
8.1	Introduction . . . . .	103
8.2	Design Envelope . . . . .	104
8.2.1	Configuration Selection . . . . .	104
8.2.2	Required Optimum Energy (On-Board) . . . . .	111
8.3	Design Philosophy . . . . .	113
8.3.1	Idea of Variable Configuration . . . . .	113
8.4	Design Details . . . . .	114
8.4.1	Wing Planform Modifications . . . . .	115
8.4.2	Design of the Airfoil Family . . . . .	116
8.4.3	Horizontal Tail Design . . . . .	123
8.5	Propulsion System . . . . .	126
8.6	Final Appearance of the two Versions . . . . .	127
8.7	Windtunnel Tests . . . . .	129
8.8	Flight Test . . . . .	138
8.9	Overall Design Conclusion . . . . .	140
<b>9</b>	<b>Conclusion</b>	<b>143</b>
9.1	Main Achievements . . . . .	143
9.2	Future Work . . . . .	144

---

A.1	Introduction . . . . .	147
A.2	Main Phases of the Challenge . . . . .	148
A.2.1	Improvements Over The Years . . . . .	149
A.3	Aerodynamic Analyses and Wind Tunnel Tests . . . . .	150
A.4	Manufacturing and Integration . . . . .	150
A.4.1	GSM Module . . . . .	153
A.5	Flight Tests and Flight to Corsica . . . . .	155
A.5.1	Certification . . . . .	155
A.5.2	The 2010 Attempt . . . . .	156
A.5.3	The 2011 Changes and Attempt . . . . .	158
A.6	Conclusion & Lessons Learned . . . . .	159
<b>B</b>	<b>Custom Design Propeller</b>	<b>161</b>
B.1	Introduction . . . . .	161
B.2	Application of Qoptimizer . . . . .	161
B.3	Run cases . . . . .	164
B.4	Manufacturing . . . . .	168
B.5	Test Results . . . . .	171
<b>C</b>	<b>Publications</b>	<b>173</b>
	<b>Bibliography</b>	<b>223</b>

# List of Figures

1.1	Critical Reynolds plot from Schmitz [1] showing the N60 airfoil's lift ( $C_a$ ) and drag ( $C_w$ ) coefficient variation with respect to the airfoil's critical Reynolds number. The huge disadvantage of low Re number is clearly visible on the plot. . . . .	10
1.2	The design wheel. . . . .	11
2.1	Various UAVs with different size and application purposes(wiki) on the left and Global Hawk UAV with on the right. . . . .	16
2.2	Condor and Aerosonde. . . . .	16
2.3	Scan Eagle while being launched with a catapult system in comparison to elastic launch of WASP mini-UAV. . . . .	17
2.4	WASP and Blackwidow from Aerovironment. . . . .	17
2.5	Global Hawk long endurance UAV (36 <i>hours</i> ) with its operating crew. . . . .	18
2.6	Solar Eagle on the left, previously known as Vulture from DARPA which is planned to be launched in 2013 and Zephyr UAV on the right, from QinetiQ. . . . .	19
2.7	Performance versus size chart showing where the new <i>Long Endurance Mini UAV Concept</i> corresponds to. . . . .	20
2.8	So Long solar UAV. . . . .	21
2.9	Sky Sailor. . . . .	21
2.10	Sun Surfer. . . . .	22
3.1	The main program flow of the early version of <i>Cdsgn</i> . . . . .	24
3.2	The flow chart of the current verion of <i>Cdsgn</i> program. . . . .	28
3.3	A closer look at the <i>Generate and Modelize Aircraft</i> block of the design loop. . . . .	28
3.4	Examples of two different automatic generated aircraft configurations by <i>Cdsgn</i> . . . . .	29
3.5	Simple solar irradiation profile used in the simulations on the left. Sun rise and sun set times are taken 6:00AM and 18:00PM consecutively. A real data from [2] on the right for comparison. . . . .	37
3.6	Interactive real time filtering program. . . . .	38
4.1	The very brief flow chart of <i>Cdsgn</i> program. . . . .	40
4.2	The aerodynamic performance degradation of SD7037 airfoil with respect to Reynolds number. Calculated by XFOIL. . . . .	41
4.3	Wing relative velocity at field point location $\vec{r}$ . . . . .	44

4.4	Velocity contribution from $n$ 'th unit horseshoe vortex. . . . .	45
4.5	Velocity at midpoint $\vec{r}_n$ of $n$ 'th horseshoe vortex. . . . .	46
4.6	Sections and strips defined in AVL program along the wing. . . . .	48
4.7	The precision of airfoil polar interpolation . . . . .	49
4.8	A generic fuselage with circular cross sections generated by AVL. . . . .	51
4.9	AVL's modified Trefftz Plane plots with and without viscous effects. . . . .	52
4.10	Comparison of inviscid calculation of AVL versus the final modified version $AVL_M$ for a conventional configuration at different speeds. . . . .	53
4.11	The plan of S4 wind-tunnel. . . . .	53
4.12	Dimensions of the internal balance that is used in the experiments. . . . .	54
4.13	Wind tunnel model specifications of the conventional and flying wing configurations. . . . .	55
4.14	Comparison of inviscid calculation of AVL, the final modified version $AVL_M$ , XFLR5 and Wind-Tunnel measurements for a conventional configuration at $8\text{ m/s}$ . . . . .	56
4.15	Comparison of conventional and flying wing configuration with numerical aerodynamic analyses programs XFLR5 and modified AVL and also the wind tunnel measurements. . . . .	57
5.1	Elements of a generic electric propulsion system. . . . .	60
5.2	A generic mission definition with multiple flight phases which are called <i>Working Conditions</i> ( <b>WC</b> ). . . . .	61
5.3	Propeller airfoil coefficients used in QPROP program. . . . .	63
5.4	Main flow chart of the QOPTIMIZER program. . . . .	64
5.5	A custom propeller designed with QOPTIMIZER for a specific application. Design and manufacturing procedure is explained in Appendix B. . . . .	65
5.6	In-runner and Out-runner Brushless motor types. . . . .	66
5.7	Equivalent circuit for a DC electric motor[3]. . . . .	67
5.8	Theoretical motor outputs versus motor rotation rate for different input voltages. . . . .	68
5.9	Motor test bench. . . . .	69
5.10	The wheel that is used in motor characterisation. . . . .	70
5.11	AXI 2212-20 characteristic performance curves at various input voltages. . . . .	71
5.12	Typical propeller efficiency curves as a function of advance ratio <b>J</b> . . . . .	73
5.13	Typical propeller thrust curves as a function of advance ratio <b>J</b> . . . . .	73
5.14	Typical propeller power curves as a function of advance ratio <b>J</b> . . . . .	74
5.15	Propeller test bench. . . . .	74
5.16	Motor and propeller matching procedure as explained in [4]. . . . .	76
6.1	The Ragone Plot. . . . .	78
6.2	The single cell specific energy variation with respect to capacity for AMICELL [5] brand. . . . .	80
6.3	The discharge plot of ThunderPower 910mAh 3-cell (11.1V) battery. . . . .	81

6.4	General working principle of fuel cells (Source: <a href="http://www.tekstak.com/">http://www.tekstak.com/</a> ).	81
6.5	Two commercially available fuel-cell packs from Horizon Energy and Protonex, Aeropak and UAV-C250. . . . .	82
6.6	Fuel-cell demonstrator from Georgia Tech with a span of 6.58m and 16.4kg of total weight. . . . .	83
6.7	General working principle of solar cells (Source: <a href="http://www.solarcell.net.in/">http://www.solarcell.net.in/</a> ).	84
6.8	Solar cell efficiencies (Rev:02.2012, NREL[6]). . . . .	85
6.9	Flexible solar cell from <i>Power Film</i> . . . . .	85
6.10	Azur Space S-32 solar cell and its specifications. . . . .	85
7.1	<i>Solar Storm</i> design. . . . .	88
7.2	Main dimensions of <i>Storm</i> design in millimetres. . . . .	89
7.3	Custom designed maximum power point tracker board.(Weights 7 g)	91
7.4	Maximum power point tracker architecture. . . . .	91
7.5	The integration of the main components of <i>Solar Storm</i> . . . . .	92
7.6	Mounting of the Storm wind-tunnel model and the internal balance integration. . . . .	93
7.7	Comparison of lift slope curve obtained from wind tunnel and AVL model. . . . .	94
7.8	Range and endurance performance curves with the pitching moment coefficient for three different reference locations. . . . .	95
7.9	Comparison of windtunnel experiment results to calculated results coming from modified AVL program with $C_{Dpar} = 0.005$ at 15 m/s .	96
7.10	Comparison of windtunnel experiment results to calculated results coming from modified AVL program with corrected $C_{Dpar} = 0.001$ at 15 m/s . . . . .	97
7.11	Flow visualisations realised for straight flight on the left and for a side slip angle of 10 degrees on the right at cruise conditions (15 m/s).	97
7.12	<i>Solar Storm</i> 's log with the time in [s] in x-axis and [V] , [W] and [I] for the y-axis. . . . .	98
7.13	Estimated flight performance of <i>Fire Storm</i> with 29.5 Wh of on-board energy. The plot includes the propulsion efficiency and the longitudinal trim losses at each corresponding flight speed. . . . .	99
7.14	<i>Fire Storm</i> demonstrated 105 minutes of flight endurance and took the "Best Outdoor Endurance Award" in IMAV 2011 competition. .	100
7.15	Estimated flight performance of <i>Fire Storm</i> with 62 Wh of on-board energy. The plot includes the propulsion efficiency and the longitudinal trim losses at each corresponding flight speed. . . . .	101
8.1	Examples of some automatic generated aircraft configurations by <i>Cdsgn</i> . . . . .	106
8.2	Performance plot of 1-meter conventional aircraft in various specifications with only battery. Circle radius represents the relative on-board energy being between 20 Wh and 210 Wh for min and max size. . . . .	106

8.3	Performance plot of 1-meter flying wing aircraft in various specifications with only battery. Circle radius represents the relative on-board energy being between 20 Wh and 210 Wh for min and max size. . . . .	107
8.4	Performance plot of 1-meter conventional aircraft in various specifications with solar cells. Circle radius represents the relative on-board energy being between 20 Wh and 210 Wh for min and max size. . . . .	108
8.5	Performance plot of 1-meter flying wing aircraft in various specifications with solar cells. Circle radius represents the relative on-board energy being between 20 Wh and 210 Wh for min and max size. . .	109
8.6	Range versus endurance performance plot of 1-meter conventional aircraft in various specifications for battery only and additional solar energy cases. Circle radius represents the relative on-board energy being between 20 Wh and 210 Wh for min and max size. . . .	110
8.7	Effect of on-board energy on endurance and range performance . . .	112
8.8	Effect of on-board energy on endurance and range performance . . .	112
8.9	CAD drawing of the wing joiner battery pack. . . . .	114
8.10	The effect of various flight speed and wing area on the endurance performance of non-solar and solar configurations with 66Wh of on-board energy. . . . .	115
8.11	The effect of various flight speed and wing area on the endurance performance of non-solar and solar configurations with 132Wh of on-board energy. . . . .	116
8.12	Candidate airfoil polars in comparison with PKMB500 custom airfoil at Re=150k. . . . .	117
8.13	Pressure distribution change for PKMB500 and SD7037 airfoils at Re=150k. . . . .	120
8.14	Performance degradation of PKMB500 airfoil with reduced Reynolds number (calculated for $Re\sqrt{C_l}$ ). . . . .	120
8.15	Designed airfoil family for <i>Eternity</i> . Bottom plot shows the real ratio and top plot shows the y-coordinates as five times scaled in order to distinguish the difference easily. . . . .	121
8.16	Placement of each airfoil is shown along the half span. The upper graphs shows the $C_l$ vs $C_d$ plots of each airfoils at their corresponding working regimes with the comparison to the root PKMB500 airfoil. The planform shown is given as demonstration and the real planform is shown later in figure 8.21. . . . .	122
8.17	Effect of horizontal tail aspect ratio on endurance performance with various tail moment arm and tail volume. Circle radius also represents the endurance relatively. . . . .	123
8.18	Effect of various horizontal tail moment arm on endurance performance for tail aspect ratio of 4. Circle radius also represents the endurance relatively. . . . .	125

8.19	Effect of various horizontal tail volume on endurance performance for tail aspect ratio of 4.0. Circle radius also represents the endurance relatively. . . . .	126
8.20	Detail view of the tail configuration of <i>Eternity</i> , there are two servos installed inside the horizontal tail pod controlling the elevator and rudder with internal push-rods. . . . .	127
8.21	<i>Eternity</i> design with two different fuselages. . . . .	128
8.22	The mounting of <i>Eternity</i> on S4 Wind-tunnel. . . . .	129
8.23	The payload compartment of the <i>Eternity</i> has been used for the mounting of the internal balance, and then the payload bay covered in order to protect the balance and to have the accurate fuselage shape. . . . .	130
8.24	Both elevator and rudder is levelled by a spirit level and the deflections are calibrated by using the wind tunnel's accurate angle measurement. . . . .	130
8.25	Flexibility effect of the mounting on the $C_{L\alpha}$ lift curve slopes and numerically corrected versions at various speeds. . . . .	131
8.26	Effect of flight speed on the range and endurance performance characteristics. . . . .	132
8.27	The effect of elevator deflection on $C_M$ , $C_L$ and $C_D$ coefficients of <i>Eternity</i> at 14 m/s wind-tunnel speed, $C_M$ coefficient is measured with respect to the reference point that corresponds to %8 of static margin. . . . .	134
8.28	Component Drag at 14m/s. . . . .	135
8.29	Laminar bubble occurrence over the top surface shown as an example. . . . .	136
8.30	Turbulator effect at 18m/s for different thicknesses $t=1,2,3$ and chord locations %50 and %75 all along the span. . . . .	137
8.31	Turbulator effect at 18m/s. . . . .	138
8.32	Comparison of wind tunnel test and the maiden flight results(Total propulsion efficiency ( $\eta_p$ ) is varied between %45 and %50 to see the effect on the performance estimation) . . . . .	139
8.33	Hand-launch moment of <i>Eternity</i> from its maiden flight. . . . .	140
A.1	Flight to Corsica mission path which is about 185 km. . . . .	147
A.2	Selected 21 Ah Lithium Polymer Battery . . . . .	149
A.3	Analysis of SPOC-2 in AVL, with the wingloading visible on the top, lift force and lift coefficient visible along the span in the middle and the airfoil chosen on the bottom. . . . .	151
A.4	SPOC-2 in the S4 Windtunnel. . . . .	152
A.5	CL versus alpha and CL versus CD plots. . . . .	152
A.6	Lift to drag ratio of SPOC-2 for different flight speeds with the equilibrium points marked for each corresponding flight speed. . .	153
A.7	Composite molds of SPOC-2. . . . .	153
A.8	Integration of the components. . . . .	154
A.9	Telit GC864 GSM/GPRS Module with antenna . . . . .	154

A.10	Trajectory of SPOC-2 before losing communication. . . . .	157
A.11	Satellite picture of the clouds taken at 6:00 AM, orange colour shows very low altitude clouds which could cause the failure of the infrared sensors. . . . .	157
B.1	Selected airfoils and their lift versus drag coefficient plot calculated by XFOIL for 60000 Reynolds number. . . . .	165
B.2	AXI 2217-12 characteristic performance curves at various input voltages, showing the significant difference between the theoretical and experimental test results. . . . .	166
B.3	Designed propeller and its spinner's CATIA drawing. . . . .	168
B.4	CNC manufactured aluminium propeller and spinner moulds . . . .	169
B.5	Required carbon fiber pieces are cut into shape in prior to wet lay-up process. . . . .	170
B.6	The cone and its molds . . . . .	170
B.7	The resulting custom propeller . . . . .	170
B.8	The global efficiency versus Thrust [N] plot for the custom designed propeller at 15 m/s speed. . . . .	172
B.9	The propeller efficiency versus Thrust [N] plot for the custom designed propeller at 15 m/s speed. . . . .	172

# List of Tables

4.1	Specifications of the CC604 internal balance. . . . .	54
5.1	Example of mission working conditions. . . . .	62
6.1	Battery specifications from different sources, numbers for Li-Po are already tested and the numbers for Li-S are rely on the manufacturer [7]. . . . .	79
6.2	Specifications of Horizon Energy and Protonex brand fuel cell systems.	82
7.1	Mass break down of Solar and Fire Storm (all in grams). . . . .	93
8.1	The range of main variables used for the design envelope of <i>Eternity</i> .	104
8.2	The design constants specified for <i>Eternity</i> . . . . .	105
8.3	Typical battery specifications. . . . .	111
8.4	Optimized on-board energy for various flight conditions. . . . .	113
8.5	Specifications of the airfoil family. . . . .	121
8.6	Geometrical specifications of the two <i>Eternity</i> configurations. . . . .	127
8.7	Expected performance of the two <i>Eternity</i> configurations. . . . .	141
A.1	Mission constraints for the conceptual design. . . . .	149
B.1	Mission working conditions of the <i>Corsica Project</i> [appendix A]. . .	162
B.2	AXI2212/26 and AXI2217/12 motor constants obtained from the manufacturer site. . . . .	164
B.3	Parameters used for the optimization . . . . .	167
B.4	Lift coefficients distributions . . . . .	167
B.5	Best global efficiencies of the motor and propeller couples for the cruise conditions are shown (note that the speed controller losses are not included). . . . .	167



# Abbreviations

<b>AGL</b>	<b>A</b> bove <b>G</b> round <b>L</b> evel
<b>CAD</b>	<b>C</b> omputer <b>A</b> ided <b>D</b> rafting
<b>CFD</b>	<b>C</b> omputational <b>F</b> luid <b>D</b> ynamics
<b>CNC</b>	<b>C</b> omputer <b>N</b> umerical <b>C</b> ontrol
<b>DC</b>	<b>D</b> irect <b>C</b> urrent
<b>FAI</b>	<b>F</b> édération <b>A</b> éronautique <b>I</b> nternationale
<b>GCS</b>	<b>G</b> round <b>C</b> ontrol <b>S</b> tation
<b>GPS</b>	<b>G</b> lobal <b>P</b> ositioning <b>S</b> ystem
<b>GSM</b>	<b>G</b> lobal <b>S</b> ystem for <b>M</b> obile <b>C</b> ommunications
<b>MAV</b>	<b>M</b> icro <b>A</b> erial <b>V</b> ehicle
<b>MTP</b>	<b>M</b> aximum <b>T</b> otal <b>P</b> ower
<b>MPPT</b>	<b>M</b> aximum <b>P</b> ower <b>P</b> oint <b>T</b> racker
<b>RC</b>	<b>R</b> adio <b>C</b> ontrolled
<b>UAS</b>	<b>U</b> nmanned <b>A</b> ir <b>V</b> ehicle <b>S</b> ystems
<b>UAV</b>	<b>U</b> nmanned <b>A</b> ir <b>V</b> ehicles



# Symbols

$AR$	Aspect ratio ( $b^2/S$ )	[-]
$b$	Span	[m]
$c$	Chord	[m]
$c_{ht}$	Horizontal tail volume coefficient	[-]
$c_{vt}$	Vertical tail volume coefficient	[-]
$C_L$	Lift coefficient	[-]
$C_D$	Drag coefficient	[-]
$C_M$	Moment coefficient	[-]
$C_{M_q}$	Pitch damping	[-]
$C_T$	Thrust coefficient	[-]
$C_P$	Power coefficient	[-]
$C_l$	Section lift coefficient	[-]
$C_d$	Section drag coefficient	[-]
$C_m$	Section moment coefficient	[-]
$S$	Surface area	[m <sup>2</sup> ]
$L$	Lift	[N]
$L_{ht}$	Horizontal tail arm length	[m]
$L_{vt}$	Vertical tail arm length	[m]
$D$	Drag	[N]
$D$	Diameter	[Nm]
$e$	Oswald efficiency factor	[-]
$P$	power	[W]
$\bar{c}$	Mean chord	[m]
$J$	Advance ratio	[-]
$Q_m$	Motor Torque	[Nm]
$I$	Current	[A]
$I_0$	Motor no load current	[A]

$I_{SC}$	Short circuit current	[A]
$K_v$	Motor speed constant	[RPM/V] , $[\frac{rads^{-1}}{V}]$
$V$	Voltage	[V]
$V$	Flight speed	[m/s]
$\mathcal{R}$	Motor internal resistance	[Ohm]
$W$	Weight	[N]
WC	Working condition	[-]
$\alpha$	Angle of attack	[deg]
$\beta$	Side slip angle	[deg]
$\eta$	Efficiency	[-]
$\rho$	Density	[kg/m <sup>3</sup> ]
$\mu$	Dynamic viscosity	[Ns/m <sup>2</sup> ]
$\nu$	Kinematic viscosity	[m <sup>2</sup> /s]
$\Gamma_{wing}$	Wing dihedral	[deg]
$\Lambda$	Sweep angle	[deg]
$\Omega$	Rotation rate	[rads <sup>-1</sup> ]
$\omega$	Angular frequency	[rads <sup>-1</sup> ]

## SUBSCRIPTS

$VT$	Vertical tail
$HT$	Horizontal tail

*Dedicated to my family and to the "Paparazzi Team"...*



# Résumé des Chapitres

## Introduction

L'utilisation accrue de véhicules aériens sans pilote exige d'atteindre des performances toujours plus grandes. Surtout sur la durée du vol, car en l'absence de pilote humain à bord, les opérations peuvent être menées sur des durées bien plus longues. En raison de l'exigence de mission de longue surveillance et de haute performance, la conception des nouveaux modèles est devenu plus difficile en raison du nombre d'opérateurs et de techniciens, de l'équipement, de la complexité et des coûts accrus. D'autre part, avec la miniaturisation de l'électronique, la possibilité de construire des drones de petite taille est devenu de plus en plus réalisable avec une grande efficacité opérationnelle et une mise en oeuvre simplifiée.

Cependant, la dégradation des performances va de pair avec les dimensions réduites. La capacité de générer de la portance diminue tandis que la traînée augmente lorsque la taille est inférieure à une certaine valeur. La figure 1.1 montre la dégradation soudaine des performances de portance et de traînée.

Dans cette étude, un nouveau concept de véhicule aérien sans pilote va être introduite, appelé *mini-drone de longue endurance*, qui doit pousser toutes les limites de chaque discipline afin de combiner les deux avantages des mini-drones et des drones de grande envergure. Le concept final doit avoir des performances relativement élevé, en particulier sur l'endurance, tout en restant facile à utiliser. L'objectif principal de cette étude sera de se concentrer sur l'approche de conception des aéronefs. Bien que les avions soient des systèmes pluridisciplinaires, la "conception d'avions" est une discipline à part entière de l'ingénierie aéronautique plutôt que la combinaison de toutes les disciplines analytiques tels que l'aérodynamique, la propulsion, le contrôle, etc .. Améliorer la performance d'un système pluridisciplinaire comme celui-ci ne peut être obtenue en se concentrant uniquement sur

un seul sous-système. L'approche doit être plus globale car chaque sous-système a un effet sur les performances du système final. Toutefois, il n'est pas toujours évident de déterminer le point de départ d'un nouveau design. La méthode de conception [8] présentée dans la figure 1.2 montre clairement que la conception peut commencer à partir de différentes étapes, tout en étant un processus itératif.

Ce fait montre clairement la nécessité d'un programme de conception qui peut être utilisé pour étudier l'effet de chaque sous-système sur la performance finale. Une méthodologie a été développée dans le but d'aborder ce problème d'une manière différente des méthodes de conception traditionnelles. La nouvelle méthode permet au concepteur d'explorer des solutions moins conventionnelles que les celles proposées par les méthodes traditionnelles.

## Concepte de mini-drone de longue endurance

Ce chapitre présente le concept de *mini-drone longue endurance* avec la description générale des drones, leurs types et leurs applications potentielles. Suite à cette brève introduction, plusieurs études récentes sont présentées. Les techniques, les domaines et les disciplines connexes qui peuvent être utiles pour l'amélioration de l'endurance sont également mises en évidence.

## Programme conceptuel pour la conception de mini et micro-drones (*Cdsgn*)

La conception d'un avion est un processus hautement multivariable et multidisciplinaire. Chaque variable a un effet sur les autres et sur la performance finale du système. En général, la définition de la mission dirige la conception vers sa forme définitive avec des contraintes prédéfinies. Un outil permettant d'analyser l'effet de chaque paramètre sur la performance finale de la conception en fonction de la définition de la mission est nécessaire afin d'optimiser la conception de manière appropriée.

A titre d'exemple, l'énergie qui peut être extraite avec les cellules solaires sont proportionnelles à leur surface. Si les cellules solaires sont placées sur le dessus de

l'aile, il est préférable d'avoir la plus grande surface de voilure par rapport au fuselage. En revanche pour une envergure d'aile donnée, une augmentation de la surface de l'aile ne sera pas favorable en termes de traînée induite, qui augmente avec une réduction de l'allongement. Toutefois, la surface de l'aile accrue permettra à l'avion de voler en croisière à une vitesse inférieure, conduisant à une consommation d'énergie plus faible. Bien d'autres aspects doivent également être pris en ligne de compte. Il n'est donc pas trivial de décider si une augmentation de la surface de l'aile est bénéfique ou non pour les performances de l'avion. Cet exemple explique brièvement la nécessité d'un outil comme *Cdsgn* pour la conception et l'optimisation de l'aéronef pour une mission spécifique. Une courte description de la première version de *Cdsgn* sera expliquée dans la première section, puis la version actuelle de *Cdsgn* de ses composants sera présentée dans le détail dans les sections suivantes.

## Aérodynamique

Dans ce chapitre, nous expliquons brièvement les principaux problèmes scientifiques qui sont soulevés par l'aérodynamique des mini et micro drones. Bien que les systèmes de propulsion de ces véhicules soient également liés à des problèmes aérodynamiques, ceux-ci seront pris en compte séparément dans le chapitre 5, *système de propulsion*.

L'objectif principal de ce chapitre est de déterminer la méthode d'analyse aérodynamique qui va être mise en œuvre dans le programme de conception (*Cdsgn*), présentée dans le chapitre 3. La figure 4.1 montre le diagramme sommaire du programme *Cdsgn*. Dans le bloc de modélisation, les caractéristiques aérodynamiques de l'aéronef doivent être analysées de manière précise et rapide. Ainsi, au lieu d'utiliser une solution complète de Navier-Stokes, l'accent est mis sur des méthodes simplifiées comme vortex-lattice et méthodes des singularités. Un certain nombre de programmes open-source pour l'analyse aérodynamique numérique vont être évalués. Leur mise en œuvre dans le programme de conception global avec certaines modifications sera également expliqué dans ce chapitre.

## Conception du système de propulsion

Pour un drone à propulsion électrique, le moteur consomme la plus grande partie de l'énergie. D'où l'importance de l'optimisation de celui-ci. Le point clé pour l'optimisation du système de propulsion est non seulement de trouver le meilleur moteur ou la meilleure hélice séparément, mais de déterminer la meilleure combinaison de ces deux éléments.

Les exigences de la mission jouent un rôle important sur la sélection et l'optimisation du système de propulsion. Plus d'une condition doivent être satisfaites, comme le décollage et le vol de croisière. Les travaux antérieurs de T.J.Mueller et al. présentent un bon exemple de choix d'un moteur et d'une hélice pour un mini-drone [9], mais il manque l'identification de chaque moteur et l'évaluation des performances lors des différentes phases du vol puisque cette information peut être utilisée comme un critère de sélection. Donc, dans ce travail, la sélection et les critères d'optimisation tiennent compte de toutes les phases de vol (*working conditions*).

Ce chapitre se concentre sur l'optimisation du processus de sélection du système de propulsion, pour une mission spécifique avec de multiples conditions. Le nouveau programme *QOPTIMIZER* sera présenté. Il permet de tester un grand nombre de combinaisons moteur/hélice. La sélection se fait en tenant compte des multiples conditions de vol dans les différentes phases de la mission.

## Energie

La source d'énergie et son stockage sont une des parties les plus critique dans la conception d'un drone de longue endurance. Plus l'énergie transportée à bord par unité de poids est importante, plus l'endurance sera grande, indépendamment des autres variables. L'amélioration de la source d'énergie et des performances de stockage est hors de la portée de cette thèse, mais la sélection de la quantité optimale de la masse d'énergie à bord est aussi important que leur performance.

Ce chapitre se concentre sur la source d'énergie et les modèles de stockage afin de prédire leurs performances pour une mission spécifique avec une grande précision. Comme indiqué dans les deux chapitres précédents, l'objectif principal est d'intégrer

ces modèles de prédiction dans *Cdsgn*. Comme l'effet de chaque prédiction du modèle joue un rôle important sur les variables finales de conception des aéronefs, il est important d'avoir une bonne connaissance et une estimation sur chaque source d'énergie possible.

## Micro-drone solaire hybride

Comme décrit dans le chapitre précédent, l'énergie solaire présente les meilleures performances en termes de faisabilité et d'application, afin d'être mis en uvre pour améliorer le temps de vol sur mini-drone.

En 2009, la Conférence/Compétition européenne Micro Air Vehicle a été organisé avec une mission distincte d'endurance. Cette possibilité a été utilisée pour concevoir le *Solar Storm* et le *Fire Storm*, et ainse voir la faisabilité de l'utilisation de cellules solaires sur des véhicules de moins de 50 cm d'envergure.

## Mini-drone de longue endurance: Eternity

Ce chapitre présente une étude de conception complète d'un mini-drone de longue endurance, appelé *Eternity*. L'objectif principal est de donner une idée claire de la faon dont le programme *Cdsgn*, expliqué dans le chapitre 3. En complément, des analyses détaillées sont présentées pour le dimensionnement de l'empennage horizontal afin de montrer les capacités supplémentaires de *Cdsgn*.

Bien que, la mission soit défini comme un vol le plus long possible avec un véhicule d'un mètre, il y a de nombreuses exigences et restrictions supplémentaires provenant du monde réel. Pour chacune d'elles, nous allons essayer de trouver une solution rationnelle offrant le meilleur compromis. En outre, au fur et à mesure de la conception, plusieurs décisions initiales ont dû être remises en cause. Les cellules solaires sont prévues pour être utilisées comme une source d'amélioration de l'endurance, une comparaison des versions solaires et non solaires étant réalisée à chaque phase de conception.

# Conclusion

## Principales Réalisations

Un nouveau concept de Mini-drone Longue Endurance a été introduit. L'importance de l'optimisation de chaque sous-systèmes vis-à-vis du système complet a également été mis en évidence. Un nouveau programme de conception, appelé *Cdsgn*, a été spécialement développé pour comprendre et étudier l'effet de chaque partie sur la performance finale du système complet.

Avec l'aide de *Cdsgn*, pour une mission de vol donné, il est possible d'étudier et de définir la configuration optimale de l'avion (avec ou sans empennage arrière), la surface de la voilure, l'envergure, la quantité d'énergie à bord, la vitesse de vol, la section et le profil aérodynamique de l'aile, etc .. En outre, avec une analyse de sensibilité permet de déterminer les parties les plus critiques de la conception en terme de performances.

Les points critiques qui empêchent l'amélioration de l'endurance pour des mini-drones ont pu être identifiés comme étant la source et le stockage de l'énergie, suivie par le système de propulsion. Comme l'amélioration du stockage de l'énergie ne sont pas l'objet de cette thèse, l'effort a été porté sur le système de propulsion. Un programme baptisé *Qoptimizer* a été développé afin de sélectionner le couple moteur/hélice optimal pour une mission donnée.

Plusieurs projets ont permis d'avoir un retour d'expérience concret sur l'utilisation de *Cdsgn*. Parmi ceux-ci, un micro-drone solaire hybride, appelé *Solar Storm* est présentée. Avec un demi-mètre d'envergure, le *Solar Storm* a démontré la faisabilité d'une amélioration de l'endurance avec 40% de sa consommation de croisière provenant de l'énergie solaire. Son compagnon le *Fire Storm* a été récompensé par le "Best Endurance Award" en 2011 lors de la compétition internationale IMAV aux Pays-Bas.

Un projet de mini-drone le longue distance, aussi appelé *Fly to Corsica*, a été lancé au sein de la thèse. L'objectif principal du projet était de voler de Nice (France) à Calvi (Corse) avec le plus petit drone possible. En conséquence, un drone de 1.5 m à propulsion électrique a été conçu avec la capacité de voler 250 km. Le projet a non seulement consisté à l'optimisation de la cellule et du système de propulsion,

mais aussi d'autres défis tels que la liaison de données par satellite, l'intégration de l'avionique et la gestion des opérations avec deux stations de contrôle distinctes.

Enfin, afin de voir la faisabilité du concept de mini-drone longue endurance, un prototype appelé *Eternity* a été conçu et fabriqué. Gardant à l'esprit les besoins pour un engin compact, *Eternity* est également conçu pour être transporté démonté dans un bagage à main de 50 cm de dimension. Avec une envergure d'un mètre, *Eternity* peut voler pendant 4h sans l'énergie solaire, et jusqu'à 8h avec l'énergie solaire dans les meilleures conditions.

## Travaux Futurs

La méthodologie de conception introduit a été maintenue aussi simple que possible pour une gamme restreinte de mini-drones, en particulier en raison de la modélisation de la structure. Afin d'élargir la taille du véhicule, les modèles peuvent être soit davantage simplifiés afin d'avoir une plus grande gamme d'échelle en faisant un compromis sur la précision ou rendue plus complexe avec des modèles différents au prix d'une augmentation de la complexité et du temps de calcul.

Sur l'amélioration de l'endurance, en plus de la conception du véhicule lui-même, le vol peut également être optimisé en terme de stabilisation et de navigation. Un meilleur contrôle de stabilisation peut être mis en œuvre afin de rester sur le point de performance optimale du véhicule. En outre, un système de navigation de niveau supérieur peut permettre d'extraire l'énergie de l'environnement, comme l'exploitation des thermiques, afin de prolonger le vol.



# Chapter 1

## Introduction

### 1.1 Motivations

Increased use of unmanned air vehicles brought together the high performance demands. Especially on the flight duration since there is no human pilot on-board limiting the safe operation durations. As a result of high performance and long time surveillance mission demands the new designs became bigger in size and more difficult to operate because of additional crew number, equipment, complexity and increased cost. On the other hand, with the miniaturisation of the electronics, the possibility of building small size of UAVs became more and more feasible with higher operational efficiencies.

However, the performance degradation comes along with the small size as a nature. The capability of producing lift decreases while the drag increases when the size becomes smaller than a certain value corresponding to the geometry. Figure 1.1 shows the sudden degradation of both lift and drag performance.

In this study, a new unmanned air vehicle concept is going to be introduced called *Long Endurance Mini UAV* which has to push all the limits to the edge on every discipline in order to combine both advantages of mini-UAVs and the bigger UAVs. The final concept is going to have comparatively high performance, especially on the endurance, and still be easy to operate. The main objective of this study will be to concentrate on the aircraft design approach. Aircraft, being a multidisciplinary system, yet "aircraft design" is a separate discipline of aeronautical engineering rather than the combination of all the analytic disciplines such

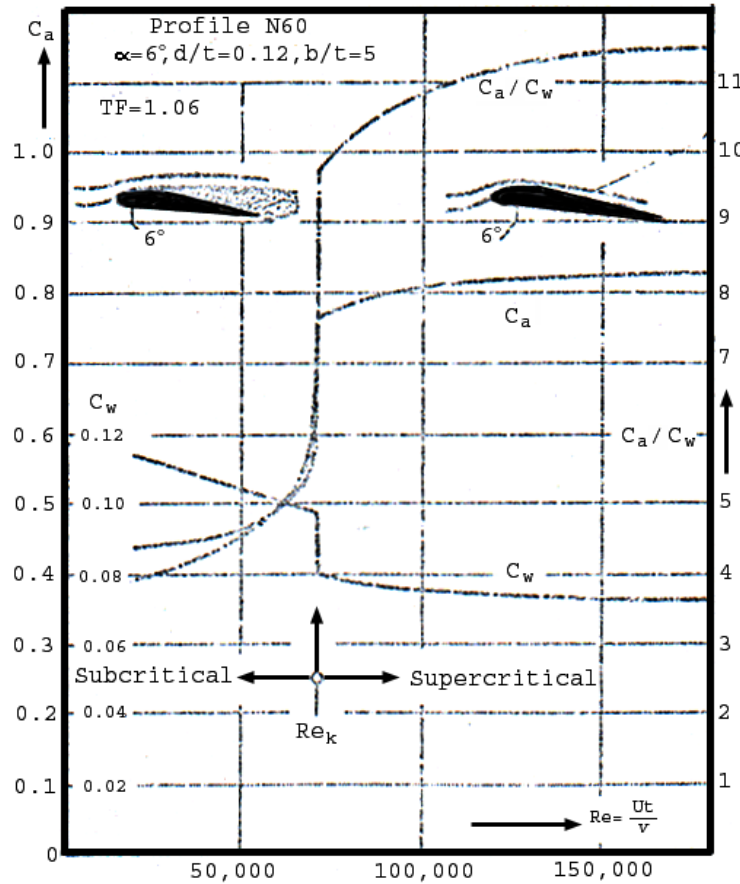


FIGURE 1.1: Critical Reynolds plot from Schmitz [1] showing the N60 airfoil's lift ( $C_a$ ) and drag ( $C_w$ ) coefficient variation with respect to the airfoil's critical Reynolds number. The huge disadvantage of low  $Re$  number is clearly visible on the plot.

as aerodynamics, propulsion, control, etc... Improving the performance of a multi-disciplinary system like an aircraft can not be obtained by only concentrating on one particular subsystem. The approach should be more global as each subsystem has an effect on the final system performance. However, it is not always obvious to state the starting point of a new design. The design wheel[8] in the figure 1.2 clearly shows that the *design* can start from different steps. The design is an iterative effort.

This fact clearly shows the need for a conceptual design program that can be used to investigate the effect of each subsystem on the final performance of the design.

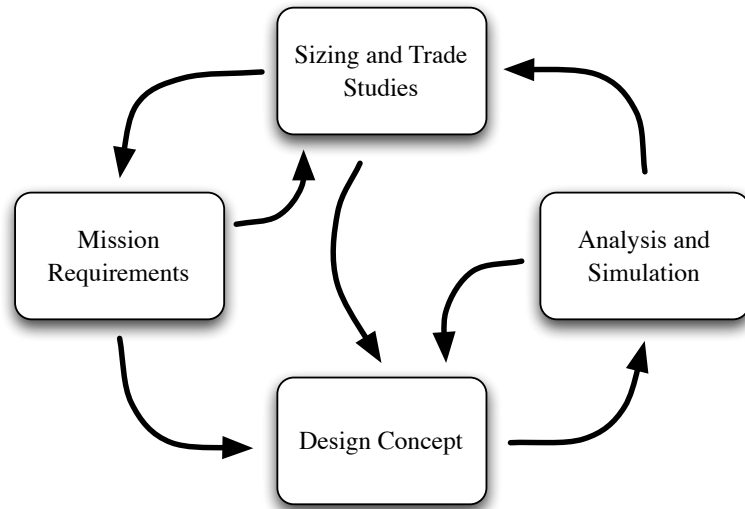


FIGURE 1.2: The design wheel.

A conceptual design methodology and program is developed in order to approach this problem in a different way than the traditional design methods. The new developed method lets the designer came up with *out of the box* design solutions that can perform better than its precedents.

## 1.2 Objectives

The main objectives of this study are :

- Show the feasibility of a long endurance mini-UAV concept.
- Clearly define and analyse the key aspects that restricts the enhancement of endurance on mini-micro scale unmanned air vehicles. State the possible path to further improve and approach to the operational limits on each aspect.
- Further understand the interactions of each subsystem with each other and their final effect on global performance of the design.
- Develop a conceptual design program (*Cdsgn*) that is simple and computationally fast, but yet physically accurate to evaluate performance of several aircraft configurations.

- Validate the *Cdsgn* program for real life applications with real operational flight tests.

## 1.3 Contributions

As a result of the effort given to develop a conceptual design methodology, particularly for mini UAVs, the following contributions have been done :

- A study is made for the feasibility of a long endurance mini UAV, including a solar micro air vehicle ”*Towards a Long Endurance MAV*”[10, 11]
- A long range mini UAV project has been started as a student project with an objective of flying from Nice to Corsica (185 *km*) with the smallest electrically powered UAV ”*Flying Autonomously to Corsica: A Long Endurance Mini-UAV System*”[12]
- A new conceptual design methodology and program is developed (*Cdsgn*) particularly devoted to mini-UAVs.
- An electric propulsion system optimisation methodology and program is developed (*Qoptimizer*) and presented as ”*Multi-Point Optimization of A Propulsion Set As Applied to A Multi-Tasking MAV*”, [13].
- Several mini-UAV prototypes manufactured *Solar-Storm*, *Fire-Storm*, *SPOC*, *Eternity* which gave hands-on experience for further improving the design methodology.

## 1.4 Structure of the Thesis Document

Following this brief introduction chapter, explaining our motivation for the subject, defining the primary objectives and stating the contributions to the field, the following chapters will explain;

- **Chapter 2** introduces the new *Long Endurance Mini-UAV* concept and the state of the art, starting with a general description of UAVs and their applications.

- **Chapter 3** explains deeply the conceptual design program (*Cdsgn*), that is developed, shows the low order models selected for each sub part of the system.
- **Chapter 4** highlights the problems that are encountered in the design of mini-micro scale UAVs in an aerodynamic point of view. Some external open source aerodynamic analysis programs are briefly presented and a comparison of these programs is shown with an example case versus wind-tunnel measurements.
- **Chapter 5** mainly concentrates on the methodology of choosing an electric motor and a propeller couple for a defined mission. The software *Qpoptimizer*, which is developed for this purpose is explained with the results of an example design case. The required basic knowledge and the experimental characterisation process for the electric motors and propellers are also presented in the chapter.
- **Chapter 6** explains the possible energy source and storage technologies that can be used for long endurance mini-UAV concept. Mass and performance prediction of lithium batteries and solar cells are shown as they have an important impact on the final performance of the vehicle via optimum amount of on-board energy selection.
- **Chapter 7** presents the world's first hybrid solar powered micro air vehicle at its scale that has the autonomous navigation capability. Being originally designed for *2009 European Micro Air Vehicle Competition and Conference* for long endurance mission task, *Solar Storm* and its non-solar version *Fire Storm* also demonstrates the feasibility of usage of solar energy systems for micro air vehicle size (50 cm maximum dimension) with a custom designed Maximum Power Point Tracker (MPPT) power management system.
- **Chapter 8** presents the main output of this thesis, a long endurance mini-uav prototype called *Eternity*. The chapter explains the application of *Cdsgn* program on the design, all the decisions made in the design phase, the expected performance, wind-tunnel measurements and flight tests.
- Final chapter **Conclusion** describes the main achievements for the study and give a brief view of the planned future work.

An appendix is included for the interested readers and UAV enthusiasts as it includes flight tests and manufacturing phase of two projects :

- A long range mini UAV system is presented, starting with mission description up to the mission attempt. All the phases between are also described including the design, manufacturing, wind-tunnel experiments, flight tests, encountered problems.
- Custom build propeller, an application of *Qpoptimizer* is explained. Once the design of the propeller is finished, the manufacturing process is shown. Finally, the wind tunnel results of the propeller is shown for different conditions.

# Chapter 2

## Long Endurance Mini-UAV Concept

### 2.1 Introduction

This chapter presents the new introduced *Long Endurance Mini-UAV* concept starting with the general description of UAVs, their types and potential applications. Following that brief explanation, a state of the art and several recent studies are presented. The techniques that can be useful for endurance enhancement are also highlighted among those studies. Finally, the most important areas and the related disciplines are determined that has to be focused on in order to enhance further the endurance capability of a *Long Endurance Mini-UAV* concept.

### 2.2 Unmanned Air Vehicles

An *unmanned air vehicle* (UAV), also known as *drone*, is a flying platform that is remote controlled by a pilot or an operator or autonomously navigates and stabilise itself without external input. Their size and shapes varies a lot as shown in figure 2.1. Miniaturisation of the on-board electronics made it possible to build operational UAVs that can fit into a pocket. On the other end of the envelope, UAVs that are in the size of commercial aircrafts exists such as Global Hawk with 35 *m* wing span shown also in figure 2.1.



FIGURE 2.1: Various UAVs with different size and application purposes(wiki) on the left and Global Hawk UAV with on the right.

Among several UAV types, only the most relevant two types will be explained in the content of the thesis, that are long endurance and mini-UAVs.

### 2.2.1 Long Endurance Unmanned Air Vehicles

Long endurance UAVs generally have spans bigger than twenty meters and have the capability to fly more than a day time. *Condor* UAV[14] from Boeing, has a span of  $60\text{ m}$  and flies  $59\text{ hours}$ . The smallest UAV that can be specified as a long endurance UAV is the *Aerosonde* with  $3\text{ m}$  span and a flight time of more than  $30\text{ hours}$  (without payload).

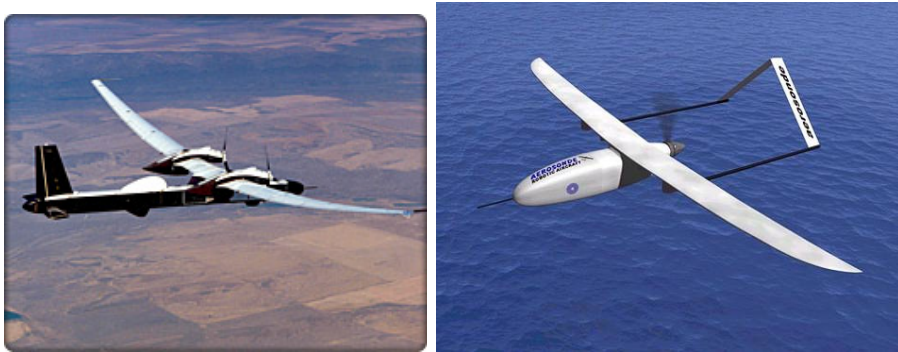


FIGURE 2.2: Condor and Aerosonde.

Figure 2.2 shows the Condor and Aerosonde UAVs. As a result of their big size, the operation of these types of UAVs requires additional complexity. Numerous people has to work in the ground segment, and usually launch and landing phases requires a real air field or in some cases complex devices such as launchers or catching mechanisms. A launcher example is shown in figure 2.3 which is required for Scan Eagle UAV in comparison to easy launch of mini-UAVs.



FIGURE 2.3: Scan Eagle while being launched with a catapault system in comparison to elastic launch of WASP mini-UAV.

### 2.2.2 Mini Unmanned Air Vehicles

Although there are several definitions for the maximum size of the Mini and micro air vehicles, generally UAVs under two meter of maximum size called as *mini* and under half a meter size is called as *micro*. Figure 2.4 shows the well known Wasp and Blackwidow from Aerovironment Company[15] who has been leading the UAV market for mini and micro scale UAVs.



FIGURE 2.4: WASP and Blackwidow from Aerovironment.

The ease of operation and being compact brings an important advantage to the mini and micro UAVs. Especially as the small size comes with a lower system cost, more and more opportunities became possible.

### 2.2.3 Potential Applications

UAVs are often preferred for missions that are too "dull, dirty, or dangerous" for manned aircraft. Despite the fact that the largest use for the UAVs were in

military applications, more and more civil applications started to arise. Several applications can be listed such as, aerial surveillance, scientific research, pipeline security and investigation, border security or even search and rescue. The decrease in cost is giving the opportunity to use UAVs in a lot of amateur use such as personal video recordings by the help of new lightweight high definition portable cameras.

## 2.3 Long Endurance Flight

As UAVs became more and more operational, the demands for their performance keep increasing everyday. Especially the need for longer flight duration arise rapidly. Long endurance flight capabilities of the UAVs became more and more important. However, as an additional outcome of long endurance flight, the aircraft size and total mass increase as well. Resulting systems became harder to operate and require more people as can be seen in figure 2.5.



FIGURE 2.5: Global Hawk long endurance UAV (36 *hours*) with its operating crew.

One of the most ambitious projects on the long endurance flight is the *Solar Eagle* previously known as *Vulture* (figure 2.6). The Defense Advanced Research Projects

Agency (DARPA) have been working on the demonstrator in order to show the feasibility of a single high-altitude UAV to operate continuously on-station for a period of five years.



FIGURE 2.6: Solar Eagle on the left, previously known as Vulture from DARPA which is planned to be launched in 2013 and Zephyr UAV on the right, from QinetiQ.

Efforts also given to minimize the size of the vehicle while trying to keep the long endurance capabilities. *Zephyr-UAV* from Qinetiq is a good example. With a span of  $22.5\text{ m}$ , *Zephyr* uses lithium sulfur batteries as the energy storage and uses high efficiency solar cells on its wing surface. Officially approved by Fédération Aéronautique Internationale (FAI) in 2010, *Zephyr* (figure 2.6) broke the world record both for endurance and altitude by flying  $336\text{ hours}$  and  $22\text{ minutes}$  and reaching up to  $70,741.5\text{ ft}$ .

### 2.3.1 Long Endurance Mini-UAV Concept

The main objective for the new *long endurance mini-UAV* concept is to combine the properties of the two concept by being compact, easy to operate and have more endurance. This will lead the use of UAVs on much simpler operations and open a bigger field of application which should result with a back loop on increase in technology and cost decrease because of increased use. Figure 2.7 shows where the new concept corresponds for size and performance in comparison to existing UAVs. The new concept should be easily carried and operated by one person only. The limited size also increase the safety of the vehicle as the lower weight and flight speeds will not be as dangerous as the big UAVs in case of a crash.

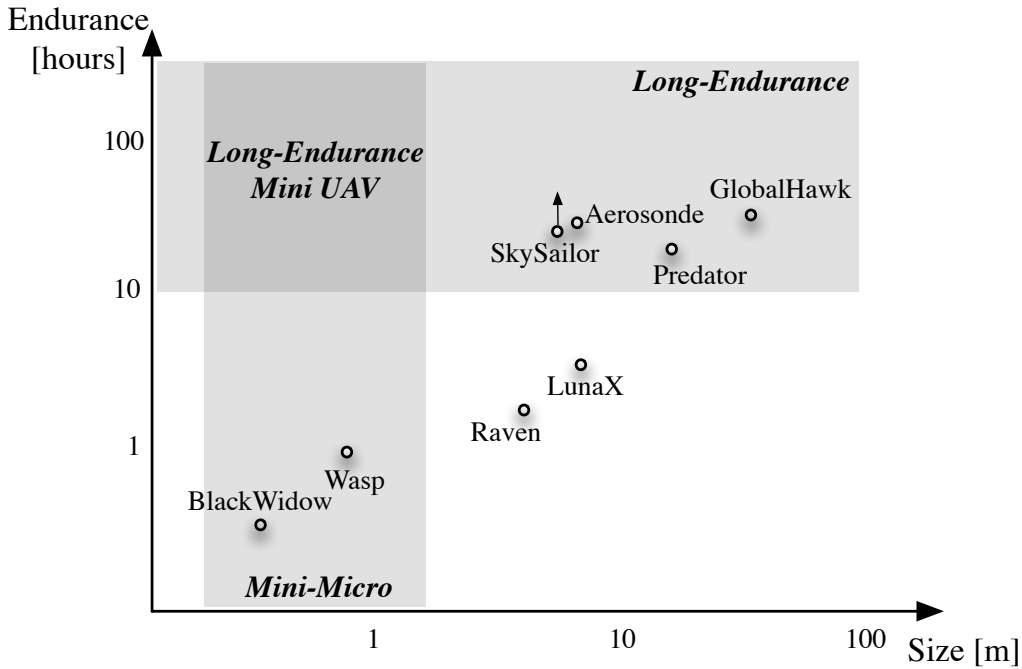


FIGURE 2.7: Performance versus size chart showing where the new *Long Endurance Mini UAV Concept* corresponds to.

## 2.4 State of the Art

The *long endurance mini uav* concept is a new concept. There are not a lot of studies on the literature, however there are some studies and projects with similar objectives but for different scale of aircrafts. Some of these studies that has the features which can be applied to mini scale UAVs are listed below. Especially the use of solar energy is very common for endurance enhancement.

So-Long solar UAV, shown in figure 2.8, managed to fly for 24 *hours* in 2005. It has a wing span of 4.75 *m* and weights 10.8 *kg*. Although it can not be counted as a mini UAV, still the record flight was the first continuous flight for its kind. The importance of high efficiency propulsion system has been enlighten in the project with a custom electronic speed controller designed by the company itself.

With the increased battery efficiencies and a more minimized approach, *Sky Sailor* demonstrated 27 *hours* of flight showing the feasibility of continuous flight with a 3.2 *m* span solar aircraft. Noth [16] developed a design methodology that investigates the day and night energy equilibrium that satisfies the continuous flight for different size of aircraft.



FIGURE 2.8: So Long solar UAV.



FIGURE 2.9: Sky Sailor.

Another very important study is the *Sun Surfer* [17] which is a scaling down study of Noth studied by Diepeveen. It is an effort to build a solar mini UAV under 1 m span size. With the help of their design program, it is proven that the required technology to have a continuous flight does not exist for that scale especially with the reduced aerodynamic and propulsion efficiencies. However the mission for *Sun Surfer* is selected to achieve a day time solar flight disregarding the night which is already a big challenge for that scale. The resulted design is a 70 cm aircraft which is powered by solar cells inside its wings. The study showed the feasibility of staying aloft by using only the solar energy in some of the test flights, however the fragile structure and the propulsion mechanisms showed the difficulties of being robust and lightweight at the same time on this scale.

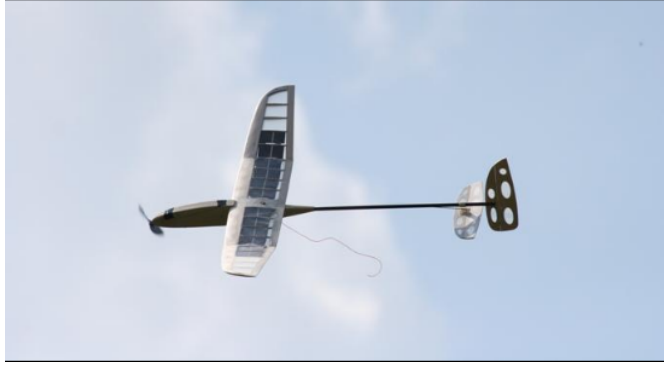


FIGURE 2.10: Sun Surfer.

## 2.5 Possible Improvement Areas

In the light of previous studies, the important areas that requires improvement for a new long endurance mini UAV concept are defined. They can be listed as to model the aerodynamics for the mini UAV scale accurately, improve the propulsion efficiency by choosing or designing a motor propeller couple specific for the long endurance mission, and finding high energy density batteries. While the three main disciplines have been defined, the most important phase is to select the correct design variables in order to design the UAV for an optimum mission performance. The next chapter will present the new conceptual design program devoted for mini UAV design and the following three chapters are going to discuss about the three main disciplines aerodynamics, propulsion and energy those have to be focused for endurance enhancement.

# Chapter 3

## Conceptual Design Program Devoted to Mini and Micro UAV (*Cdsgn*)

### 3.1 Introduction

The design is a highly multivariable and multidisciplinary process. Each variable has an effect on the other variables and on the final performance of the system. Generally the mission definition leads the design to its final shape with the pre-defined constraints. If there is not enough constraints, then the optimisation of the design becomes even more difficult as the choices are increased with increased range of parameters. A tool that can analyse the effect of each parameter to the final performance of the design according to the mission definition is needed in order to optimise the design appropriately.

As an example, the design study of a solar powered MAV with a limited wing span can be given. The energy that can be extracted with the solar cells are proportional to their surface area, basically the more the better. If the solar cells are decided to be placed on top of the wing, it is preferable to have relatively larger wing surface area. On the other hand for a given wing span, after a point, increasing the wing area will not be favourable in terms of induced drag component which is increasing because of reduced aspect ratio (in the case of limited span for mini and micro aerial vehicles). However, the increased wing area will let the

aircraft cruise at a lower speed which will lead to lower power consumption. Also with the increased wing surface area, the amount of extra on-board energy that can be carried will be increased for a given wing loading. The given example case will be examined more deeply in chapter 7. Finally it is not trivial to decide if the increased wing area is beneficial or not for endurance or range performance of the aircraft. This example briefly explains the need for a tool like *Cdsgn* for designing and optimising aircraft for a specific mission. A small description of the early version of *Cdsgn* will be explained with the required modifications in the next section, and then the following sections will explain the current version of *Cdsgn* program and its components one by one in detail.

## 3.2 Early Version of *Cdsgn*

For the first versions of *Cdsgn*, the main optimisation parameter was the range and endurance performance. The program was focused on the feasibility of maintaining a certain range or endurance performance on the design that is created with the given variables. Figure 3.1 shows the main program flow of the earlier version of *Cdsgn*.

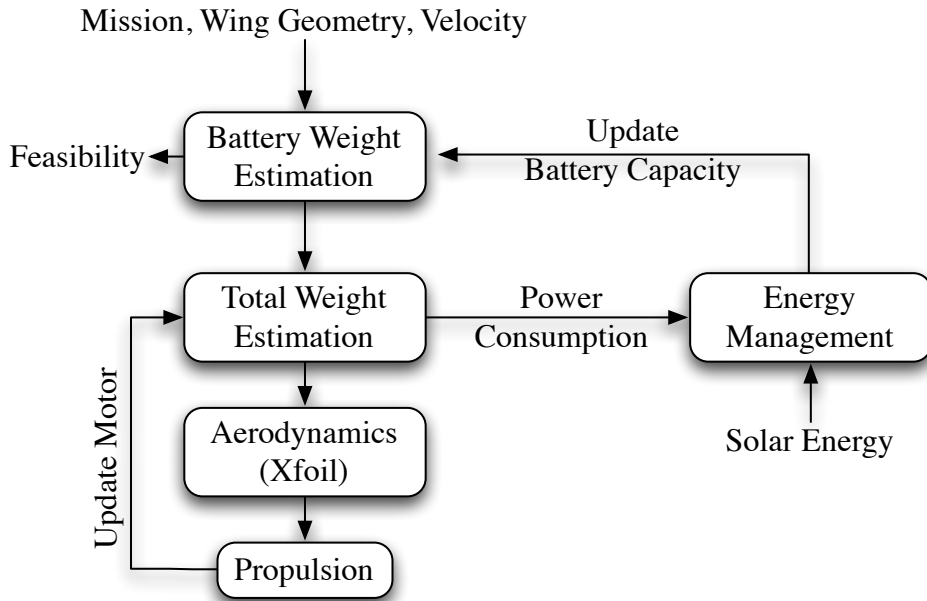


FIGURE 3.1: The main program flow of the early version of *Cdsgn*.

The mission is given as either range or endurance performance, and wing geometry is given as a range of span and surface area, the limitation of the flight speed also

exists as minimum and maximum values. Then each possible span and surface area combination is examined within the given flight speed range to reach the mission range or endurance performance. As a starting point of the design loop, first the battery estimation is done, usually this is a small value just to get started. Then according to the span and the wing surface area the other components of the aircraft are selected automatically. As an example, the tail moment arm is defined as a ratio of the wing span, and with the predefined tail volume coefficient and tail aspect ratio, the horizontal tail dimensions are calculated.

Next, the total weight of the aircraft is estimated including all the structure, on-board electronics, battery, propulsion system, payload. Knowing the estimated total weight and the desired cruise speed, the level flight cruise lift coefficient can be derived from equation 3.1.

$$W = L = \frac{1}{2}\rho V^2 S_{wing} C_{Lcruise} \quad (3.1)$$

The total drag of the aircraft is calculated via equation 3.2 which includes all the component drag sums shown in equation 3.3 which are normalised by  $S_{wing}$  wing surface area.

$$D = \frac{1}{2}\rho V^2 S_{wing} C_{Dtotal} \quad (3.2)$$

$$C_{Dtotal} = C_{Dwing} + C_{Dhtail} \frac{S_{htail}}{S_{wing}} + C_{Dvtail} \frac{S_{vtail}}{S_{wing}} + C_{Dfuselage} \frac{S_{fuselage}}{S_{wing}} + C_{Dinterference} \quad (3.3)$$

The drag component generated by the wing has two main subcomponents, profile and induced drag, where profile drag being the sum of form and skin friction drag components. The induced drag is simply calculated by equation 3.5 with a fixed span efficiency factor. Assuming a fixed span efficiency factor keeps the approach simple enough to be fast in computation with a compromise of disregarding the additional effects of different wing planform shapes. The profile drag coefficient of the wing is determined from an airfoil database calculated by XFOIL<sup>1</sup> for each Reynolds number. The corresponding airfoil drag polar is selected according to the mean aerodynamic chord and the flight speed of the aircraft. Then the drag

---

<sup>1</sup>[raphael.mit.edu/xfoil/](http://raphael.mit.edu/xfoil/)

coefficient that corresponds to the cruise flight lift coefficient is taken as parasitic drag of the wing airfoil.

$$C_{D_{wing}} = C_{D_{profile}} + C_{D_{induced}} \quad (3.4)$$

$$C_{D_{induced}} = \frac{C_{L_{wing}}^2}{\pi A Re} \quad (3.5)$$

Referring to Prandtl-Naylor theorem (which states that the minimum drag will be obtained once the tail is aligned with the down-wash of the wing so that it does not generate any lift or down force), it is assumed that the wing generates all the necessary lift and the tail does not generate any lift or down force. This simplification determines the lift coefficient of the horizontal tail as zero, thus the induced drag becomes zero as well. The same type of airfoil database determined profile drags are used on both horizontal and vertical tail drag coefficient calculations.

The maximum thickness of the fuselage is determined in the inputs which is a function of the size of the electronics that needs to fit inside. As the length of the fuselage is determined by a ratio of the wing span, the surface of the fuselage therefore calculated with an elliptic fit. Then the drag component of the fuselage is calculated in terms of its surface area's skin friction drag corrected by its fineness ratio, which is calculated by the ratio of the diameter of the fuselage to the length of it,  $d/l$  [18].

$$C_{D_{wetfuselage}} = C_f [1 + 1.5(d/l)^{3/2} + 7(d/l)^3] \quad (3.6)$$

Where the laminar and turbulent skin friction coefficients are calculated by equation 3.7 and 3.8. The length of the laminar flow can be determined externally, but in most of the calculations, all the surface assumed to have turbulent flow as the propeller slipstream assumed to go through the whole fuselage.

$$C_{f-laminar} = \frac{1.328}{\sqrt{Re_l}} \quad (3.7)$$

$$C_{f-turbulent} = \frac{0.427}{[\log Re_l - 0.407]^{2.64}} \quad (3.8)$$

Finally all of the component drag coefficients are summed. Additionally a user defined constant interference drag coefficient is added to the total drag, which can be based on previous experiences or empirical methods. After obtaining the total drag of the aircraft, the required power is calculated with fixed propulsion efficiency coefficients. According to the required power, motor weight is updated and the total weight estimation loop continues till convergence. Once it is converged, the additional energy source merging is done if exists and final power consumption is obtained.

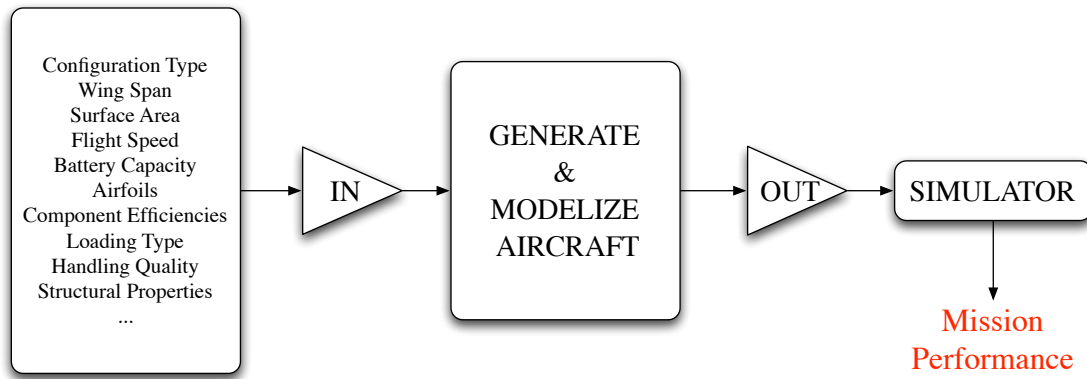
The mission performance is calculated with the available battery on-board to see the feasibility. The battery update loop continues till the mission performance is being satisfied or the battery weight range exceeds. If it is proven to be feasible then the combination of wing geometry, flight speed and the battery weight are saved as a candidate aircraft. Whole envelope of the inputs are tried and finally the selection is done among the feasible candidates.

Calculating everything analytically makes it extremely fast to compute for each candidate, thousands of candidate can be evaluated in few seconds. However, in order to make the design program more accurate, the modified AVL program, which has been described in chapter 4, is added into the design loop. Having the modified AVL program running in the design loop made the computation much slower, but on the other hand it allowed to have the wing tail interaction, different planform effects of each lifting surfaces, complete trim drag addition, more accurate span efficiency determination, better stall estimation and the comparison of different wing section airfoils.

### 3.3 Current Version of *Cdsgn Program*

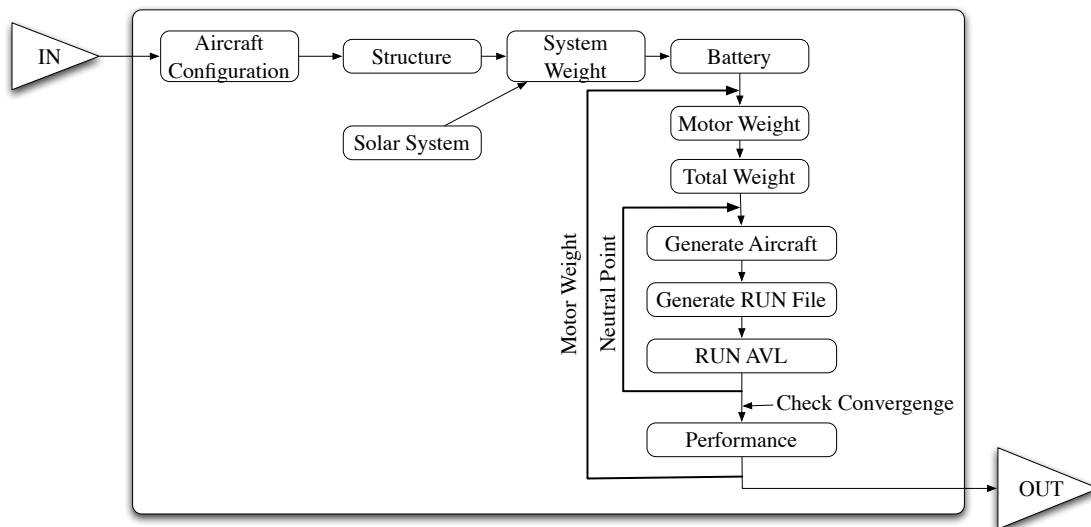
The addition of the modified AVL program into the design loop increased the precision of the computations but with the additional complexity. In order to keep the design procedure simple and flexible for future improvements, the flow of the design loop has been changed as shown in figure 3.2.

Basically, the variables in the input file is increased because of the required AVL variables, then the aircraft generation and analyse is done in a separate block, finally all the characteristics of the aircraft is generated as output. The simulation is also done in a separate block in order to be more flexible. By that way, the

FIGURE 3.2: The flow chart of the current version of *Cdsgn* program.

simulation can be as simple as maximum distance flight or more complex like an endurance flight with different speed setting and addition of solar cells with a realistic sun irradiation change during the flight time and the optimisation of exact launching time of the aircraft. Being a separate block gives the flexibility of using an external simulation program in case of need.

A closer look at the *Generate and Modelize Aircraft* block is shown in figure 3.3.

FIGURE 3.3: A closer look at the *Generate and Modelize Aircraft* block of the design loop.

### 3.3.1 Aircraft Configuration Selection

In the current version of the program, there are two types of configurations, *Conventional* and *Flying wing*. In order to compare and analyse a wide range of span

and wing area for the two configuration, a simplified approach is used. The main idea is to relate every basic dimension of the aircraft to span and wing area. Otherwise the program would have more complexity and unreliability. Figure 3.4 shows two different automatic generated configuration.

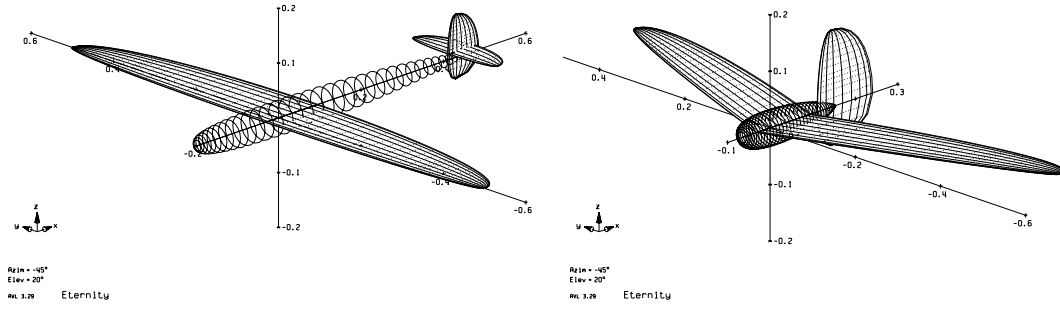


FIGURE 3.4: Examples of two different automatic generated aircraft configurations by *Cdsgn*.

As the propeller wing interaction is not modelled, there is no specifications for the motor number on the configurations, propulsion set is defined by its efficiencies only.

For conventional configuration, fuselage length is taken as a fixed percentage of the wing span, and tail moment arm is also taken as a fixed percent of the fuselage length by referring to some of the same scale model aircrafts and UAVs. Vertical and horizontal tail moment arms are assumed to be identical. These values are taken as constant for the beginning, however they can be changed in the input file or can be used as a variable to make a sensitivity analysis. Fineness ratio is defined by the length to the maximum width of the fuselage as in equation 3.9 and is selected as 15 for default which can be changed in the input file.

$$FR = \frac{l_{fuselage}}{d_{max}} \quad (3.9)$$

For flying-wing configuration, fuselage length is taken in reference to mean aerodynamic chord and the fineness ratio is selected as 10 for default. The wing sweep angle  $\Lambda$  is added to the inputs as a variable, the horizontal tail moment arm  $L_{HT}$  is taken as zero automatically and the vertical tail moment arm  $L_{VT}$  is calculated by equation 3.10.

$$L_{VT} = \tan(\Lambda) \frac{b_W}{2} \quad (3.10)$$

After fixing the volume coefficients and tail moment arm lengths, required area for vertical and horizontal tail is calculated by equation 3.11 and 3.12.

$$S_{VT} = \frac{c_{VT} b_W S_W}{L_{VT}} \quad (3.11)$$

$$S_{HT} = \frac{c_{HT} \bar{c}_W S_W}{L_{HT}} \quad (3.12)$$

The tail volume coefficients are defined in input file normally, but as a default they are taken as  $c_{VT} = 0.02$  and  $c_{HT} = 0.5$  as suggested in [8].

Later, in order to have the corresponding Reynolds regime of the tail surfaces, mean chords are calculated by the equations below. Aspect ratios of the surfaces are fixed and defined in the input file for horizontal and vertical tail consecutively.

$$b_{htail} = \sqrt{S_{htail} AR_{htail}} \quad (3.13)$$

$$b_{vtail} = \sqrt{S_{vtail} AR_{vtail}} \quad (3.14)$$

$$\bar{c}_{htail} = \frac{S_{htail}}{b_{htail}} \quad (3.15)$$

$$\bar{c}_{vtail} = \frac{S_{vtail}}{b_{vtail}} \quad (3.16)$$

The fuselage information only consists of the length and the maximum diameter. The generation of the fuselage surface is going to be taken care of in the modified AVL program further in the loop, but for the structural weight estimation a rough value is required. For that reason, the fuselage surface is calculated by the help of fineness ratio and fuselage length. Additionally, as it is assumed that the fuselage is going to be thicker in the front and becomes much thinner at the tail section, a correction factor  $k_{fuselage-form}$  (defined in the input file and an appropriate value is around 0.6) is used to estimate the wetted area more accurately as shown in equation 3.17.

$$S_{fuselage} = l_{fuselage} d_{max} \pi k_{fuselage-form} \quad (3.17)$$

### 3.3.2 Structural Mass

After selection of the aircraft configuration, the structural mass of each component needs to be estimated. Each component mass is estimated by empirical formulas which can be changed according to user needs.

#### Wing Mass

Wing mass is directly proportional to the surface area. Also as the wing span increases, the bending moment acting on it increase proportionally especially at the root section. So an empirical formula is used with a span correction to calculate the wing mass for a variety of span and surface area.

As we have been interested in a mini-micro UAV scale, a possible building technique and candidate materials are taken into account for determining the mass density for unit surface area. Latest building techniques use composite materials with sandwich structures, which is proven to be the best technique for the mini UAV scale.

The assumed building technique uses a lightweight thin fiber glass cloth on the surface, a sandwich core material (such as Airex) in the middle for increasing the area moment of inertia of the skin and finally another layer of thin fiber glass to have a closed sandwich skin. This brings up the top surface skin together, and the bottom surface skin is build up of the same materials and the same technique. Kevlar and carbon tissue is also used on the necessary places like the flaperon hinge line, leading edge closed structure D-box, etc... The main spar is assumed to be made of unidirectional carbon fiber connected with a shear web between. Equation 3.18 is used to calculate the wing mass.

$$M_{wing} = \left[ (2\rho_{Core}d_{Core}) + \left( \left( \frac{b_{wing}}{0.5} \right)^{0.5} 4\rho_{Layup} \right) \right] S_{wing} + k_{spar}(\bar{c}_{wing})^2 b_{wing} \quad (3.18)$$

$\rho_{Layup}$  =Layup density

$\rho_{Core}$  =Sandwich Core density

$d_{Core}$  =Sandwich Core thickness

$k_{spar}$  = Spar weight coefficient

It can be realised that in the first part of the equation, a core weight corresponding to the wing wetted area (two times the total wing area) is taken. Tissue weight is being calculated directly proportional to the wetted area as well with taking into account the span effect. Which is, as the span increases, the bending moment carried by the root part of the wing needs to be reinforced with more additional material.

The second part of the equation roughly estimates the additional spar mass proportional to the wing span, mean chord and wing's thickness.

### Fuselage Mass

Fuselage mass is calculated simply by using the fuselage wetted area and the composite tissue mass. The fuselage length is added as a multiplier in order to simulate the additional need for reinforcement and mass when it enlarges.  $k_{fuselage}$  (appropriate value is usually between 4-6 according to build-up experience) coefficient is determined according to estimated composite layer number.

$$M_{fuselage} = S_{fuselage} \rho_{Layup} k_{fuselage} L_{fuselage} \quad (3.19)$$

### Horizontal and Vertical Tail Masses

Horizontal and vertical tail masses are calculated with the same method used in wing mass calculation. Differently, there is no additional spar mass.

### Miscellaneous Mass

A fixed percentage of the total wing mass is taken as miscellaneous mass representing the connections, additional hinge material, building errors, etc... Taking  $k_{miscellaneous} = 0.08$  gave good results when compared to previously build composite parts.

$$M_{miscellaneous} = M_{Wing} k_{miscellaneous} \quad (3.20)$$

## Total Structure Mass

Total structure mass is simply the sum of all above explained parts.

$$M_{TotalStructure} = M_{Wing} + M_{Fuselage} + M_{H.Tail} + M_{V.Tail} + M_{miscellaneous} \quad (3.21)$$

### 3.3.3 System Mass

System mass includes all of the fixed and predefined components of the aircraft which are defined in the input file, such as :

- Autopilot
- Payload
- Sensors
- Modem
- Servo(s)
- Additional boards
- etc...

### 3.3.4 Motor Mass

Motor mass is being calculated separately as it is not fixed. Selected as a "rubber motor", it is being updated in every loop according to the calculated ideal power value, which is simply the multiplication of aircraft drag and flight speed. Among the well known electric motor brands, the  $k_{motor}$  coefficient in  $[kg/W]$  is estimated to be around 0.003. In the case of a need for steep climb performance, this value can be defined up to 0.01 in the input file.

$$M_{motor} = P_{ideal} k_{motor} \quad (3.22)$$

### 3.3.5 Battery Mass

Battery mass is calculated according to a fixed specific energy value which is defined in the input file by the user. A reasonable value for  $k_{battery}$  will be between  $185 - 230 Wh/kg$  according to current lithium polymer battery technology that is explained in chapter 6.

$$M_{battery} = \frac{(Capacit_{ybattery} * Volt_{battery})}{k_{battery}} \quad (3.23)$$

### 3.3.6 Total Mass

In Total Mass part, all of the component masses are summed.

$$M_{TotalMass} = M_{TotalStructure} + M_{System} + M_{Motor} + M_{Battery} \quad (3.24)$$

### 3.3.7 Aircraft Generation for AVL

The AVL program uses an input file that defines all the geometric specifications of the aircraft. *Cdsgn* automatically generates the AVL-input file from its own input file. Comparing different wing planforms or airfoils becomes much easier and faster with this automatic input file generation. Later the AVL-run file is also generated automatically, which states the flight conditions, and the constraints like being longitudinally in equilibrium state (including total pitching moment). These features of the AVL program increases the accuracy of *Cdsgn* by including the trim drag and the span efficiency to the design loop.

Then a first run of AVL is done in order to get the exact neutral point of the aircraft, and then the centre of gravity position in the AVL-run file is updated accordingly by the user defined static margin. A second run is required to obtain the aerodynamic characteristics of the aircraft. The trim convergence of the aircraft is also controlled before continuing on the next step in the design loop.

### 3.3.8 Performance

Performance module is responsible for determining the final state of the configuration. After obtaining the aerodynamic characteristics of the aircraft, the total drag, ideal aerodynamic power is calculated.

$$P_{ideal} = D_{total}V \quad (3.25)$$

The motor mass is updated according to the calculated  $P_{ideal}$ , and the iteration continues till the motor mass converges. Later, the electrical current that is required to be drawn from the battery is calculated by taking into account efficiency losses. It is possible to use the Qprop program which is explained in chapter 5 in order to calculate the efficiencies of a selected pair of motor and propeller. However, for the sake of simplicity, the efficiencies are taken as fixed and defined in the input file. It has been thought that a full optimisation of the propulsion system according to the mission definition will be more advantageous rather than one point optimization. For this purpose *Qpoptimizer* will be used in order to define the final motor and propeller of the selected aircraft later in preliminary design phase.

As an example, the efficiencies can be taken as :

- ESC Efficiency = 0.95
- Motor Efficiency = 0.7
- Propeller Efficiency = 0.7
- Miscellaneous Efficiency losses = 0.95

$$P_{required} = \frac{P_{ideal}}{\eta_{motor}\eta_{prop}\eta_{esc}\eta_{misc}} \quad (3.26)$$

In order to find the total power, the power necessary for the avionics (autopilot, servos, modem, payload, etc ...) is added to  $P_{required}$

$$P_{total} = P_{required} + P_{avionics} \quad (3.27)$$

Finally all the aerodynamic characteristics and the power consumption information saved as an output in order to be used in the mission simulation.

### 3.4 Mission Simulation

Both simple or complex mission simulation of the aircraft can be done. It can be as basic as calculating the range or endurance performance for a continuous level flight as in equation 3.28 and 3.29.

$$Endurance = t = \frac{E_{battery} \eta_{battery}}{P_{total}} \quad (3.28)$$

$$Range = d = t V \quad (3.29)$$

More complex simulation can be done as it is required for the conditions when solar energy is used. The energy consumption needs to be calculated while taking into account the variable solar irradiation. A simple solar irradiation model that is used in the simulations is shown in figure 3.5 and generated with the equation 3.30 where  $IR_{max}$  is the maximum estimated irradiation for the given conditions,  $t_{sr}$  is sun rise time,  $t_{ss}$  is sun set time of the day. Additionally a real data from [2] is plotted for comparison in figure 3.5.

$$IR(t) = \frac{IR_{max}}{2} [1 - \cos(2\pi \frac{t - t_{sr}}{t_{ss} - t_{sr}})] \quad (3.30)$$

As it is known that the endurance and range performance of a solar aircraft will be highly dependent on the launch time, a simple optimiser is also located in the simulation. Basically, the optimiser launches the aircraft at a specified day time and simulates the energy consumption with a time march analyses in realtime. Then with the increments in the launching time, the optimum launch time is obtained by looking at the maximum endurance and range performances.

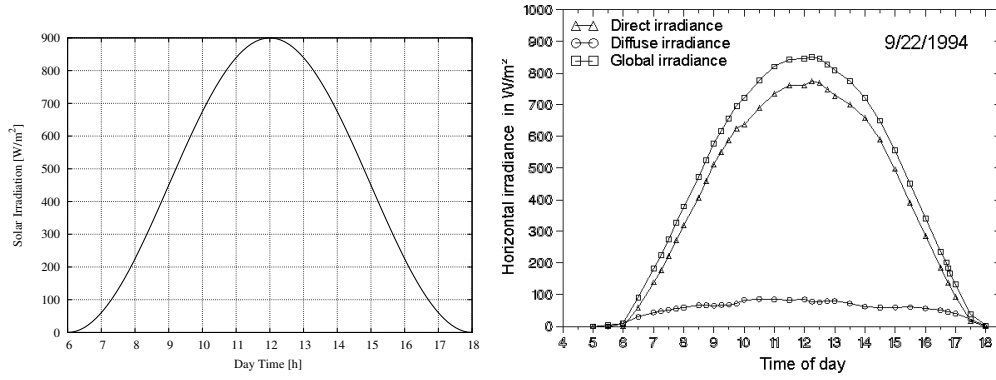


FIGURE 3.5: Simple solar irradiation profile used in the simulations on the left. Sun rise and sun set times are taken 6:00AM and 18:00PM consecutively. A real data from [2] on the right for comparison.

### 3.5 Final Selection

Thanks to the AVL program that is integrated in to the *Cdsgn*, the output information of the candidate aircrafts are not only limited with the endurance and range performance. All the aerodynamic characteristics and the stability derivatives are defined, and can be used in selection of the final design. An automatic filtering of the final candidates can be done according to certain variables, such as a certain pitch damping coefficient, stall speed, wing loading, on-board battery weight to total weight ratio, etc... However, an experienced designer is needed for the final selection as usual.

### 3.6 Interactive Real-Time Filtering

Having all the candidates for a given mission and selecting the best one is not always trivial. Most of the time there occurs some complex situations such as several aircraft seems to accomplish the mission, each with different battery capacity and different flight speed and so on. An interactive real time filtering program has been developed with the helps of Alexandre Bustico in order to select the best candidate design. The software also allows users to do a sensitivity analyses as each parameter can be limited real time. Figure 3.6 shows the graphical user interface of the real time filtering program.

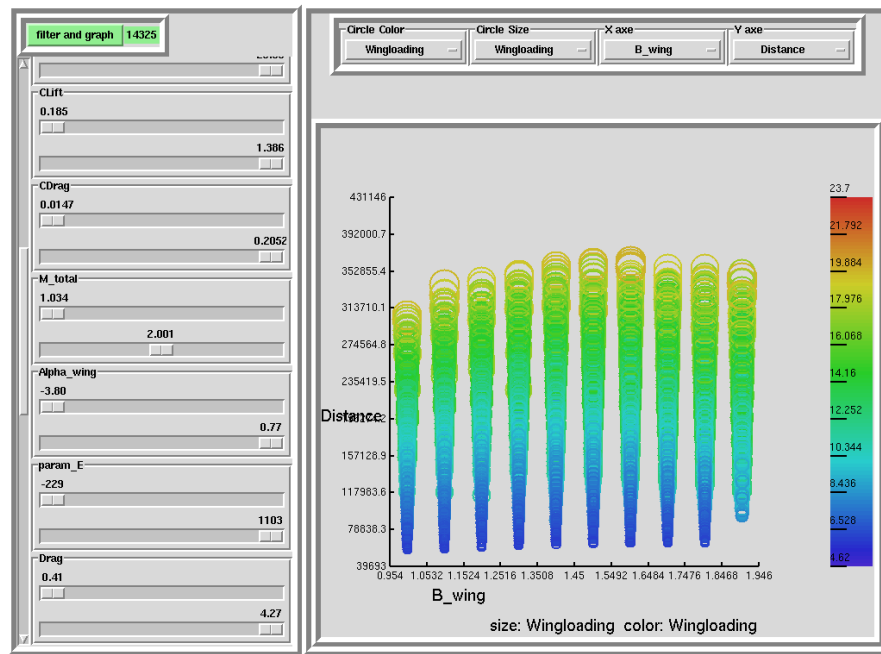


FIGURE 3.6: Interactive real time filtering program.

Each circle represents one candidate. The output data can be evaluated by using four dimensions such as, x-axis, y-axis, colour bar, circle size. On the left, each variable has its minimum and maximum values. By changing the upper and bottom limit of any variable, one can see the influence of corresponding variable on the selected performance of the candidates.

# Chapter 4

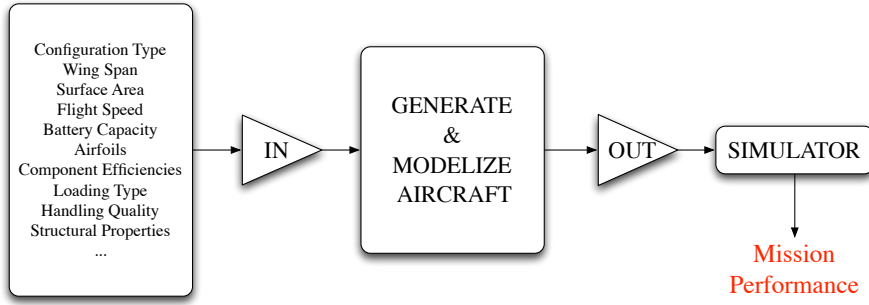
## Aerodynamics

### 4.1 Introduction

In this chapter, we briefly explain the main scientific problems that are encountered by mini and micro air vehicle aerodynamics. Although the propulsion system of these vehicles are certainly related to aerodynamic problems as well, those will be taken into account separately in the next, *Propulsion System* chapter, chapter 5.

The main objective of this chapter is to determine an aerodynamic analysis method in order to implement in the conceptual design program (*Cdsgn*), that is explained in chapter 3. Figure 4.1 shows the brief flow chart of the *Cdsgn* program. There, in the modeling block, the aerodynamic characteristics of the given aircraft has to be analysed in an accurate and fast way. Therefore instead of using a full Navier-Stokes solution, the focus given to more simplified methods such as vortex-lattice and panel codes. Some of the selected existing open source numerical aerodynamic analyses programs will be introduced, and implementation of some required modifications will be explained further in the chapter.

In order to validate these programs and their capabilities, performance characteristics of a conventional and a flying wing configuration will be examined. The comparison of wind tunnel and numerical analyses results will be shown. After showing the satisfactory correspondence of theoretical and experimental results, further capabilities of the modified AVL program will be demonstrated shortly.

FIGURE 4.1: The very brief flow chart of *Cdsgn* program.

## 4.2 Main Aerodynamic Challenges

The nature of mini and micro UAVs restricts the maximum dimensions, thus the weight of these vehicles. The small size restriction brings the biggest problem in terms of aerodynamic performance which is the low-Reynolds effect.

Being the most important dimensionless parameter in fluid flow, Reynolds number is nicely expressed by Martin Simons [19] as : *"Experimental work by Osborne Reynolds in 1883 showed there are two distinct types of flow, laminar and turbulent. These may change from one to the other according to particular conditions. Which type of flow prevails in the boundary layer at any point depends on the form, waviness and roughness of the surface, the speed of the mainstream measured at a distance from (usually ahead) the surface itself, the distance over which the flow has passed on the surface, and the ratio of density and viscosity of the fluid. A variation in any of these factors can bring about a change in the boundary layer. Reynolds combined them all except surface condition, into one figure, the Reynolds number (Re)."*

$$Re = \frac{\rho V l}{\mu} \quad (4.1)$$

Figure 4.2 shows the aerodynamic performance degradation of SD7037 airfoil with respect to Reynolds numbers. The excessive amount of efficiency loss can be easily seen when the Reynolds number decreases. Mainly, minimum drag coefficient  $C_{D0}$  increases, maximum lift to drag ratio  $C_L/C_D$  decreases and maximum lift coefficient  $C_{Lmax}$  decreases with the decreased Reynolds number. Typical Reynolds number operation range for mini and micro UAVs is between 20,000 – 500,000. According to the wing planform, the local Reynolds number seen by each chord

section varies a lot too. The aerodynamic analysis method has to take into account this particular phenomena of mini, micro UAVs.

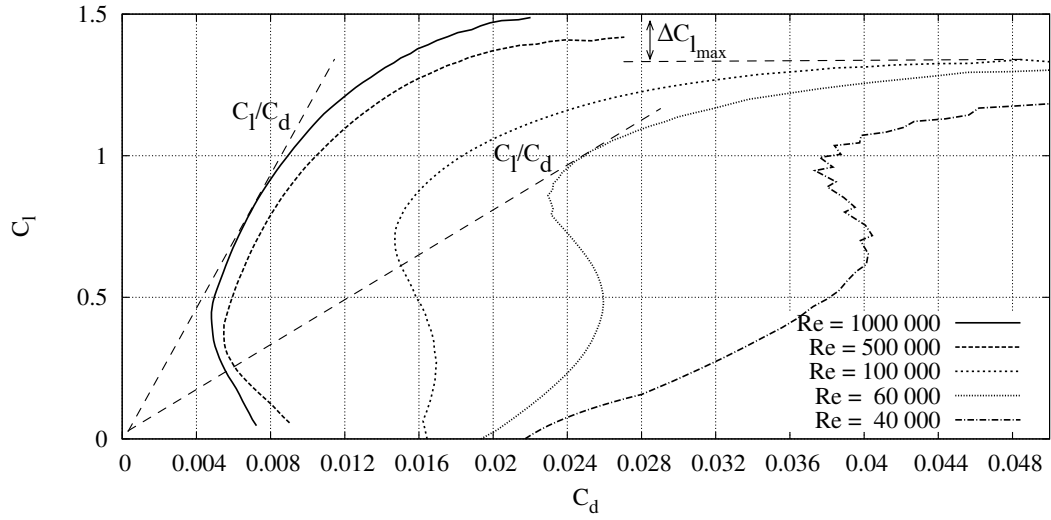


FIGURE 4.2: The aerodynamic performance degradation of SD7037 airfoil with respect to Reynolds number. Calculated by XFOIL.

Another aerodynamic disadvantage that comes with the restricted size is the low aspect ratio. The reason lies behind the need for increased surface area as the typical flight speeds for MAVs vary between  $10 - 20 \text{ m/s}$ . Taking into account all the necessary electronics and payload the increased surface is needed in order to generate the required lift at these flight speeds. Mueller et al.[20] showed that below an aspect ratio of 1.25, the lift curve and the slope becomes highly non-linear and as the aspect ratio increases, most planform shapes exhibits more linear behaviour. Especially above an aspect ratio of 1.5, the classical aerodynamic theories becomes more meaningful and in terms of planform shapes, the elliptical planform exhibits more efficient results. The aerodynamic analyses method that is going to be selected in the content of this thesis has to take into account the effects encountered by low aspect ratio wings. Because of this reason, the well proven lifting-line method will not be considered as a candidate as it will not be able to take into account of low aspect ratio and as well the high sweep angles coming from the nature of mini-micro UAVs.

## 4.3 Aerodynamic Analysis Programs

There are numerous aerodynamic analyses programs available on the market and also on the internet. Nevertheless, we will only focus on some of the selected open source programs. First of all, it should be mentioned that a full Navier-Stokes solver has not been considered as a suitable method for our application since it requires a complex grid generation and excessive amount of computation time for each calculation. Our philosophy is to choose a method that is computationally fast and simplified enough without leaving the physical reality of the problem. The desired criteria for the computational time is selected as to analyse an aircraft's aerodynamic characteristics in less than ten seconds. Additionally, it is favourable that the selected analyses programs can run in a batch mode in order to be used inside an optimisation routine. Finally, having an access to the original source code is a big advantage for customising the code according to the needs.

### 4.3.1 XFOIL

XFOIL is an interactive program for the design and analysis of subsonic isolated airfoils written by Mark Drela from MIT. It has the capability of combining viscous or inviscid effects of an existing airfoil, allowing forced or free transition. Lift and drag predictions can be done beyond maximum lift coefficient at fixed or varying Reynolds number cases.

The design of the airfoil can be done by interactive modification of the geometry itself or by the modification of the surface speed distribution. Changing the camber, max thickness, highpoint positions, leading edge radius, trailing edge thickness is possible. Another useful property that can be used frequently on the design is the blending of airfoils.

Since XFOIL is an open source program, it has been widely used in numerous academic studies and real life applications varying from wind-turbine airfoil design [21] to human powered airplane projects [22] since the creation of program.

## Formulation

The author explains the formulation here [23] as , the inviscid formulation is a linear-vorticity stream-function panel method. A finite trailing edge base thickness is modeled with a source panel. The equations are closed with an explicit Kutta condition [24]. A Karman-Tsien compressibility correction is incorporated, allowing good compressible predictions all the way to sonic conditions.

The boundary layers and the wake are described with a two-equation lagged dissipation integral boundary layer formulation and an envelope  $e^n$  transition criterion. The entire viscous solution is strongly interacted with the incompressible potential flow using a surface transpiration model, which allows the calculation of limited regions of separated flow. The drag is determined from the momentum thickness of the wake far downstream. A special treatment [25] is used for a blunt trailing edge which fairly accurately accounts for base drag. The total velocity at each point on the airfoil surface and wake, with contributions from the freestream, the airfoil surface vorticity, and the equivalent viscous source distribution, is obtained from the panel solution with the Karman-Tsien correction added. This is incorporated into the viscous equations, yielding a nonlinear elliptic system which is readily solved by a full-Newton method

### 4.3.2 AVL Vortex-Lattice Code

AVL is another program written by Mark Drela for the aerodynamic and flight-dynamic analysis of rigid aircraft of arbitrary configuration. It employs an extended vortex lattice model for the lifting surfaces, together with a slender-body model for fuselages and nacelles. General nonlinear flight states can be specified. The flight dynamic analysis combines a full linearization of the aerodynamic model about any flight state, together with specified mass properties.

## AVL Formulation

The author briefly explains the summary of vortex lattice method in [26] as following :

At a field point location  $\vec{r}$  as shown in figure 4.3, the total wing-relative velocity  $\vec{V}_{(\vec{r})}$  is:

$$\begin{aligned}\vec{V}_{(\vec{r})} &= \vec{V}_{\infty} - \vec{\Omega} \times \vec{r} + \frac{1}{4\pi} \int \Gamma \frac{d\vec{l}' \times (\vec{r}' - \vec{r})}{|\vec{r}' - \vec{r}|^3} \\ &= \vec{V}_{\infty} - \vec{\Omega} \times \vec{r} + \sum_{n=1}^N \Gamma_n \hat{V}_n(\vec{r})\end{aligned}$$

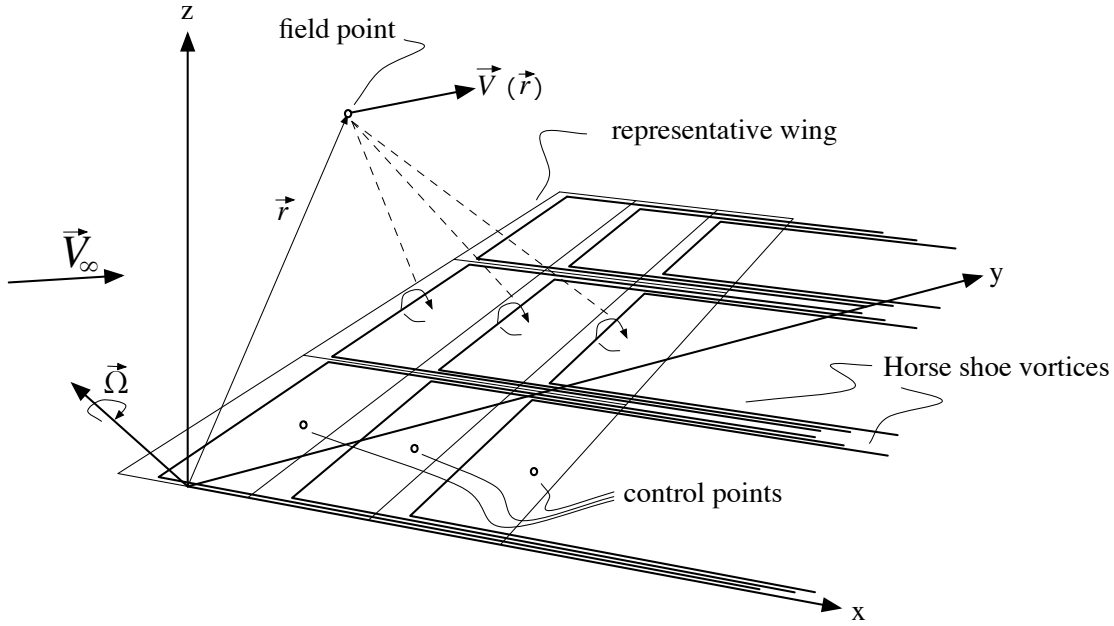
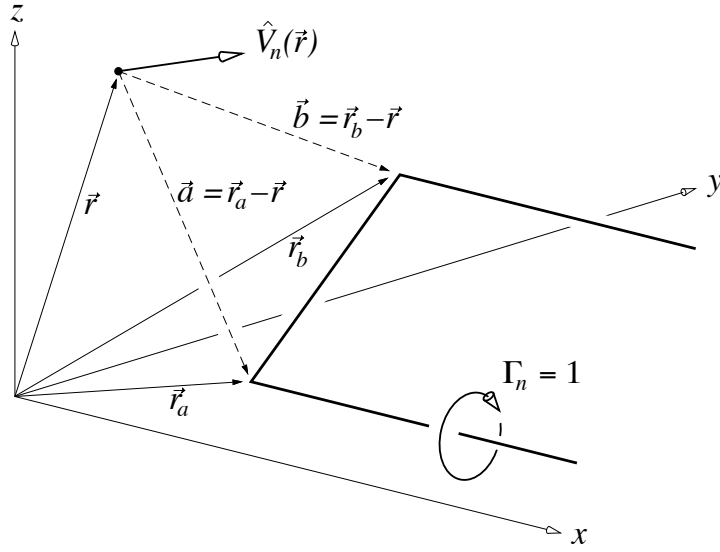


FIGURE 4.3: Wing relative velocity at field point location  $\vec{r}$ .

Velocity contribution ( $\hat{V}_{n(\vec{r})}$ ) from  $n$ 'th unit horseshoe vortex can be expressed as in equation 4.2 and shown in figure 4.4.

$$\hat{V}_{n(\vec{r})} = \frac{1}{4\pi} \left\{ \frac{\vec{a} \times \vec{b}}{|\vec{a}||\vec{b}| + \vec{a} \cdot \vec{b}} \left( \frac{1}{|\vec{a}|} + \frac{1}{|\vec{b}|} \right) - \frac{\vec{a} \times \hat{i}}{|\vec{a}| + \vec{a} \cdot \hat{i}} \frac{1}{|\vec{a}|} + \frac{\vec{b} \times \hat{i}}{|\vec{b}| + \vec{b} \cdot \hat{i}} \frac{1}{|\vec{b}|} \right\} \quad (4.2)$$

Flow tangency condition at control point  $\vec{r}_m$  is :

FIGURE 4.4: Velocity contribution from  $n$ 'th unit horseshoe vortex.

$$\begin{aligned} \vec{V}_{(\vec{r}_m)} \cdot \hat{n}_{m(\delta_l)} &= 0 \\ \left( \vec{V}_\infty - \vec{\Omega} \times \vec{r}_m + \sum_{n=1}^N \Gamma_n \hat{V}_n(\vec{r}_m) \right) \cdot \hat{n}_{m(\delta_l)} &= 0 \end{aligned}$$

Where  $\delta_l$  is the control deflections.

Or it can be written as :

$$\sum_{n=1}^N A_{mn} \Gamma_n ; A_{mn} = \hat{V}_{(\vec{r}_m)} \cdot \hat{n}_{m(0)} , b_m = (\vec{\Omega} \times \vec{r}_m - \vec{V}_\infty) \cdot \hat{n}_{m(\delta_l)}$$

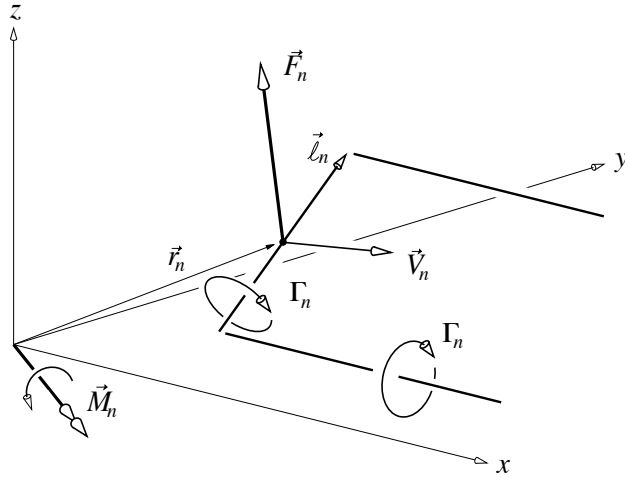
Choosing  $m = 1 \dots N$  control points at 75% panel locations gives  $N \times N$  linear system :

$$[A_{mn}] \{ \Gamma_n \} = \left\{ b_{m(\vec{V}_\infty, \vec{\Omega}, \delta_l)} \right\} \quad (4.3)$$

Equation 4.3 has to be solved for all  $\Gamma_{n(\vec{V}_\infty, \vec{\Omega}, \delta_l)}$

Velocity at midpoint  $\vec{r}_n$  of  $n$ 'th horseshoe vortex is as shown in figure 4.5 :

$$\vec{V}_n = \vec{V}_\infty - \vec{\Omega} \times \vec{r} + \sum_{m=1}^N \Gamma_m \hat{V}_m(\vec{r}_n) \text{ where } \vec{r}_n = \frac{1}{2}(\vec{r}_a + \vec{r}_b)$$

FIGURE 4.5: Velocity at midpoint  $\vec{r}_n$  of  $n$ 'th horseshoe vortex.

Force and moment on  $n$ 'th horseshoe vortex are :

$$\vec{F}_n = \rho \vec{V}_n \times \vec{l}_n \Gamma_n \quad (4.4)$$

$$\vec{M}_n = \vec{r}_n \times \vec{F}_n \quad (4.5)$$

where  $\vec{l}_n = \vec{r}_b - \vec{r}_a$

Total forces and moments are defined as :

$$\vec{F}_{(\vec{V}_\infty, \vec{\Omega}, \delta_l)} = \sum_{n=1}^N \vec{F}_n \quad (4.6)$$

$$\vec{M}_{(\vec{V}_\infty, \vec{\Omega}, \delta_l)} = \sum_{n=1}^N \vec{M}_n \quad (4.7)$$

$$L = \vec{F} \cdot (\hat{k} \cos \alpha - \hat{i} \sin \alpha) \quad (4.8)$$

$$D_i = \vec{F} \cdot \vec{V}_\infty / |\vec{V}_\infty| \quad (4.9)$$

### 4.3.3 XFLR5

XFLR5<sup>1</sup> is an analysis tool for airfoils, wings and planes operating at low Reynolds Numbers. It includes, XFOil's (version 6.94) direct and inverse analysis capabilities,

<sup>1</sup>[www.xflr5.com](http://www.xflr5.com)

wing design and analysis capabilities based on the Lifting Line Theory, on the Vortex Lattice Method (with the same basics as explained), and on a 3D Panel Method. The latest version has the stability analysis capability as an addition. Xfoil code has been translated to C language and included in XFLR5's code. It has an elegant user interface that makes it easier to use and more attractive for certain users, that is the reason why it has been well known among the radio controlled model airplane world.

## 4.4 Program Selection

Among the presented XFLR5 and AVL open source aerodynamic programs, AVL is chosen to be used for the calculations needed in the design method that is going to be explained further in chapter 3. Although, XFLR5 has already a built-in airfoil database for the addition of viscous effects, the graphical user interface makes it difficult to integrate in an optimization routine. As the idea is to call the analyse program several times and make automated modifications to the aircraft geometry, AVL fits more appropriately for the selection because of its command driven interface. Additionally, AVL can compute any given flight state, such as equilibrium level flight, this capability is also a reason why AVL outperforms XFLR5 for our application purpose.

However, the missing capabilities that exists in XFLR5 has to be implemented to AVL as well. So the viscous drag coming from the airfoil is implemented for each strip located in the span via an XFOIL database. The additional skin friction drag coming from the fuselage surface also has to be integrated. With these modifications, the highly important Reynolds number effect for mini micro scale UAVs can be clearly seen and computed on the final calculations of the conceptual design program (*Cdsgn*).

## 4.5 Modifications

### Airfoil Database Integration via XFOIL

The force and moment acting on each horse shoe vortex is shown in equation 4.4. Each strip defined on the wing surface has a number of panels, so horse shoe vortices, located chordwise. Integration of these forces and moments gives the total values corresponding to that single strip. As the surface area of the strip and the reference values of the aircraft is known, the local lift, drag and moment coefficients are defined for each particular strip. In order to add the viscous drag component, corresponding airfoil drag coefficient is added which is calculated by XFOIL according to the local Reynolds number of the strip. The drag coefficient is selected by matching the strip's lift coefficient to the airfoil's lift coefficient. As the airfoil coefficients are calculated for a set of lift coefficient, for the cases where the lift coefficient of the strip does not exactly match to the airfoil's existing lift coefficients, an interpolation is made between the closest two values in order to obtain a match. No change has been made to the local moment or lift coefficient of the strip as these modifications would require massive changes on the code, as AVL can also calculate the equilibrium flight states.

Main section airfoils are already defined in the airframe file of AVL. By the help of XFOIL, all necessary airfoil polars can be calculated for the corresponding Reynolds number of each section. There are additional strips between each section as shown in figure 4.6, new polars have to be calculated for each strip with its corresponding Reynolds numbers as well.

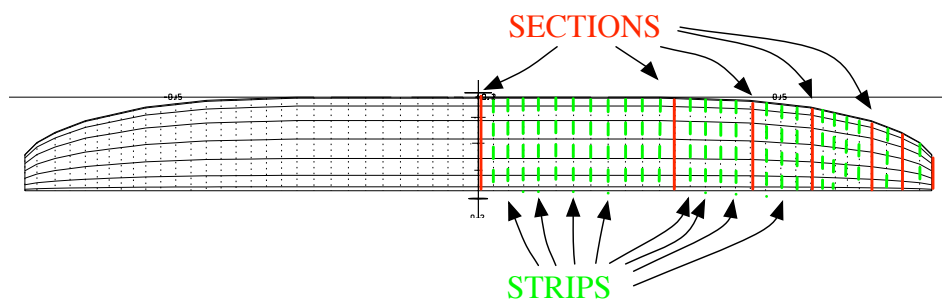


FIGURE 4.6: Sections and strips defined in AVL program along the wing.

Two solutions are possible :

- Generate a new airfoil by interpolating the section airfoils according to their ratio and calculate the polar for the new airfoil.
- Interpolate the pre-calculated section airfoil polars according to their ratio without needing new airfoil generation and recalculation.

As it can be seen on Figure 4.7, the difference between geometrically new generated airfoil's calculated polar and the interpolation of polars does not have a significant difference for the accuracy. So the second solution is chosen as it does not need additional new airfoil generation and analysis. Equation 4.10 is used for the interpolation of the airfoil polars in order to obtain the required  $C_d$  coefficient.

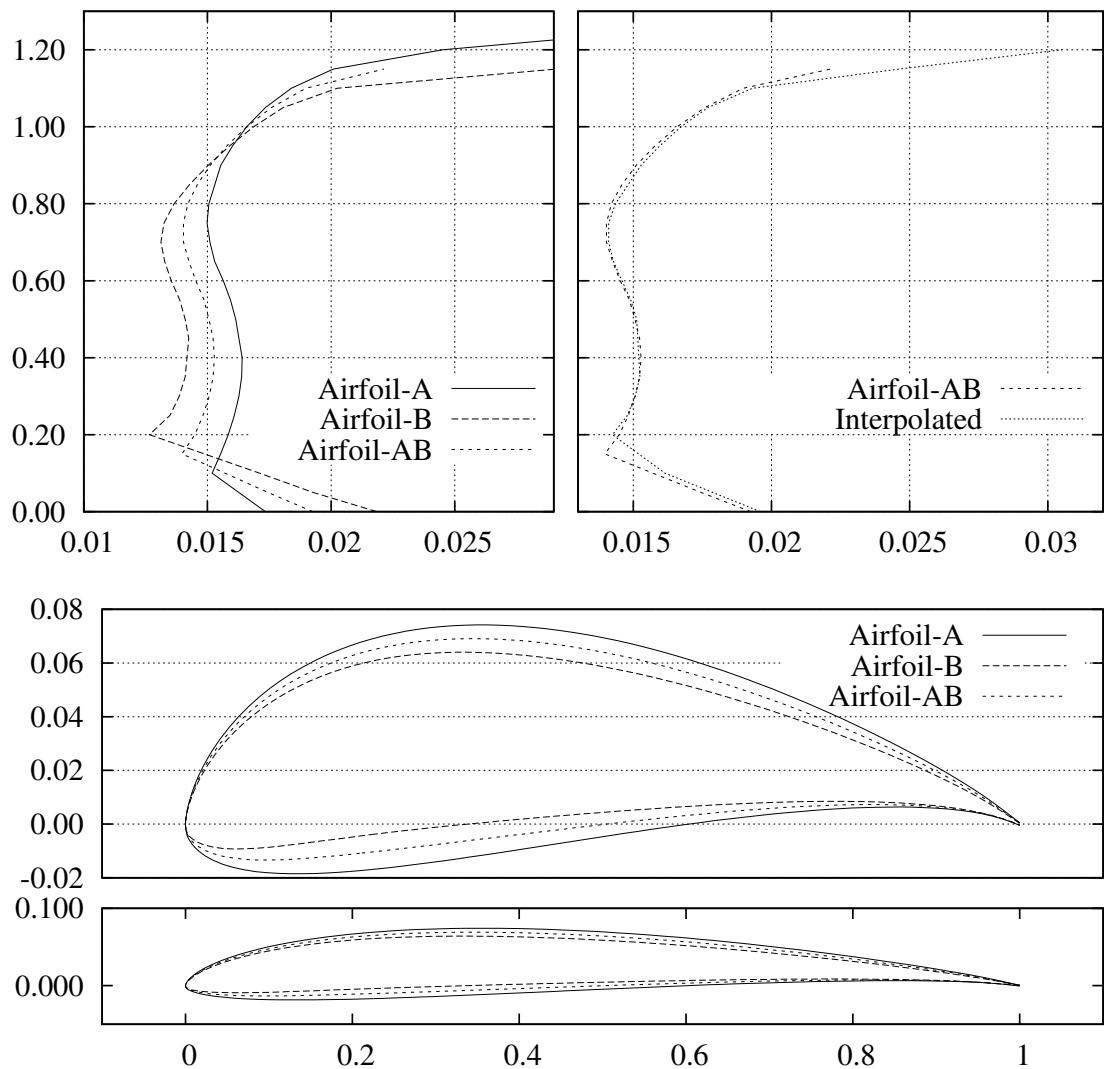


FIGURE 4.7: The precision of airfoil polar interpolation

$$C_d = C_{d-a} + (C_{d-b} - C_{d-a}) \frac{(C_l - C_{l-a})}{(C_{l-b} - C_{l-a})} \quad (4.10)$$

In the analyses, every time AVL calculates a case, new airfoil polars needed as the cruise speed, size of the wing, weight of the aircraft changes. Instead of recalculating each airfoil for a set of Reynolds numbers at each analysis, a database is generated and saved which can be reached again whenever the data is needed. This method ensures the fast analyses and also robustness of the program.

## Fuselage viscous drag

The body model of AVL is given by the top and bottom coordinates. Then, desired number of circular sections are defined according to the given coordinates as shown in figure 4.8. In order to add the fuselage drag to AVL, first the surface area is calculated by summing all the surface between each sections. Then the drag component of the fuselage is calculated in terms of its surface area's skin friction drag corrected by its fineness ratio [18], which is calculated by the ratio of the diameter of the fuselage to the length of it,  $d/l$ .

$$C_{Dwetfuselage} = C_f [1 + 1.5(d/l)^{3/2} + 7(d/l)^3] \quad (4.11)$$

Where the laminar and turbulent skin friction coefficients are calculated by equation 4.12 and 4.13. The length of the laminar flow can be determined externally, but in most of the calculations, all the surface assumed to have turbulent flow as the propeller slipstream assumed to go through the whole fuselage.

$$C_{f-laminar} = \frac{1.328}{\sqrt{Re_l}} \quad (4.12)$$

$$C_{f-turbulent} = \frac{0.427}{[\log Re_l - 0.407]^{2.64}} \quad (4.13)$$

The implied modification is not sufficiently enough to model the fuselage/body drag precisely as it only uses an empirical formula and not take into account a lot of three dimensional fluid phenomenon. On the other hand, it is a widely used

method in the mini UAV design procedure because of its fast prediction of the approximate fuselage drag.

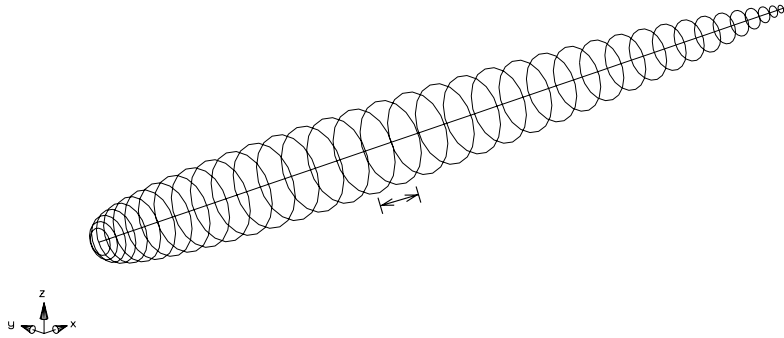


FIGURE 4.8: A generic fuselage with circular cross sections generated by AVL.

## Sustained Flight Envelope, Stall Information

One of the missing information on AVL's output was the flight envelope limits of the analysed aircraft. Using a linear model, AVL can predict equilibrium state with enormously high angles of attack before the control surface trims fails to converge. This usually leads to unrealistic situations such as  $45^\circ$  of angle of attack where in most of the cases the main wing would have stalled. In order to prevent this situation, an additional subroutine is added to AVL to get the stall information. Mainly, this subroutine checks the lift coefficient of each wing strip and compare with corresponding airfoil's  $C_{L_{max}}$  maximum lift coefficient at the defined Reynolds number. If the required strip lift coefficient is higher than the airfoil's  $C_{L_{max}}$  then, an error message is written into an external log file without disturbing any calculation of AVL. By the help of the log file, the user or the external program that calls AVL, can see if the aircraft can sustain the equilibrium with the selected airfoil without stall or not. This information is used to validate the flying candidates for the *Cdsgn* program.

Finally, additional informations such as the lift to drag ratio, local viscous drag coefficient and the total drag coefficient along the span are integrated to the plotting routine of original AVL. Figure 4.9 shows the additional information. This modification does not have any effect for the conceptual design program, however

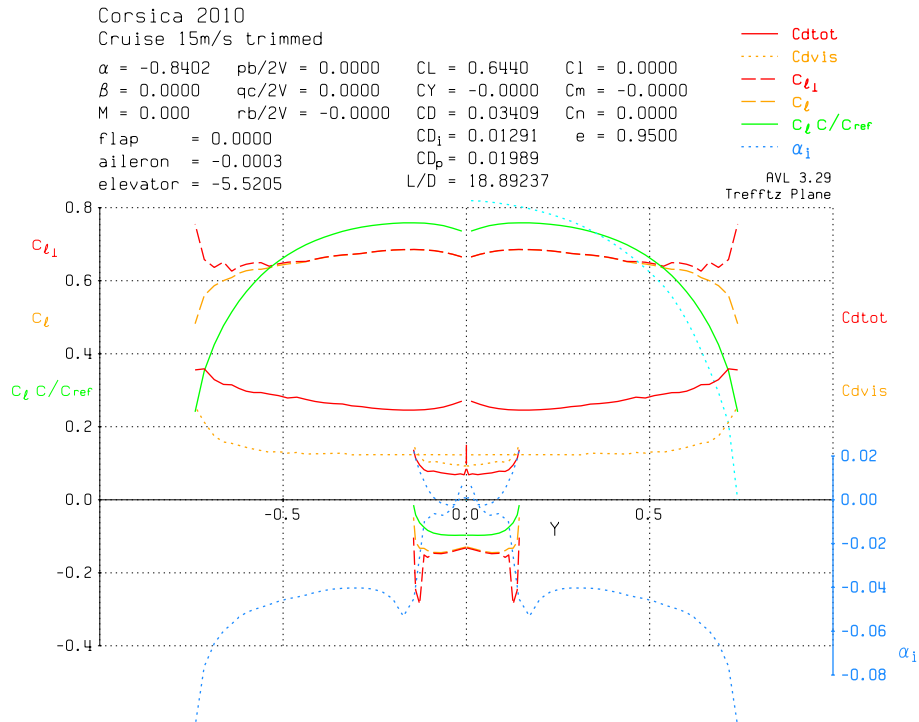


FIGURE 4.9: AVL's modified Trefftz Plane plots with and without viscous effects.

it is useful to be able to see the additional viscous drag coming from each local span location for the user while making manual modifications and analysis.

The effect of Reynolds number is clearly visible as it is shown in figure 4.10 as well as the successive performance change due to flight speed. This result proves that the Reynolds number effect is well modelled in the analyses with the help of implemented modifications.

## 4.6 Validation of the Programs

### 4.6.1 S4 Wind-Tunnel

S4 wind-tunnel belongs to Aerodynamic, Energy and Propulsion Department(DAEP) of ISAE, and is located in the city centre of Toulouse,France. It is an Eiffel type closed-loop wind-tunnel with the returning flow passing through side corridors of

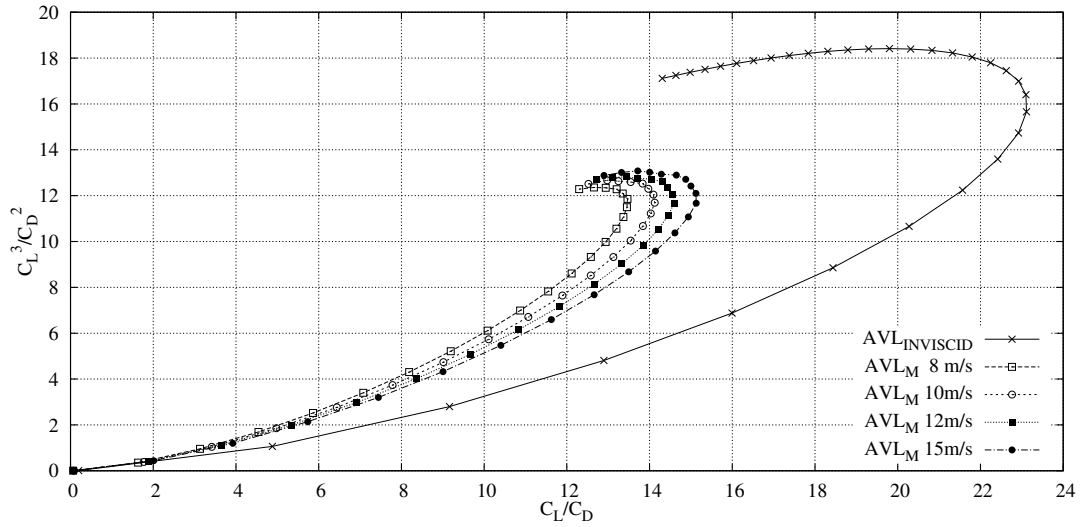


FIGURE 4.10: Comparison of inviscid calculation of AVL versus the final modified version  $AVL_M$  for a conventional configuration at different speeds.

the building. The open test section is elliptical with three meters wide and two meters height. The main plan of the wind tunnel is shown in figure 4.11. The operational speed of the wind tunnel varies from 5 m/s up to 40 m/s.

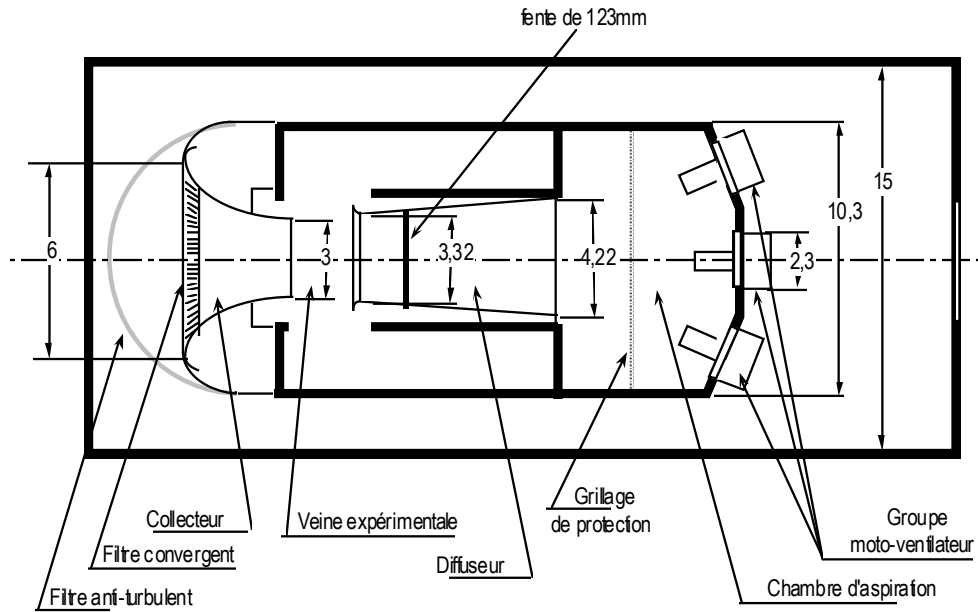


FIGURE 4.11: The plan of S4 wind-tunnel.

### 4.6.2 Internal Balance

In order to measure the moments and forces, a six component internal balance is used which is shown in figure 4.12. Maximum 30 *kg* of models can be tested with the CC-604 balance, and the measuring limits of each axis is shown in table 4.1.

X	Y	Z	L	M	N
[ <i>daN</i> ]	[ <i>daN</i> ]	[ <i>daN</i> ]	[ <i>m.daN</i> ]	[ <i>m.daN</i> ]	[ <i>m.daN</i> ]
$\pm 30$	$\pm 50$	$\pm 50$	$\pm 1.5$	$\pm 1.5$	$\pm 2$

TABLE 4.1: Specifications of the CC604 internal balance.

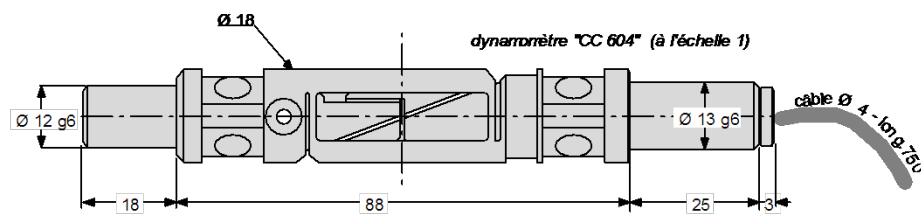


FIGURE 4.12: Dimensions of the internal balance that is used in the experiments.

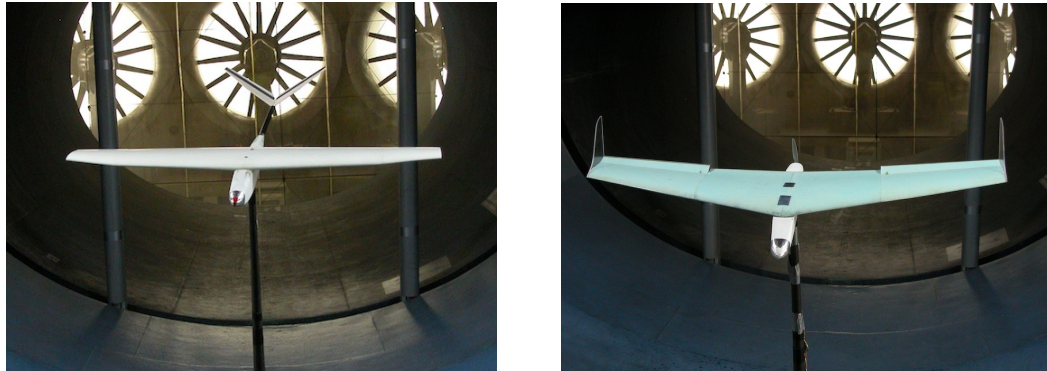
### 4.6.3 Experimental Comparison

Validation of the selected programs and the implemented modifications can be best performed by an experimental comparison. In 2009, a wind tunnel campaign has been done in order to compare the performance difference of one meter wing span conventional configuration and flying wing configuration aircrafts, and released as an internal report[27]. The range and endurance performance results of this study are used for the validation process.

Two configurations, that are conventional and flying-wing were examined. One meter span was fixed in order to stay in the content of this thesis subject. Both wing planforms are designed as elliptical as possible within the easy hot-wire cutting manufacturing technique limitations. Multiple trapezoidal foam panels are cut and covered with fiberglass by using mylar film and vacuum bag technique. Figure 4.13 shows the main specifications of the two configurations.

The main objective is to see the variation between wind-tunnel measurements and the numerical programs, not only in a quantitative matter but also compare

the optimum point trends such as maximum lift to drag ratios, minimum power consumption flight speed, etc...



Conventional Configuration		
Wingspan	$m$	1.0
Surface Area	$m^2$	0.156
Airfoil	-	RG-15
Weight	$kg$	0.6

Flying-Wing Configuration		
Wingspan	$m$	1.0
Surface Area	$m^2$	0.176
Airfoil	-	MH-45
Weight	$kg$	0.6

FIGURE 4.13: Wind tunnel model specifications of the conventional and flying wing configurations.

## Windtunnel Measurements versus Modified AVL and XFLR5

Figure 4.14 shows the performance estimation comparison of the conventional configuration at  $8\text{ m/s}$  with different methods. Compared with the wind-tunnel measurements, the inviscid calculation highly overestimates the performance. However the modified AVL and XFLR5, which simply takes into account the viscous effects, estimates the performance with a higher accuracy.

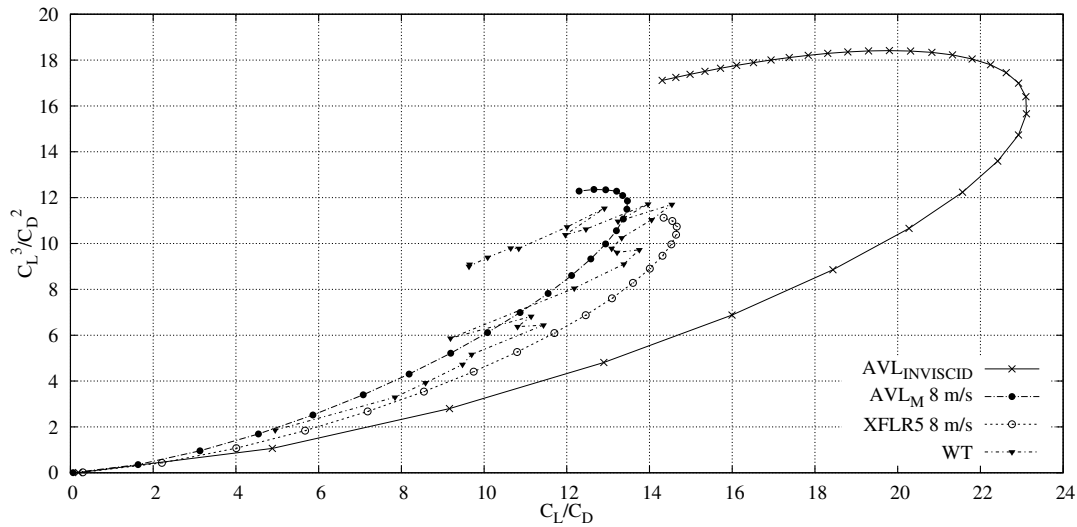


FIGURE 4.14: Comparison of inviscid calculation of AVL, the final modified version  $AVL_M$ , XFLR5 and Wind-Tunnel measurements for a conventional configuration at  $8\text{ m/s}$ .

## 4.7 Conclusion

Figure 4.15 shows additional comparisons between wind tunnel measurements and the numerical programs for two different aircraft configurations. In general, the modified AVL exhibits a closer estimation to windtunnel measurements in comparison to XFLR5. The main reason is coming from the ability to add an additional parasitic drag coefficient to AVL program. So that it is possible, somehow, to replace the interference and other sources of drag by a constant coefficient which is obtained by previous experiences. As the amount of accuracy found to be satisfactory for our applications, the modified AVL is going to be used in the conceptual design program *Cdsgn* as the main aerodynamic analyses subprogram, which is explained in chapter 3 in more detail.

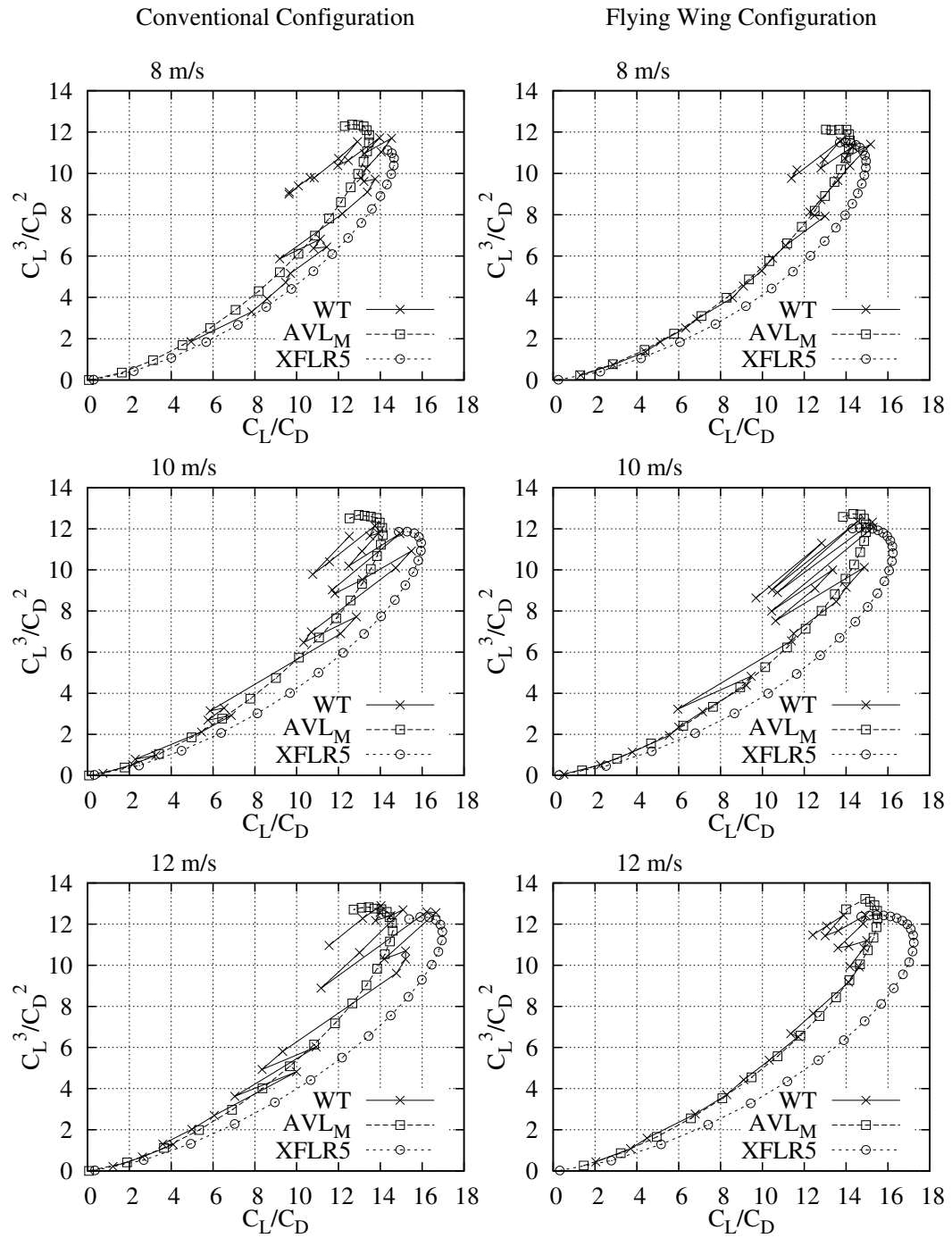


FIGURE 4.15: Comparison of conventional and flying wing configuration with numerical aerodynamic analyses programs XFLR5 and modified AVL and also the wind tunnel measurements.



# Chapter 5

## Propulsion System Design

### 5.1 Introduction

For an electric powered UAV, the motor consumes the biggest percentage of the total energy consumption. This clearly states the importance of optimisation of it. The system approach is the key point on propulsion system optimisation, that is, not only finding the best motor or the best propeller separately, but determining the best motor plus propeller combination.

The mission requirements plays a big role on the selection and optimisation of the propulsion system. These usually consists more than one condition that needs to be satisfied such as take-off and cruise flight. Previous works from T.J.Mueller et al. presents a good example of motor and propeller selection for a MAV [9], but it lacks the identification of each motor and propeller combination's performance evaluation during different phases of the flight since this information can be used as a selection criteria. So in this work, the selection and the optimisation criteria will consider all of the prescribed flight phase (*working conditions*) requirements.

This chapter focuses on the optimisation of the propulsion system selection process, for a specific mission with multiple conditions. The new developed *QPOP-TIMIZER* program will be presented, which is a motor and propeller coupling program for a large number of input motors and propellers. It uses a set of mission defined working conditions with weighted functions in order to select the best

motor and propeller couple for the specific mission. Then the open source programs used in *QOPTIMIZER* will be explained. Following that, the matching process of motor and propeller couple will be explained including the basics of the electric motor, propeller theoretical models and experimental characterisation test processes.

## 5.2 Problem Definition

### 5.2.1 Elements of Propulsion System

Electric propulsion system mainly consists of four sub-elements, shown in figure 5.1; the battery, the motor controller (also called as electronic speed controller, ESC), electric motor and the propeller. A gear system can also be found between the motor and the propeller but mainly it is included in the motor sub-element.

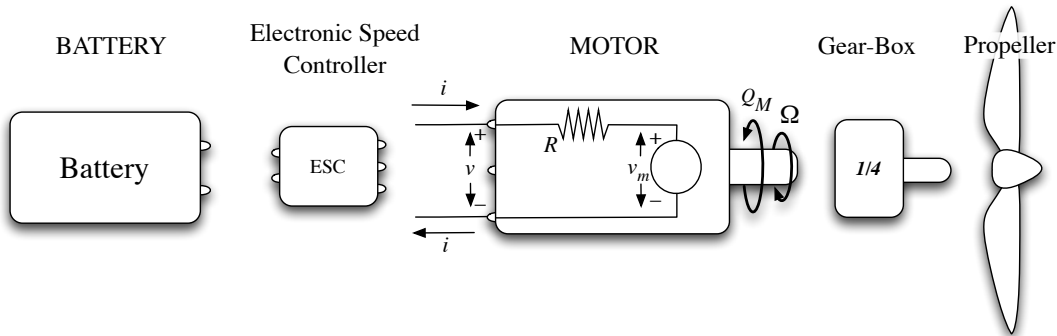


FIGURE 5.1: Elements of a generic electric propulsion system.

The electronic speed controller design is out of scope of this thesis, therefore its design will not be included into the optimisation routine, however an efficiency coefficient is included as there exists an effect coming from different brands and types of speed controllers. The same is true for the battery, it is not included in the optimisation routine as they do not have a direct effect on the propulsion system as long as an appropriate type is selected taking into account of its continuous discharge rate. The weight of each element is disregarded in this stage as this makes sense if only when the complete aircraft optimisation is done with the propulsion system included. *Cdsgn* program, presented in chapter 3, takes into account the weight of each element while calculating the performance of the aircraft. The main interest is going to be on motor and propeller selection on this chapter.

### 5.2.2 Mission Definition

The most important part in the optimisation of the propulsion system is the definition of the mission requirements. Generally it is only the cruise flight conditions which are taken into account while selecting and optimising the motor and propeller selections. In reality, there exists other phases of the flight which the propulsion system has to satisfy additional requirements.

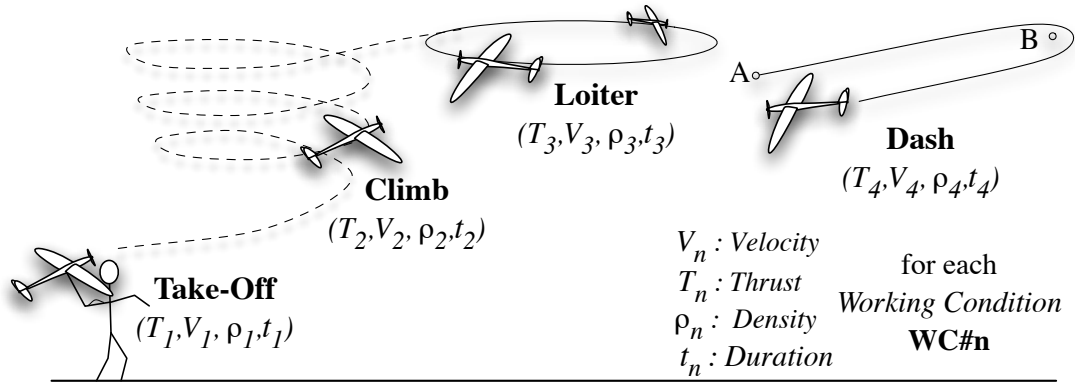


FIGURE 5.2: A generic mission definition with multiple flight phases which are called *Working Conditions* (**WC**).

Figure 5.2 shows several flight phases of an aircraft such as take-off, climb to an altitude, loiter at a constant altitude for surveillance and finally go from point A to B and return at a higher speed for an emergency situation. In each phase of the flight, the aircraft operates at different velocity (**V**) and thrust (**T**), the altitude can also be different so that the density will be different ( $\rho$ ) and the duration of the phase ( $t$ ) varies according to the mission definition.

Such a flight envelope clearly shows that optimising the propulsion system only for cruise conditions can not be optimum for the overall performance of the aircraft for that given mission. Each phase (will be called as **Working Condition**) has to be taken into account in the optimisation with its specific variables ( $T_n, V_n, \rho_n, t_n$ ) in order to achieve an optimum selection for the propulsion system.

Finally, the *Mission Definition* will be described by the *Working Conditions* and their duration time ( $t$ ). The duration time is only taken as a weight factor here and can be modified if one of the working conditions needs more priority than its duration time compared to the whole mission time.

### 5.3 QOPTIMIZER Program

QOPTIMIZER Program is developed in order to select a motor and propeller couple for a given mission definition with multiple conditions as described previously. Numerous motors and propellers from databases can be numerically tested and given a score according to their performance on the defined mission. The mission definition is not only limited with one working conditions, the user can define several working conditions such as in table 5.1 as previously shown in the figure 5.2.

	Unit	WC#1	WC#2	WC#3	...	WC#n
Thrust	[N]	1.2	1.8	4.5	...	...
Power	[W]	0	0	0	...	...
Speed	[m/s]	15.0	20.0	3.5	...	...
$\rho$	[kg/m <sup>3</sup> ]	1.225	1.225	1.225	...	...
WeightFactor	[—]	900	150	30	...	...

TABLE 5.1: Example of mission working conditions.

These *Working Conditions* mainly act as an objective and also as a constraint in the optimisation process. One can define a **WC** with a weight factor of only 1, relatively low compared to a working condition representing cruise flight with 900 weight factors, so that the program makes sure that the propulsion system satisfies the **WC** but does not give a big score for its performance.

The program uses QPROP and QMIL as its main analyser core and gather their outputs in order to define a score for each motor and propeller couple. This score represents the performance of each motor and propeller couple for the selected mission.

#### 5.3.1 QPROP and QMIL

QPROP is an open source analysis program for predicting the performance of propeller-motor or windmill-generator combinations. QMIL is the companion propeller and windmill design program which is also open source. Both programs are written by Mark Drela from MIT.

The theoretical aerodynamic formulation is explained in [28]. There, the author remarks that QPROP and QMIL use an extension of the classical blade-element / vortex formulation, developed originally by Betz[29], Goldstein[30], and Theodorsen[31], and reformulated by Larrabee[32]. The extensions include

- Radially varying self-induction velocity which gives consistency with the heavily-loaded actuator disk limit
- Perfect consistency of the analysis and design formulations
- Solution of the overall system by a global Newton method, which includes the self-induction effects and powerplant model
- Formulation and implementation of the Maximum Total Power (MTP) design condition for windmills

QPROP uses three motor specification coefficients ( $K_v$ ,  $\mathcal{R}$ ,  $i_0$ ) as an input in order to model the electric motor. For modelling the propeller, it requires the geometry of the propeller which is defined by chord length ( $c_n$ ) and the pitch angle ( $\beta_n$ ) of each spanwise location ( $r_n$ ) and the airfoil properties which is approximated by a polynomial curve fit as shown in figure 5.3. This method results with an extremely rapid analyses of motor propeller couples for various conditions.

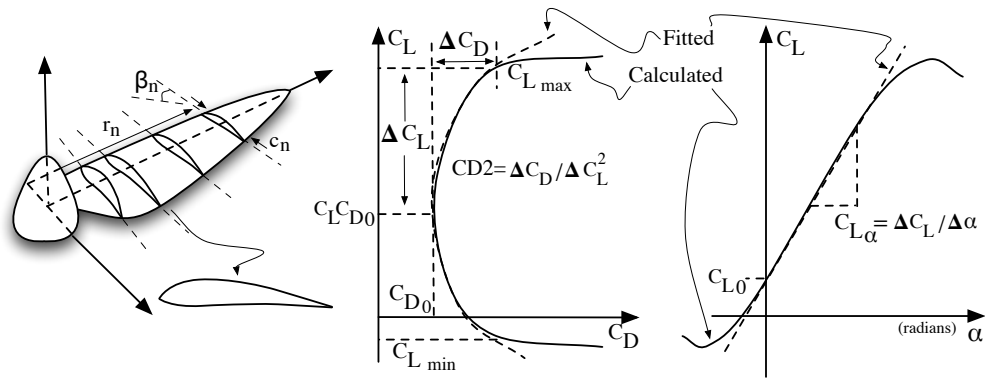


FIGURE 5.3: Propeller airfoil coefficients used in QPROP program.

Likewise QMIL requires the working conditions of the propeller that is going to be designed and optimised for. These information include the aerodynamic properties of the airfoil ( $C_{D0}$ ,  $C_L C_{D0}$ ,  $C_{Lmin}$ ,  $C_{Lmax}$ ,  $C_{L\alpha}$ ,  $C_{L0}$ ,  $C_{D2upper}$ ,  $C_{D2bottom}$ ) that is planned to be used, lift distribution along the span, operating flight speed, desired RPM, diameter and the desired thrust or power generated.

### 5.3.2 QOPTIMIZER Program Flow

QOPTIMIZER program has two main capabilities. First is to match the most appropriate motor and propeller combination among the motor and propeller databases according to the defined mission requirements. Second is to design the best probable propeller while matching it to the motors from the database. In both cases the final selection is done while taking into account the working conditions and their weight factors. Figure 5.4 shows the main flow of the program.

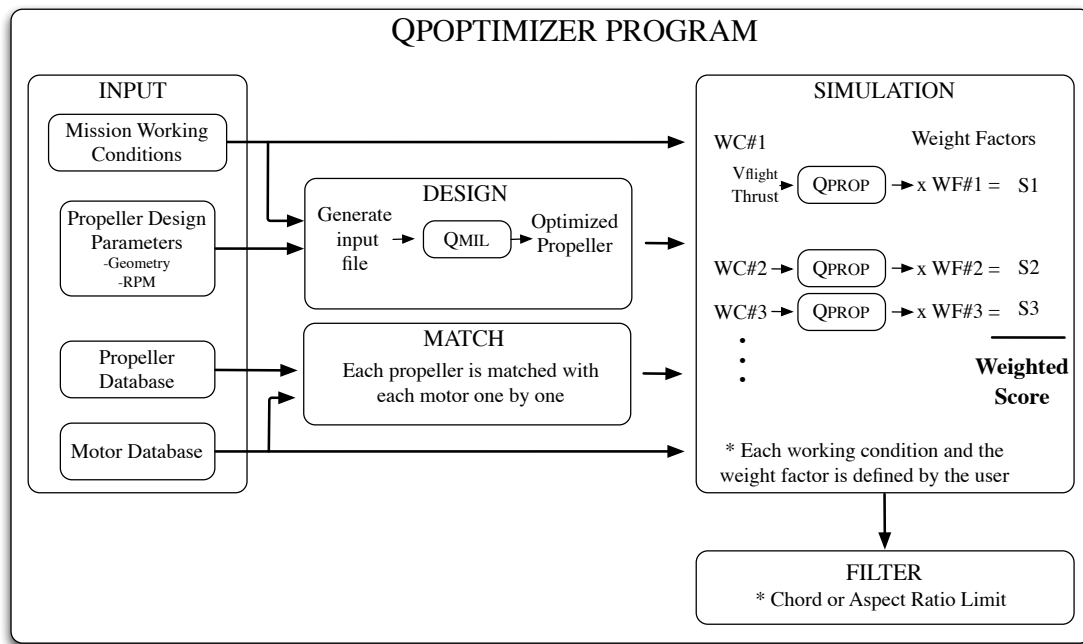


FIGURE 5.4: Main flow chart of the QOPTIMIZER program.

The existing motors and propellers are defined with their characteristic coefficients in the corresponding databases. If a custom propeller is going to be designed, then the possible geometry (min and max radius) and RPM envelope has to be defined by the minimum and maximum values that they can get. The mission is mainly defined in the *INPUT* with the working conditions. These working conditions are both used while determining the propeller design conditions and also in the *SIMULATION* phase.

In the *DESIGN* phase, the input file for QMIL is generated according to the mission definition, required working condition specifications and the design envelope which was defined by possible geometry and the RPM minimum and maximum limits. Then QMIL outputs the custom propeller specifications with optimised chord and twisting law.

The MATCH phase simply generates different cases for each possible combination of motor and propeller out of the given propeller and motor databases.

Most important phase is the SIMULATION phase, where each of the motor propeller combination is analysed by QPROP for each of the defined working conditions. After the analyses, each working condition's result is multiplied with its weight factor and finally by summing out all of the working conditions score, a total weighted score is obtained for the motor propeller couple.

An additional FILTER is also defined in order to cancel certain candidates, such as propellers with too low or too high aspect ratios (limited between 3 and 15 as a default) or a maximum weight limit can also be defined (which has to be defined in the INPUT otherwise there is no limitation as a default) for the motor and propeller couple.

An example use of QPOPTIMIZER is explained in Appendix B including all the design, manufacturing and test phases. Figure 5.5 shows the resulting propeller designed by QPOPTIMIZER and then build in house. As a brief information, the efficiency of the custom designed propeller was %71 at the defined cruise conditions ( $V_{cruise} = 15 \text{ m/s}$  and  $T_{cruise} = 1.3 \text{ N}$ ) while matching the electric motor's high efficiency working regime ( $> \%75$ ). The total propulsion system efficiency resulted as %50 including the electronic speed controller and the miscellaneous losses (such as cables, connectors...).



FIGURE 5.5: A custom propeller designed with QPOPTIMIZER for a specific application. Design and manufacturing procedure is explained in Appendix B.

## 5.4 Modelling Electric Motor and Propeller

### 5.4.1 Electric Motor

Basically, electric motors are electromechanical machines that convert electrical input power into mechanical output power. The general power supply used in the UAVs is DC (Direct Current) so DC motors will be investigated in this chapter. Most common types are brushed and brushless motors. Brushed motors use mechanical and brushless motors use electronic commutation in order to change the direction of electric current and generate a pulling magnetic force between the stator and the magnets. Brushless motors have numerous advantages such as having a higher efficiency than brushed motors, longer lifetime, generating less noise, having higher power to weight ratio. Therefore they are more reliable for the UAV applications. And also they have become more available with the increased interest on radio controlled model aircraft world. Two types of brushless motors exist as shown in figure 5.6, In-runner and Out-runner. In the in-runner configuration, the magnets are placed on the shaft of the motor and the windings are at the outer part of the motor. Whereas the out-runner configuration has the magnets turning around the stator. The low inertia of in-runner motor shaft makes them reach to higher rotation speeds compared to out-runner motors. However the out-runner motors are commonly preferred for their cooler running and high torque specifications which eliminates the use of additional gear-box.

The important task is to choose the suitable motor for the specified mission requirements. In order to be able to select the correct motor, the characterisation is a must.

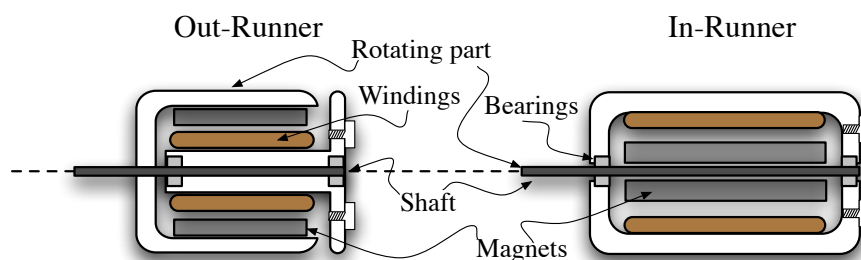


FIGURE 5.6: In-runner and Out-runner Brushless motor types.

First order simplified model using three motor constants, and experimentally obtained characteristics of DC motors will be explained in this section. Figure 5.7 shows an equivalent circuit model of an electric motor.

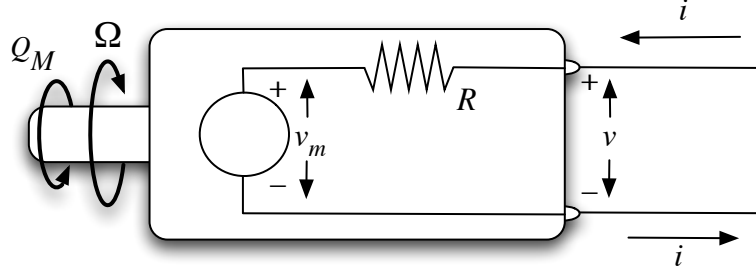


FIGURE 5.7: Equivalent circuit for a DC electric motor[3].

As described in [3], the resistance  $\mathcal{R}$  of the motor is assumed to be constant and the motor shaft torque  $Q_m$  is proportional to the current  $i$  according to motor torque constant  $K_Q$ . The friction based losses can be represented by the no load current  $i_0$  as a subtraction.

$$Q_m(i) = (i - i_0)/K_Q \quad (5.1)$$

Internal voltage  $v_m$  is assumed to be proportional to the rotation rate  $\Omega$  according to the speed constant  $K_v$  of the motor.

$$v_m(\Omega) = \Omega/K_v \quad (5.2)$$

Then the motor terminal voltage can be obtained by adding the internal voltage and the resistive voltage drop.

$$v(i, \Omega) = v_m(\Omega) + i\mathcal{R} = \Omega/K_v + i\mathcal{R} \quad (5.3)$$

The above model equations can be rewritten in order to give power, torque, current and efficiency as a function of terminal voltage and rotation rate of the motor. Firstly, the current function is obtained from equation 5.3.

$$i(\Omega, v) = \left(v - \frac{\Omega}{K_v}\right) \frac{1}{\mathcal{R}} \quad (5.4)$$

Then the others follow ;

$$Q_m(\Omega, v) = [i(\Omega, v) - i_0] \frac{1}{K_Q} = \left[ \left( v - \frac{\Omega}{K_v} \right) \frac{1}{\mathcal{R}} - i_0 \right] \frac{1}{K_Q} \quad (5.5)$$

$$P_{shaft}(\Omega, v) = Q_m \Omega \quad (5.6)$$

$$\eta_m(\Omega, v) = \frac{P_{shaft}}{i v} = \left( 1 - \frac{i_0}{i} \right) \frac{K_v}{K_Q} \frac{1}{1 + i \mathcal{R} K_v / \Omega} \quad (5.7)$$

As a reminder,  $K_v$  is usually given in RPM/Volt in motor specifications, however here it is taken as rad/s/Volt and  $K_Q$  is taken in Amp/Nm. It should be also noted that  $K_Q \approx K_v$ .

By knowing the first order motor constants ( $K_v, K_Q, i_0, \mathcal{R}$ ) of any off the shelf motor, the theoretical characteristic plots can be obtained by using above equations. General view of the motor outputs are shown in figure 5.8.

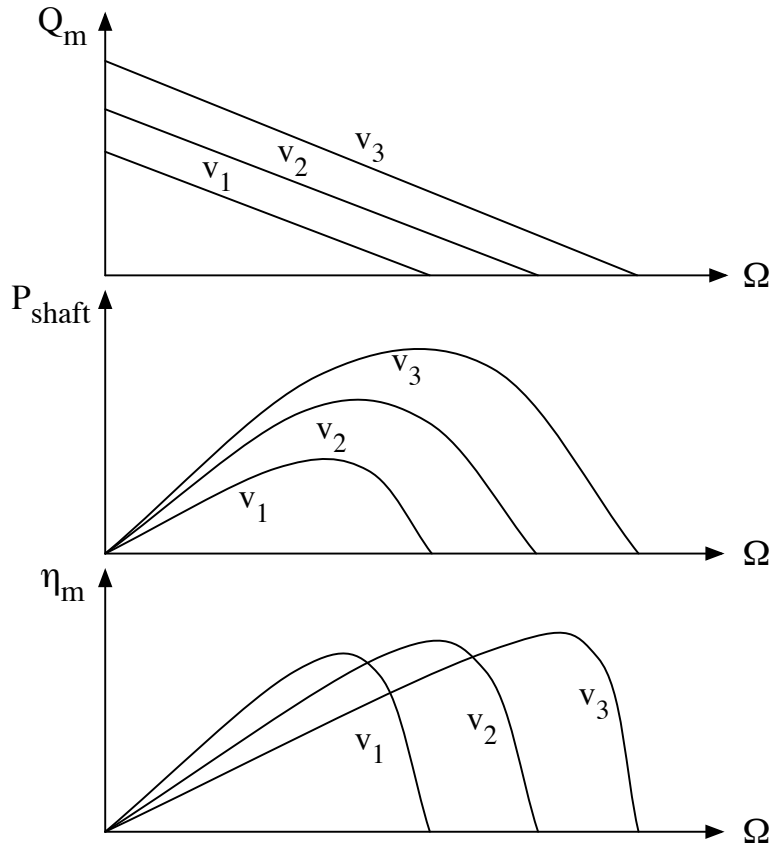


FIGURE 5.8: Theoretical motor outputs versus motor rotation rate for different input voltages.

## Experimental Motor Characterisation

In order to characterise the electric motors experimentally, the test bench which is shown in figure 5.9 is used. The motor is fixed on a free turning axle supported with ball bearings, and a torque sensor limits the turning of this axle in order to measure the torque generated by the motor while running. An optical speed sensor located near the motor measures the rotation speed. The power supply that is connected can directly record the voltage and the current consumed by the motor. Finally, all these sensors are integrated in a synchronised way in *Labview*<sup>1</sup> program.

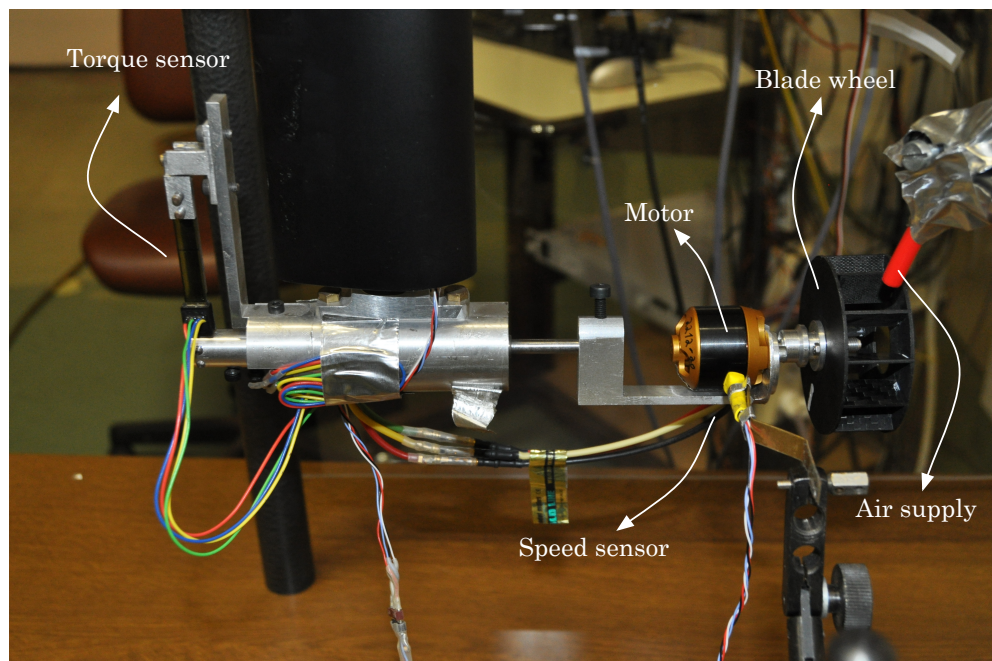


FIGURE 5.9: Motor test bench.

The key point is to generate variable resistance for the motor while running on a *constant voltage*. Figure 5.10 shows the wheel that is used for this purpose. Simply, an air supply is used in order to generate a breaking force on the motor and the flow rate of the air supply is increased in order to cover all of the working envelope of the motor. By this way the whole characteristics of the motor for a given voltage input can be viewed. The procedure is repeated for different voltages and the whole performance characteristics are extracted.

The characterisation of the motor can also be done by other methods such as using a second motor connected to the shaft of the first one in order to generate and

<sup>1</sup><http://www.ni.com/labview/>

vary the resistance load or a magnetic breaking system can be implied which will result with a higher precision on the resistance change. However the simplicity of using an air break at the moment of the tests outweighed all of the possible the disadvantages.

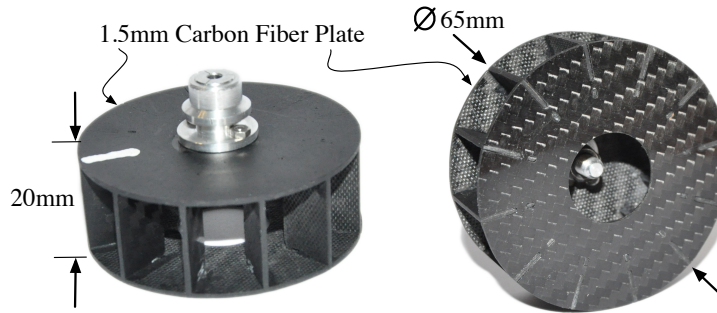
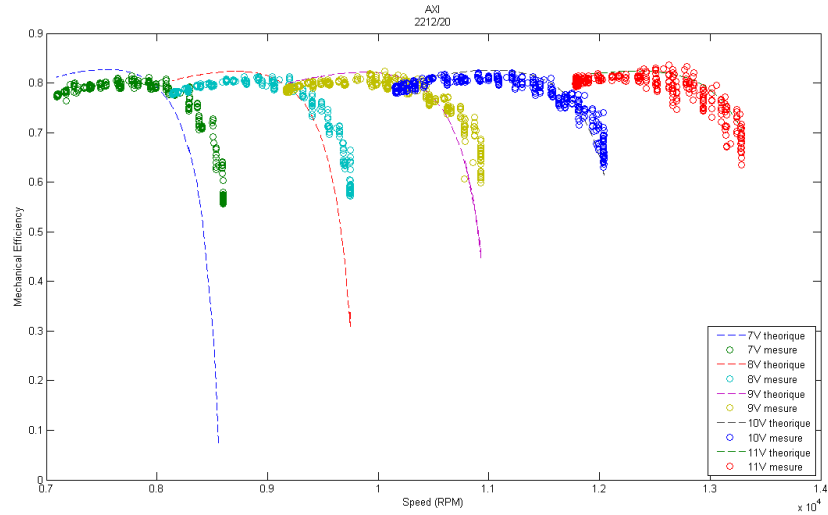
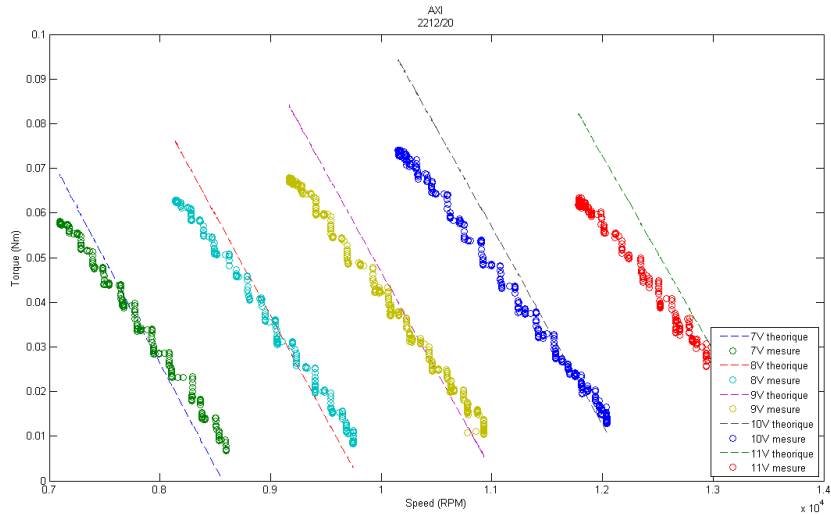


FIGURE 5.10: The wheel that is used in motor characterisation.

Figure 5.11 shows the comparison of performance curves that are measured experimentally and calculated with the previously explained theoretical model for AXI 2212-20 motor. It can be seen that the simple model has an error of approximately 5% on average. As a conclusion, this theoretical and experimental match shows that in the absence of experimental testing of the electric motors, the characteristic specifications which are given by the manufacturer can be used for the initial selection of the motor.



(a) Theoretical and experimental mechanical efficiency curves versus rotation rate for various input voltages.



(b) Theoretical and experimental shaft torque curves versus rotation rate for various input voltages.

FIGURE 5.11: AXI 2212-20 characteristic performance curves at various input voltages.

### 5.4.2 Propeller

The propeller is a rotating wing which utilises the mechanical power input in order to accelerate the air particles to generate thrust.

The basics of characterisation of the propeller is going to be explained here, however a deeper explanation can be found in [4]. The thrust and power coefficients are used to characterise a propeller, which depend on the advance ratio  $\lambda$ , the average blade Reynolds number  $Re$ , and the geometry of the propeller.

$$C_T = C_T(\lambda, Re, geometry) \quad (5.8)$$

$$C_P = C_P(\lambda, Re, geometry) \quad (5.9)$$

Reynolds number of the propeller is defined according to its average chord length  $c_{ave}$

$$Re = \frac{\rho \Omega R c_{ave}}{\mu} \quad (5.10)$$

Advance ratio  $\lambda$  is also well known as  $J$  in most of the literature.

$$\lambda(\Omega, V) = \frac{V}{\Omega R} \quad (5.11)$$

$$\lambda(\Omega, V) = J(\Omega, V) = \frac{V}{nD} \quad (5.12)$$

where  $n$  is,

$$n = \frac{\Omega}{2\pi} \quad (5.13)$$

Thrust and torque of the propeller as a function of rotation speed and the velocity,

$$T(\Omega, V) = \frac{1}{2} \rho (\Omega R)^2 \pi R^2 C_T = \frac{1}{2} \rho V^2 \pi R^2 \frac{C_T(\lambda, Re)}{\lambda^2} \quad (5.14)$$

$$Q(\Omega, V) = \frac{1}{2} \rho (\Omega R)^2 \pi R^3 C_P = \frac{1}{2} \rho V^2 \pi R^3 \frac{C_P(\lambda, Re)}{\lambda^2} \quad (5.15)$$

Finally, the efficiency of the propeller is,

$$\eta_{propeller}(\Omega, V) = \frac{T(\Omega, V)V}{Q(\Omega, V)\Omega} = \frac{C_T}{C_P} \lambda \quad (5.16)$$

## Typical Propeller Performance Curves

Typical propeller performance plots  $\eta$ ,  $C_T$  and  $C_P$  versus advance ratio are shown in figures 5.12, 5.13 and 5.14 for a variable pitch propeller at different angles (the chord distribution is always the same) [33].

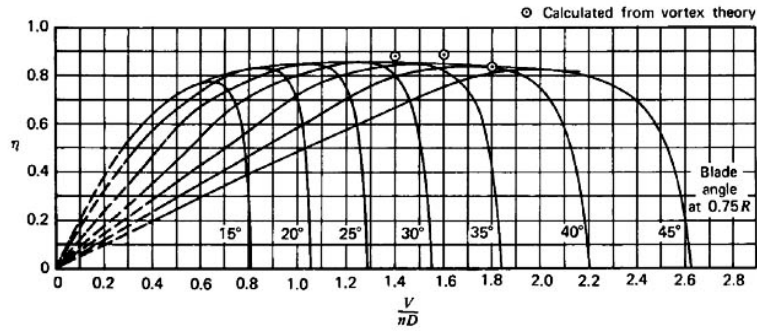


FIGURE 5.12: Typical propeller efficiency curves as a function of advance ratio  $J$ .

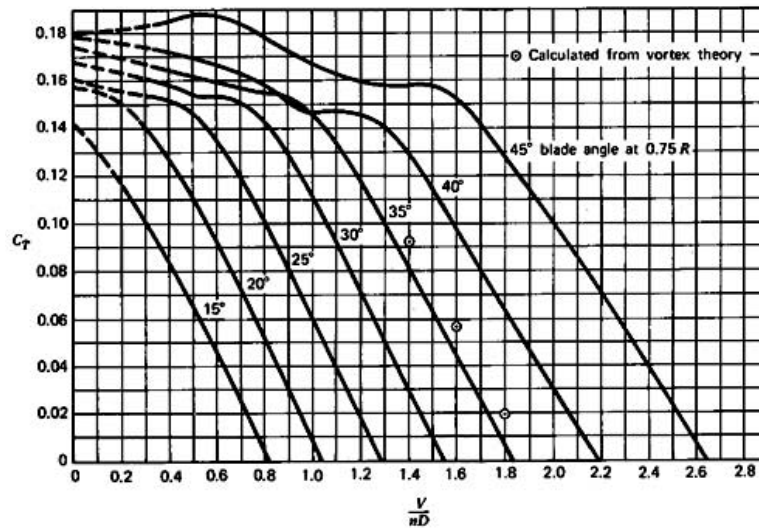


FIGURE 5.13: Typical propeller thrust curves as a function of advance ratio  $J$ .

## Experimental Propeller Characterisation

The same test bench which has been shown in section 5.4.1 is also used for the experimental characterisation of the propellers. Instead of the resistance generating wheel, the propellers that are going to be tested, are mounted to the test bench. Rotational speed, torque and the thrust of the propeller is measured at different wind tunnel speeds. Test bench is shown in figure 5.15.

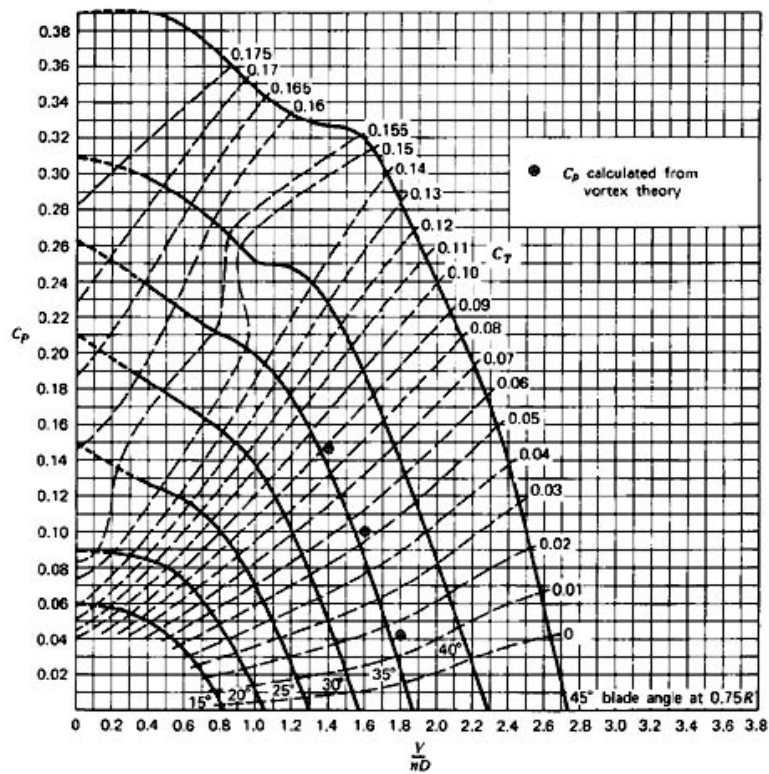


FIGURE 5.14: Typical propeller power curves as a function of advance ratio  $J$ .

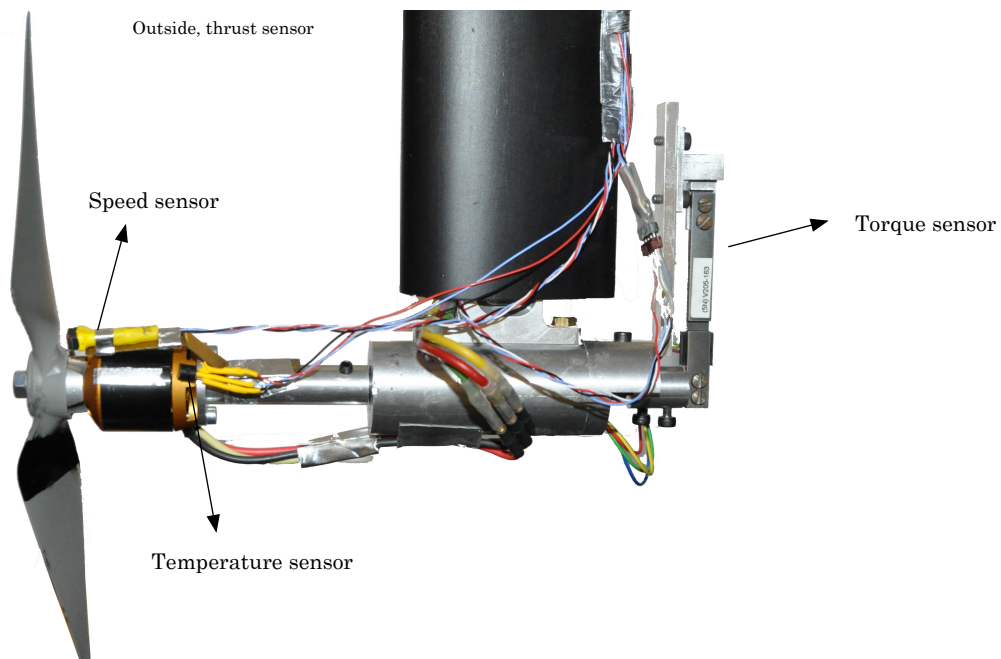


FIGURE 5.15: Propeller test bench.

## 5.5 Motor and Propeller Matching

Regardless of its maximum efficiency of an electric motor or a propeller, if they are not matched correctly for the given mission specifications, the resultant total efficiency will be poor. The theoretical and the experimental characterisation of the electric motors and the propellers have to be used in order to match the motor and propeller couples. Figure 5.16 explains the matching process with steps.

The mission requirements states the *Thrust* ( $T_p$ ) (Step 1) needed at a certain flight speed  $V$  for the propeller, according to propeller's thrust versus rotation speed characteristic curve, the corresponding rotation speed ( $\Omega$ ) is found (Step 2). The rotation speed at the given flight speed  $V$  will determine the efficiency of the propeller ( $\eta_p$ ) (Step 3). In optimal case, the efficiency peak of the propeller should roughly correspond to the given rotation speed. Then the torque of the propeller  $Q_p$  defined for the given flight speed is plotted and the torque value corresponding to the rotation speed ( $\Omega$ ) is found (Step 4). In order to match the motor and the propeller's torques ( $Q_m = Q_p$ ), the required voltage of the motor is calculated ( $v$ ) (Step 5). The resultant voltage and the rotation speed of the motor gives the efficiency point,  $\eta_m$ , where the motor works (Step 6). Finally, the multiplication of the motor and the propeller efficiencies gives the total propulsion set efficiency (speed controller efficiency has to be added separately). If the motor's efficiency is on the peak region, then the matching can be defined as good. Otherwise, a gear can be used to shift the peak efficiency region of the motor in order to match with the propeller's rotation speed. The explained method has already been built-in the QPROP program.

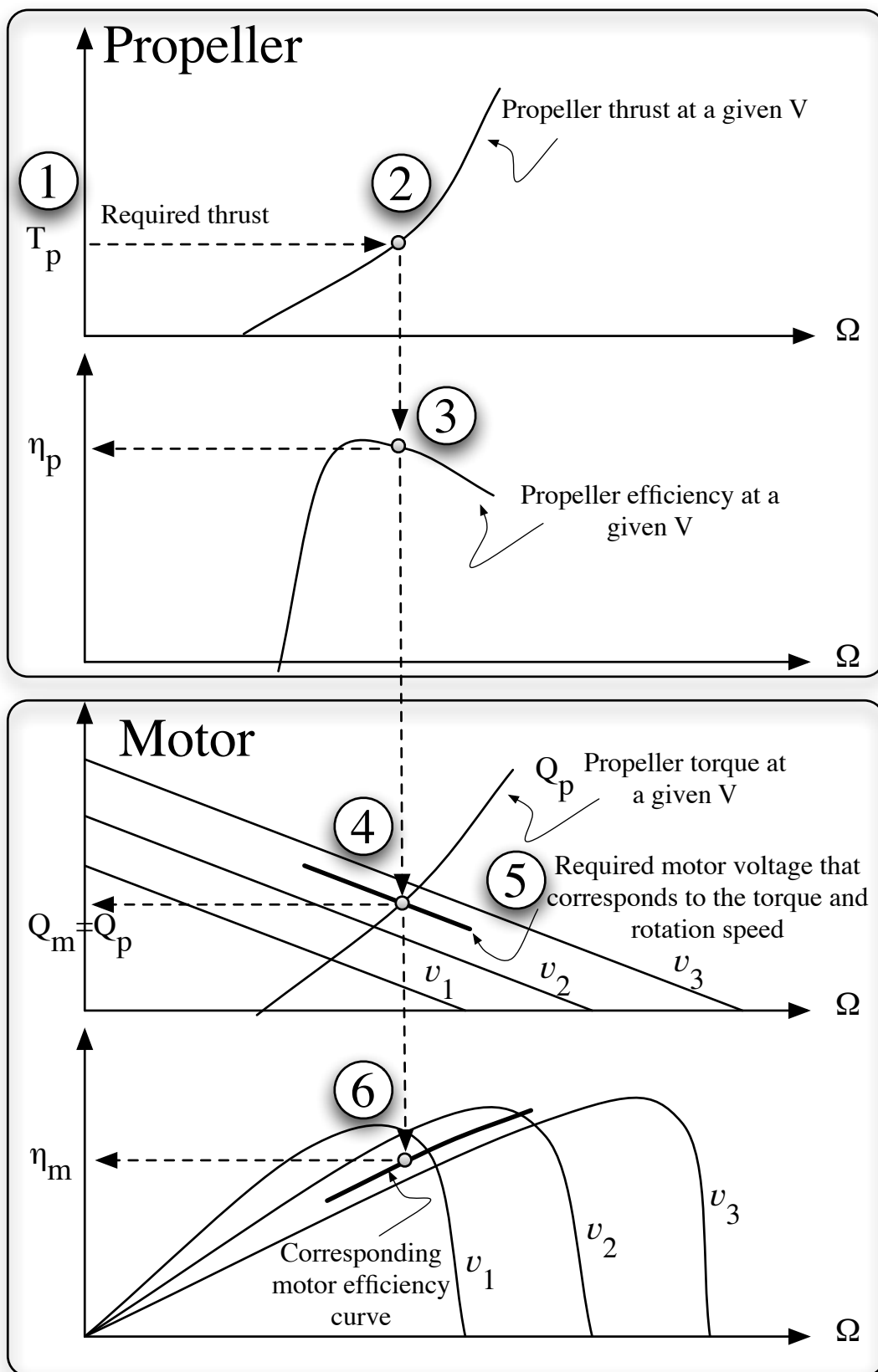


FIGURE 5.16: Motor and propeller matching procedure as explained in [4].

# Chapter 6

## Energy

### 6.1 Introduction

Doubtlessly the energy source and the storage is the most critical and important part of the design for long endurance flight. The higher the energy carried on-board per unit weight the better the endurance will be regardless of other variables. Improving the energy source and storage performance is out of the scope of this thesis, however the selection of optimum amount of on-board energy mass is as important as its performance.

This chapter concentrates on the energy source and storage models in order to predict their performances for a specific mission with high accuracy. As stated in the previous two chapters, the main objective is to integrate these low order prediction models into *Cdsgn* conceptual design program. As the effect of each model prediction plays a big role on the final aircraft design variables, it is important to have a good knowledge and estimate about each possible energy source and storage technology. Following sections explain the possible technologies that can be used.

### 6.2 Energy Storage

The energy storage method has to be chosen appropriately according to the mission, for a long-endurance aircraft, it has to be light weight and extremely efficient. Various ways of energy storage can be listed [34] :

- Chemical (Hydrogen, biofuels...)
- Electrochemical (Batteries, fuel-cells...)
- Electrical (Capacitors, supercapacitors)
- Mechanical (Flywheel, compressed air storage)
- Thermal

Figure 6.1 shows the Ragone Plot, peak power and specific energy density, of various energy storage methods. The dominance of gasoline can be clearly seen, where the batteries perform with one order of magnitude less performance. However, in the content of this thesis, the biggest importance has been given to electrochemical storage such as batteries as they are much more easy to use and robust as required for the *Mini-Long Endurance* concept.

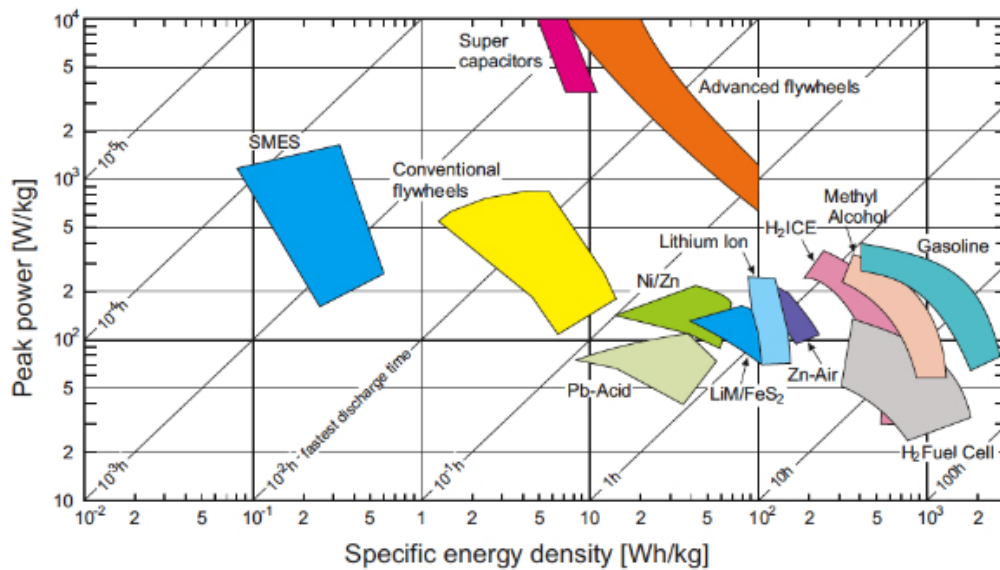


FIGURE 6.1: The Ragone Plot.

### 6.2.1 Batteries

An electrochemical battery is a device that can convert the stored chemical energy into electrical energy. Reverse process is also possible hence there exists two types of batteries: *primary batteries* (disposable batteries), which are designed to be used only once till complete discharge, and *secondary batteries* (rechargeable batteries),

which are designed to be recharged and used multiple times [35]. The secondary batteries are more interesting in terms of application especially when charging is an option during the mission, for example in the case of a solar panel equipped vehicle.

The increased demands of cell phones, portable computers, radio controlled aircrafts had a positive impact on the performance of batteries, especially on the lithium types. Table 6.1 shows the average specifications of different types of batteries commercially available on the market. Lithium sulfur type of battery from Sion Power[7] is clearly the most promising one among the available technologies, unfortunately company policies restricts the availability of this technology to school projects. Likewise in ten years from now, Lithium Air batteries will be the breakthrough for the energy storage as they have an theoretically  $+10kWh/kg$  of specific energy.

	Ni-Cd	Ni-Mh	Li-Po	Li-S
Specific Energy ( $Wh/kg$ )	40	80	180	350
Energy Density ( $Wh/l$ )	100	300	300	350
Specific Power ( $W/kg$ )	300	900	2800	600

TABLE 6.1: Battery specifications from different sources, numbers for Li-Po are already tested and the numbers for Li-S are rely on the manufacturer [7].

Lithium-polymer batteries are widely available and easy to obtain. Different package size and capacities are available as well as possible custom shapes for specific applications. The most important specification of the batteries for the long endurance mission is the specific energy ( $Wh/kg$ ). One of the leading brands on the market, ThunderPower [36] batteries have  $185 Wh/kg$  average specific energy for their *Pro-lite* battery series. The packaging of the battery plays a big role on the specific energy as the ratio becomes more significant for the small sizes. Figure 6.2 shows the increase of specific energy for bigger capacity batteries from AMICELL [5] brand. The bigger the capacity, the better the specific energy up to a certain value. It should also be noted that those values are only valid for single cells, for a three or four cell battery package, the additional connection cables and safety circuits reduces the real specific energy of the complete battery package. The safety circuits usually protects the battery packs from over discharging and sudden short circuits which can completely damage the batteries.

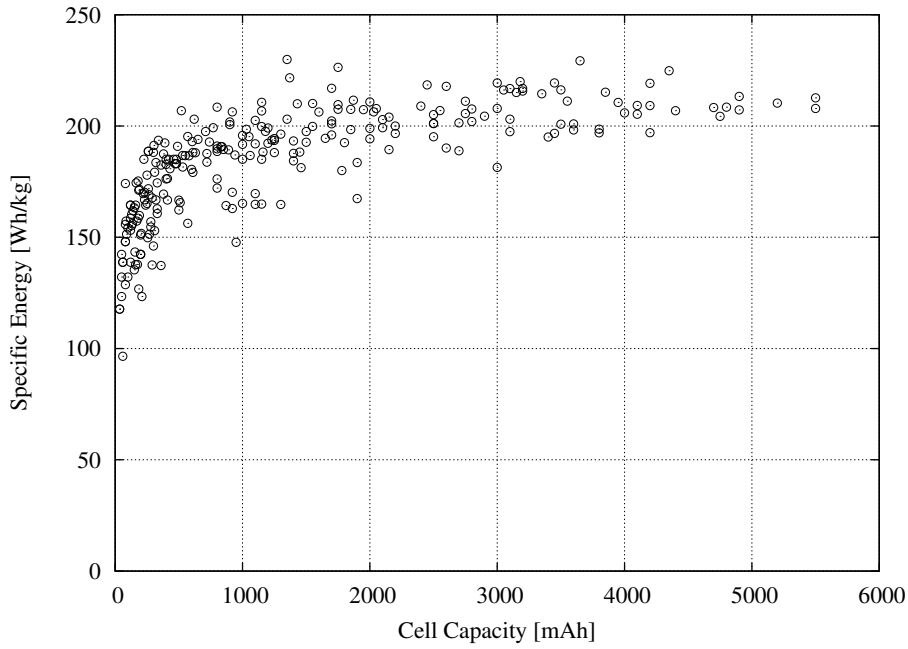


FIGURE 6.2: The single cell specific energy variation with respect to capacity for AMICELL [5] brand.

In order to model the battery for the conceptual design program (*Cdsgn*), several different brand and capacities are bought from the market and experimentally tested by controlled discharge. Figure 6.3 shows an example discharge plot of one of the lightest commercially available battery from ThunderPower [36] at room temperature. In order to keep the model simple, the battery is defined by its energy capacity, specific energy and discharge efficiency (6.1).

$$\eta_{Battery} = \frac{\text{Maximum Discharged Energy}}{\text{Specified Battery Energy}} \quad (6.1)$$

### 6.2.2 Fuel-cells

Fuel-cell is a device which convert energy from a fuel to electricity through chemical reactions. Figure 6.4 shows the basic working principles of a fuel-cell. The fuel-cell itself is the place where the reaction occurs, and the reactants are stored in separate tanks. The most commonly used fuel type is the hydrogen because of its high gravimetric energy density. Hydrogen as a reactant has a specific energy about  $34.44 \text{ kWh/kg}$ . In comparison to lithium batteries, which has around  $0.2 \text{ kWh/kg}$  specific energy, hydrogen looks extremely efficient, in fact there has

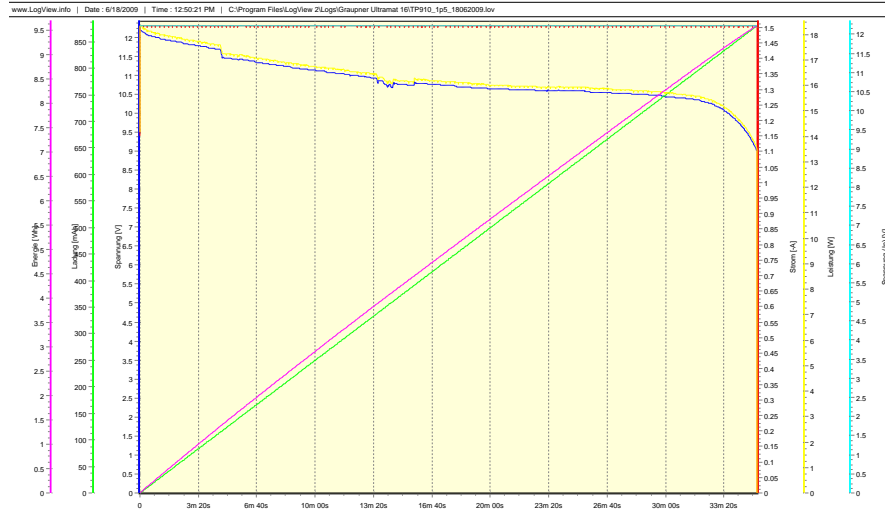


FIGURE 6.3: The discharge plot of ThunderPower 910mAh 3-cell (11.1V) battery.

to be a complete system including the storage tanks, fuel-cell stack, pumps, connection pipes, filters, etc... in order to produce energy. Taking into account the complete system, the packaged specific energy is around 400 to 1000  $Wh/kg$  [37]. Regenerative fuel cell system[38, 39] is really beneficial for a long endurance flight however the total system weight and the low round-trip efficiencies limits the possible usage of them.

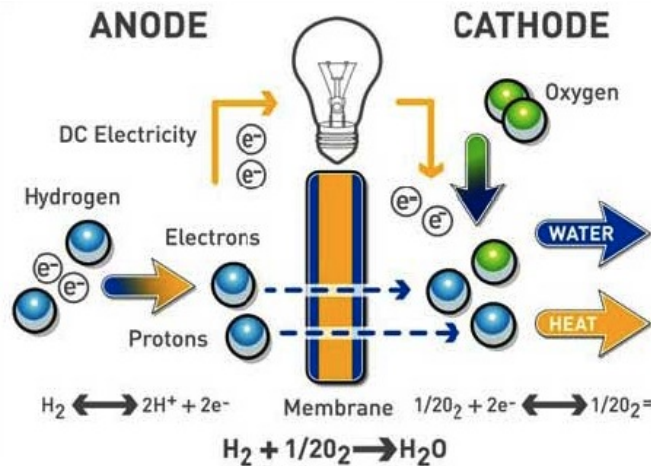


FIGURE 6.4: General working principle of fuel cells (Source: <http://www.tekstak.com/>).

Fuel-cell technology is still not easily available and additionally expensive. Two brands released their product to the commercial market, with dedicated designs specifically for UAV usage. *Aeropak* from Horizon Energy [40] and *UAV C-250*

from Protonex [41] are shown in figure 6.5 with their specifications in table 6.2. Fuel-cell technology is one of the leading technologies towards long endurance flight, however for a mini-UAV scale, even the lightest system available is too heavy to take into considerations. In the objective of this thesis, the mini-UAV design is decided to be kept under  $2\text{ kg}$  of maximum total weight which allows easier to obtain the permission to fly by the French UAV regulations [42].



FIGURE 6.5: Two commercially available fuel-cell packs from Horizon Energy and Protonex, Aeropak and UAV-C250.

	AEROPAK-1	AEROPAK-2	UAV-C250
Specific Energy ( $Wh/kg$ )	450	607	500
Energy ( $Wh/kg$ )	900	2125	1500
Continuous Power ( $W$ )	200	200	200
System Weight ( $kg$ )	0.47	0.47	1.2
Cartridge Weight ( $kg$ )	1.53	3.03	1.8
Total Weight ( $kg$ )	2.0	3.5	3.0

TABLE 6.2: Specifications of Horizon Energy and Protonex brand fuel cell systems.

However several successful projects have been demonstrated with fuel-cells without the limitation of  $2\text{ kg}$  of maximum total weight[43, 44].

### 6.3 Energy Extraction

As an option to energy storage on-board, energy extraction can also be used for performance enhancement of long endurance aircrafts. The biggest advantage occurs especially if there is not a lot of additional weight requirement for the energy extraction process.



FIGURE 6.6: Fuel-cell demonstrator from Georgia Tech with a span of 6.58m and 16.4kg of total weight.

### 6.3.1 Thermal Soaring

Thermal soaring have been used successfully by the glider pilots for decades and now it is applicable for the mini-UAV scale with the new miniaturised sensors and high on-board processing power available. Michael J. Allen demonstrated autonomous soaring flight with a 4.25 *m* span glider by using a commercial autopilot modified with an outer loop for the autonomous soaring algorithm [45]. The updraft model that is developed in order to use by the autonomous glider is explained in more detail here [46]. Following Allen, a successful implementation of cross-country flight algorithm is developed and demonstrated by Edwards [47], those resulted with certain autonomous soaring records. This will be kept out of the scope of this thesis and is included as a planned future work.

### 6.3.2 Solar Energy

Another way of energy extraction is to use the solar energy by photovoltaic cells. A photovoltaic cell or solar cell is a device that convert solar energy into electricity. Several types of solar cells exists depending on the material used, manufacturing type, etc, but the mostly used material is the silicon as it is cheap and easily found on earth. Figure 6.7 shows the basic working principle of solar cells.

Figure 6.8 shows the recent efficiency trend for different types of solar cells. Currently the multijunction concentrator solar cells can reach an efficiency of 43.5%

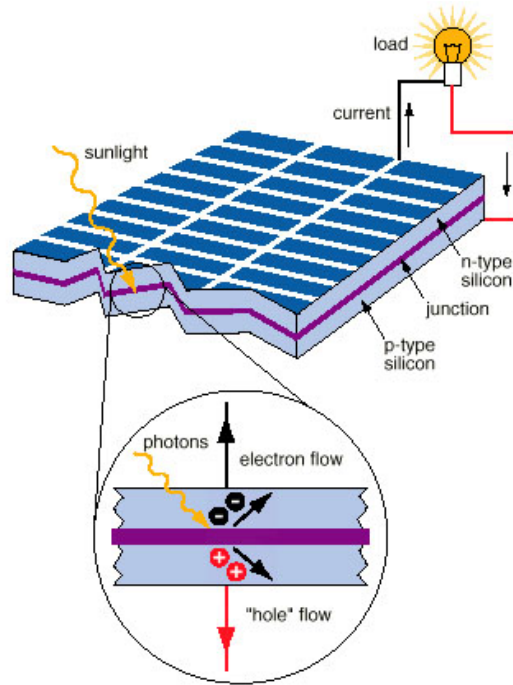


FIGURE 6.7: General working principle of solar cells (Source: <http://www.solarcell.net.in/>).

where the non-concentrator ones can reach up to 34.1%. The thin-film technologies reported to reach to 20.3% but the Amorphous type are still at 12% levels. The commercially available thin-film cells have even lower efficiencies ( 5%).

For the long endurance mini-UAV concept, the location of the solar cells are selected to be placed on top of the wing surface. This brings the requirement of flexible type cell usage. The widely used flexible solar cells (figure 6.9) on the market are generally designed for architectural usage such as covering the buildings, or roof tops. They are cheap in comparison, easy to maintain and use but unfortunately they have low efficiency (%2.5 – 3.0 from Power Film) compared to some other candidates such as RWE S-32 from Azur Space with efficiencies reaching up to %17.

The RWE S-32 solar cell, shown in figure 6.10 with its specifications, are mainly used for space applications. The light weight and semi flexible properties added with its high efficiency were the reasons to be selected for the projects that are presented in the following chapters.

Despite being lightweight, solar cells needs additional management system in order to extract the maximum amount of energy that they are capable of supply at a

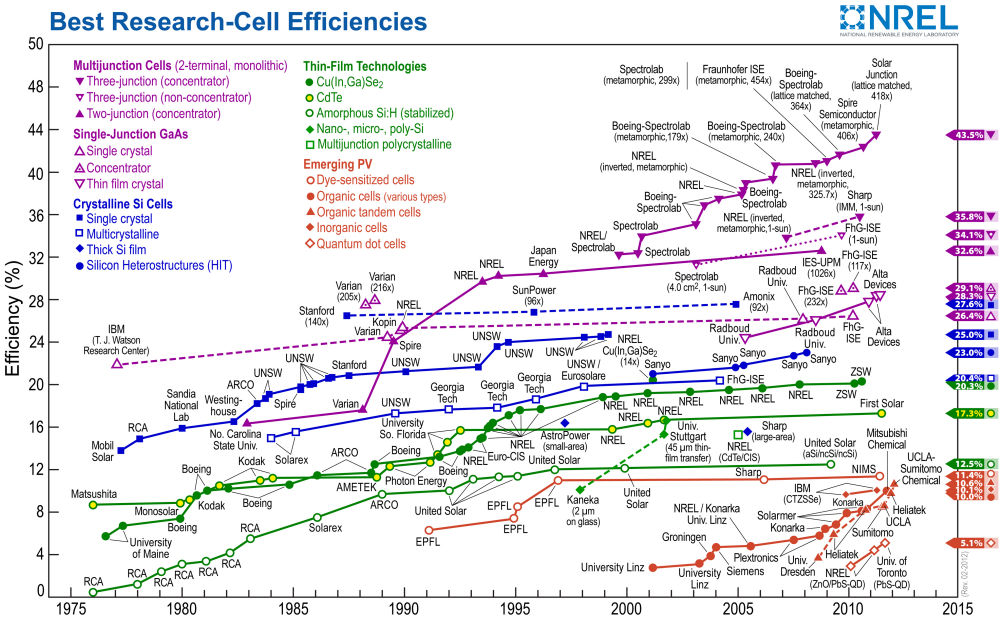
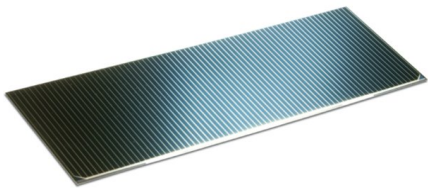


FIGURE 6.8: Solar cell efficiencies (Rev:02.2012, NREL[6]).



FIGURE 6.9: Flexible solar cell from *Power Film*.



RWE S-32	
Open circuit V (mV)	628
Open circuit I (mA/cm <sup>2</sup> )	45.8
Voltage @ Pmax (mV)	528
Current @ Pmax (mA/cm <sup>2</sup> )	43.4
Avg. Efficiency (%)	16.9

FIGURE 6.10: Azur Space S-32 solar cell and its specifications.

certain solar irradiance. This management device is called maximum power point tracker (MPPT). In chapter 7, a custom developed MPPT is presented with a brief explanation about how it works.



# Chapter 7

## Hybrid Solar Micro Air Vehicle

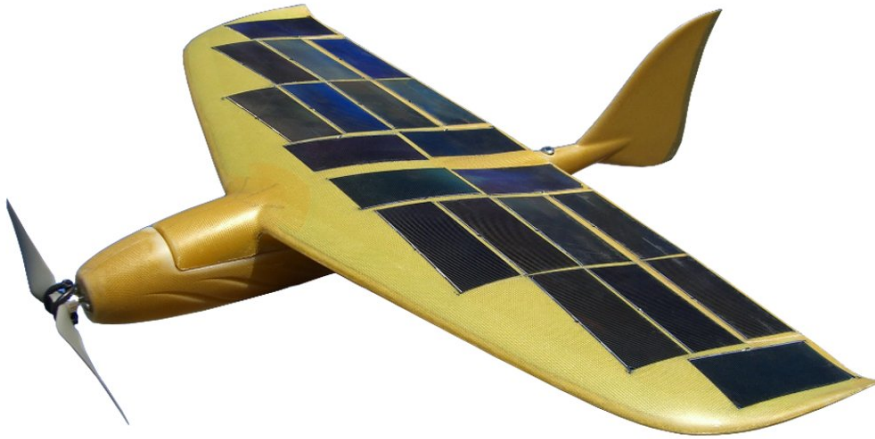
### 7.1 Introduction

As described in the previous chapter, solar energy exhibits the best performance in terms of feasibility and application in order to be implemented for enhancing flight time on MAVs. In 2009, the European Micro Air Vehicle Conference and Competition has been organised with a separate endurance mission for MAVs. This opportunity is used to design the *Solar Storm* and *Fire Storm* and see the feasibility of the usage of solar cells on such small vehicles are within 50 *cm* maximum dimension. *Solar Storm* is the **first** autonomous micro air vehicle that utilise solar energy to enhance its endurance in **its scale in the world**.

This chapter explains the design of the *Solar Storm* and gives an idea about all the requirements needed to have an efficient hybrid solar MAV. The flight performance of the design is presented as well as the windtunnel data and the real life competition results.

### 7.2 Design of *Solar Storm*

The design is mainly driven by EMAV'09 competition rules, but still the biggest objective was to see the feasibility of the solar energy usage on MAVs. The competition rules has a maximum size coefficient for the final flight score which promotes designing the smallest vehicles possible. Therefore a parametric study has been

FIGURE 7.1: *Solar Storm* design.

realised for an equal on-board energy of  $10.1\text{ Wh}$  for two different maximum size constrained vehicles ( $30\text{ cm}$  and  $50\text{ cm}$ )[10]. The surface area of the vehicles are optimised for best endurance, and performance analysis are done for both with and without addition of solar energy configurations.

The results clearly showed that for the same on-board energy, the bigger  $50\text{ cm}$  MAV benefits the solar energy much more than the small  $30\text{ cm}$  one for enhancing endurance in comparison. This is a result of the reduced wing surface area of the small sized MAV reducing the total solar cell area which is proportional with energy extracted from the sun. Another important issue is the weight ratio of the solar cells and the required electronics to the weight of the MAV. This ratio is becoming larger when the MAV gets smaller in size, reducing the overall efficiency of the MAV. Looking at these results, it can be concluded that under a certain size, there is almost no benefit of using solar cells. It should be noted that these conclusions are made taking into account the Paparazzi autopilot and electronics weights from 2009. When the on-board equipment and airframe weight go down, the solar energy benefiting minimum size vehicle will be smaller too.

In the light of these results, a  $50\text{ cm}$  MAV with the solar cells is concluded to be designed. The early version of *Cdsgn* program, which has been described in the previous chapter, is used for the design phase. In the time of design, *Cdsgn* was in the early development phase and all the calculations was being investigated by analytical and empirical formulas. Despite being fast in calculation, it lacks the

longitudinal moment equilibrium and also the trim drag necessary for having this equilibrium. These had a big influence on the accuracy of the analyses especially when big control deflections are needed in order to have equilibrium conditions. Knowing these limitations, the program is only used in order to get the rough information about the total wing surface area, the appropriate airfoils and optimum flight speed with respect to on board battery weight. According to these values, design is improved on AVL program manually.

The wing platform is optimised in order to place the maximum number of solar cells safely on the surface while keeping in mind the span efficiency, elliptical loading and the tip stall issues. This was especially important in order to reach the same percentage of solar cell area to wing area that we have assumed in the calculations.

After determining the main airfoil of the design, again XFOIL airfoil analysis and design program is used to design the airfoil family along the span. There are three different custom airfoils along the span, which are particularly designed according to their corresponding Reynolds number for the cruise speed while observing the stall behaviour and maximum lift coefficient. The same type of spanwise transition and the design procedure will be described more deeply in the following chapter 8.

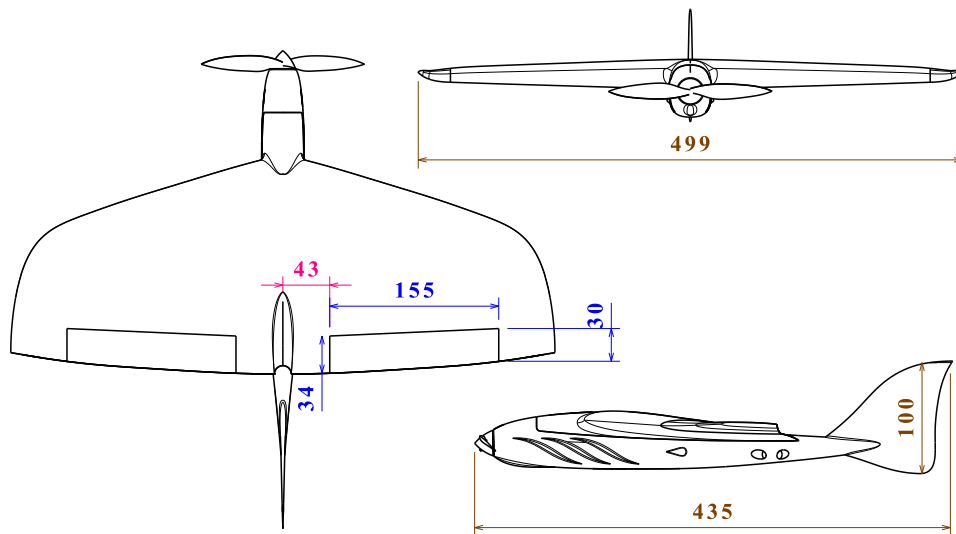


FIGURE 7.2: Main dimensions of *Storm* design in millimetres.

## 7.3 Solar Energy Management

Despite being lightweight, solar cells requires special management to be integrated into propulsion system. As described in section 6.3.2, the maximum amount of power that can be extracted from solar cells varies according to irradiance, environmental conditions or the attitude of the cell according to sun rays. In order to have the maximum benefit from solar cells, these changes needs to be tracked precisely and the power extraction has to be done with a maximum power point tracker unit.

### 7.3.1 Maximum Power Point Tracker *MPPT*

In the design parameters of *Solar Storm*, the efficiency of the solar cells are taken as constant and at maximum value (16.9%), this is not exactly true for all cases in real life as explained. In the working mechanism of solar cells, when the pads of the solar cells are not connected, the voltage between the pads is  $V_{OC}$ , the open circuit voltage and the current is null. When the pads are short circuited, the voltage becomes zero and the current is  $I_{SC}$ , the short circuit current. The maximum output power has to be found between these two points. This point is called maximum power point (*MPP*) and the voltage and the current at this particular point are  $V_{MPP}$  and  $I_{MPP}$ . If a higher current than  $I_{MPP}$  is drawn by the system, then as a result the voltage is going to be reduced. This leads to a lower power extraction. In the other sense, if a lower current than  $I_{MPP}$  is drawn, then the voltage increase will not be sufficient in order to counter balance the current decrease and the extracted power will be again lower than optimum. Thus the search for the *MPP* requires an ad hoc electronics circuitry adapted in real time with a control loop. Figure 7.3 shows the custom designed *MPPT* board and figure 7.4 shows the schematics of this board. Note that it includes a micro-controller which can be linked to the autopilot to be monitored from the ground station.

## 7.4 Manufacturing and Integration

In order to obtain the required high quality surface and precise form of the structure, the manufacturing is done by using CNC made molds. Composite materials

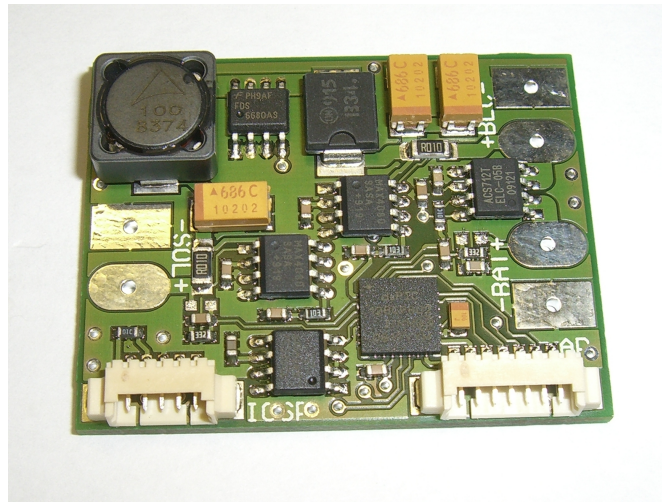


FIGURE 7.3: Custom designed maximum power point tracker board.(Weights 7 g)

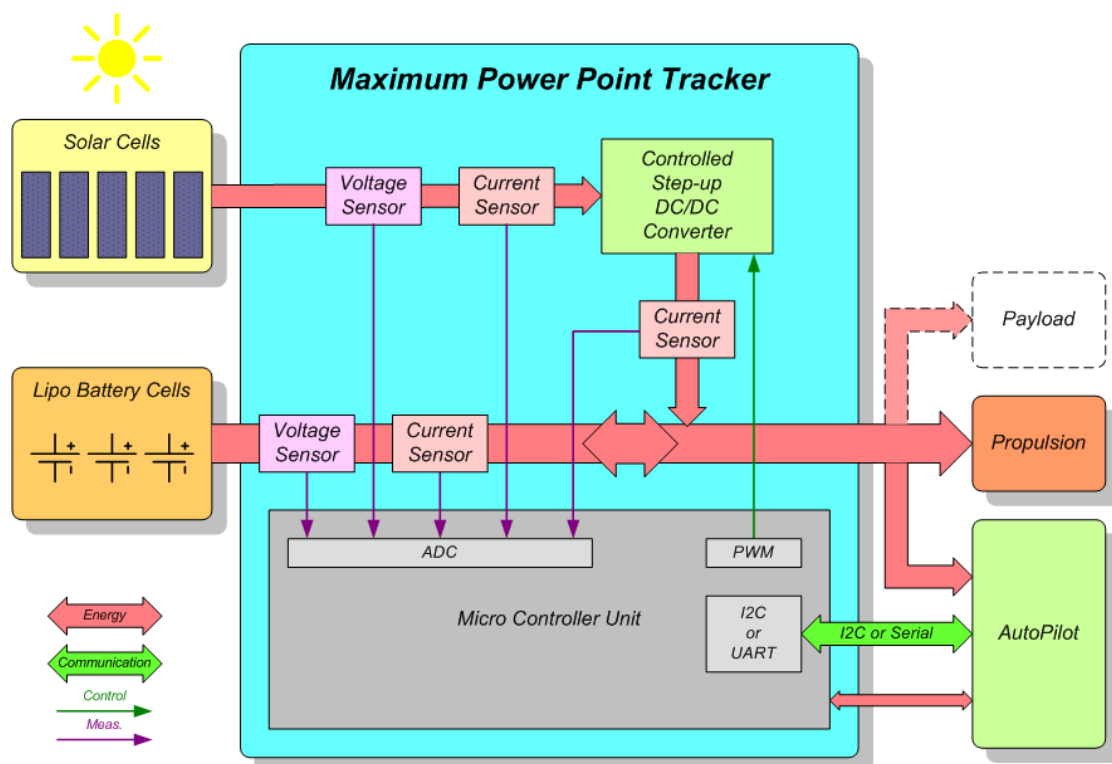


FIGURE 7.4: Maximum power point tracker architecture.

used, with sandwich and vacuum bag method in order to keep the structure light and robust. To keep the design simple, only two control surfaces are used as elevons. The servos are embedded inside the wing and the controls are coupled internally to have an aerodynamically clean wing. The wing skin is used as the control surface hinge. This ensures a light weight and more reliable joint while having less disturbance on the wing surface. Twenty thin RWE Si-32 silicon solar cells<sup>1</sup> are placed on top of the wing. Also, the wing and the fuselage are designed as two separate pieces in order to transport easily. Two frames have been built. The *Solar Storm* which is equipped with the solar cells and the *Fire Storm* which does not have the solar cells and mainly designed to be used in test flights, and bad weather conditions just in order to prevent any unwanted damage to the solar cells. For the autonomous stabilisation and navigation capability, Paparazzi Autopilot System has been used as the author being a member of the team and the laboratory that the system is developed in. Table 7.1 shows the mass breakdown of both *Solar* and *Fire Storm*.

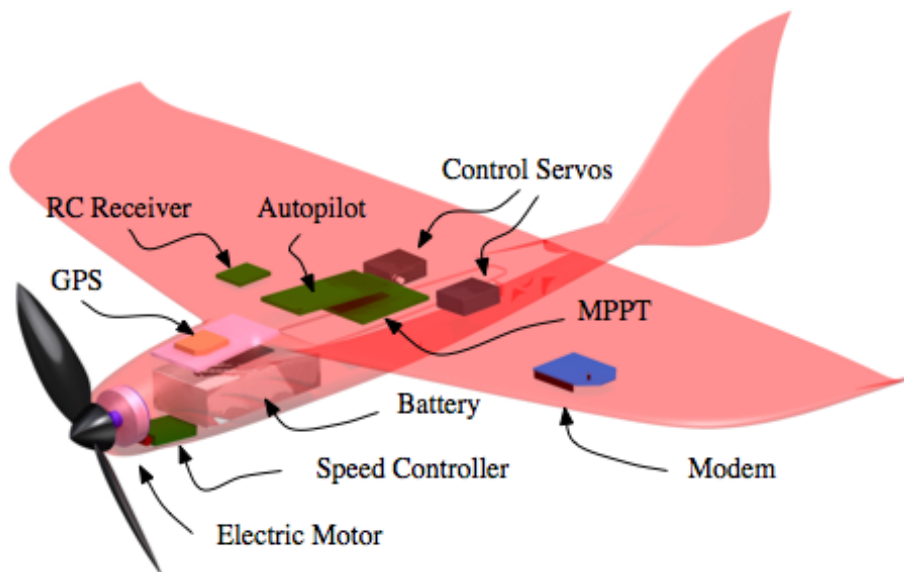


FIGURE 7.5: The integration of the main components of *Solar Storm*.

## 7.5 Wind-tunnel Tests

Wind tunnel campaign is performed at ISAE-ENSICA S4 windtunnel. A six component internal balance is used in order to measure the forces and moments which

<sup>1</sup>Azur Space

	Fire-Storm	Solar-Storm
Wing Structure	95	90
Fuselage Structure	28	27
Solar cells	-	22
MPPT	-	8
Motor	23	23
Speed Controller	5	5
All Electronics	51	50
Battery	180	90
Total	384	305

TABLE 7.1: Mass break down of Solar and Fire Storm (all in grams).

has been previously introduced in section 4.6.2. A specific *Storm* model is manufactured just for the wind-tunnel experiments which is highly reinforced in order to handle the high wing loading of the tests and also in black colour for the planned flow visualisations. Figure 7.6 shows the mounting of the model onto the strut. The fuselage is empty and only used to cover and protect the balance.

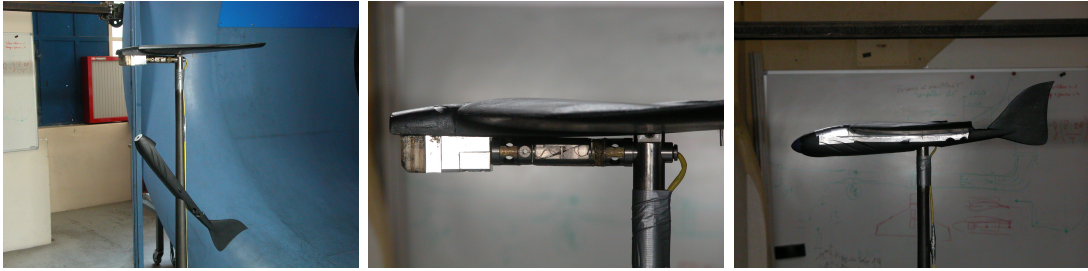


FIGURE 7.6: Mounting of the Storm wind-tunnel model and the internal balance integration.

Figure 7.7 shows the lift slope comparison between the wind tunnel measurements and the linear model obtained by AVL program. The model estimates the maximum lift coefficient a little bit higher than the obtained measurements but the lift slope is estimated correctly.

Figure 7.8 shows the range ( $C_L/C_D$ ) and endurance ( $C_L^{1.5}/C_D$ ) wind tunnel performance plots with pitching moment coefficient with respect to three different reference locations. The control surfaces were fixed at 0 degrees in all conditions. The three different reference points have been examined in order to define the exact position of center of gravity that corresponds to zero pitching moment at desired lift coefficient with no control surface deflection. This situation will lead to minimum trim loss in the cruise flight of 15 m/s.

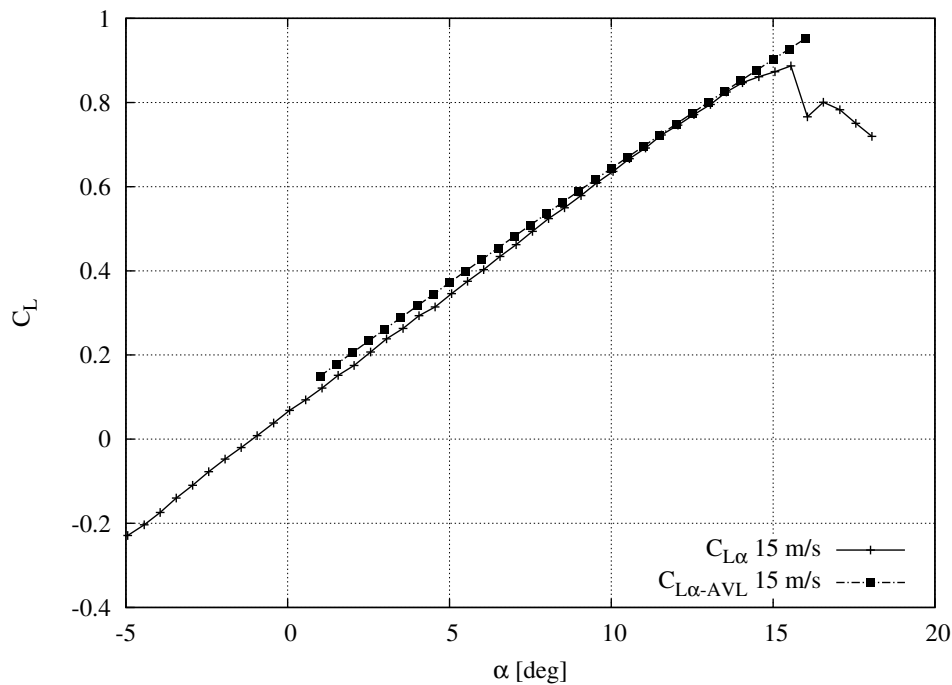


FIGURE 7.7: Comparison of lift slope curve obtained from wind tunnel and AVL model.

Figure 7.9 shows the wind tunnel measurements versus the expected coefficients obtained by the modified AVL program which has been explained in chapter 4. The parasite drag coefficient which includes the interaction drag and various additional drag was assumed to be  $C_{Dpar} = 0.005$  in the calculations. As it can be seen from the figure 7.9, this coefficient was too pessimistic compared to windtunnel results. Thus figure 7.10 shows the corrected calculations with respect to wind tunnel results again, the only correction is the change of  $C_{Dpar}$  coefficient from 0.005 to 0.001.

The wind tunnel model did not have the elevons. So the efficiency of the elevons could not be identified. Still the accuracy of the numerical model in comparison to wind tunnel results is satisfying enough to use it for the rest of the performance estimations in equilibrium state.

## Flow Visualisation

At the end of the wind-tunnel campaign, the balance is removed and replaced with a fake balance and flow visualisation experiments have been conducted. Figure 7.11 shows two images from the experiments, the one on the left shows the straight flight

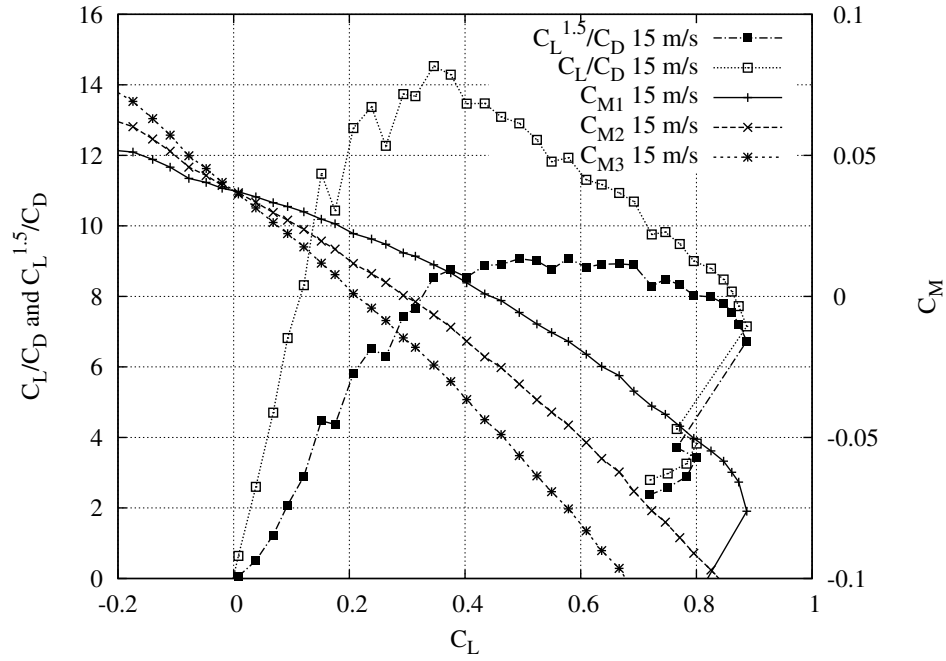


FIGURE 7.8: Range and endurance performance curves with the pitching moment coefficient for three different reference locations.

condition and the one on the right shows the flow generated while a 10 degrees of sideslip angle, both of them are for the cruise speed of  $15\text{ m/s}$ , which corresponds to  $Re = 150k$  for the mean aerodynamic chord, while the lift generated equals to the weight of the aircraft.

The laminar bubbles on top of each wing can be clearly seen on both conditions. The effect of fuselage is also visible in the middle of the wings as it transforms the laminar flow into turbulent just after the nose cone.

## 7.6 Flight Performance

The first flights and the tuning of the autopilot control gains are done with *Fire Storm*. The reason was to prevent any damage that can come to the fragile solar cells of *Solar Storm* because of a system or safety pilot error. For the maiden flight, *Fire Storm* is equipped with a lower capacity battery according to the desired one, this helped for the first hand launch of the plane as the wing loading is reduced because of the lower weight.

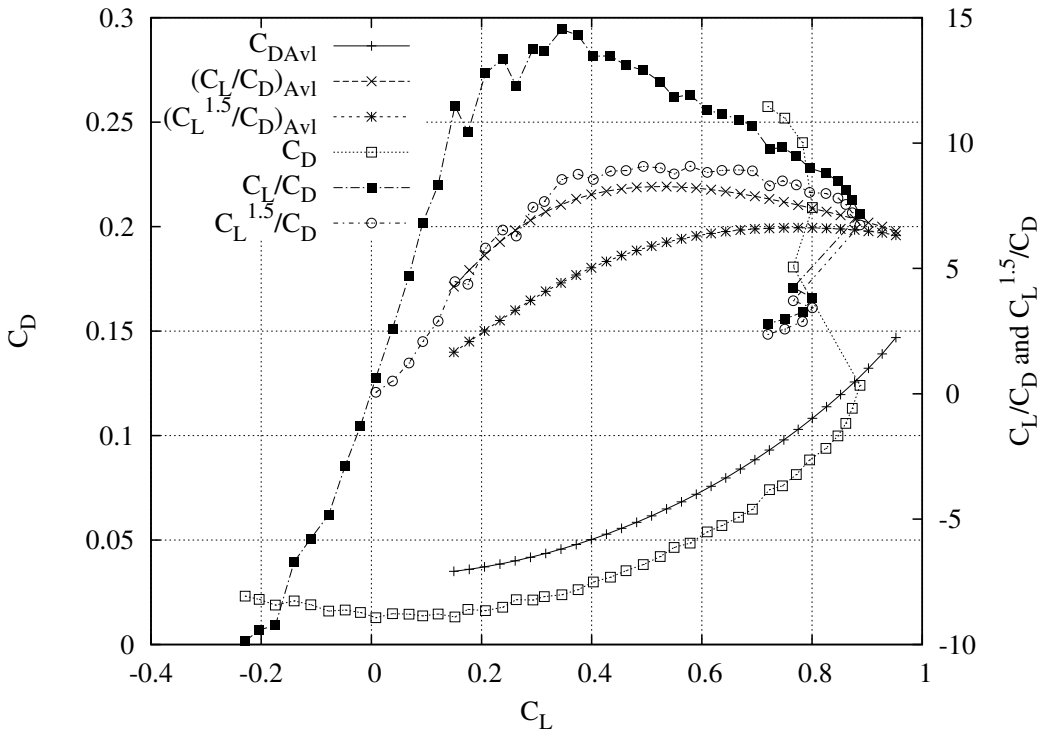


FIGURE 7.9: Comparison of windtunnel experiment results to calculated results coming from modified AVL program with  $C_{Dpar} = 0.005$  at  $15\text{ m/s}$

The small battery with  $14.6\text{ Wh}$  of energy (3-cell Thunder Power 1320mAh) last for 59 minutes of flight which includes tuning of the control loop parameters and some manual controlled flights. The obtained autopilot parameters are directly used on the *Solar Storm* and the maiden flight is done in autopilot assisted mode and later in the flight, complete autonomous mode is tuned, no manual flight attempted. The main reason why manual flight was prohibited is the low pitch damping and low static margin ( $< 5\%$ ) of the design, and also the inertia of the plane on y-axis is low due to the concentrated mass distribution at the centre of gravity.

The maiden flight of *Solar Storm* lasted 53 minutes with a battery that contains  $8.1\text{ Wh}$  (3-cell Thunder Power 730mAh) of energy. After this first tuning flight, a second flight has been done with the same battery that has been used on the first flights of *Fire Storm*,  $14.6\text{ Wh}$  3-cell Thunder Power 1320mAh. The achieved endurance was 90 minutes, which is about 30 minutes longer than the previously achieved flight time with the same battery energy without the solar energy contribution. The flight analyses showed that almost 40% of the level flight power consumption was coming from solar cells while the rest is powered by the on-board

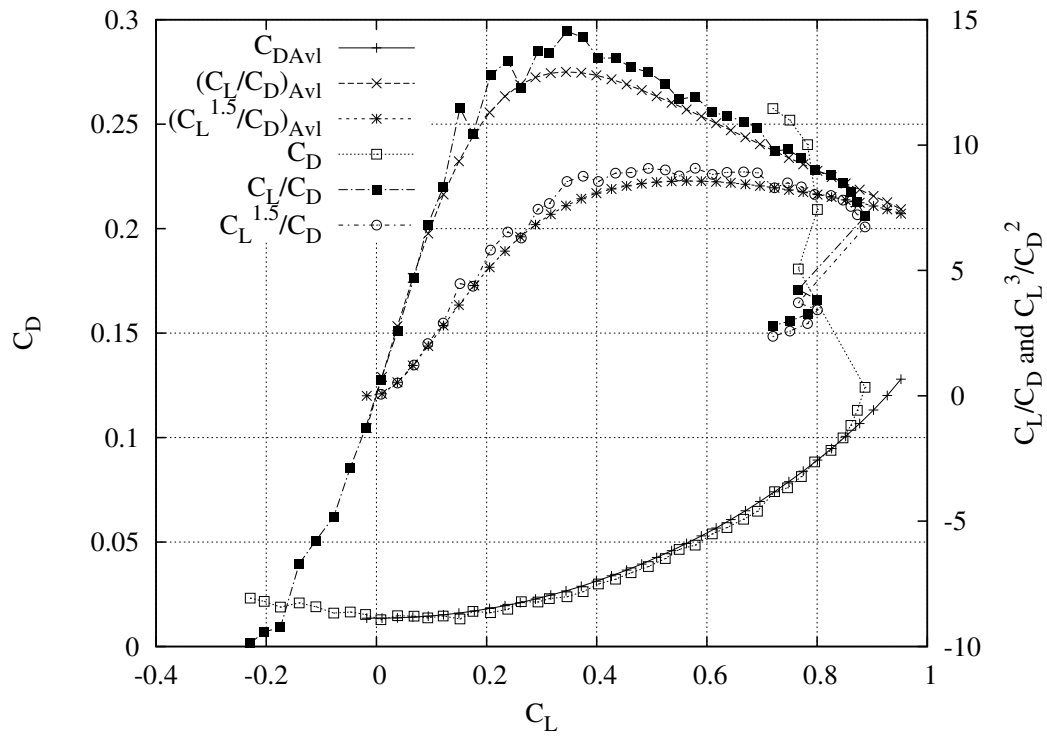


FIGURE 7.10: Comparison of windtunnel experiment results to calculated results coming from modified AVL program with corrected  $C_{Dpar} = 0.001$  at  $15\text{ m/s}$



FIGURE 7.11: Flow visualisations realised for straight flight on the left and for a side slip angle of 10 degrees on the right at cruise conditions ( $15\text{ m/s}$ ).

battery. In this flight the additional weight required for solar energy and its management was about  $30\text{ g}$  ( $22\text{ g}$  for the solar cells plus  $8\text{ g}$  for the MPPT board). Figure 7.12 shows the variation of the solar cell voltage, power extracted from solar cells, current drawn from battery only and the total system current draw for a small portion of the real flight. The flight path was a circle with a fixed centre point at  $90\text{ m}$  AGL, although there were perturbations coming from the

non-perfect environment, the aircraft was continuously banking with a fixed angle in order to have the sustained turn. The effect of this can be immediately seen in the figure 7.12 on the variation of the solar power. When the angle between sun rays and the solar cells decreases, the maximum power that can be extracted decreases as well. Another very important achievement that can be seen on the figure is the negative battery current, showing that the batteries have been charged for a short period of time.

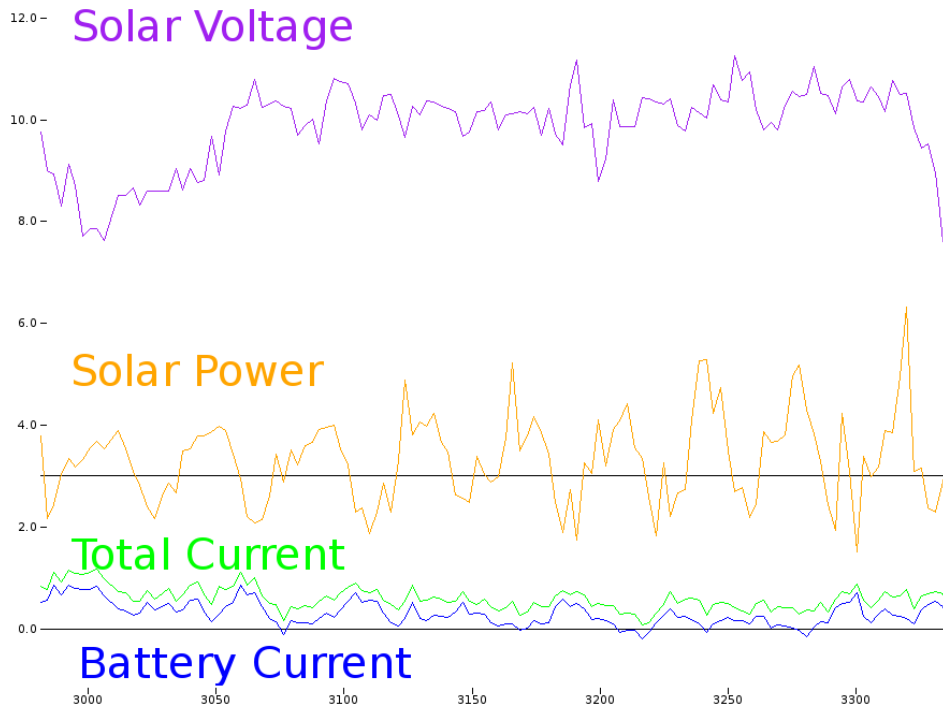


FIGURE 7.12: *Solar Storm*'s log with the time in [s] in x-axis and [V] , [W] and [A] for the y-axis.

The *Fire Storm* frame was being tested in parallel, and as its mission is more for a higher speed than *Solar Storm* the battery carried on board had to be bigger in capacity. A test flight with two Thunder Power 1320mAh connected in parallel is attempted. The achieved endurance was 100 minutes and the average flight speed was 16 m/s resulting about 100 km of range. These results are all fitting well with the previously estimated performance coming from numerical model. Figure 7.13 shows the numerical model's expected flight performance values in equilibrium state. It should be noted that the plot includes the propulsion efficiency which is calculated at each flight speed. QPROP program is used for the propulsion calculations and as it doesn't take into account the speed controller efficiency, a simple linear model is used to estimate the speed controller efficiency as a function of throttle percentage used in each flight condition. The power consumption of the

on-board electronics are also included and taken constant as  $3\text{ W}$  after investigating ground and no-motor glide tests of previously flown other MAVs. The numerical model also assumes that the battery efficiency is %95 meaning that the battery is capable of discharging %95 of its specified energy capacity.

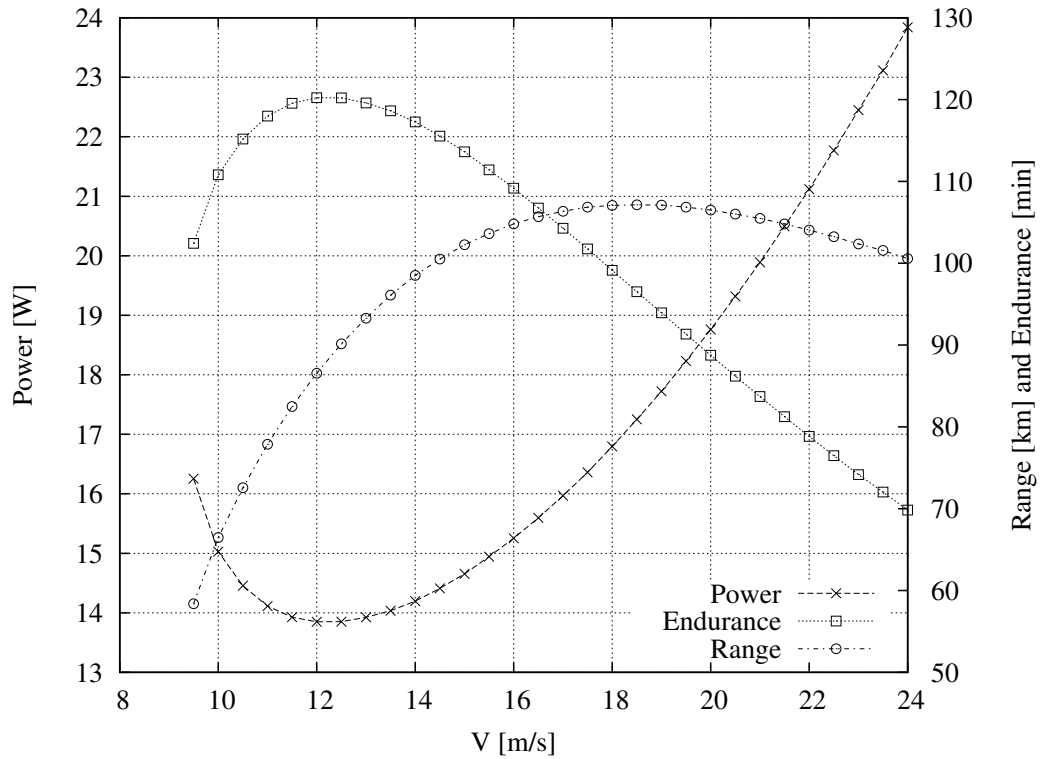


FIGURE 7.13: Estimated flight performance of *Fire Storm* with  $29.5\text{ Wh}$  of onboard energy. The plot includes the propulsion efficiency and the longitudinal trim losses at each corresponding flight speed.

Although the *Storm* frame was designed for EMAV 2009 competition<sup>2</sup>, the weather forecast on the day of outdoor competition was bad so that the "Endurance Mission" of the competition is cancelled. Luckily, two years later in IMAV2011 competition<sup>3</sup>, the same mission element has been placed into the rules, and *Fire Storm* participated to it. High wind conditions made it more favourable to fly with *Fire Storm* as its cruise speed is higher than *Solar Storm*. The mission was to fly as many laps as possible between two poles which are separated  $250\text{ m}$  from each other. In order to make it possible to fly for every team in one single day, the mission time was kept restricted to 30 minutes, and a battery capacity check is done to estimate the real capacity of the vehicles that are participating to the endurance element of the competition. As a result, *Fire Storm* stayed in the air

<sup>2</sup>[www.emav09.org](http://www.emav09.org)

<sup>3</sup>[www.imav2011.org](http://www.imav2011.org)

a little bit over 21 minutes while using only  $5.739\text{ Wh}$  of its  $29.52\text{ Wh}$  measured total battery energy capacity. This was a demonstration of 105+ minutes of flight, and can be called as an official endurance world record in its class up to that date. Figure 7.14 shows the *Fire Storm* and its award after the flight.



FIGURE 7.14: *Fire Storm* demonstrated 105 minutes of flight endurance and took the "Best Outdoor Endurance Award" in IMAV 2011 competition.

## 7.7 Further Improvements

In the light of wind tunnel tests and flight tests, it is easy to realise that the high-end performance of the *Storm* frame is not reached at all, both for *Fire Storm* and *Solar Storm*. The main restriction that prevents pushing the performance further was as usual the possibility of failure because of a sudden attempt and lack of time for repair or newly build while being in preparation for a competition. However, now we have the confidence to reach to higher endurance and range performance by placing higher on-board energy. Figure 7.15 shows the estimated performance with the  $62\text{ Wh}$  Amicell<sup>4</sup> 14.8V 4.2Ah battery.

Ideally the aircraft should operate at  $14\text{ m/s}$  in order to reach the maximum endurance time of 218 minutes and at  $20.5\text{ m/s}$  for maximum range of  $220\text{ km}$ . At  $14\text{ m/s}$  the aircraft will be close to its stall speed which makes the flight speed regulation a critical point. Currently, *Storms* are not equipped with any true

<sup>4</sup>[www.amicell.co.il](http://www.amicell.co.il)

air speed measuring sensor and uses ground speed corrected with a wind speed estimation coming from circular flight patterns. Therefore adding an airspeed sensor is planned as a further improvement for the next versions of the *Storm* frames. Additionally, high wing loading will bring the difficulty of hand launching which has to be solved by another launching system like an elastic bungee. The landing speed will also increase as the stall speed increases, the on board air speed sensor can help about limiting the minimum speed for a safe approach with the autopilot.

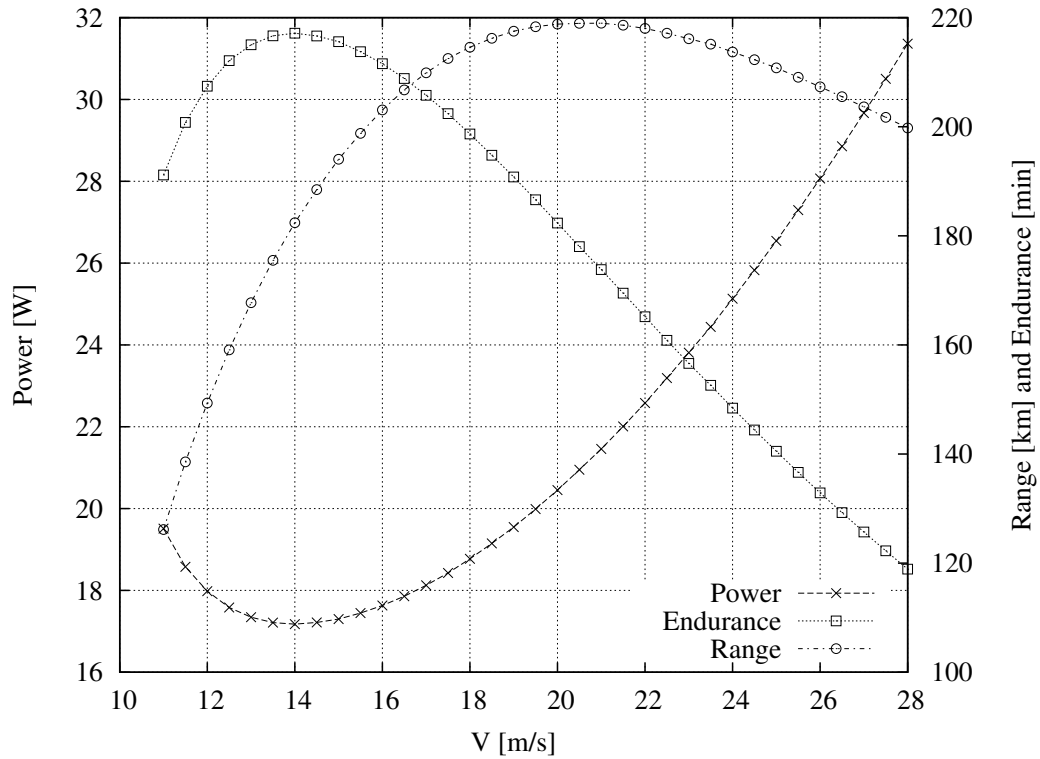


FIGURE 7.15: Estimated flight performance of *Fire Storm* with 62 Wh of on-board energy. The plot includes the propulsion efficiency and the longitudinal trim losses at each corresponding flight speed.



# Chapter 8

## Long Endurance Mini-UAV : Eternity

### 8.1 Introduction

This chapter presents a full design study of a long endurance mini-UAV, called *Eternity*. The main objective is to give a clear idea of how *Cdsgn* program, explained in chapter 3, can be used to define the conceptual design specifications of an aircraft for a specific mission. As an addition, detailed analyses are presented for the horizontal tail sizing in order to show the further capabilities of *Cdsgn*.

Although, the mission definition is defined as staying aloft in the air with a one-meter span air vehicle as long as possible, there are numerous additional requirements and restrictions coming from the real world application itself. For each of them, we will try to find a rational solution with optimal compromise. Also, as the conceptual design continues, several decisions had to be changed or improved as previously expected. Solar cells are planned to be used on the design as an endurance enhancement, comparison of solar and non-solar versions are going to be done at each design phase. Following sections will go through the main selections and their criteria for each part of *Eternity* design. The reader is strictly advised to cover chapter 3 before reading following sections.

## 8.2 Design Envelope

In order to see the limits of the endurance and range performance of a one-meter aircraft, various configuration "cases" are investigated methodically. Table 8.1 shows the main variables and their ranges. Each of these variables are examined on different aircraft configurations with different airfoils, wing planforms, energy systems, stability characteristics. This facilitates the performance comparison of each *case* for the whole variable space. Comparisons will be explained in the related sections.

Main Variables	Range	
Aircraft Configuration	Conventional or Flying-Wing	
Energy Source	Battery only or +Solar energy	
Wing Surface Area	0.05 – 0.2	$m^2$
Flight Speed	8 – 20	$m/s$
Battery Energy	20 – 210	$Wh$

TABLE 8.1: The range of main variables used for the design envelope of *Eternity*.

### 8.2.1 Configuration Selection

Although there exist several aircraft configurations, in order to keep the design simple and parametric over the main variables shown in table 8.1, only conventional and flying wing configurations are chosen to be considered. Each aircraft is generated automatically by *Cdsgn* for each single main variable value. Figure 8.1 shows some of the automatically generated aircraft configurations as an example.

The main objective of this design phase is to see the high-end performance capabilities of each configurations. Afterwards, the best configuration will be selected according to the mission requirements and then it can focused on the selected configuration for the further design improvements.

Following figures shows mainly the endurance and range performance for each configurations. Each circle represent one "case", which has a specified configuration, wing area, flight speed and on-board battery energy. All of the other constraints, shown in table 8.2, are fixed for ease of comparison. Circle radius represents the amount of on-board energy with the weight calculated according to the selected battery's specific energy.

Parameter	Value	Unit	Description
$C_{D0}$	0.0095	-	Parasite drag coefficient
$SM$	0.08	-	Static margin
$D_{fuse}$	0.03	m	Fuselage diameter (max)
$\Lambda_{wing}$	0.0	deg	Sweep angle of wing quarter chord
$\Lambda_{htail}$	0.0	deg	Sweep angle of horizontal tail quarter chord
$\Lambda_{vtail}$	0.0	deg	Sweep angle of vertical tail quarter chord
$\Gamma_{wing}$	7.0	deg	Dihedral angle of wing
$\Gamma_{htail}$	0.0	deg	Dihedral angle of horizontal tail
$S_{Xwing}$	0.8	-	Sinus exp of wing chord distribution
$S_{Xhtail}$	0.9	-	Sinus exp of horizontal tail chord distribution
$S_{Xvtail}$	0.9	-	Sinus exp of vertical tail chord distribution
$Air f_{wing}$	PKMB500	-	Airfoil of the wing
$Air f_{htail}$	HT22rev	-	Airfoil of the horizontal tail
$Air f_{vtail}$	HT12	-	Airfoil of the vertical tail
$AR_{htail}$	4.0	-	Aspect ratio of horizontal tail
$AR_{vtail}$	2.0	-	Aspect ratio of vertical tail
$c_{ht}$	0.40	-	Volume coefficient of horizontal tail
$c_{l_{ht}}$	0.45	-	Moment arm coefficient of horizontal tail
$c_{vt}$	0.03	-	Volume coefficient of vertical tail
$c_{l_{vt}}$	0.45	-	Moment arm coefficient of vertical tail
$M_{payload}$	0.050	kg	Mass of the payload
$M_{avionics}$	0.090	kg	Mass of the avionics
$M_{misc}$	0.01	kg	Miscellaneous mass
$M_{servo}$	0.007	kg	Mass of the servo (D60)
$n_{servo}$	4	kg	Number of the servos
$IR_{solar}$	900.0	$W/m^2$	Maximum solar irradiance
$k_{solar}$	0.70	-	Solar cell ratio over the wing area
$\eta_{solar}$	0.16	-	Solar Cell Efficiency
$\eta_{mppt}$	0.9	-	MPPT Efficiency
$\eta_{chrg}$	0.95	-	Solar Charging Efficiency
$S_{solarcell}$	0.0023	$m^2$	Solar cell surface area (S32)
$M_{solarcell}$	0.0006	kg	Mass of one solar cell (S32)
$M_{solarmisc}$	0.0005	kg	Mass of miscellaneous
$k_{mppt}$	0.0005	kg/W	Mass to power ratio of MPPT
$P_{av}$	3.0	W	Power of avionics
$\eta_{motor}$	0.75	-	Motor efficiency
$\eta_{prop}$	0.7	-	Propeller Efficiency
$\eta_{esc}$	0.95	-	Speed Controller Efficiency
$\eta_{batt}$	0.89	-	Battery Discharge Efficiency
$\eta_{misc}$	0.99	-	Miscellaneous Efficiency Losses
$k_{batt}$	190.0	Wh/kg	Battery Specific Energy
$k_{motor}$	0.007	kg/W	Mass to power ratio of motor

TABLE 8.2: The design constants specified for *Eternity*.

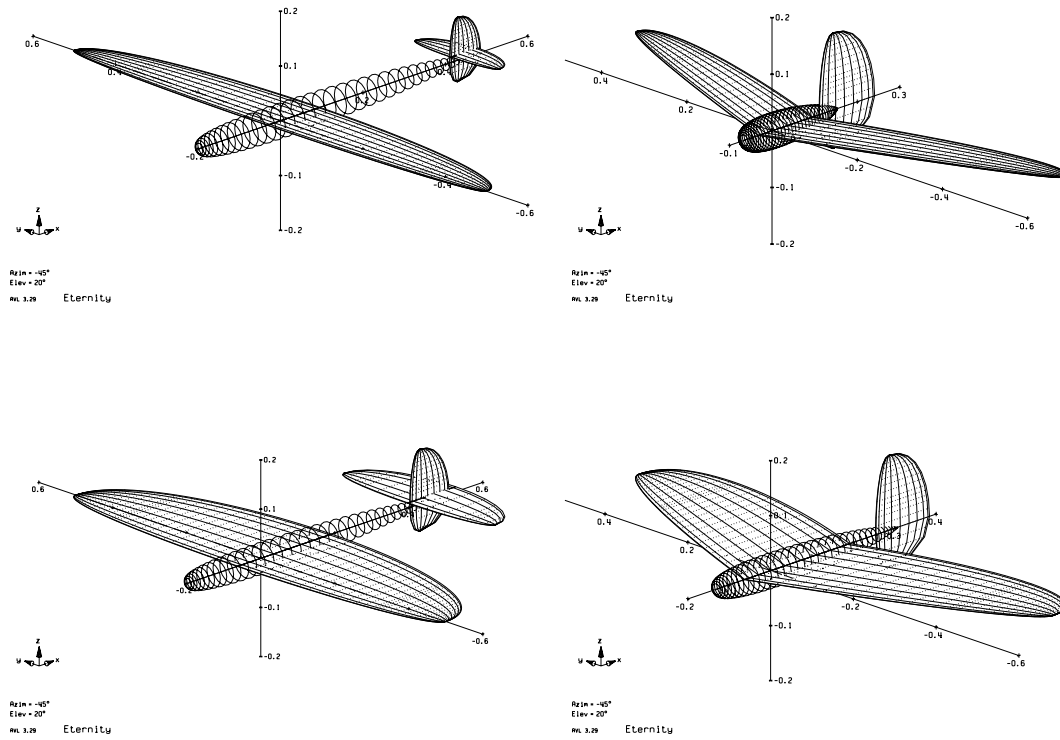


FIGURE 8.1: Examples of some automatic generated aircraft configurations by *Cdsqn*.

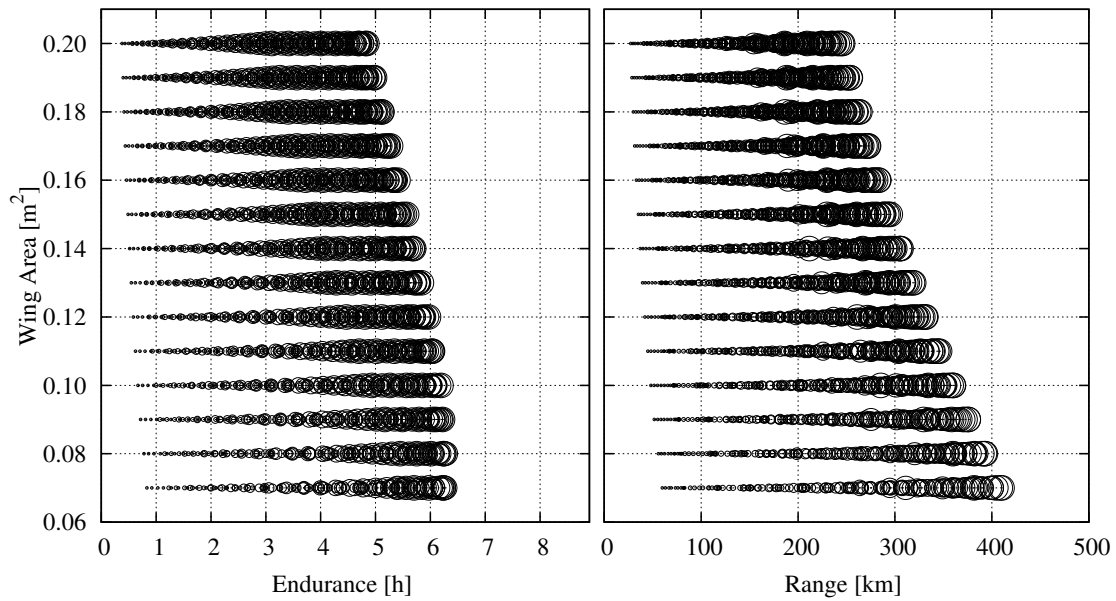


FIGURE 8.2: Performance plot of 1-meter conventional aircraft in various specifications with only battery. Circle radius represents the relative on-board energy being between 20 Wh and 210 Wh for min and max size.

Figure 8.2 shows the theoretical performance potentials of 1-meter conventional aircraft within our specified design constants shown in table 8.2. The on-board energy, represented by the circle radius relatively, varies between  $20\text{ Wh} - 210\text{ Wh}$  corresponding to  $0.1\text{ kg} - 1.5\text{ kg}$  pure battery mass respectively. It can be seen that as the wing area increases, the saturation of maximum on-board energy reduces the maximum endurance and range performance. This was an expected behaviour, the performance of bigger surface area configurations can be increased easily by increasing the maximum on-board energy limitation. Yet the ease of operation (like hand launching) and also certain UAV regulations favours to keep the total mass of the UAV under  $2\text{ kg}$  [42].

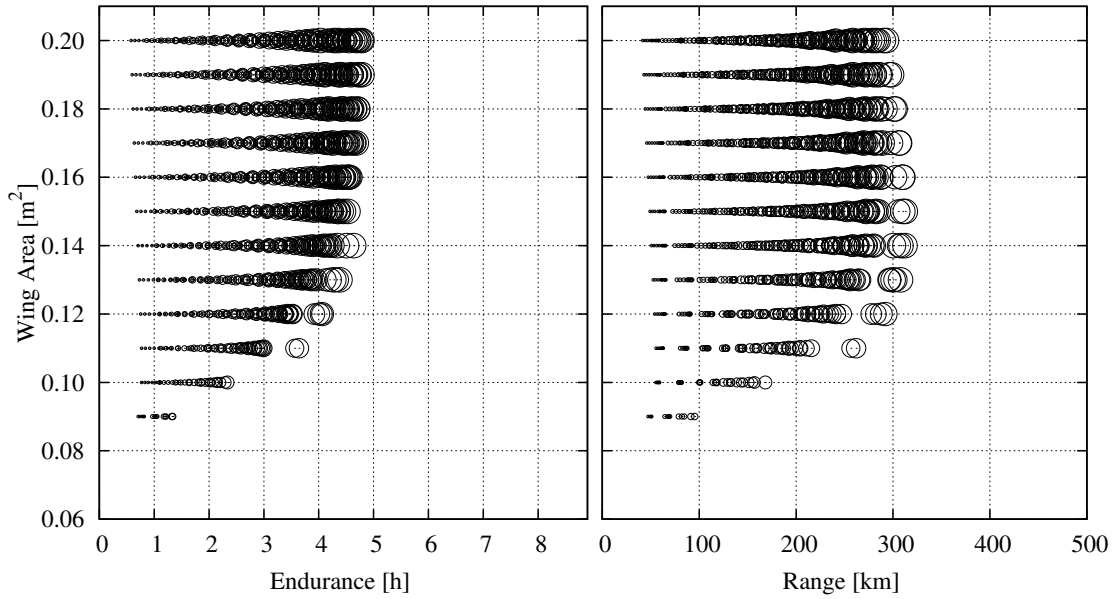


FIGURE 8.3: Performance plot of 1-meter flying wing aircraft in various specifications with only battery. Circle radius represents the relative on-board energy being between  $20\text{ Wh}$  and  $210\text{ Wh}$  for min and max size.

Figure 8.3 shows the same type of performance plot for flying wing type of configuration. As an opposite manner to the conventional configuration, flying wing configuration tends to have better endurance and range performance for increased wing area. This is mainly due to having a lower maximum lift coefficient  $C_{Lmax}$  in trimmed level flight conditions in comparison to conventional configuration because of airfoil type and not having a separate horizontal tail. It can be realised that in the lower right of the figure 8.3, there are some converged cases which looks unrealistic as they are separated from the rest of the other cases. The main reason for a case being not converged is having a “stalled” strip in the wing or being impossible to trim longitudinally. For those converged-unrealistic cases, it

is the XFOIL airfoil database which has an optimistic maximum lift coefficient converged in a certain Reynolds number regime. This is the reason why we do not see this effect everywhere but only in a certain part of the computations. The database files were not corrected as we think that this could be a good example of how *Cdsgn* works for convergence and what are some of its limitations.

### Effect of Solar Energy

As the solar energy has been chosen for enhancement of the performances, the same type of analyses has to be done while taking into account the solar energy and its management requirements, such as additional weight of the solar cells, maximum power point tracker, cables, etc. By this way, it is easier to identify the effect of solar energy on the same aircraft configurations.

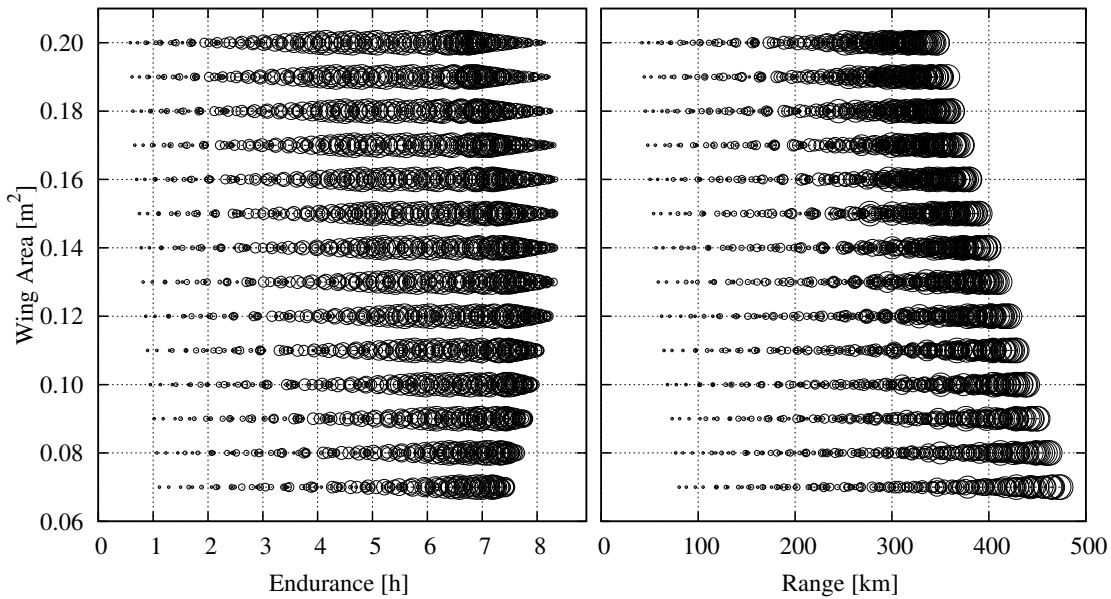


FIGURE 8.4: Performance plot of 1-meter conventional aircraft in various specifications with solar cells. Circle radius represents the relative on-board energy being between  $20\text{ Wh}$  and  $210\text{ Wh}$  for min and max size.

The effect of solar energy on the performance of various 1-meter conventional type of aircraft configuration are shown in figure 8.4. The increase of both endurance and range performance is clearly visible if it is compared with figure 8.2. Solar energy enhances the endurance up to  $8 + \text{hours}$  where it was around  $6 \text{ hours}$  before. The range increases  $100 - 150 \text{ km}$  on average. Also noticeable that maximum endurance is evenly distributed over the various wing areas. The need

of additional on-board energy is still visible for the bigger wing areas, but this time by the effect of solar cells covering the wing area, it is possible to use a smaller amount of on-board energy in order to be light. This ensures to reduce the required flight power, which is maintained by the solar cells on the big wing surface. This is the reason why we see the configurations with smaller on-board energy are having better endurance performance for the bigger wing surfaces although the bigger wing creates more drag than the smaller wings at the same flight speed.

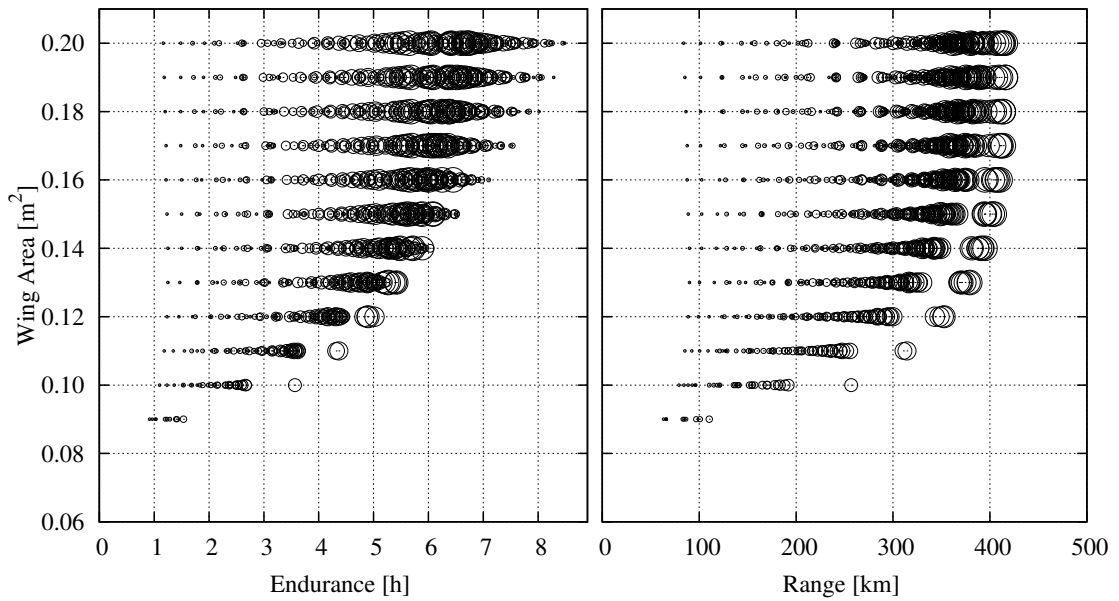


FIGURE 8.5: Performance plot of 1-meter flying wing aircraft in various specifications with solar cells. Circle radius represents the relative on-board energy being between  $20\text{ Wh}$  and  $210\text{ Wh}$  for min and max size.

Figure 8.5 shows the same performance plots for flying wing configurations. In comparison to figure 8.3, the endurance performance seems to increase from  $4.5\text{ hours}$  to  $8\text{ hours}$  in some certain cases. The cases with bigger wing areas, which carry small amount of on-board energy, hence have slower cruise speed obtain more advantage from the solar energy. It should still be noted that these cases are too sensitive for the flight conditions and environment. Such as, a small amount of difference in the cruise flight speed or a decrease in solar irradiation will end up shifting the performance values dramatically. Some of these effects will be investigated more deeply in the following sections.

### Conventional or Flying-Wing ?

Previous figures showed that both conventional and flying wing configurations are able to achieve  $8 + \text{hours}$  of flight time with the help of solar energy. However, flying wing configuration is only able to reach that goal with a limited number of *cases*, while conventional configuration has well proven that the goal is reachable for a wide range of design variables. This is mainly due to the airfoil performance and the longitudinal trim issues that are limited with the flying wing configuration, especially at higher lift coefficients. This proves that the conventional configuration is going to be more robust for a real world application, where the conditions and environment changes constantly. Additionally, non-solar performance of conventional configurations highly outperformed flying wing configurations on average. While making these conclusions, the whole envelope of design variables have been taken into account for both configurations. It should be also noted that, the best candidates have to be suitable for the additional mission requirements that needs to be decided such as, maximum wind speeds that it needs to cope with, minimum landing speed, certain wingloading for hand launch possibility, etc...

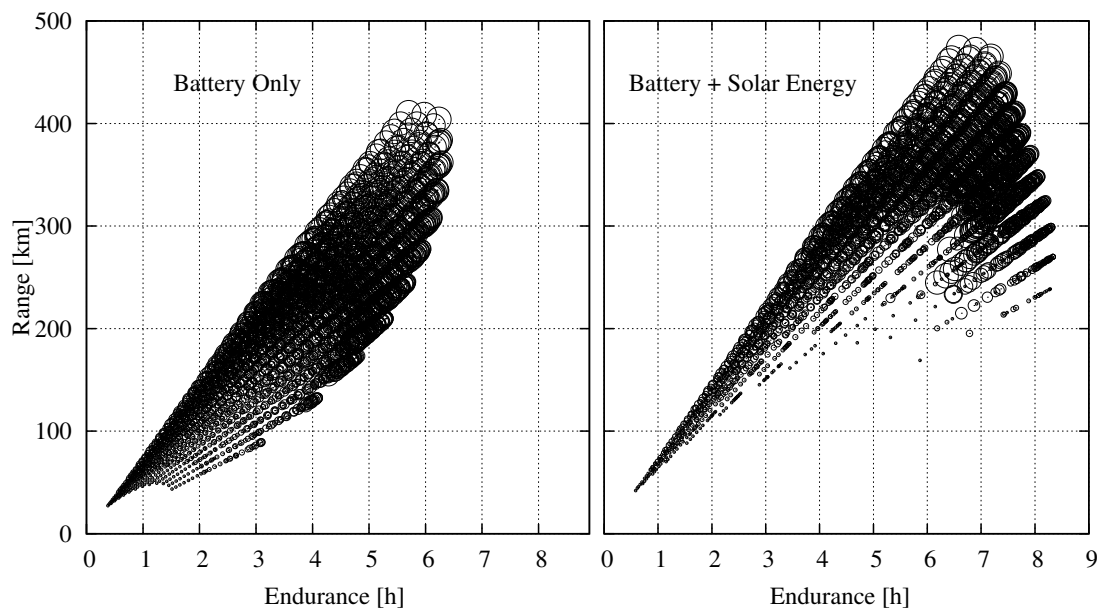


FIGURE 8.6: Range versus endurance performance plot of 1-meter conventional aircraft in various specifications for battery only and additional solar energy cases. Circle radius represents the relative on-board energy being between  $20 \text{ Wh}$  and  $210 \text{ Wh}$  for min and max size.

As a preliminary conclusion, the conventional type of configuration has been selected to continue with for the *Eternity* design. Figure 8.6, non-solar and solar

conventional configurations respectively, show a different type of plot where the endurance and range performances can be easily compared.

### 8.2.2 Required Optimum Energy (On-Board)

The weight of the stored on-board energy is one of the key points in enhancing the platform performances so it is important to select the optimum on-board energy that is going to give the best range and endurance performances for both solar and non-solar conditions. Table 8.3 shows the general specifications of the off-the-shelf batteries. Lithium-Polymer batteries are used in all of the analyses, since Lithium-Sulfur batteries are almost impossible to obtain for our project because of their supplier policies (Sion Power [7]). As a result of several discharge tests, the specific energy is taken as  $190 \text{ Wh/kg}$  different than the general table.

		Ni-Cd	Ni-Mh	Li-Po	Li-S
Specific Energy	( $\text{Wh/kg}$ )	40	80	180	350
Energy Density	( $\text{Wh/l}$ )	100	300	300	350
Specific Power	( $\text{W/kg}$ )	300	900	2800	600

TABLE 8.3: Typical battery specifications.

In order to see the effect of on-board energy on performance, the same analyses which were done previously are plotted in a different way. Figure 8.7 show the endurance and range performance of different designs for non-solar configuration versus on-board energy. As it can be seen from the first graph, the effect of additional on-board energy is getting to a saturation around  $150 \text{ Wh}$ , and above that value carrying more energy on board has no advantage for endurance performance. For the range performance, although there is a reduction on the increase, it keeps increasing with the additional energy. Caution should be given to the point that the given battery volume after a certain value, will not be possible to carry on board which is related with the sizing of the plane. This problem will be taken into account in the following sections.

Figure 8.8 show the same kind of comparisons for solar flight conditions. It is assumed that 70% of the wing area is covered with solar cells. As it can be seen, solar energy has a big influence on the endurance performance, especially for the configurations that have low on-board energy thus lower weight. This result was already presented in the previous analysis, but the clear relation with the on-board

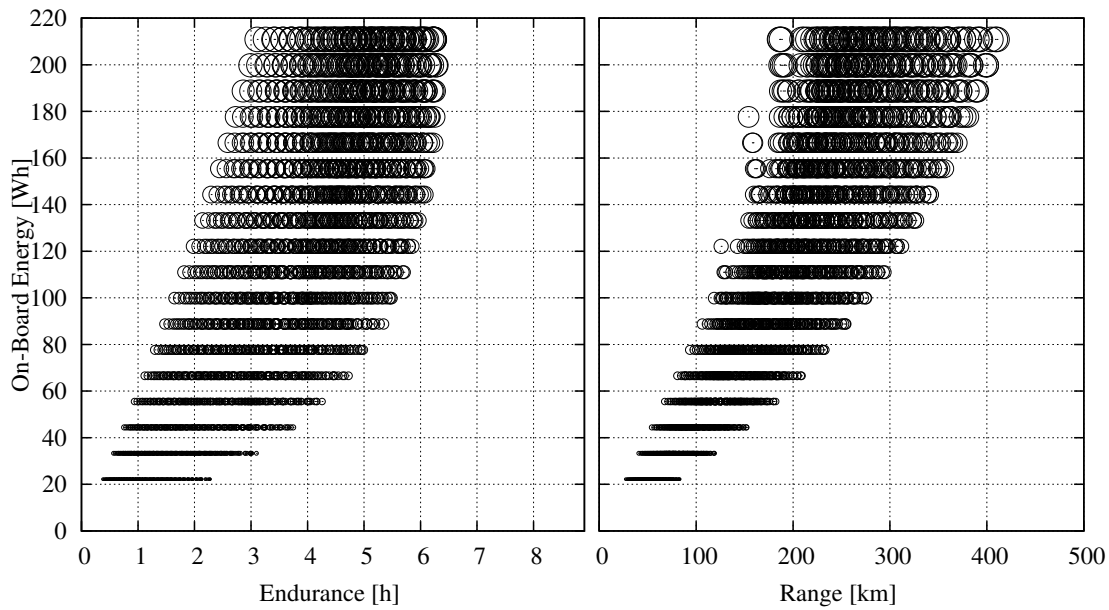


FIGURE 8.7: Effect of on-board energy on endurance and range performance .

energy has just been shown again. Given in figure 8.8 an optimum on-board energy of  $50\text{ Wh}$  gives the best endurance performance. In these calculations, the specific energy of the battery was chosen as  $190\text{ Wh/kg}$  which results around  $250\text{ gr}$  of battery weight for maximum endurance performance for a  $1\text{ m}$  spanned aircraft in solar conditions. For the range performance, the behaviour is not different than the non-solar flight results. The more on-board energy that is carried on the aircraft, results for better range performance.

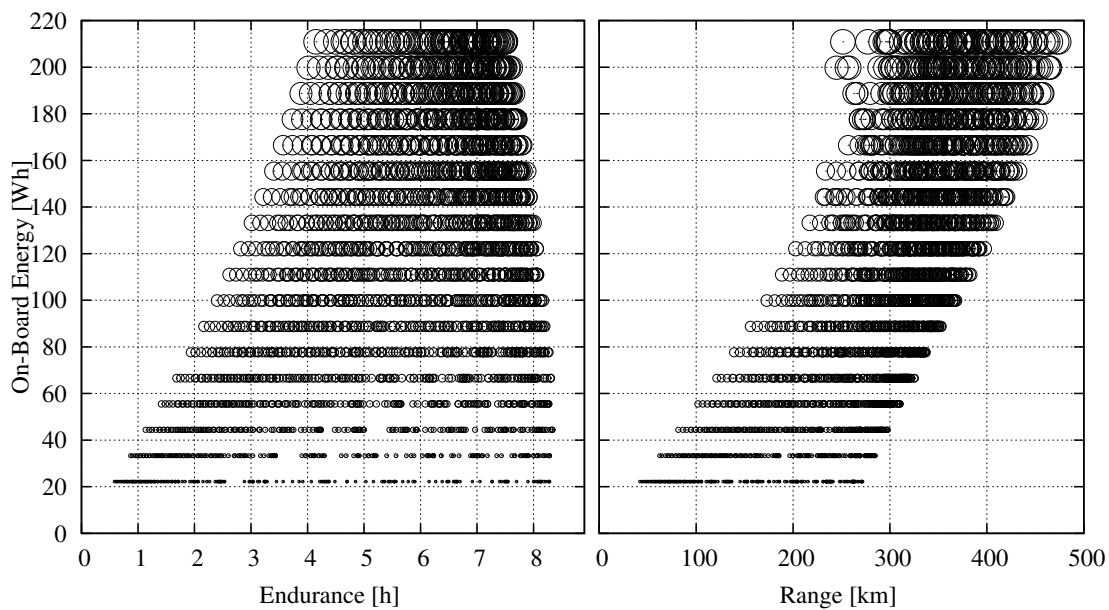


FIGURE 8.8: Effect of on-board energy on endurance and range performance .

	Endurance Performance	Range Performance
Solar Flight	Maximized around 50Wh of on-board energy	the more the better
Non-Solar Flight	Saturated around 150Wh of on-board energy	the more the better

TABLE 8.4: Optimized on-board energy for various flight conditions.

It is easy to see that one configuration is never going to be capable of having the best endurance and best range performances at the same time without compromise. Especially as there is both solar and non-solar conditions taken into account. Table 8.4 shows a brief conclusion. So, it is more favourable to think about separate configurations which are more customised for the requirements of the mission.

## 8.3 Design Philosophy

It has been shown in the previous section that one configuration will not be capable of having the optimum performance in both endurance and range performance at solar and non-solar conditions. Designing the aircraft for only one particular condition will make it fail during almost all of the other flight conditions which are different from the design point. Previous experiences proved this kind of behaviour. The main focus of the design is to have a long-endurance aircraft, and the design philosophy is to obtain long-endurance performance in the operational cases as well, and not only just on one particular condition.

### 8.3.1 Idea of Variable Configuration

It is possible to design different aircraft for different missions and conditions, however *Eternity* long endurance mini UAV should be as compact as possible. Therefore, concentrating on one wing planform which can be usable with two different fuselage and various battery packages found to be the most promising option. Finally, there will be different systems that will be appropriate for various missions and flight conditions.

Keeping mainly the endurance performance in mind for the priority in the design, it is obvious from the previous figures that a light weight frame construction is one of the keys for success. As the system should be capable of carrying a light battery pack for solar long endurance and a heavy battery pack for non-solar

range missions at the same time, it is decided that the battery pack itself to be self sustained meaning that it doesn't need any structural reinforcement to be durable and protected. Favourably, this self-sustained battery pack could even be used as a structural element in order to reduce the weight of the frame. With this decision made, the battery pack is selected to be designed as a wing joiner at the same time. Figure 8.9 shows a CAD drawing of the desired wing joiner battery pack. The sizing of the joiner battery pack is also a key point as it plays a big role on the wing planform and airfoil limitations. Searching through the battery candidates, AMI cell<sup>1</sup> ( $155mm \times 60mm \times 4mm$ ),  $4.5 Ah$   $3.7 V$  seemed to be the best fit for the wing joiner battery pack. Finally, a four cell battery pack is planned to be built in the joiner.

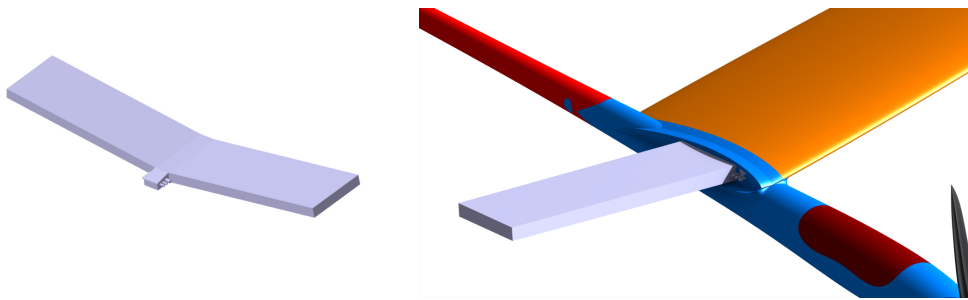


FIGURE 8.9: CAD drawing of the wing joiner battery pack.

## 8.4 Design Details

Having the battery cell type selected, the on-board energy happened to be decided partially as well. The wing joiner will consist a four cell  $4.5 Ah$  ( $66 Wh$ ) battery, which is suitable for long endurance mission in a sunny day. For an overcast weather or long range mission, it is preferable to use 2 packs ( $132 Wh$ ) of battery. In order to fit an additional battery pack to the system, the fuselage has to be enlarged. This is not going to be beneficial for the long endurance version as it will cost some additional drag. These points concludes to have two separate fuselages in order to optimize the system for both endurance and range missions for the same wing and tail parts. This decision also makes it possible to use different propulsion systems (propeller, motor, speed controller) optimized particularly for each mission rather than compromised between them.

---

<sup>1</sup><http://www.amicell.co.il/>

Figures 8.10 and 8.11 shows the endurance performance for various wing area and flight speeds for 66 Wh and 132 Wh on-board energy in both solar and non-solar conditions. These figures are mainly used to decide the optimum wing area for the *Eternity* system. Both circle radius and the colours represents the flight speed since the on-board energy is fixed on each figure. Considering the four conditions,  $0.14\text{ m}^2$  of wing area performs the best of all.

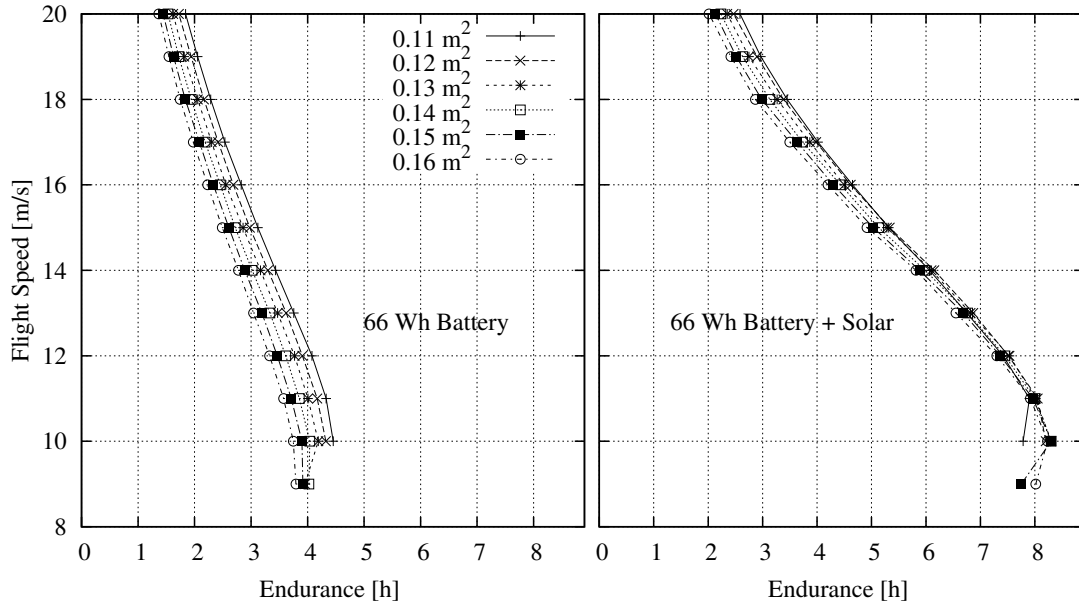


FIGURE 8.10: The effect of various flight speed and wing area on the endurance performance of non-solar and solar configurations with 66Wh of on-board energy.

### 8.4.1 Wing Planform Modifications

The wing planform is selected to be almost elliptical with a slightly lower wing tip loading (with  $c_{local}(y) = c_{root} \sin^{0.9}(y)$  chord distribution, where  $y = (0 : b/2)$ ) in all of the previous calculations. However, the final wing planform selection is going to be driven by two main factors, which are the placement of the solar cells and the span efficiency. Curvature analyses showed that it is possible to cover the wing with solar cells up to %86 of the chord (for the candidate airfoils, some are shown in figure 8.12) starting from trailing edge. Going further than that will increase the possibility of damaging the solar cells. The wing area was chosen as  $0.14\text{ m}^2$  in the previous section. In order to fit the solar cells to wing surface efficiently, the power coefficient of the  $\sin$  is changed to 0.8 for wider tips resulting with  $0.145\text{ m}^2$  of wing area. This lets us to place two more cells to the wing. The span

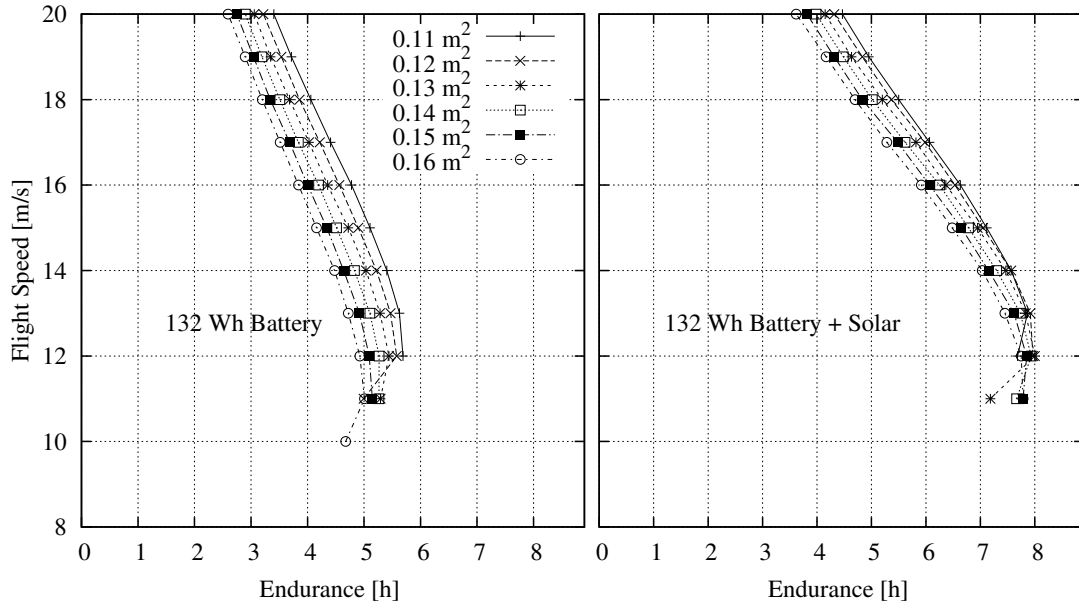


FIGURE 8.11: The effect of various flight speed and wing area on the endurance performance of non-solar and solar configurations with 132Wh of on-board energy.

efficiency reduction was lower than %0.4 in assumed cruised conditions, which still ends up with a higher overall performance because of the additional solar energy generation.

### 8.4.2 Design of the Airfoil Family

In the conceptual design phase, suitable airfoils were selected as candidates by examining their maximum power coefficient ( $C_l^{1.5}/C_d$ ) values. Then the effect of different airfoils to the endurance and range performance are investigated. Finally by using the best existing airfoil as a starting geometry, a custom airfoil is designed by using XFOIL<sup>2</sup> according to the main requirements of the design. The author would like to thank Philip Kolb for contributing to this very important phase by his enormous knowledge and experience. PKMB500 airfoil is designed by Philip Kolb, which outperformed all the previous airfoils existed in the selected database for our application. Some of the candidate airfoil polars are shown in figure 8.12 in comparison to PKMB500 airfoil at Re=150k.

The main reason why PKMB500 can give better results than its precedents relies on the fact that it is designed according to the *Eternity*'s specifications. The wing

<sup>2</sup>xfoil.mit.edu

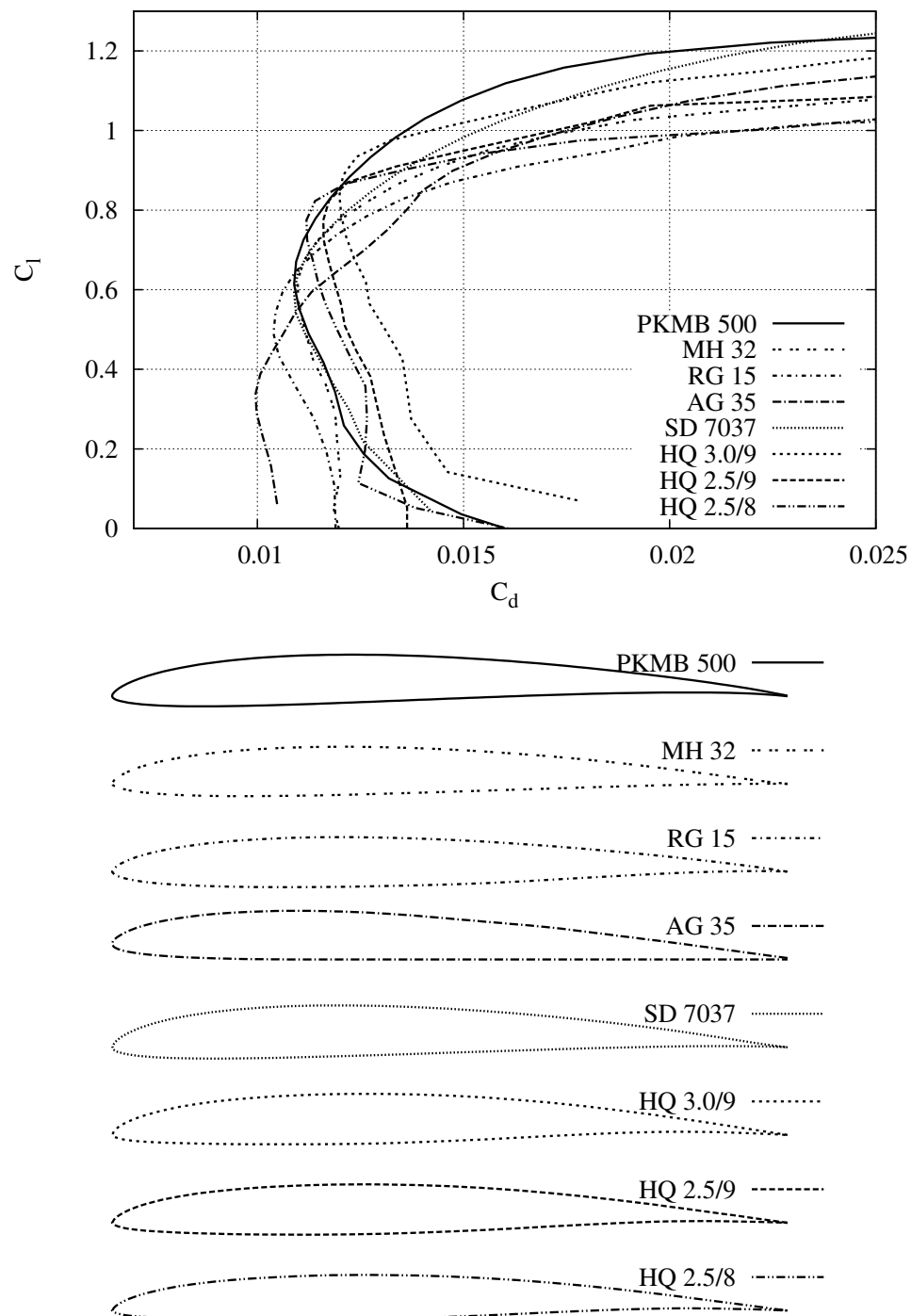


FIGURE 8.12: Candidate airfoil polars in comparison with PKMB500 custom airfoil at  $Re=150k$ .

area was chosen  $0.145 \text{ m}^2$  and the battery weights were determined by the selected optimum capacities for solar and non-solar conditions. Since almost all of the main parameters of the design has been selected, it is easy to calculate the  $Re\sqrt{C_L}$  of the mean aerodynamic chord by the equation 8.1 and later define for all of the particular chord lengths proportionally. Using  $Re\sqrt{C_L}$  for the comparison of airfoil ensures that the lift is going to be always fixed so that for each lift coefficient the speed is going to be calculated and the analysis of the airfoil is going to be done at the corresponding Reynolds number that is calculated from the new speed. This type of airfoil polars called as fixed-lift or type-2 polars.

$$Re\sqrt{C_L} = \frac{1}{\mu} \sqrt{\frac{2\rho W}{AR}} \quad (8.1)$$

The equation 8.1 can be derived from the two basic equation of lift and Reynolds number as :

$$L = W = \frac{1}{2}\rho V^2 S C_L \quad (8.2)$$

$$Re = \frac{V\bar{c}\rho}{\mu} \quad (8.3)$$

Taking  $V$  out of equation 8.2 and placing in to equation 8.3 results :

$$V = \sqrt{\frac{2W}{\rho C_L S}} \quad (8.4)$$

$$Re = \sqrt{\frac{2W}{\rho C_L S}} \frac{\bar{c}\rho}{\mu} \quad (8.5)$$

Where,

$$\frac{\bar{c}^2}{S} = \frac{1}{AR} \quad (8.6)$$

Keeping the variables on the left hand side results the equation 8.5 to turn into equation 8.1.

For the two configuration of *Eternity* (66 Wh and 132 Wh) calculated  $Re\sqrt{C_L}$  is 90k and 110k respectively. After obtaining the working regime, the priority is given to the  $((C_l^{1.5}/C_d)_{max})$  value of the airfoil as the endurance performance is the main objective for the design. SD7037 airfoil is selected as a reference as it is widely known and used in soaring competition gliders. By using the QDES routine

of XFOIL the laminar run on the top surface is extended by increasing the aft-loading the airfoil. The transition ramp slope is slightly reduced and the pressure distribution at the bottom end is increased. This resulted an increase on the pitching moment increase on the final airfoil ( $\Delta C_m = 0.025$ ) which was acceptable as the conventional configuration is selected. The suction peak is smoothed resulting a better continuity of the flow and postpone the transition. It is known that the bubble loss contributes significantly to the form drag on the low-Reynolds airfoils. One way of reducing the bubble size is to move it farther upstream by forcing the transition earlier. However, it will not be beneficial to completely prevent the occurrence of the bubble as the laminar flow will be shortened dramatically. There is an optimum position for the bubble placement and size that corresponds to the minimum drag and in low Reynolds airfoil design the control of the bubble becomes more critical compared to minimizing the skin friction [22]. Figure 8.13 shows the pressure distributions of the SD7037 and the new designed PKMB500 airfoil at different lift coefficients.

The transition point development can be marked easily as the laminar bubble generates a bump on the pressure distribution. The increased laminar run on the PKMB500 is also visible when compared to SD7037 airfoil. The pressure distributions around  $C_l = 1.0$  is shown especially in the figure 8.13 as this is the region that is improved on PKMB500 compared to SD7037. The performance difference around  $C_l = 1.0$  can be seen in the previous figure 8.12.

In order to improve the airfoil performance along the span and decrease the viscous drag caused by inappropriate airfoil location, a series of airfoils are designed by referencing PKMB500. Figure 8.15 shows the designed airfoils and their specifications in table 8.5.

PKMB500 airfoil could have been used through out the whole span, but it is known that with the decreased chord along the wing tip region, the performance of the airfoil will decrease due to low Reynolds number effects. The airfoil is analysed for various  $Re\sqrt{C_l}$  numbers in order to see the degradation. As shown in figure 8.14, a dramatic performance decrease occurs around  $Re\sqrt{C_l} = 30k$ .

This regime corresponds to %95 of the wing span, proving that the wing tip is the main part that has to be focused, where the airfoil has to be designed particularly for its own flow regime.

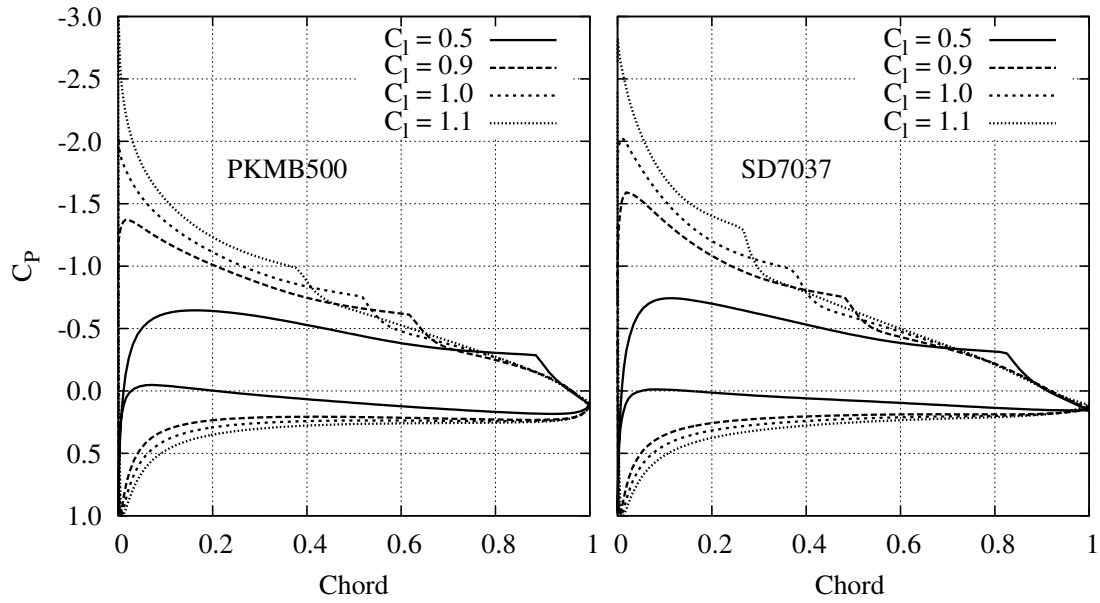


FIGURE 8.13: Pressure distribution change for PKMB500 and SD7037 airfoils at  $Re=150k$ .

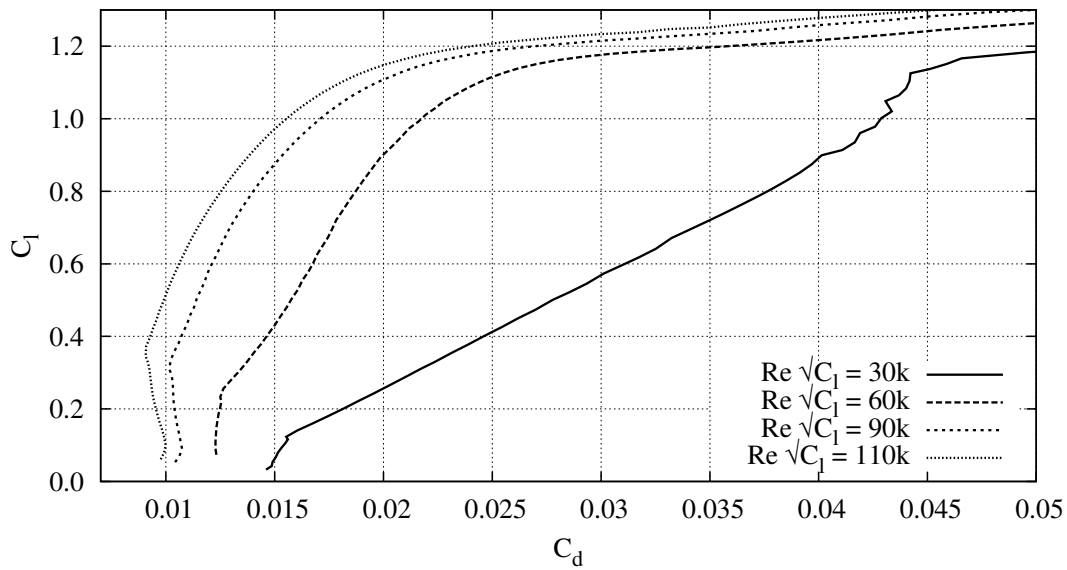


FIGURE 8.14: Performance degradation of PKMB500 airfoil with reduced Reynolds number (calculated for  $Re\sqrt{C_l}$ ).

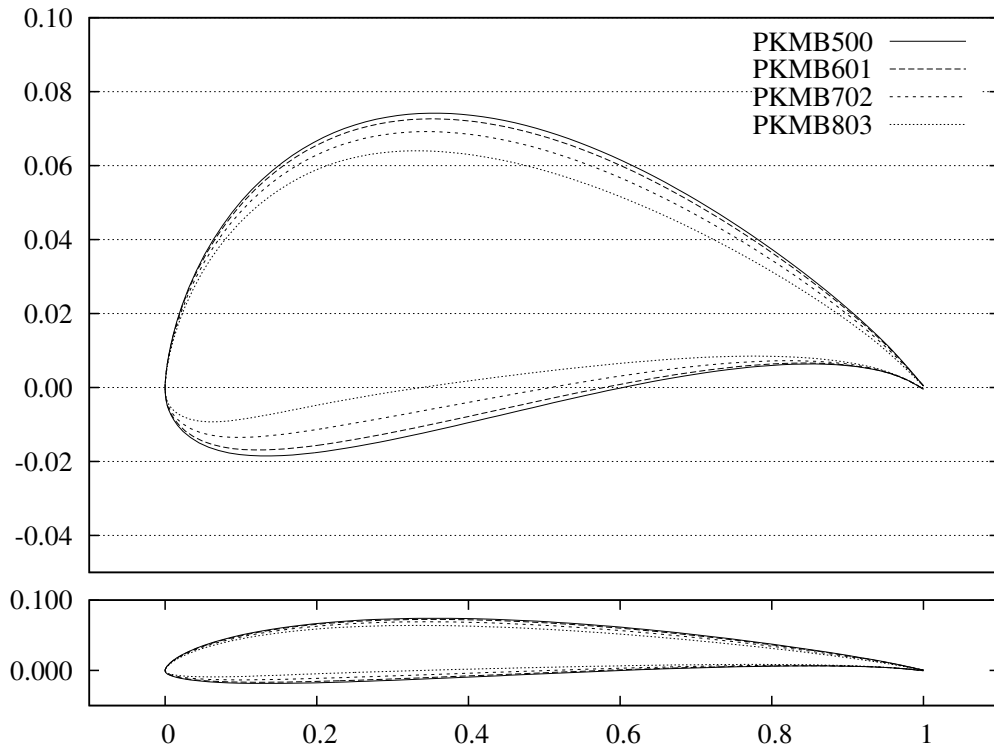


FIGURE 8.15: Designed airfoil family for *Eternity*. Bottom plot shows the real ratio and top plot shows the y-coordinates as five times scaled in order to distinguish the difference easily.

		PKMB500	PKMB601	PKMB702	PKMB803
Max Thickness	[%c]	8.75	8.42	7.66	6.52
Max Thickness Location	[%c]	28.5	28.4	27.9	26.9
Max Camber	[%c]	3.25	3.24	3.24	3.24
Max Camber Location	[%c]	46.3	45.5	43.4	40.0
Leading Edge Radius	[%c]	0.552	0.516	0.453	0.384
$\Delta\Theta_{TE}^\circ$	[deg]	4.94415	4.74891	4.30798	3.63086
Average Thickness	[%c]	5.70	5.48	4.99	4.25

TABLE 8.5: Specifications of the airfoil family.

PKMB803 is designed particularly for its own working regime, which is  $Re\sqrt{C_L} = 30000$ . The main difference is made on the thickness of the airfoil which has been reduced to %73 of PKMB500, and the maximum camber position is moved to front as shown in table 8.5. While these modifications improved the performance of the airfoil, as expected they resulted a peaky  $C_l$  vs  $C_d$  polar around  $C_l = 1.1$ . In order to smooth the resultant polar, leading edge radius is increased %30. All of the other modifications are made in QDES, mixed inverse design routine of Xfoil, with directly changing the surface speed over the airfoil. Figure 8.16 shows the

placement of the designed airfoils along the span with a drag comparison of each with the root airfoil PKMB500 in their corresponding flow regime.

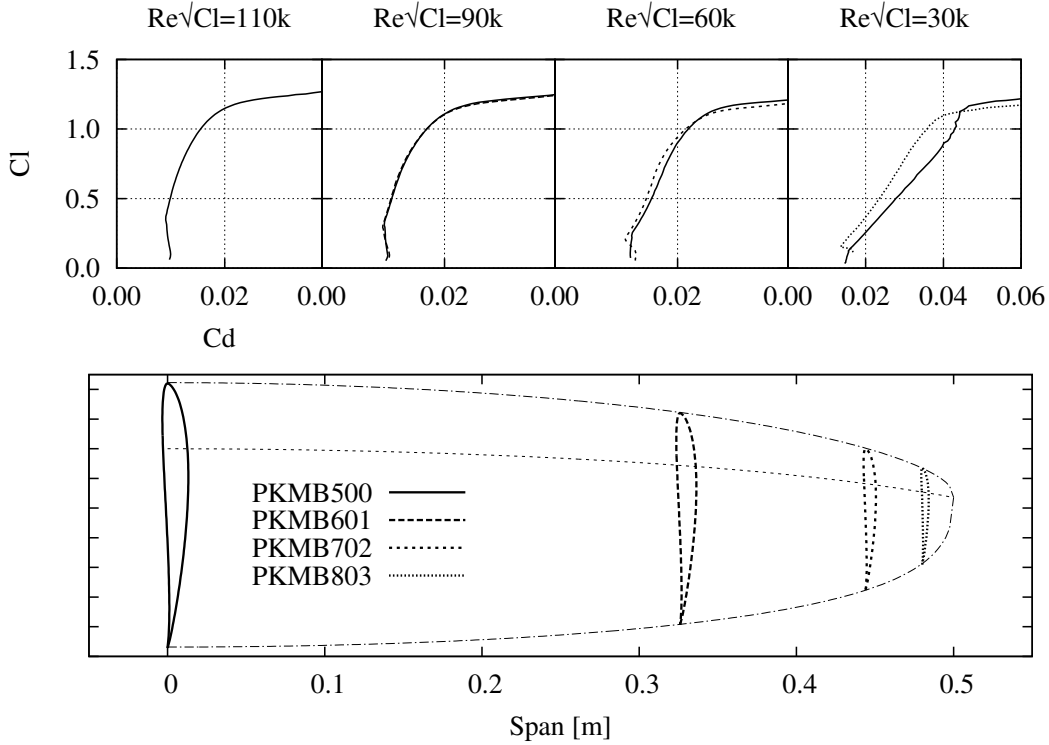


FIGURE 8.16: Placement of each airfoil is shown along the half span. The upper graphs shows the  $C_l$  vs  $C_d$  plots of each airfoils at their corresponding working regimes with the comparison to the root PKMB500 airfoil. The planform shown is given as demonstration and the real planform is shown later in figure 8.21.

Having a smooth surface on the wing while transitioning from PKMB500 to PKMB803 on elliptical planform created a dominant restriction on the thicknesses of PKMB601 and PKMB702. As the chord distribution has already been fixed, adding the root and the tip airfoil thickness values automatically define the thickness distribution. With this thickness restriction, the only way found to slightly improve the performance of the middle airfoils was to compromise from the maximum lift coefficient and concentrate on the cruise coefficient regime corresponding to best endurance which is around  $C_L = 0.9 - 1.0$ .

As it is mostly concentrated on optimizing the endurance performance, the high speed performance of the aircraft started to decrease which is going to be needed for real life applications like penetrating into wind, or reaching to a way point faster with priority. A solution for increasing the high speed performance without decreasing the endurance is described more deeply in section 8.7.

### 8.4.3 Horizontal Tail Design

Horizontal tail volume coefficient, aspect ratio and the tail moment arm was assumed to be constant in all previous calculations. After converging on the wing area, further analyses are examined in order to see the effect of tail volume coefficient, tail moment arm and the aspect ratio of horizontal tail on endurance performance. Figures 8.17 to 8.19 shows the results for 66 *Wh* non-solar version with the predefined wing from section 8.4 while each circle representing one candidate with a certain tail arm, horizontal tail volume coefficient and horizontal tail aspect ratio.

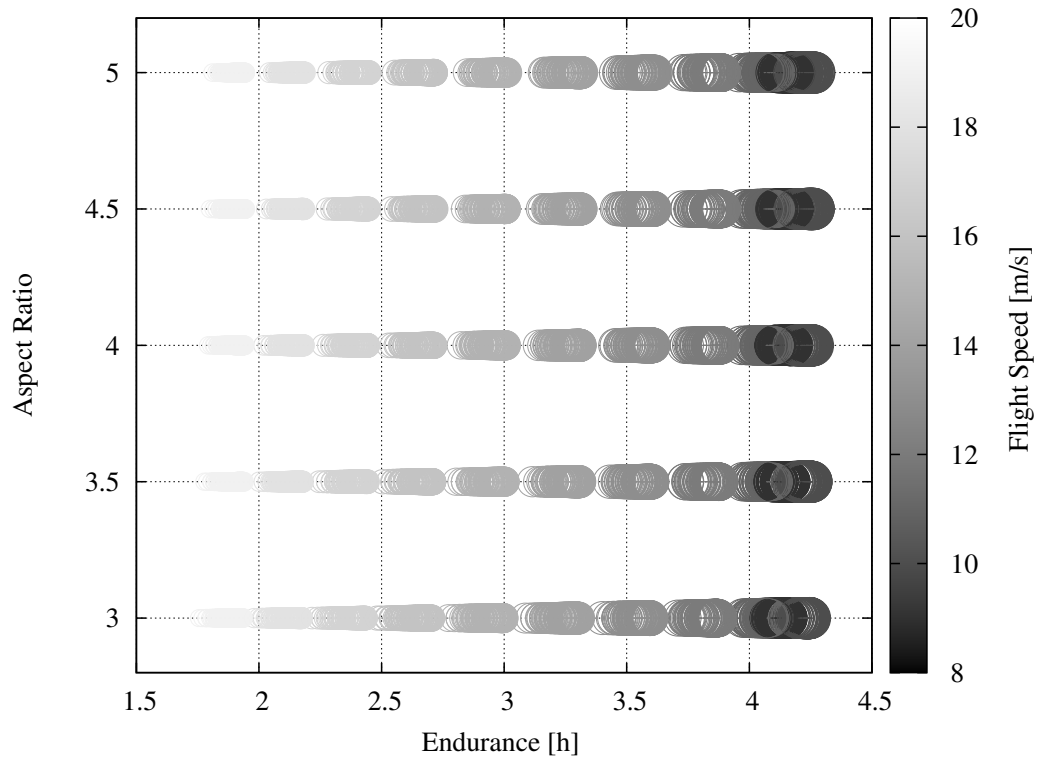


FIGURE 8.17: Effect of horizontal tail aspect ratio on endurance performance with various tail moment arm and tail volume. Circle radius also represents the endurance relatively.

It is favourable to have a neutral horizontal tail that does not generate lift or down force in terms of maximum aerodynamic efficiency referring to Prandtl-Naylor Theory (1946). This would require a bigger tail volume coefficient which can be obtained either by longer tail arm or bigger tail surface or combination of both. However, taking into account the additional weight that is going to come from longer tail structure of bigger tail surface can result with a different conclusion, for example, having a shorter tail length equilibrated with a down-force generating

tail can be more efficient as it will be lighter. Following analyses (always done by *Cdsgrn*) will take into account the structural mass differentiation while comparing different tail moment arm, horizontal tail volume and horizontal tail aspect ratio. Additionally, every case is equilibrated for lift and total pitching moment at specified speed always with a fixed static margin of %8 of mean aerodynamic chord.

The effect of aspect ratio of the horizontal tail on endurance performance is not easily noticeable. Figure 8.17 shows the influence on the endurance performance. The only visible effect is that increasing the aspect ratio has a tendency of reducing the performance variation caused by inappropriate tail volume coefficient and tail moment arm selection. The higher the aspect ratio, the lower the performance variations seen. Selecting an aspect ratio of 5 results with a horizontal tail mean aerodynamic chord of only 6 cm. Taking into account an appropriate tail airfoil thickness, (which will be lower than %5 *mac* of horizontal tail) it is favourable to select wider chord both for structural issues (wider chord will be thicker so lighter as well) and for manufacturing and integration of the aircraft. Therefore it is selected as  $AR_{ht} = 4$  and it will be fixed for the following analyses.

The optimum tail moment arm for endurance performance varies with the flight speed. Figure 8.18 shows the variation. It is noticeable that for higher flight speeds  $L_{ht} = 0.6\text{ m}$  gives a better performance where for lower flight speeds it is better to select a  $L_{ht}$  between 0.35 m to 0.50 m. Finally, the moment arm is selected to be  $L_{ht} = 0.45\text{ m}$  with both structural, compactness and stability issues in mind.

Figure 8.19 shows the effect of horizontal tail volume coefficient on endurance performance for an horizontal tail aspect ratio as well. There is a small increase in endurance performance at low speeds when the horizontal tail volume coefficients decreases, but mostly it is insignificant. So the selection of  $C_{ht}$  is made mainly according to other issues like longitudinal stability (having a pitch damping  $C_{M_q} < -10$ ), easy manufacturing and system integration (servo linkage system) and finally determined as  $C_{ht} = 0.4$ .

Finally, the resultant horizontal tail generates a small amount of down force which corresponds to tail's lift coefficient of about 0.15. As being compact was one of the main requirements, the horizontal tailed is designed to be removable for easy transportation. Figure 8.20 shows the mounting of the tail on top of the small

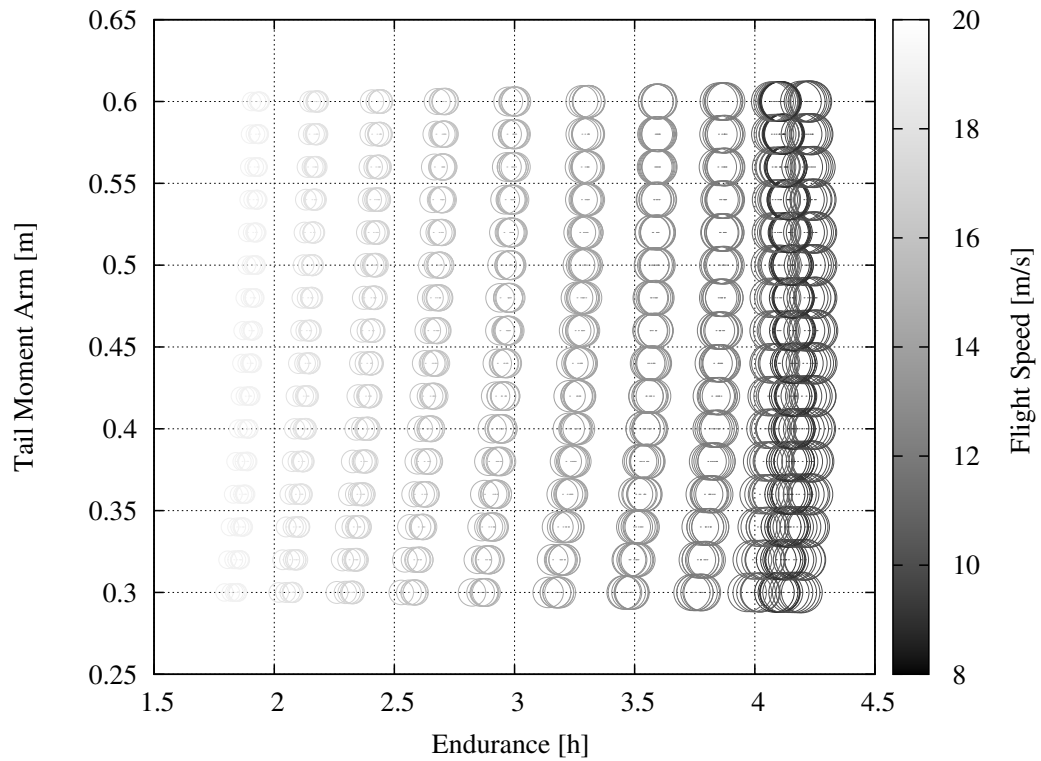


FIGURE 8.18: Effect of various horizontal tail moment arm on endurance performance for tail aspect ratio of 4. Circle radius also represents the endurance relatively.

pod which is on the tail boom. The pod includes two small servos which controls the elevator and the rudder through internal push-rod connections.

The vertical tail is placed separately after the horizontal tail with a clearance in order to work effectively. The wings are designed to have flaperons for agility and appropriate camber change according to the flight envelope, but on the other hand,  $7^\circ$  of dihedral is also build in the wings. The reason for the dihedral was not having a strong roll stability (spiral mode) but to have have a roll moment generation as a response to side slip. As a result of this, the aircraft will have the possibility to be controlled by only elevator and rudder inputs. The main reason behind this is to place the solar cells easily and reduce the total weight as two servo reduction will gain approximately  $45 - 55g$  (two servos, torque-rods, additional hinge material, flaperon reinforcements, electric cables and connectors...).

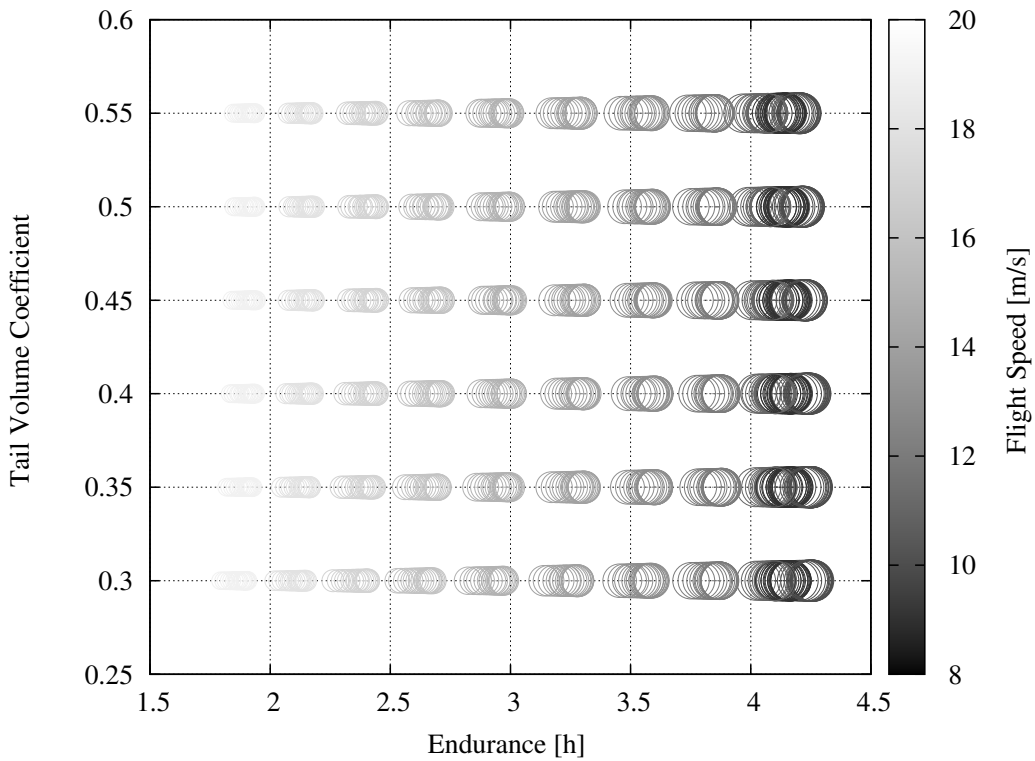


FIGURE 8.19: Effect of various horizontal tail volume on endurance performance for tail aspect ratio of 4.0. Circle radius also represents the endurance relatively.

## 8.5 Propulsion System

Selection of an optimized propulsion system is the key point for the enhanced performance as each component efficiency plays a big role. To give an example from the current *Eternity* design, %1 of propulsion efficiency reduction creates 7.8 minutes and 6.7 *km* on solar conditions, or 4.2 minutes and 3.5 *km* of performance reduction. In an other words, %1 of propulsion efficiency increase will have the same result with a mass reduction of 30 *g* in non-solar and 22 *g* in solar configuration which is much harder to achieve compared to propulsion system optimization. Fortunately, having countless off-the-shelf components available gives us the freedom to choose and match the suitable motor and propeller for particular flight condition and mission requirements. For the previous analyses, the efficiencies of the propulsion group components have been kept fixed in order to understand the direct effect of the different configurations. This also makes the calculations much faster as there will be no necessity to optimise a propulsion group for each *case*. The fixed efficiency coefficients seen in table 8.2, has been selected according to previous projects.

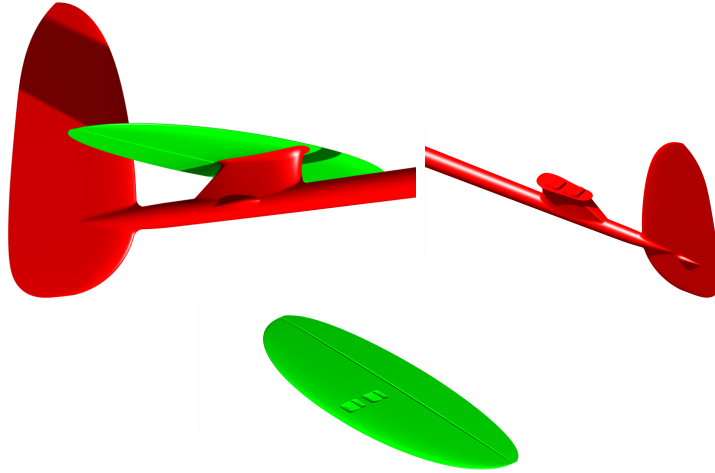


FIGURE 8.20: Detail view of the tail configuration of *Eternity*, there are two servos installed inside the horizontal tail pod controlling the elevator and rudder with internal push-rods.

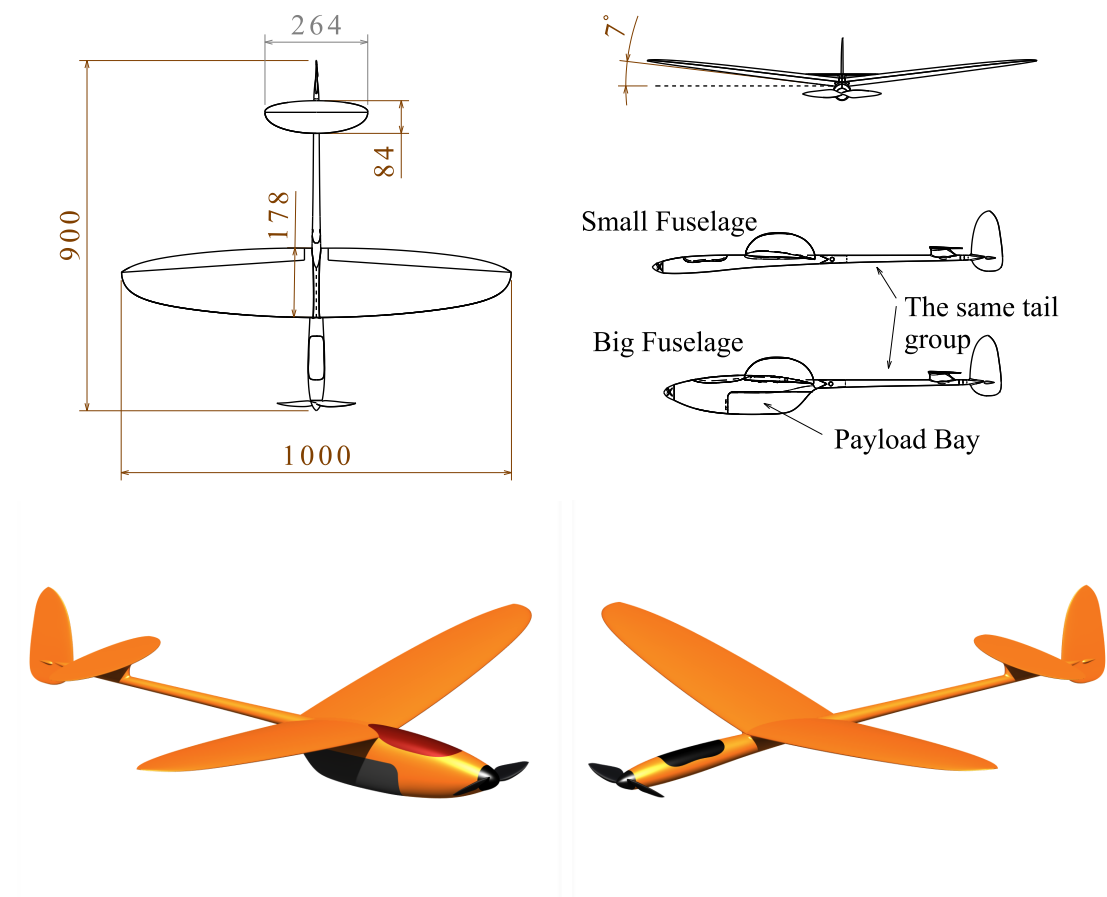
Propulsion group matching and optimization have been done as explained in chapter 5 for the two *Eternity* versions (66 *Wh* and 132 *Wh*). However, although having the ability to design and manufacture a custom propeller (Appendix B), because of the time restrictions it has been chosen to use an off-the-shelf propeller for the first prototypes.

## 8.6 Final Appearance of the two Versions

Final dimensions of the two *Eternity* versions are shown in the figure 8.21 with their specifications in table 8.6.

		Small	Big
Wing Area	$[m^2]$	0.145	0.145
Total Mass	$[kg]$	0.85	1.35
Length	$[m]$	0.9	0.87
Wing AR	$[-]$	6.89	6.89
Horizontal tail AR	$[-]$	4.0	4.0
Vertical tail AR	$[-]$	2.0	2.0
Horizontal tail volume	$[-]$	0.4	0.4
Horizontal tail arm	$[m]$	0.45	0.45
Vertical tail volume	$[-]$	0.03	0.03
Vertical tail arm	$[m]$	0.53	0.53

TABLE 8.6: Geometrical specifications of the two *Eternity* configurations.

FIGURE 8.21: *Eternity* design with two different fuselages.

## 8.7 Windtunnel Tests

In order to obtain the aerodynamic characteristics of the aircraft in a controlled environment, a wind-tunnel campaign has been conducted at *S4*. The specifications of the wind-tunnel is described in section 4.6. An internal six component force and moment balance is used for the measurements as described previously in the section 4.6.2



FIGURE 8.22: The mounting of Eternity on S4 Wind-tunnel.

Instead of manufacturing a separate wind-tunnel model, a fully equipped ready to fly version is manufactured and used for the tests. This has been initiated in order to save some time as one particular model takes about 3-4 weeks to build by one person including all the necessary equipment integration. Figure 8.22 shows the mounting of the aircraft in the wind-tunnel. A 1.5 cm diameter circular strut goes directly to the bottom of the fuselage and holds the internal balance rigidly from one end. The balance is fixed to the fuselage from the other end as seen in figure 8.23. The control surfaces and the motor of the aircraft were controlled by the on-board Paparazzi autopilot which is connected to a computer via serial connection. A separate power supply is used in order to supply the motor, servos and the autopilot on-board and also to record the power consumption during the tests. All sensor cables, power cables of the motor and the communication cable

of the autopilot are connected to the strut in a flexible way so that they do not affect the force and moment measurements.

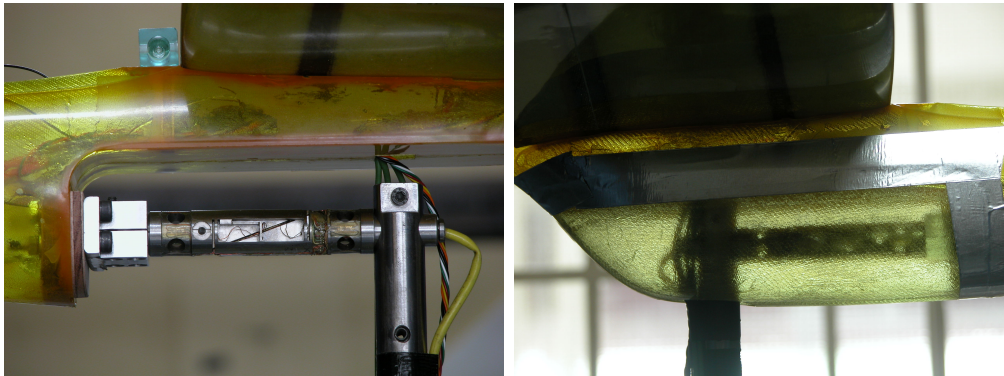


FIGURE 8.23: The payload compartment of the Eternity has been used for the mounting of the internal balance, and then the payload bay covered in order to protect the balance and to have the accurate fuselage shape.

Both elevator, rudder and aileron surface deflections are calibrated by the help of a spirit level which results with an accuracy of less than half a degree. The whole angle of attack of the aircraft is changed to 5, 10, 15, *etc...* and then the corresponding signal value from the autopilot, which makes the spirit level centred, is recorded. Two pictures from the calibration procedure is shown in figure 8.24.



FIGURE 8.24: Both elevator and rudder is levelled by a spirit level and the deflections are calibrated by using the wind tunnel's accurate angle measurement.

A special care has been taken in order to have additional strength on the model as it is also planned to be used for the wind-tunnel tests. Finally, the manufactured model ended up 140 g heavier than the assumed flight version and still not rigid enough for the wind-tunnel's high wing-loading cases. The flexibility of the fuselage created an unwanted angle of attack shifting as much as 2° under heavy

wing-loading cases. As this is only a reference shifting, not a significant shape deformation, the slope has been corrected as a function of vertical lift force applied on to the aircraft. The angle of attack differentiation is defined as a function of vertical force component ( $z$ ) of the balance by a polynomial as shown in equation 8.7. The coefficients  $k_1$  and  $k_2$  found to be 0.001 and 0.1 respectively satisfying the overlapping of lift curve slopes between different wind speed measurements as it is known that the lift curve slopes should not vary. Figure 8.25 shows the flexibility effect on the lift curve slope and the corrected plots.

$$\Delta\alpha(z) = k_1 z^2 + k_2 z \quad (8.7)$$

$$\alpha_{corrected} = \alpha - \Delta\alpha(z) \quad (8.8)$$

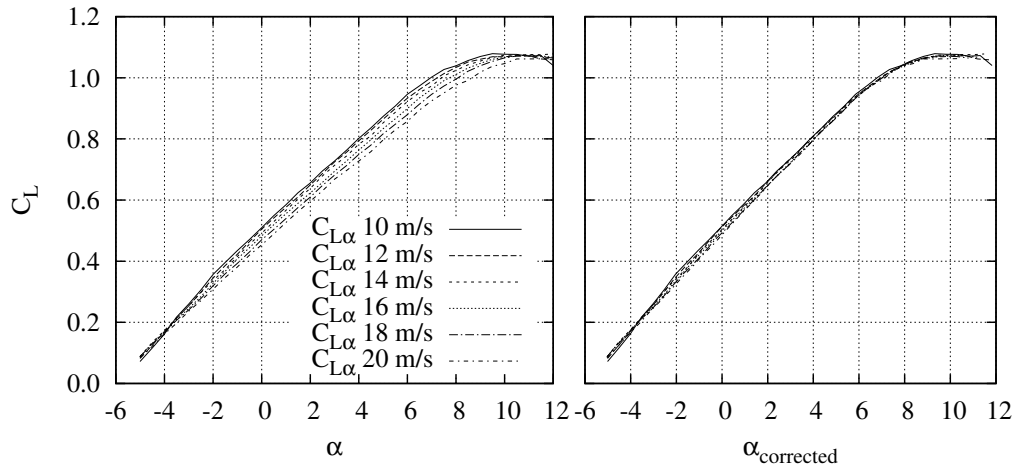


FIGURE 8.25: Flexibility effect of the mounting on the  $C_{L\alpha}$  lift curve slopes and numerically corrected versions at various speeds.

The experiments are conducted for different speeds in order to see the performance of the aircraft at each flight speed and evaluate the aerodynamic characteristics for a wider flight range. For each wind-tunnel speed the aircraft pitched from  $-6$  to  $12$  degrees in order to obtain the performance polars. The expected influence of the Reynolds number is clearly visible on figure 8.26, as the flight speed decreases both the range ( $C_L/C_D$ ) and the endurance ( $C_L^{1.5}/C_D$ ) performance decrease. Attention should be given that figure 8.26 does not presents the equilibrium condition performance. In order to have the equilibrium plot, elevator deflection has to be

taken into account as well at which it corresponds to zero pitching moment. The effect of elevator deflection on moment ( $C_M$ ), lift ( $C_L$ ) and drag ( $C_D$ ) is shown in figure 8.27.

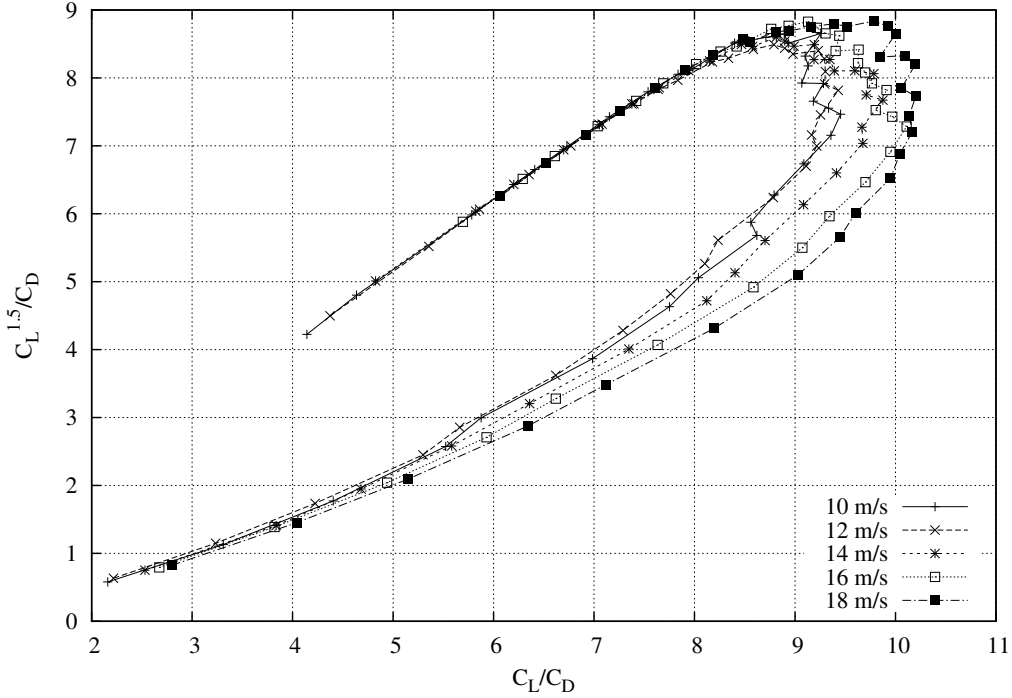


FIGURE 8.26: Effect of flight speed on the range and endurance performance characteristics.

According to the previous analyses, the best endurance performance is achieved at  $C_L = 0.9 - 1.0$  where the cruise speed corresponds to  $12.5 - 13.0 \text{ m/s}$  which is really close to stall speed of the big configuration that is  $11.5 \text{ m/s}$ . In the real life applications, for mini-micro UAV scale that are generally flying around  $10 - 25 \text{ m/s}$ , sustaining the airspeed so accurately is really hard when the small momentum of the aircraft and the big ratio of the wind gusts to the flight speed considered. Therefore increasing the flight speed results a reasonable safety margin. In the end of this decision, the cruise speed is selected as  $14 \text{ m/s}$ . The effect of the elevator is investigated at the desired cruise speed of  $14 \text{ m/s}$ . The deflection is made for  $-10$  to  $15$  degrees (being the positive deflection is downward) with a step of  $5$  degrees. The reference point for the moment calculations is taken where the static margin is equal to  $\%8$  of the mean aerodynamic chord. The effect of  $5$  degrees of elevator deflection on the pitching moment is linearly shifting the moment curve ( $C_M$  vs  $\alpha$ ) between  $-6$  to  $8$  degrees of angle of attack. In this

region there is no particular lift jumps as the  $C_{L\alpha}$  lift curve slope is also linear, so during the flight this should result with a smooth behaviour. The additional lift generated by the elevator deflection is also visible on the  $C_L$  lift coefficients, they have a constant shift according to the elevator deflection.

The aircraft is designed to be perfectly aligned with the free stream, especially the fuselage in order not to generate any additional drag. The wings have an incidence angle with respect to the fuselage that generates the required lift at the 14 m/s cruise speed and the horizontal tail incidence angle is designed to equilibrate the total pitching moment (at 8% static margin) with an elevator deflection angle of zero degree which finally resulted with a slight down force generation (theoretically  $C_{L_{ht}} = -0.15$ ). It can be seen on the top plot of figure 8.27 that the equilibrium point of pitching moment for zero degrees of elevator deflection corresponds to approximately 1 degrees of angle of attack in reality. Although there is a visible error, 1 degrees of difference between the theoretically expected and the measurements is totally acceptable.

Finally, the drag generated by the elevator deflection is shown on the bottom part of the figure 8.27. It can be seen from the figure that, the more lift generated by the horizontal tail, the more drag addition occurs to the whole aircraft. At first glance, it looks like flying with  $-10$  degrees of elevator deflection will result with a significant drag reduction but in reality  $-10$  degrees of elevator deflection is only in equilibrium state while the aircraft is at 11 degrees of angle of attack which corresponds to the stall regime.

## Component Drag

In the conceptual design phase, each part of the aircraft has been modelled in terms of structural weight and aerodynamic characteristics. In order to see each part's drag and lift coefficient with respect to the whole aircraft, a component drag analysis have been conducted. A reference curve is generated by changing the pitch angle of the aircraft from  $-6$  to  $12$  degrees at the cruise speed of 14 m/s and then the same procedure is repeated after removing the horizontal tail (*w/o HT*), then the tail boom and the vertical tail (*w/o Boom*) and then the wings are also removed in order to leave the fuselage alone (*Fuselage*). Each case is presented for the lift and drag coefficients versus angle of attack in the figure 8.28

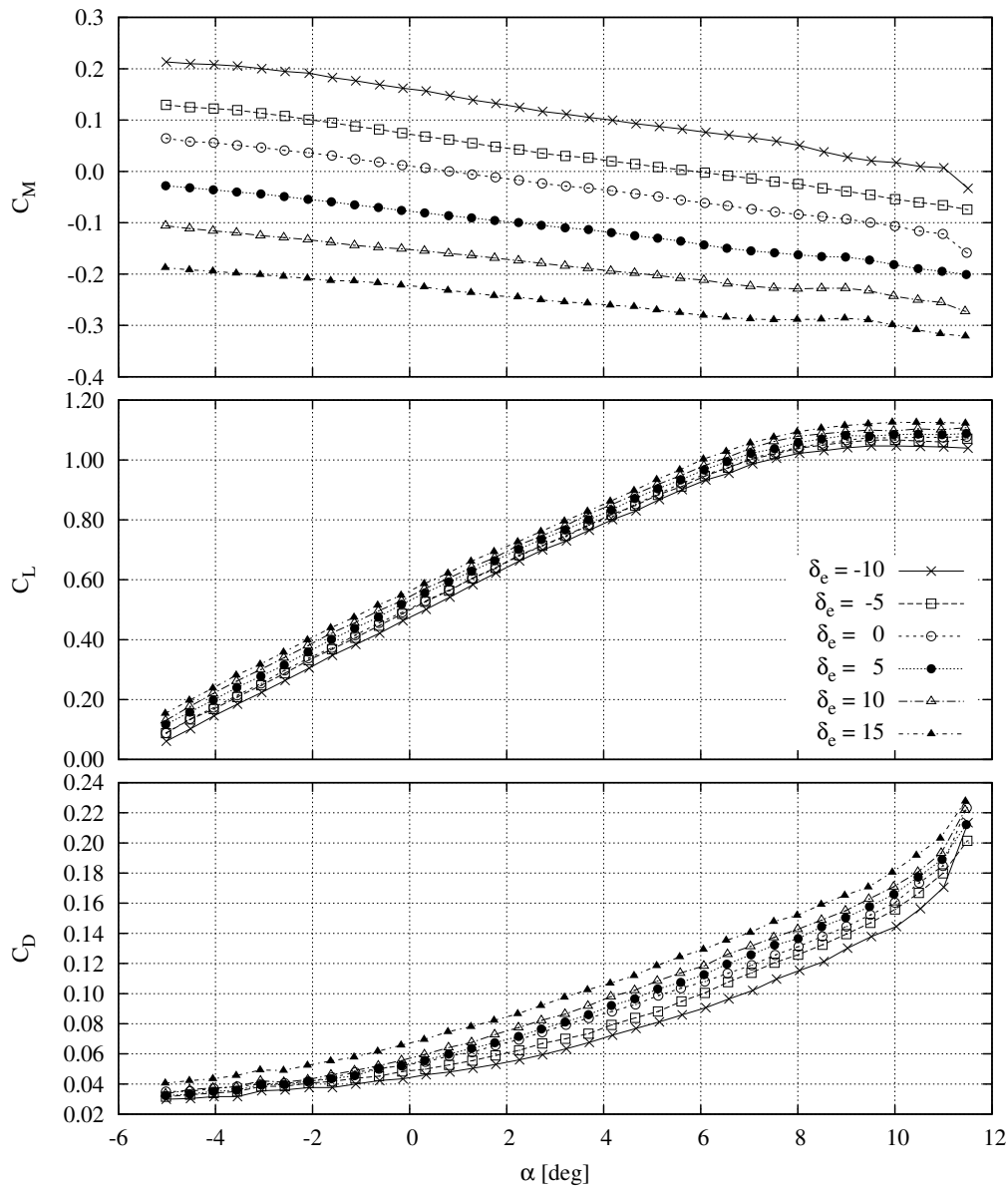


FIGURE 8.27: The effect of elevator deflection on  $C_M$ ,  $C_L$  and  $C_D$  coefficients of *Eternity* at 14 m/s wind-tunnel speed,  $C_M$  coefficient is measured with respect to the reference point that corresponds to %8 of static margin.

The first thing that is seen on the lift coefficient plots is the additional lift of horizontal tail, it is clearly visible that when the aircraft pitches up there is an additional lift coming from the horizontal tail, and the opposite is also true as the aircraft pitches down the down force generated by the horizontal tail reduces the total lift coefficient. The lift and down-force generated by the tail boom and the vertical tail is not visible as all the curves coincides perfectly over each other. The fuselage lift is negligible through out the whole angle of attack values.

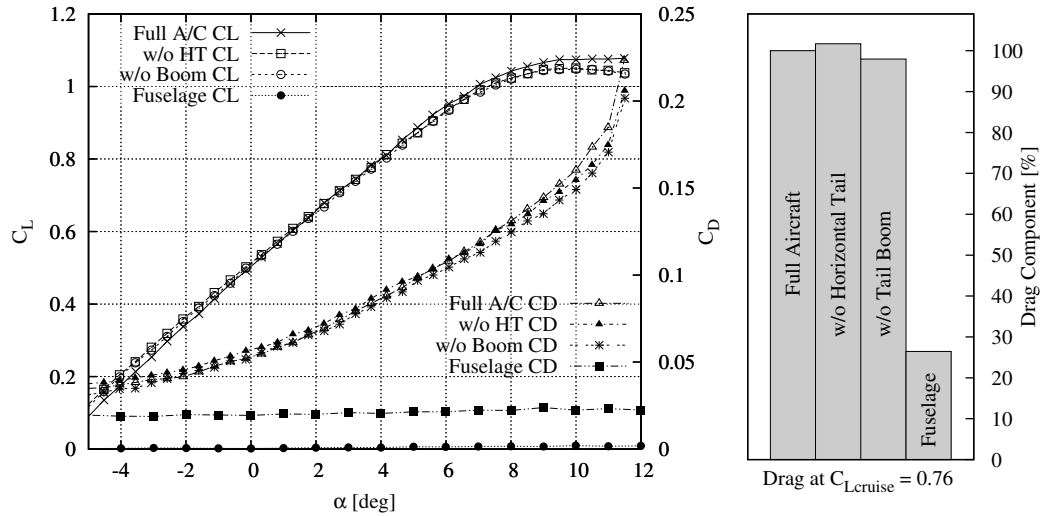


FIGURE 8.28: Component Drag at 14m/s.

The drag addition coming from the horizontal tail seems to be negative at cruise angle (as seen on the right part of figure 8.28), meaning that when the horizontal tail is removed the drag is increasing. This can be a false measuring from the balance like a repetition error as the forces are too small, or the horizontal tail pod is generating more drag when it is left alone. The tail boom and the vertical tail does not generate a significant amount of drag. As a conclusion the main drag is coming from the wings and the fuselage as expected. The fuselage has almost a constant drag addition for all angle of attack values and it corresponds to almost one third of the total aircraft drag in cruise conditions ( $C_L = 0.76$ ). A constant lift and drag generation of the fuselage at every pitch angle is a good property as it does not add a non-linear effect on the stability and flight dynamics of the aircraft. However, generating one third of the total drag shows the need of refinements of the fuselage in order to be used for high performance missions like long-endurance flight.

## High Speed Performance

In order to have a safety margin for the stall, the cruise speed is increased to 14 m/s where the lift coefficient corresponds to  $C_L = 0.76$  for the aircraft (big configuration). However, in the conceptual design of the *Eternity*, the cruise speed was chosen to be where the endurance is at its maximum value. The corresponding

cruise lift coefficient is around  $C_L = 0.9 - 1.0$ . This region was always the most important region while selecting and designing the airfoil sections.

However in the real life applications, there will be some situations where the aircraft will have to go out of this design region such as penetrating into wind or reaching to a point faster for priority. In order to improve the high speed performance of the aircraft, the low lift coefficient region of the airfoil sections has to be improved. The most important thing while doing this is not to reduce the performance at and around the upper lift coefficients that corresponds to cruise.

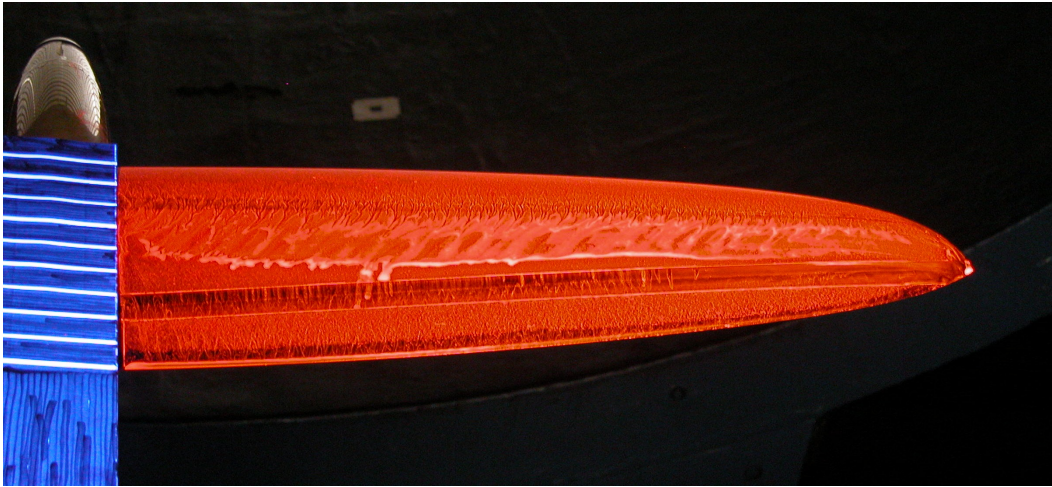


FIGURE 8.29: Laminar bubble occurrence over the top surface shown as an example.

The main performance reduction for the PKMB500 airfoil at high speed (over  $18\text{ m/s}$  in our case) comes from the extended laminar bubble located at the aft part of the airfoil's top surface. This was already foreseen in the design phase of the airfoil in XFOIL program.

In order to prevent this, a turbulator strip was planned to be used around %75 of the chord all along the wing span which will turn the flow from laminar to turbulent before the laminar bubble occurs. In order to see the effect of the different thickness and location of the turbulator strips, five experiments have been conducted as shown in figure 8.30 with a strip tape of  $1.57\text{ mm}$  wide and  $0.15\text{ mm}$  thick. In order to increase the thickness, two and three layer taped on top of each other.

As it can be seen in the figure 8.30, the high lift coefficient regime, where the cruise flight will be, is not affected from the turbulator strip and at the point where the

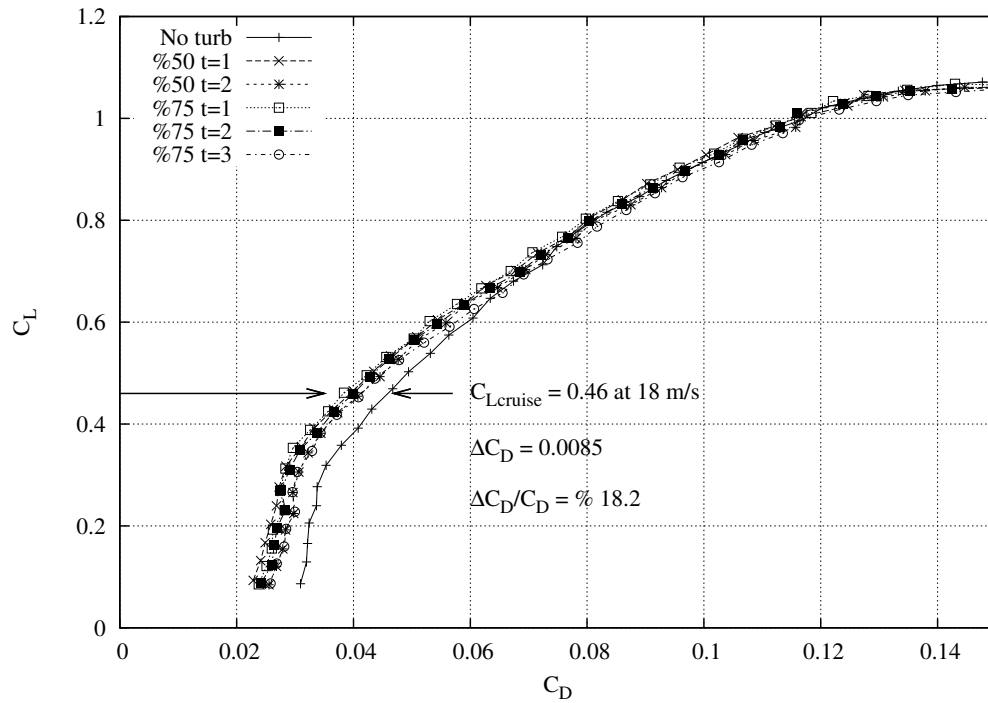


FIGURE 8.30: Turbulator effect at 18m/s for different thicknesses  $t=1,2,3$  and chord locations %50 and %75 all along the span.

18 m/s flight will be ( $C_L = 0.46$ ) there is an drag reduction of  $\Delta C_D = 0.0085$  which corresponds to %18.2 of improvement for the range performance at 18 m/s.

The development of the laminar bubble starts before the strip, so that the strip does not harm the cruise lift coefficients but reduces the drag over the lower lift coefficients where the higher speed flight will be. Figure 8.29 shows the laminar bubble as an example (Unfortunately, the shown case was for 14 m/s so at  $C_L = 0.76$  as the pictures from high speed cases came out blurry.)

Additionally, figure 8.31 shows the endurance ( $C_L^{1.5}/C_D$ ) performance versus the ( $C_L/C_D$ ) range performance for various turbulator strip thickness and locations. The best performing combination is one layer strip ( $t=1$ ) at %75 location. The points shown with the arrows corresponds to the equilibrium point where  $C_L = 0.46$ , as it can be seen the range performance is improved about %20 without affecting the endurance performance at all. This concludes that having a turbulator strip attached at every flight will be beneficial.

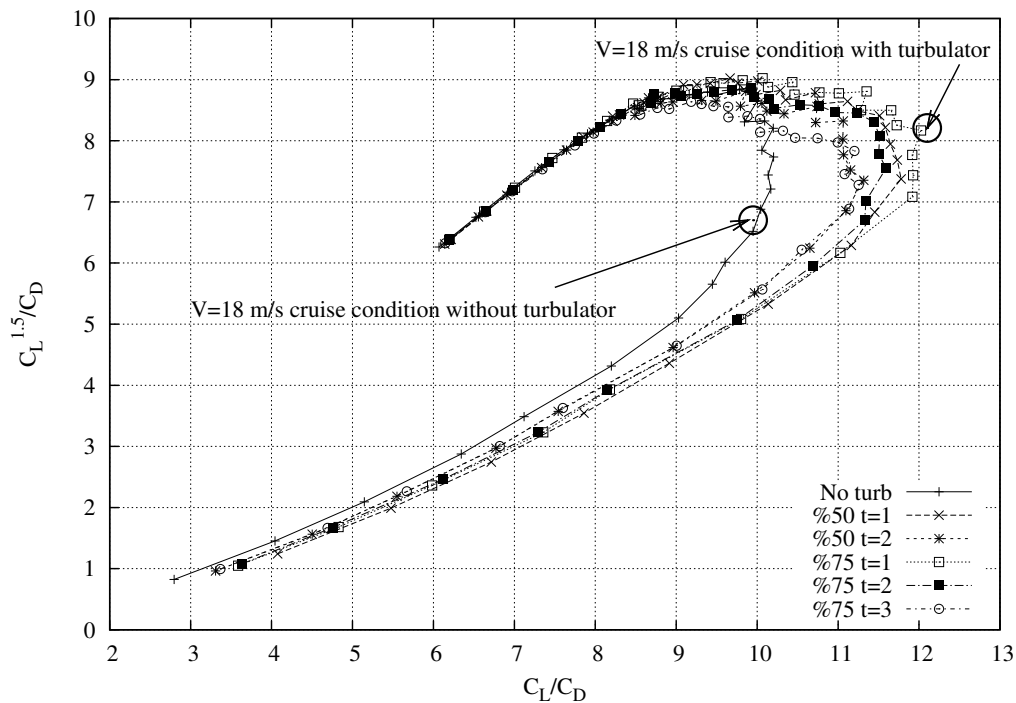


FIGURE 8.31: Turbulator effect at 18m/s.

## 8.8 Flight Test

We had only one opportunity to make a flight test because of time restrictions. The same model that is used on the wind-tunnel is used for the flight tests. For the first flight in order to stay on the safe side, a small battery pack has been used as it decreases the total weight and increases the chances to recover the aircraft from an unusual situation in the air.

There has been a new autopilot board specially designed for the *Eternity* called *UMARIM*. As the boards were not received at the time of the flight tests, older version *Tiny V2* autopilot board with the *Ardu IMU* is used. AXI 2212/26 motor with Graupner CAM Slim 9x6 propeller is used for the propulsion system. Thunder power 910mAh 11.1V battery pack is used for the initial test. The ready-to-fly weight was 0.650 kg instead of the designed 0.85 kg because of smaller battery pack.

The take-off has been made in manual mode controlled by an RC pilot up to reaching a safe altitude and later the stability gains have been tuned in order to make it ready to fly in autonomous navigation mode. The prototype was not

equipped with a pitot tube to measure the true airspeed, thus the flight speed was stabilised by fixing the pitch (via elevator deflection) and throttle combination. In a calm day this procedure results with precise flight speed stabilisation but in a windy day the true airspeed moves around the desired set point. In autonomous flight mode, constant radius circle patterns have been flown in level flight, resulting the average of true airspeed becoming equal to the average ground speed which is obtained from GPS on-board the aircraft.

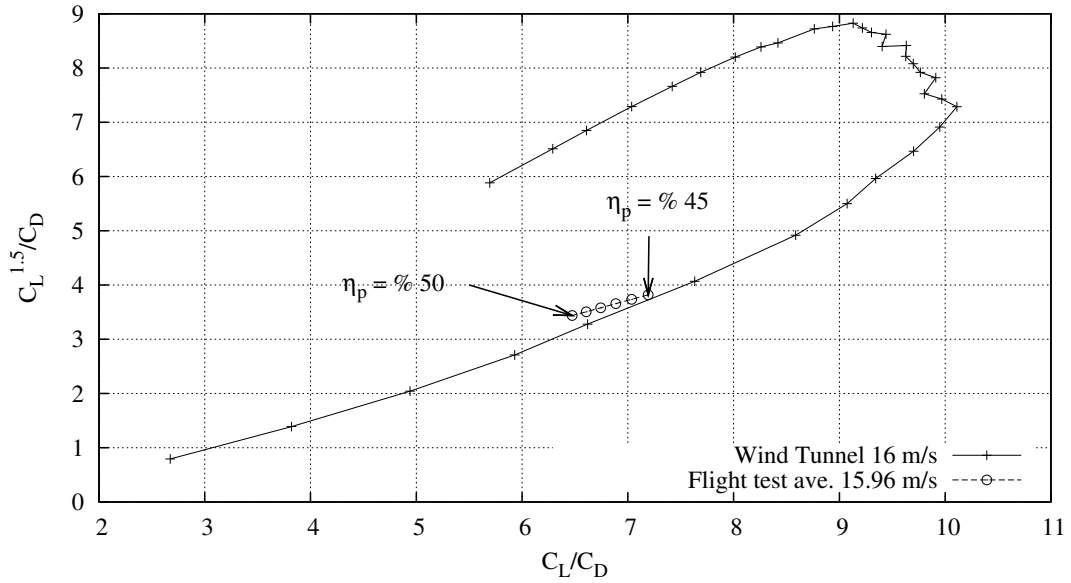


FIGURE 8.32: Comparison of wind tunnel test and the maiden flight results (Total propulsion efficiency ( $\eta_p$ ) is varied between %45 and %50 to see the effect on the performance estimation) .

After extracting these constant circle pattern's information from the flight log, it has been seen that  $7.824\text{ km}$  has been flown in 460 seconds with a consumption of  $4.409\text{ Wh}$  energy. The average flight speed corresponds to  $15.96\text{ m/s}$  where the optimum flight speed was designed to be  $14\text{ m/s}$ . For the safety reasons of the maiden flight, a small battery pack was used instead of the original battery pack which has more ( $62.16\text{ Wh}$ ) energy. Extrapolation of these numbers for the original single battery capacity that is planned to be used gives approximately 115 minutes of flight time and  $110\text{ km}$  of range performance. The expected endurance was 135 minutes and the range was around  $115\text{ km}$  for the single battery flight. As the test flight was too short, trying to have a conclusion out of it can lead to wrong results. However, using these figures the average lift coefficient and the corresponding drag coefficient of the prototype can be extracted. Figure 8.32 shows

the extracted values compared with wind tunnel measurements at  $16\text{ m/s}$ . As the efficiency of the propulsion group was not accurately known, six different values are used from %45 to %50 in order to see the effect. The extracted test values shows a close relation with the wind tunnel measurements. Additionally, thinking that it was the first flight (including testing and tuning the control gains), the overall performance and flight behaviour from launch to landing was satisfactory. Figure 8.33 shows the first take off of *Eternity* as a handlaunch.



FIGURE 8.33: Hand-launch moment of *Eternity* from its maiden flight.

## 8.9 Overall Design Conclusion

The main objective of this thesis is to show the feasibility of *Long Endurance Mini UAV* concept. *Eternity* shows a great perspective about what can be achieved with a one-meter aircraft. In this chapter, the new developed *Cdsgn* conceptual design program has been used to design a long endurance mini-UAV, while taking into account all the real life application restrictions. The resulted design is manufactured out of composite materials by using precise CNC molds. The main aerodynamic characteristics have been evaluated in wind-tunnel and a smooth flight behaviour have been observed for the level flight manoeuvres. Later, a short flight test has been done in order to see the real performance of the aircraft. Table 8.7 shows the expected performance of the two configurations. It should be noted

that the obtained battery gave  $62.5\text{ Wh}$  instead of the  $66\text{ Wh}$  value that has been used previously in the calculations. Additionally the payload difference has to be considered while observing the different configurations in the table. As an other comment, the effect of improvements that has been done for higher flight speed, such as the turbulator that enhanced the range performance for about 20 %, has not been taken into account while defining the range performance of the configurations in the table.

Finally, it can be concluded that with a **one-meter** aircraft, that fits into an even smaller half a meter carry-on luggage, **4 hours** of flight is possible while this can be enhanced up to **8 hours** in a sunny day by the help of solar cells.

		Small	Big
Cruise Speed	$[m/s]$	11.5	14.0
Cruise Lift Coefficient	$[-]$	0.71	0.76
Stall Speed	$[m/s]$	9.2	11.6
Max Bank Angle at $V_{cruise}$	$[deg]$	50.0	46.0
Turn Radius at Max Bank	$[m]$	11.3	19.3
Battery capacity	$[Wh]$	62.5	125
Payload Mass	$[kg]$	0.05	0.10
Total Mass	$[kg]$	0.85	1.35
<b>Solar Conditions</b>			
Endurance	$[h]$	7.48	6.2
Range	$[km]$	309	312
<b>Non-Solar Conditions</b>			
Endurance	$[h]$	3.3	3.92
Range	$[km]$	138	197

TABLE 8.7: Expected performance of the two *Eternity* configurations.



# Chapter 9

## Conclusion

### 9.1 Main Achievements

A new concept has been introduced being the Long Endurance Mini-UAV. The importance of optimization of each sub-systems that are coming together in order to form the complete system is highlighted. A new conceptual design program devoted to mini and micro UAVs, called *Cdsgn*, has been developed specially to understand and investigate the effect of each sub-system on the final performance of the complete system. With the help of the *Cdsgn* program, for a given flight mission, it is possible to investigate and define the optimum aircraft configuration (conventional or flying wing), wing surface area, wing span, on-board energy amount, flight speed, wing section airfoil, etc... Further more with a sensitivity analyses, the most important sub-systems can be defined in order to improve for a better performance.

Critical points that prevents the endurance enhancement for mini UAV scale have been identified. The most important one being the energy source and storage. In second place there is the propulsion system which has a huge improvement potential by just selecting the good motor and propeller combination. As the improvement of energy storage and sources are not an interest of this thesis, the effort is focused on propulsion system. A program is developed, called *Qpoptimizer*, in order to select the optimum motor and propeller couple for a given mission with multiple working conditions.

Hands on experience is gained by several project those use *Cdsgn* program for the conceptual design of the platform. Among the projects, an hybrid solar power micro UAV, called *Solar Storm* is presented. *Solar Storm* with half a meter span, demonstrated the feasibility of endurance enhancement on micro scale size by obtaining %40 of its total cruise power consumption from solar energy. Its companion *Fire Storm* has been awarded with "Best Outdoor Endurance" title in 2011 International Micro Air Vehicle Competition and Conference in Netherlands.

A long range mini UAV project, also called as *Fly to Corsica*, has been started within the thesis. The main objective of the project was to fly from Nice (France) to Calvi (Corsica) with the smallest UAV. As a result, a 1.5 m spanned electric powered mini UAV called Spirit of Corsica (*SPOC*) has been designed with the capability of flying 250 km of range. The project consists of not only the airframe and propulsion system optimisation but also other challenges such as satellite data link and communication, integration of all avionics and operation management with two separate ground control stations.

Finally, in order to show the feasibility of the new long endurance mini-UAV concept, a prototype called *Eternity* has been designed, manufactured and tested in a wind tunnel. In order to be compact and easy to operate, *Eternity* is designed to be disassembled and fitted into a carry-on flight luggage with 50 cm maximum inner dimension. Being only one meter wing span, *Eternity* is capable of flying 4 hours with the on-board batteries, and up to 8 hours with the additional solar energy in the best day-time conditions.

## 9.2 Future Work

The introduced design methodology was kept as simple as possible for a small range of scale of mini-UAVs, especially because of the selected structure model. In order to enlarge the vehicle size envelope, the models can be either further simplified in order to have a bigger range of scale with a compromise on accuracy or made more complex with different models for each envelope of scales with a compromise on computational time.

On the endurance enhancement, besides the design of the vehicle itself, the flight can be also optimised in term of stabilisation and navigation. Better control and stabilisation algorithms can be implemented in order to stay on the optimum

---

performance point of the vehicle. Additionally, a higher level navigation can be implemented in order to get benefit from external environmental energy extraction such as using thermals [\[45, 47\]](#).



# Appendix A

## A Long Range Mini UAV

### A.1 Introduction

The long range mini UAV project started back in 2009 as a student project between ENAC and SUPAERO in the name of *Fly to Corsica*. The main objective is to design the smallest electric powered UAV that can cross the Mediterranean sea from Nice to Calvi (approximately 185km) as shown in figure A.1. The project includes all the disciplines that brings together an UAV system as a whole such as the design of the airframe, structural design, manufacturing, integration of the on-board electronics, communication, autonomous stabilisation and navigation, etc...

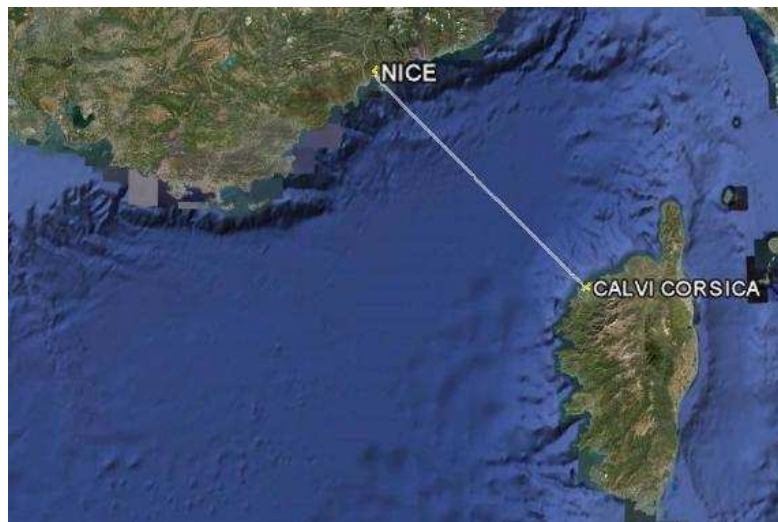


FIGURE A.1: Flight to Corsica mission path which is about 185 *km*.

Since the projects continues for several years, the following sections will go through the steps accomplished each year with different student teams and experiences.

## A.2 Main Phases of the Challenge

The mission is defined in 2009 as crossing from Nice to Calvi which is about  $185\text{ km}$  ground distance. The whole journey takes place over the sea which demands additional challenges to the project. The long range demand is the first challenge, especially when minimising the size is important. The smaller the size gets the lower the aerodynamic efficiencies that can be obtained by the wing and the propulsion system gets. This phenomena leads to lower performance where the projects needs a highly ambitious performance values.

The structure of the aircraft has to be light weight and robust for the mission. Manufacturing of the first prototypes have been handled by the students in the first year of the project. In the following years, the process has been taken over by the professionals from the composite laboratory of ISAE for more accurate and high quality building which results with reduced weight as well.

Autonomous navigation and stabilisation of the aircraft is decided to be handled by the Paparazzi Autopilot System [48]. Being an open-source system and developed in-house makes it easier to modify as oppose to the specific requirements of the mission when needed.

The communication over the sea also presents a big problem. As using traditional long range modems would lead to excessive weights that will reduce the performance of the system, light weight GSM module is selected as a candidate for the first and second year and switched to satellite communication on the third year of the project.

The cross-wind conditions over the sea demands the real flight distance differ from the actual ground distance. Therefore as a safety margin, a requirement of being able to resist to  $2.5\text{ m/s}$  of head wind is taken. According to the selected cruise flight speed this will lead to different total range performance requirement for the actual  $185\text{ km}$  of ground distance. Table A.1 shows the main constraints for the challenge that has been decided after the first year's experiences.

Design Constraints			
Stall Speed	<11	( <i>m/s</i> )	
Ground Distance	185	( <i>km</i> )	
Head-Wind	2.5	( <i>m/s</i> )	
Span	<2	( <i>m</i> )	

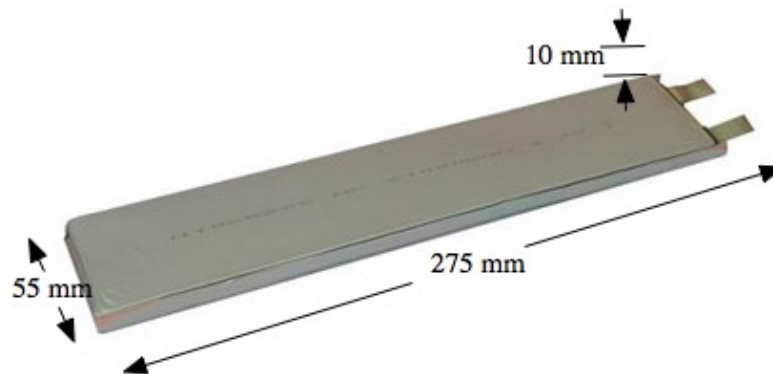
TABLE A.1: Mission constraints for the conceptual design.

### A.2.1 Improvements Over The Years

The project started without much experience on certain subjects such as the long range communication, integration of high capacity batteries to the system, low power to weight ratio flight. In the light of first year's experiences, the propulsion system is optimised and a higher specific energy battery found and used. From the first flight tests, it has been seen that there will be a lot of test-crashes especially caused by the low power to weight ratio of the aircraft, so that in order to manufacture identically the same airframe each time, CNC milled molds have been designed and produced. The attained surface accuracy and the manufacturing technique also served in a positive way on gaining some structural weight and aerodynamic performance.

Finally these improvements lead to a significant mass reduction from 3.1 *kg* to 1.95 *kg* in one year.

Specifications	SPOC 2009	SPOC 2010	SPOC 2011
Structural Mass ( <i>Kg</i> )	1.0	0.75	0.75
Total Mass ( <i>Kg</i> )	3.1	1.95	1.95
Communication	GSM	GSM	Satellite

FIGURE A.2: Selected 21 *Ah* Lithium Polymer Battery

### A.3 Aerodynamic Analyses and Wind Tunnel Tests

As a result from the conceptual design program, we obtain the wing area, span, airfoil, tail surfaces and the moment arm of the tail surfaces. After, preliminary sizing has been evaluated with analytical methods and numerical methods ( AVL<sup>1</sup> and XFLR5<sup>2</sup>) using a classical vortex lattice method (Figure A.3). The wing planform shape has been designed to have almost elliptical lift loading along the span so as to have a higher span efficiency. It has been also taking into account for the low Reynolds problems near the small tip chords, avoiding tip stalls for favourable flight characteristics and integration of the batteries. Figure A.3 shows the lift and lift coefficient distribution along the span for total equilibrium cruise condition at 15 m/s. Finally, the horizontal tail sizing have been done by using Naylor-Prandtl Theorem in order to calculate the downwash of the wing over horizontal tail. The horizontal tail has been designed as a zero lifting surface while satisfying %5 longitudinal static margin. In figure A.3, it can be easily seen that the horizontal tail is almost at zero lift condition.

A specific wind tunnel campaign has been carried out as well in order to compare the theoretical and experimental results. Figure A.5 shows the typical lift coefficient versus angle of attack and drag coefficient of SPOC-2 for different speeds. The effect of increased flight speed over lift to drag ratio is clearly visible in figure A.6.

### A.4 Manufacturing and Integration

In order to achieve the required surface quality and the accuracy in the integration, CNC-machined molds have been used in the manufacturing of the UAV (Figure A.7).

Manufacturing process has been accomplished by the professionals of the composite laboratory of ISAE, which resulted in a high quality airframe as required. *SPOC2* is made out of fully composite materials with wet layup and vacuum bag technique. One of the particular property of the UAV is to carry large capacity of lithium polymer batteries, which are embedded inside the hollow molded wing.

---

<sup>1</sup>[raphael.mit.edu/avl](http://raphael.mit.edu/avl)

<sup>2</sup>[xflr5.sourceforge.net](http://xflr5.sourceforge.net)

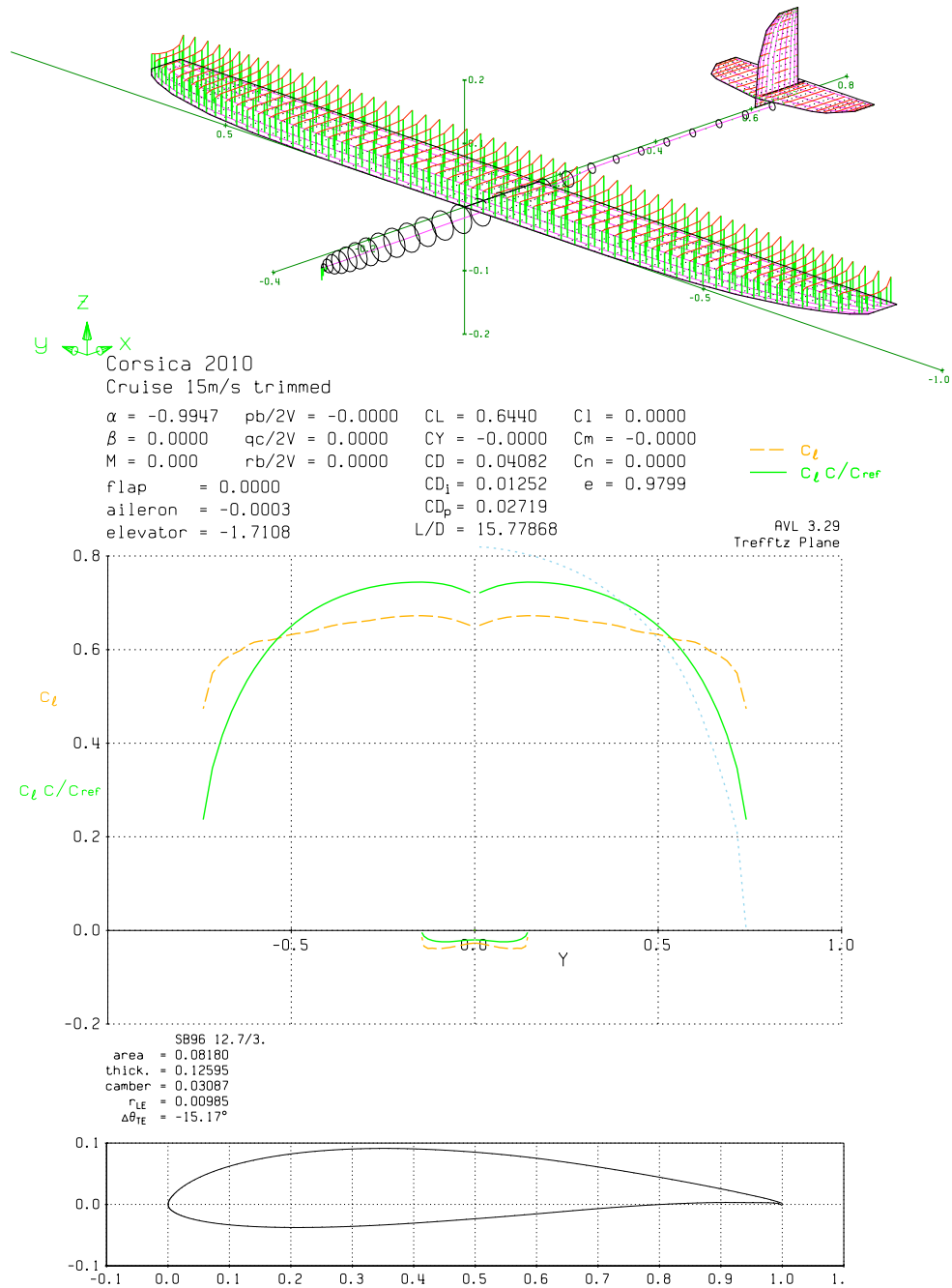


FIGURE A.3: Analysis of SPOC-2 in AVL, with the wingloading visible on the top, lift force and lift coefficient visible along the span in the middle and the airfoil chosen on the bottom.

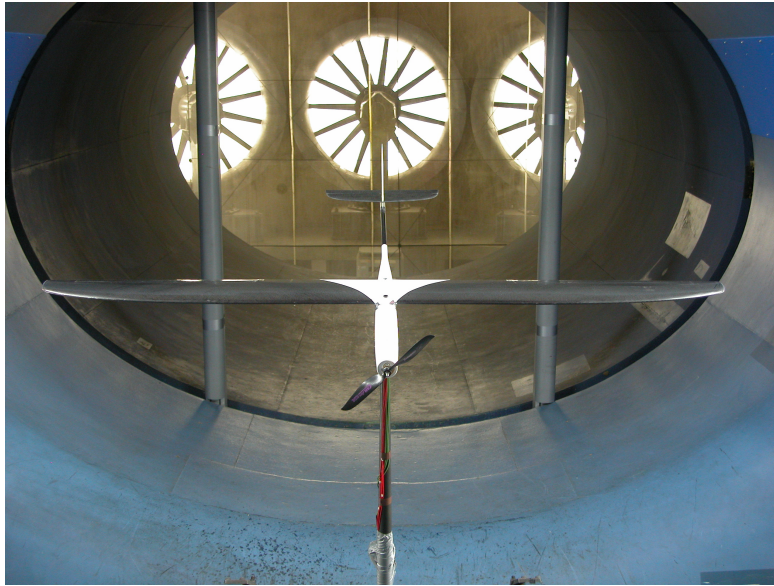


FIGURE A.4: SPOC-2 in the S4 Windtunnel.

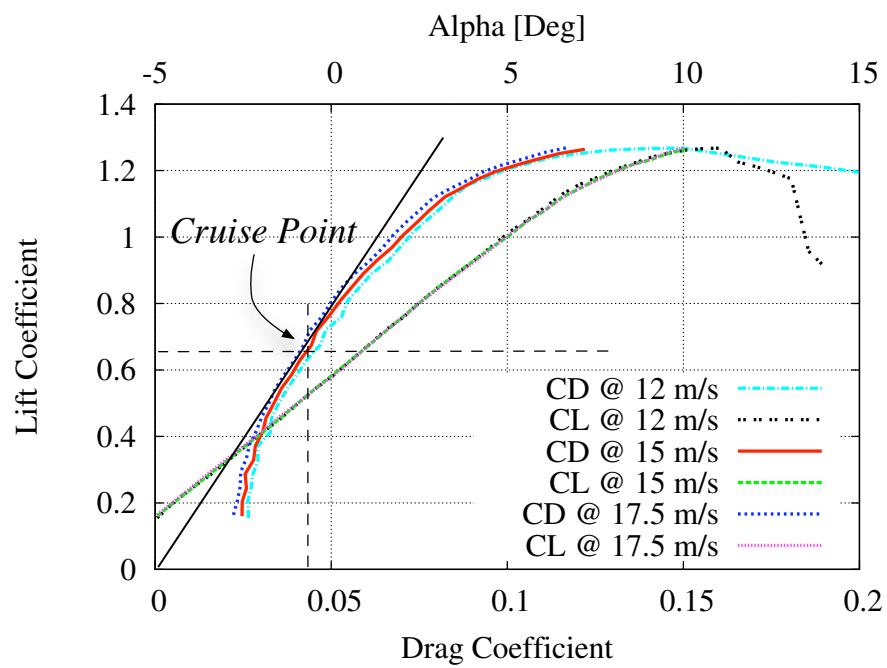


FIGURE A.5: CL versus alpha and CL versus CD plots.

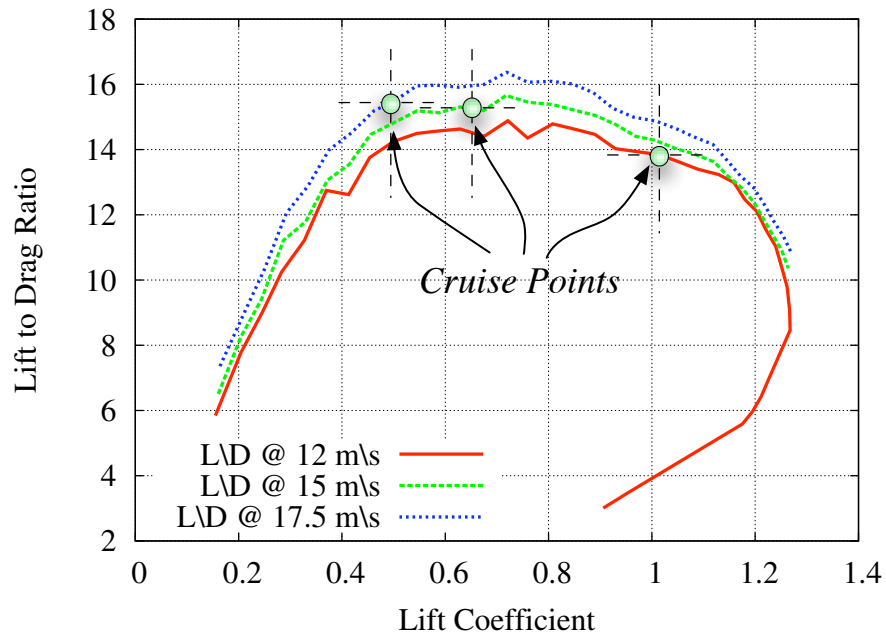


FIGURE A.6: Lift to drag ratio of SPOC-2 for different flight speeds with the equilibrium points marked for each corresponding flight speed.



FIGURE A.7: Composite molds of SPOC-2.

The integration of the batteries is done in the mold before combining the top and bottom wing skins together. Through out the whole project in 2010, four wings, four tail group and six fuselages have been manufactured in five months. Figure A.8 shows the final integration of main components.

#### A.4.1 GSM Module

As expected, typical low power radio-modem ranges are not sufficient to keep contact during the whole flight (midpoint range is approximately 90 km from the two GCS). It was also not possible to use a high power radio-modem because of

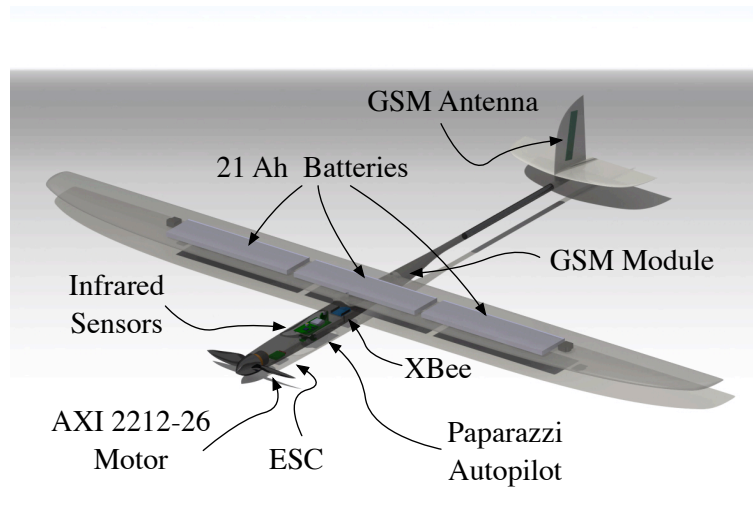


FIGURE A.8: Integration of the components.

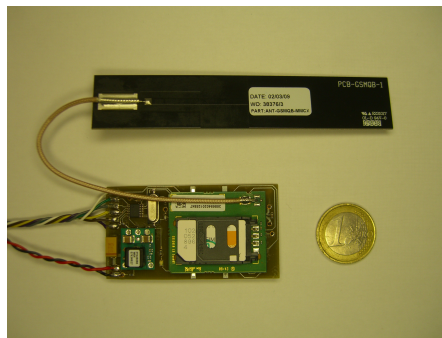


FIGURE A.9: Telit GC864 GSM/GPRS Module with antenna

power emitting regulations in France. A GSM module was planned to be used for the telecommand and telecontrol communications. This would enable us to keep track of the extremely important information such as GPS location, power consumption and the remained energy on-board during the flight. It would also allow us to abort the flight if an unexpected and unrecoverable situation happens. These communications were also required for a periodic reporting of the position of the aircraft to the air traffic control.

Because of its small size and weight, Telit GC864 GSM/GPRS module is chosen. It requires an UART connection to exchange data, but as there were no UART connections left available on the Paparazzi module, the remaining SPI ports are used. And an all-in-one embedded GSM module is developed for Corsica mission,

including a switching power supply (SMPS), a Maxim MAX3100 SPI/UART converter, and the GSM/GPRS module. The Telit GC864 is connected to a standard patch antenna which is located in the tail. For the ground stations, two of the same module is used one at Menton, one at Lozari/Calvi with an additional FTDI serial-to-USB cable which allows us to connect these ground stations directly to laptops.

With regard to the software, two additional pieces of code have been developed. The embedded code is designed to initialize the Telit GC864 settings, then to send a text message every minute. These messages contain the position of the plane, its altitude, its speed, the battery voltage and the strength of the GSM signal. The code for the ground stations reads messages as soon as they are received, and parse them in order to get the data in a readable form.

## **A.5 Flight Tests and Flight to Corsica**

### **A.5.1 Certification**

In order to operate UAVs in a legal way, several authorizations from the DGAC (Direction Générale de l'Aviation Civile, French Civil Aviation Authority) need to be obtained dealing with different aspects of the system. For the platform (plane or helicopter), it is needed to have a "Permit to Fly" which will allow to use the platform with in the conditions mentioned in the permit. The DSAC department of DGAC has been contacted in order to obtain Permit to Fly which is only given after a certification visit composed by a technological analysis and a flight demonstration.

When a "Laisser-passer" type permit to fly obtained, the restricted area in which the UAV will fly needs to be determined. Therefore, a file including all GPS coordinates which describe the area and flight altitude, has been provided to DGAC. Then the DSR department has been contacted in order to "build" the area for the mission. Finally the last point to fly legally was to obtain the a matriculation number for SPOC-2 (*F-WZSC*) has been taken from DGAC in order to fly legally.

### A.5.2 The 2010 Attempt

A good knowledge of the weather conditions was a key parameter for the success of the mission. That's why AROME and ALADIN forecasts models from Meteo France were used, in order to choose the best day for the launching. A few minutes before the launching, the weather was checked one final time with the current data of the local Meteo France centers.

At 6.30 AM the 23<sup>rd</sup> June 2010 the weather conditions were favourable. Unfortunately, just after the take off, the pilot lost the RC link, probably due to a considerable electromagnetic pollution, and the mode of the plane changed to HOME (meaning that the plane should go directly to Calvi). The plane intended to climb to reach its cruise altitude too rapidly and a stall happened resulting with a crash on the rocks near the harbor. Immediately, preparations have been started for the next attempt, starting by finding the reason of failure.

- The HOME mode has been replaced by the AUTO2 mode with a low altitude reference, to avoid any stall in case of RC loss.
- After several tests in different environments, we concluded that there was too much electro-magnetic influence on the coast. We took the decision to pilot the plane directly through the Xbee (2.4GHz Datalink) with a remote control plugged on the ground station.
- In order to avoid the risk related to the proximity with the boats, we changed the take off place, using a large free beach.

On the second day of attempt, at 6.10 AM the 24<sup>th</sup> June 2010, the take off happened without any problems, final trimming and the tuning occurred quickly and without difficulties. After 6 minutes, it is decided to stop circling for testing and send the plane to Corsica for its real mission. Finally, when the plane was in direction to Calvi, the altitude, the speed, and the direction([A.10](#)) were perfect during the first eight minutes. We have lost the contact with the plane after flying 5 km as expected. GSM module was not in operation as we had some problems in the first attempt. Finally, we couldn't have had any more information from SPOC-2. Without data, we are not able to give the real failure reason. Of course, some hypotheses can be imagined like path through low clouds ([Figure A.11](#)), wind gust,... but without certitudes.

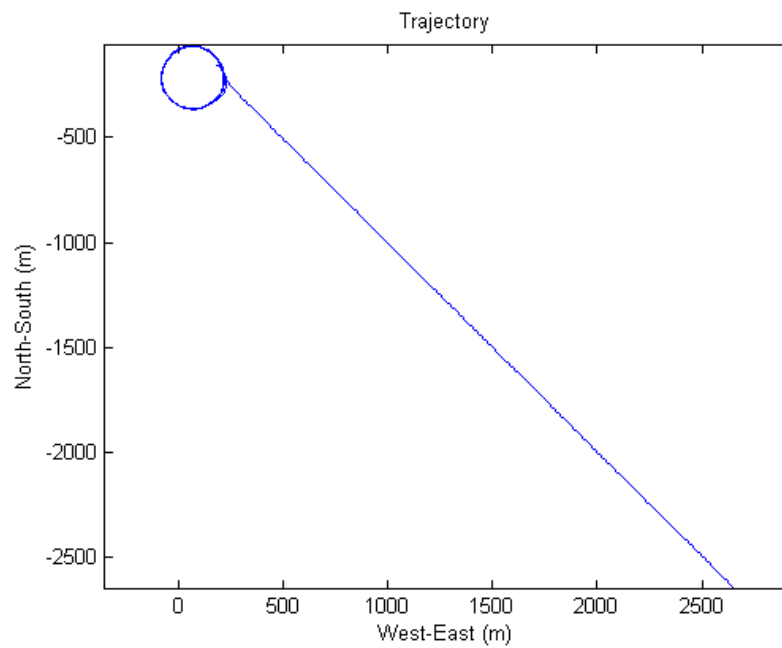


FIGURE A.10: Trajectory of SPOC-2 before losing communication.

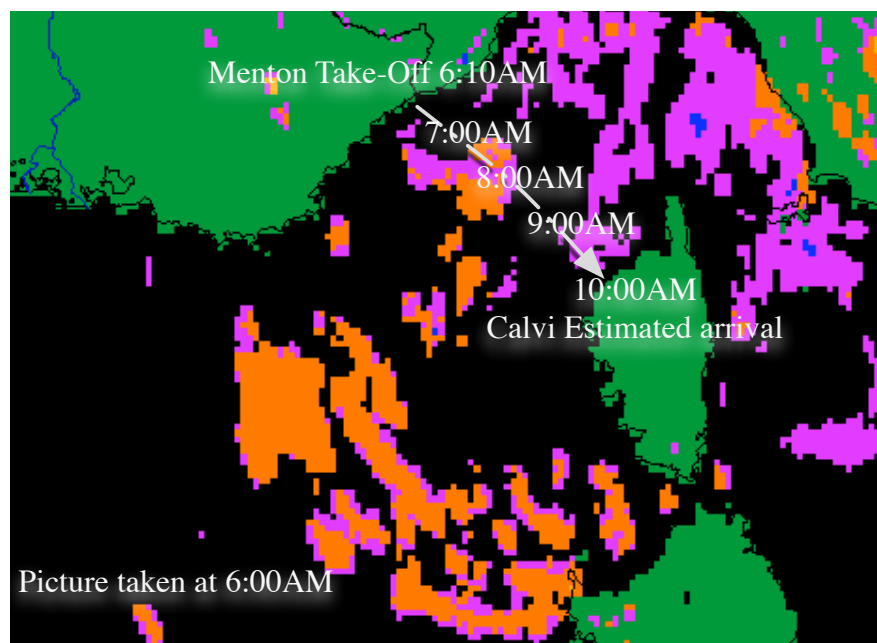


FIGURE A.11: Satellite picture of the clouds taken at 6:00 AM, orange colour shows very low altitude clouds which could cause the failure of the infrared sensors.

### A.5.3 The 2011 Changes and Attempt

The strongest hypothesis for 2010 attempt to fail was the infra-red sensors failing during the flight through the cloud over the sea. A change in the attitude sensors have been made in order to over come this problem and started to use ArduIMU instead of infra-red sensors. And also as it is known that the *SPOC* has an optimized limited flight envelope with a high wing loading ( $91\text{ N/m}^2$ ) and a cruise speed of  $15\text{ m/s}$  which is close to its stall speed of  $11.5\text{ m/s}$ . These increases the requirement of the airspeed management for *SPOC*'s mission. So that the new airframes are equipped with pitot-static tube. Additionally, in order to have a better data link connection, GSM module is replaced with a satellite communication module.

Although having build four new airframes, the expected amount of test hours was not achieved. The new integrated IMU to the system generated a lot of problem to overcome, especially during the launch phase where there is an acceleration coming from a hand launch or bungee. In order to test this effect, a less expensive foam aircraft, Fun-Jet is used as a test platform, and a lot of hand launch attempts have been made to improve the software. Later on the real test attempt with the *SPOC* airframe it has been seen that the ArduIMU is not taking into account the huge accelerations for the correction when they exceeds the measuring range of the sensors.

The *SPOC* is being bungee launched with an acceleration of around 8-9Gs, which makes the ArduIMU freeze for the accelerometers and use only the gyros for the attitude corrections during that time. Although this phenomena solving *SPOC*'s take-off issues, it is always favourable to be able to use a better IMU and have the software really taking into account all the necessary corrections in every possible case. Unfortunately this decision add more complexity and an additional source of failure to the system at the end.

On the day of attempt, the information coming from airspeed sensor was not completely integrated into the control loops yet, the SATCOM module was not performing in a robust way and frequently has to be rebooted in order to start working. Addition to all these unsuccessful new integrations, a new software issue was coming up everyday with the IMU. Unfortunately it happened at the launch of the attempt as well, ideally when the aircraft makes a turn, the acceleration generated by the turn is being corrected in order not to change the gravity vector

and make the aircraft sense a false bank angle. The same situation occurs in the high acceleration take-off case as well, when the aircraft accelerates rapidly, the gravity vector shifts back and the plane makes a pitch down correction as it senses it is pitching up, and as it is not the case the pitch down correction ends up with a crash. In order to correct this high longitudinal acceleration case, the gravity vector correction was disabled at low speed ( $< 5\text{ m/s}$ ) and high throttle ( $> 80\%$ ). Unfortunately, the speed value has not been checked from the correct source and as the throttle was 82% during the take-off the corrections have been kept disabled. After the take-off a left hand side climb is performed at full throttle and already in the middle of the turn, the aircraft started not to turn as its gravity vector has been shifted and according to its reading it is at maximum bank angle. When it is realised that it does not continue turning left, the attempt to turn right has completely tumbled the aircraft and went directly to a spin crash again because of the shifted gravity vector.

## A.6 Conclusion & Lessons Learned

The design of a long-range mini UAV so called *SPOC-2* has been described with all of its development phases. A specific wind tunnel campaign has been accomplished in order to verify the real specifications of the design. As a result of this wind tunnel campaign, it has been proven that for 1.5 m span UAV, a lift to drag ratio of 16 is feasible to obtain. A specific method for matching the propeller and motor according to the mission requirements has been briefly described, and shown that at least 50% of total efficiency for the propulsion system is feasible to achieve at this scale. Also a solution found for a lightweight long range communication by using a GSM modem but later switched to SATCOM module in order to have a more robust connection. Although not being able to accomplish the mission, the 2010 attempt is done with a perfect take-off and start phase. *SPOC-2* has left the coast of Menton/Nice and flew towards Calvi/Corsica smoothly before disappearing in the sky. And a lot of lessons learned from the 2011 attempt especially for the IMU and airspeed sensor integration. For the future of this project it will be more beneficial to have a progressive mission testing procedure starting from the real basics of the flight, like having to problem at all at launch and landing phase. Then move on to the 4 hours endurance test flights at the same location. Later on, test the out of sight communication with SATCOM and perform a "real mission"

scenario with two GCSs and switch the control between them. These will give a better confidence on the day of next attempt.

## Acknowledgements

I would like to point out that the present work has been a team work which contributors are gratefully acknowledged: J.M.Moschetta, D.Bernard, X.Foulquier, G.Mirabel, F.Dupont, L.Rion, C.Plachot, P.Toucas, M.Morere, P.Joachim, G.Soete, B.Fragniere, C.Ronfle-Nadaud, M.Gorraz, FX.Marmet, J.Scattolin, T.Lefez and G.Hattenberger.

# Appendix B

## Custom Design Propeller

### B.1 Introduction

In the content of *Long Range Mini UAV* project, which is described in appendix [A](#), the need for a custom propeller design has arised because of the project's high efficiency requirements. This appendix is going to show the application of QPOP-TIMIZER on *Fly to Corsica* project's real mission requirements. The selection of motor and the design of the custom propeller will be explained starting from the mission requirement input phase to the final manufacturing and wind tunnel test results. Benjamin Fragnière, Pierre Joachim, Miguel Morere Y Van Begin and Guillaume Soete from SUPAERO/ISAE have contributed to the presented study starting from the beginning to the end.

### B.2 Application of Qpoptimizer

As explained in section [5.3.2](#) the most important input is the working conditions which is defined by the mission itself. The final performance criteria is also going to be evaluated according to these working conditions and their weight factor which implies the importance of each working condition.

## Working Conditions

The first calculations and later the wind tunnel test of the aircraft, *SPOC*, that is designed for the long range mini UAV project showed that the thrust needed at cruise speed is around  $1.3 N$ . This condition created the first working condition and as the main flight is going to be almost flown in this condition, the weight factor has been selected to be 70 for it. In the time of this custom propeller design phase, the first flight tests of the *SPOC* was already accomplished. There, the need of an instant climbing ability has been seen to be required. Constant climb with  $2 m/s$  vertical speed requires  $3 N$  of thrust at  $15 m/s$  flight speed for *SPOC*, this condition created the second working condition. The weight factor is selected to be 10 as it is not that much significant for the final mission performance, the important thing is to be able to achieve that condition. As the last condition, the stall phase has been selected, from the wind tunnel tests, it is known that the stall speed for *SPOC* is around  $11 m/s$  and the required equilibrium thrust is  $1.4 N$ , given with a really small weight factor of 5, the third working condition has been created. The sum of the weight factors do not necessarily need to be 100, they are normalised within the program. The table B.1 show all of the selected working conditions for QPOPTIMIZER.

	Unit	WC#1	WC#2	WC#3
Thrust	$[N]$	1.3	3.0	1.4
Speed	$[m/s]$	15.0	15.0	11.5
WeightFactor		70	10	5

TABLE B.1: Mission working conditions of the *Corsica Project* [appendix A].

## Motor Database

The ability of using a big motor database in QPOPTIMIZER gives a big freedom on choosing motors but in the content of the project there was only two motors to be used while designing the optimised propeller. These motors are selected according to their experimental bench test results and finally the fuselage of the *SPOC* is optimised according to the use of these motors. They are AXI 2212-26 and AXI 2217-12. Another important reason why these motors were chosen for the project is the rapid availability of them for the school.

## Airfoil Selection

The airfoils that are going to be used in the propeller design needs to be defined in the inputs for QPOPTIMIZER. The definition is simply done by a polynomial curve fit to the aerodynamic characteristics plot of the airfoil, which are drag coefficient versus lift coefficient and lift coefficient versus angle of attack plots.

Some off-the-shelf propellers were already experimentally tested previously at the cruise speed and required thrust. These tests gave an approximate value about the average chord reynolds number of the propeller which is around 60000. Additionally, the dominance of thin cambered airfoils in the low reynolds conditions is shown in several work [? ]. Firstly, some existing thin airfoils have been searched through the internet databases <sup>1</sup> and M.Selig's books [49–51]. The comparison is made between 60000 and 100000 reynolds number regime, also a smooth stall and consistent drag change versus lift is considered as selection criterias. After some investigation, five airfoils are selected as candidates, BE-50, GOE-417a, BW-3, CR-001 and GM-15.

One of the most important criteria while airfoil selection was the manufacturability. As we already selected a computer assisted numerically driven CNC milling machine manufacturing with moulds, controlled variation of thickness along the chord was achievable. This gives the opportunity of selecting better performing airfoils rather than curved constant thickness (plate like) airfoils. As a next step, a custom airfoil is designed fulfilling a wider range of lift regime. The five candidate airfoils and the designed MBP-006 airfoil geometries and their aerodynamic characteristics are shown in figure B.1.

For our application, the best suited airfoil among the first five selected candidates was BE-50, because of its smoother behaviour around  $C_l = 1.0 - 1.2$  and lower drag value at corresponding smaller lift coefficients than 1.0. All the other airfoils have a sudden peak of change in drag coefficient, and also have higher drag coefficient at lift coefficients that are lower than 1.0.

BE-50 is taken as the reference airfoil to start the design with XFOIL. The objective was to improve the already existing good characteristics and work on the lower lift coefficient part. In order to smooth the high lift coefficient regime a little bit more and reduce drag coefficient around  $C_l = 0.2 - 1.0$  lift coefficient regime,

<sup>1</sup>UIUC, <http://www.ae.illinois.edu/m-selig/ads.html>

maximum lift coefficient is compromised.

The resultant MBP-006 airfoil has %10 less maximum lift coefficient but performs smoother in overall. Ideally, the required thrust should stay almost constant over the entire flight, but it is already known from the previous tests that there will be fluctuations on the required thrust while controlling the aircraft. Obtained reduced drag around  $C_l = 0.2 - 1.0$  regime becomes very important for the airfoil performance of the propeller and makes it more optimised in a practical way.

### B.3 Run cases

The two motors which are selected for the project previously, were AXI2217-12 and AXI2212-26. Table B.2 shows the motor constants and the weight of the motors. The bench test results showed that there is a significant difference between the expected theoretical performance and the experimental performance of AXI2217-12, the theoretical performances are almost %10 overestimated than the experimental ones. The performance plots are calculated as explained in section 5.4.1 and shown in figure B.2. As an additional to this, there is an 13g of weight penalty for AXI2217-12 as it is a bigger motor than AXI2212-26. Being a bigger motor also means that the throttle percentage is going to be low while cruise flight conditions, so that the speed controller efficiency will be lower than expected for this case as well. The only advantage is going to be the additional maximum thrust value for safety reasons. Taking into account all these facts, the design of the new propeller is selected to be made primarily for the small AXI2212-26 motor and try to have the bigger AXI2217-12 motor for some critical test flight where the additional power can be necessary.

		AXI 2212/26	AXI 2217/12
$K_V$	$[RPM/V]$	920	1380
No load current $I_0$	$[A]$	0.45	0.4
Internal Resistance $R_m$	$[Ohm]$	0.21	0.061
Weight	$[kg]$	0.057	0.0695

TABLE B.2: AXI2212/26 and AXI2217/12 motor constants obtained from the manufacturer site.

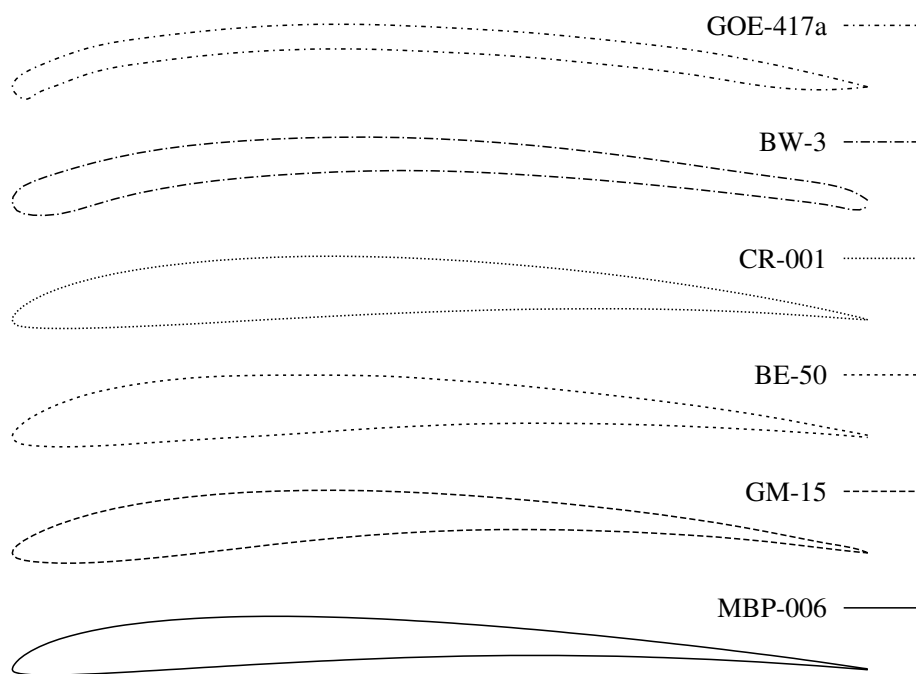
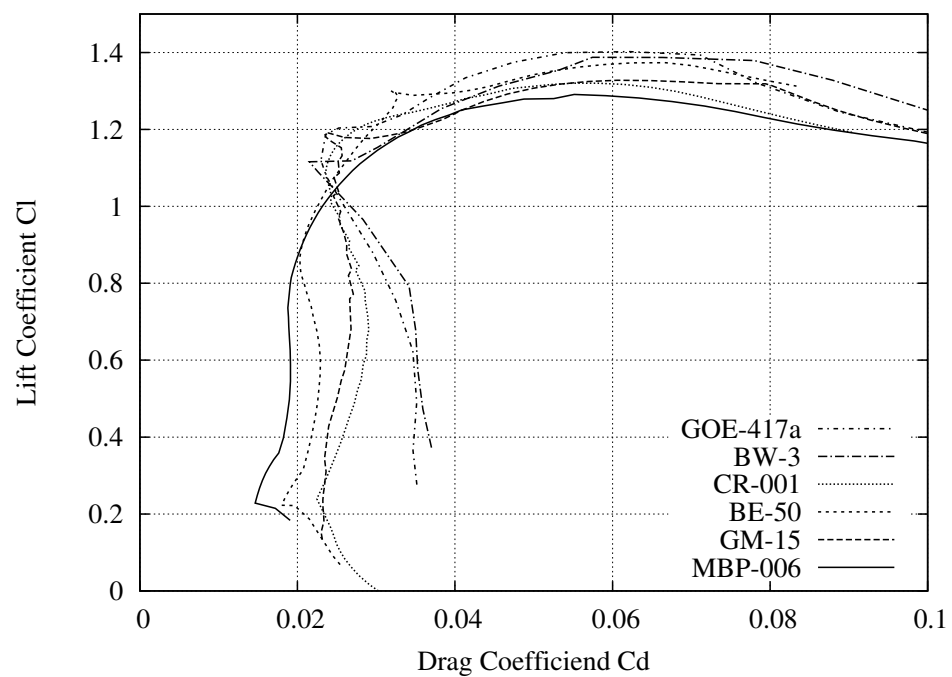
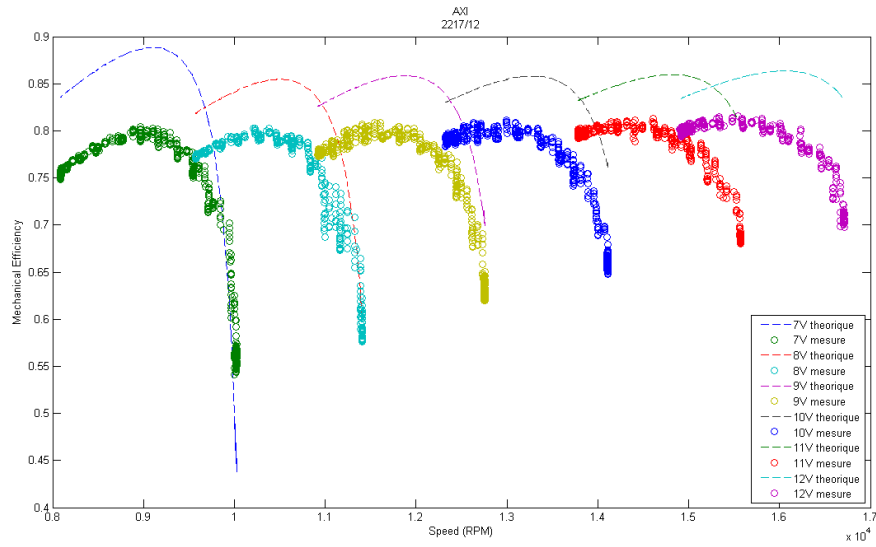
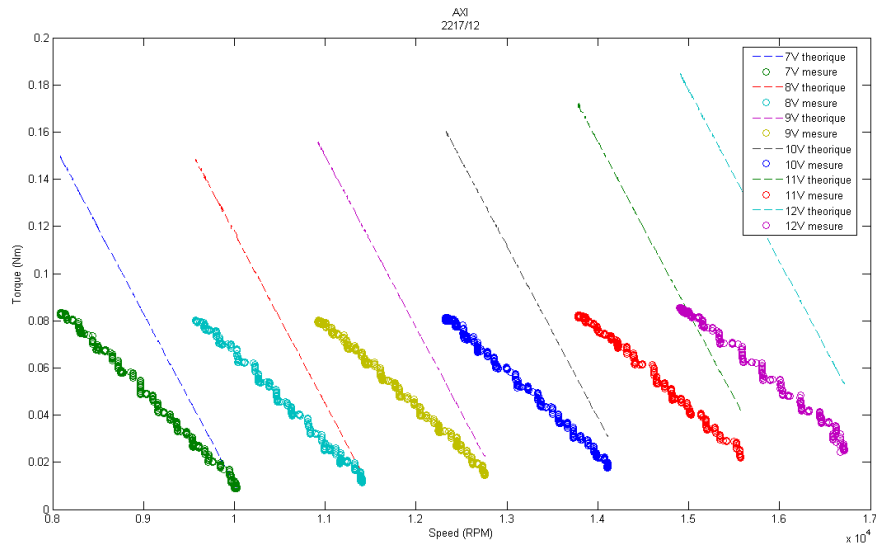


FIGURE B.1: Selected airfoils and their lift versus drag coefficient plot calculated by XFOIL for 60000 Reynolds number.



(a) Theoretical and experimental mechanical efficiency curves versus rotation rate for various input voltages.



(b) Theoretical and experimental shaft torque curves versus rotation rate for various input voltages.

FIGURE B.2: AXI 2217-12 characteristic performance curves at various input voltages, showing the significant difference between the theoretical and experimental test results.

As an input, the RPM and propeller tip radius ranges must be defined in order to run the simulations. The precision of the optimisation is defined by the step of both parameters. Table B.3 shows the selected envelope for the design.

Spanwise location	Minimum	Maximum	Step
RPM	2000	12000	50
Tip radius [mm]	10	200	1

TABLE B.3: Parameters used for the optimization

Additionally, the desired spanwise lift coefficient distribution required to be defined for QPOPTIMIZER (QMIL program needs this information). Two spanwise  $C_L$  distributions were tested and are shown in table B.4.

Spanwise location	0.10	0.50	1.00
$C_L$ distribution 1	0.75	0.65	0.40
$C_L$ distribution 2	0.60	0.45	0.40

TABLE B.4: Lift coefficients distributions

Previously selected working conditions, shown in table B.1, used for every run case. As a common result in every run case, the higher  $C_L$  distribution gave better performances. Table B.5 shows the best results of all the run cases.  $C_L1$  distribution is selected to be used for the final design.

		Cruise efficiency	RPM	Tip radius [cm]
AXI2212-26	$C_L1$	59.5%	5800	11
AXI2212-26	$C_L2$	58.9%	5700	11.5
AXI2217-12	$C_L1$	63%	5000	12.5
AXI2217-12	$C_L2$	61.9%	5000	12

TABLE B.5: Best global efficiencies of the motor and propeller couples for the cruise conditions are shown (note that the speed controller losses are not included).

The resultant global efficiency is higher using the bigger AXI2217-12 motor as expected. As it is already known that the AXI2217-12 is over estimated for the efficiency and also heavier, the small AXI2212-26 motor fits more appropriately for our application.

A monoblade propeller was also designed using the same approach. Demanding the same thrust with only one blade created a propeller with wider chords. This improved the overall airfoil efficiencies along the span because of increased Reynolds number. The best estimated overall efficiency for the motor and monoblade propeller couple is calculated as 62.6% by QPOPTIMIZER. Unfortunately, because of the limited time span of the project and the expected possible problems that could come with a monoblade propeller cancelled the investigation of the monoblade concept and the manufacturing continued with the bi-blade propeller design.

## B.4 Manufacturing

The manufacturing of the propeller is decided to be done in house, in composite laboratory of ISAE. Thinking about each landing phase of the tests flights and having no landing gear on the SPOC plane, the propeller was in danger of breaking while landing. In order to prevent this, the hub of the propeller is designed for a folding root, and finally a custom spinner is also build in the exact needs of SPOC plane. Figure B.3 shows the integration of the folding blade with the spinner.

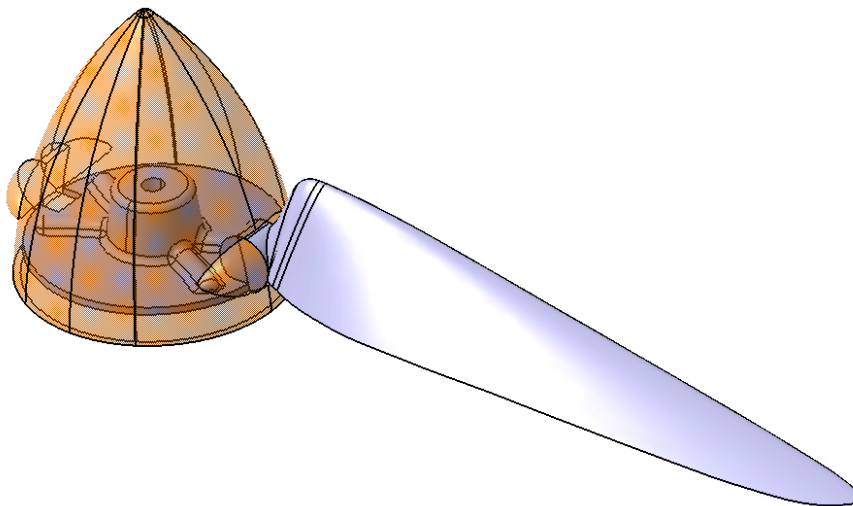


FIGURE B.3: Designed propeller and its spinner's CATIA drawing.

Moulds are designed in Catia V5 and manufactured with CNC milling machines in order to achieve the necessary precision. Each blade is build out of three piece of moulds, top, bottom and the folding axis pin. The spinner cone is build by using six pieces of moulds, two sides, two folding axe pins and two prop blade root inserts. Finally the base of the cone is build by using three moulds, top bottom

and the rotation axis pin. The spinner cone and the base moulds are designed to fit each other in order to maintain the base to the cone in the same rotation axis perfectly to prevent any possible balance problems. The main moulds are shown in figure B.4 without the inserts and the pins.

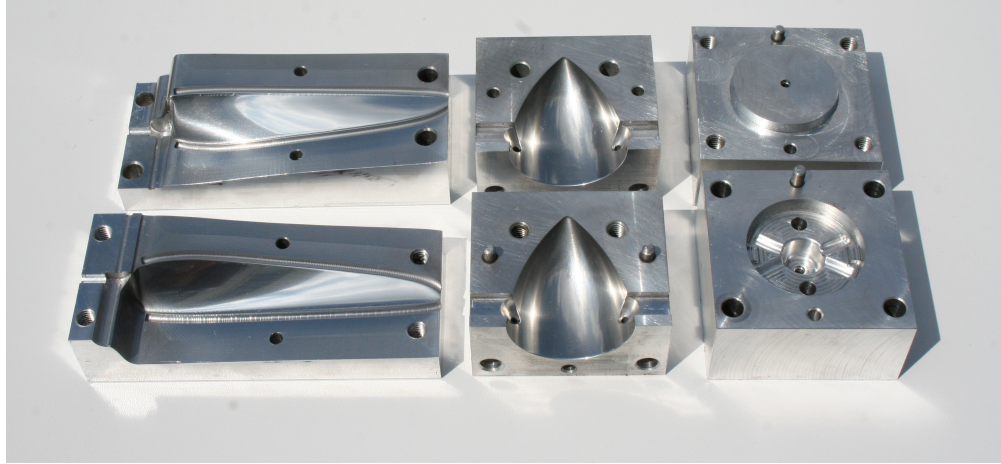


FIGURE B.4: CNC manufactured aluminium propeller and spinner moulds

The propeller was made of carbon fiber. The material was chosen because of its low weight and its high strength. The required pieces are first cut into shape as shown in figure B.5, then wet lay-up is done by hand into the moulds. Different orientations ( $45^\circ$  and  $90^\circ$ ) of carbon fiber woven were used on the skin for the torsional strength of the propeller. Additionally, unidirectional carbon fiber mesh were placed in order to sustain the bending forces of the blade. As the propeller blade has a specific airfoil, a certain amount of material should have filled the thickness. The exact required material quantity is found by trial and error as the weight of each blade was only 1.5 g. There was no need to use vacuum bagging process as the two mould halves completely fits onto each other.

The spinner cone is also build by wet lay-up by hand, in order to achieve a smooth surface and fix the layer on the skin of the cone, a balloon is inflated inside the cone. A silicon insert should have given better results but this method is used because of the time restrictions. The figure B.6 shows the resulting cone and its molds.

Finally after manufacturing two blades, spinner cone and the base, they are integrated into each other to form the custom designed propeller. The figure B.7

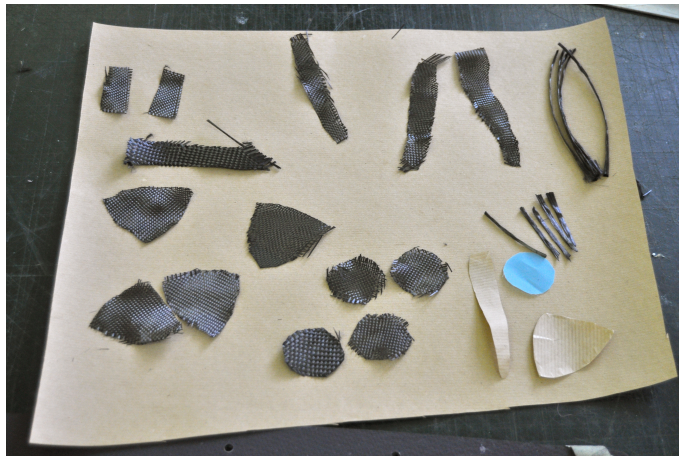


FIGURE B.5: Required carbon fiber pieces are cut into shape in prior to wet lay-up process.

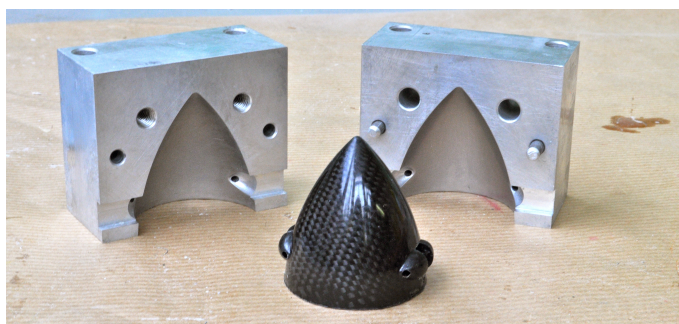


FIGURE B.6: The cone and its molds

shows the resulting propeller. The fixation of the spinner to the motor shaft is done internally. First the two blades should have removed and then the inner fixation screws that are placed on the spinner base plate can be reached. This method makes the fixation a little bit complex but once it is fixed there will not be any gap between the spinner and the nose of the plane or any protruding screws that can create additional drag.



FIGURE B.7: The resulting custom propeller

## B.5 Test Results

The propeller test bench which is shown in section 5.4.2 figure 5.15 is used for the tests. The main point of interest was to measure the performance at cruise conditions which are  $15\text{ m/s}$  of flight speed and  $1.3\text{ N}$  of thrust generation. Additionally, as expected from the theoretical calculations, the propeller has to have more than  $4\text{ N}$  of thrust at this flight speed at full throttle. Figures B.8 and B.9 show the global efficiency (speed controller + motor + propeller) and propeller efficiency alone versus thrust generated at  $15\text{ m/s}$  flight speed condition. It can be seen that the propeller efficiency is around 71% at cruise condition thrust, and the final global efficiency is around 50% which includes the speed controller, motor and the propeller. The maximum thrust measured at full throttle was  $4.25\text{ N}$  at  $15\text{ m/s}$  speed.

Expected global efficiency was 59.5% however, the measured efficiency was only 50%. The assumptions and the simplifications that is done in theoretical calculations will cause a difference between the real world and the calculations, but there are also several reasons that cause difference. First of all the theoretically assumed 59.5% efficiency does not take into account the speed controller, which usually have around 95% of maximum efficiency. Additionally, the designed spinner could not have used in the wind tunnel tests because of the additional pressure drag that it generates without having the real fuselage behind it. Instead of spinner, an aluminium piece is manufactured in order to hold the two folding propeller blades together in the wind tunnel, there is additional drag coming from this piece resulting with lower efficiency. Finally the manufactured airfoil shape and the propeller geometry could have differ from the designed and analysed one which results normally reduction on the expected efficiency as well.

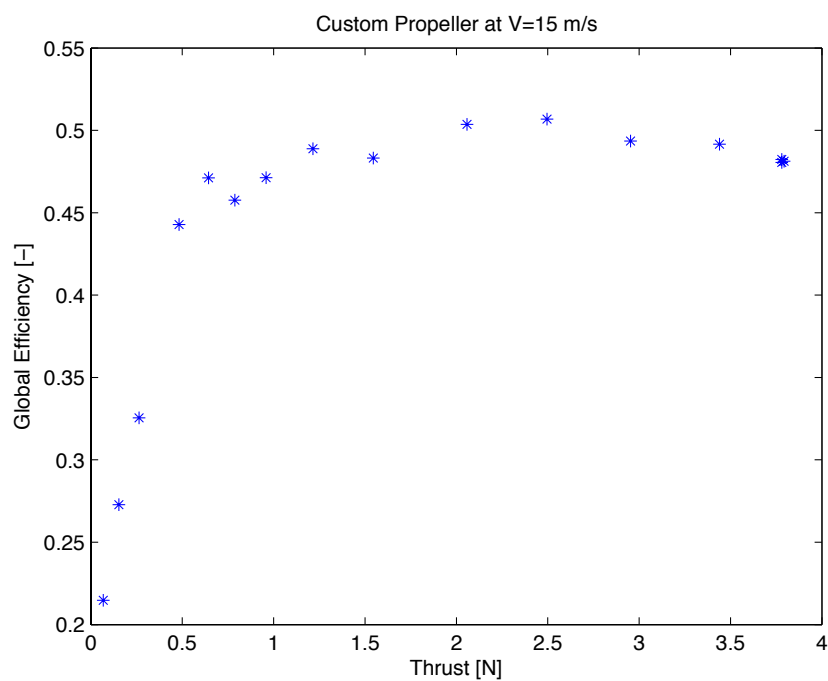


FIGURE B.8: The global efficiency versus Thrust [N] plot for the custom designed propeller at 15  $m/s$  speed.

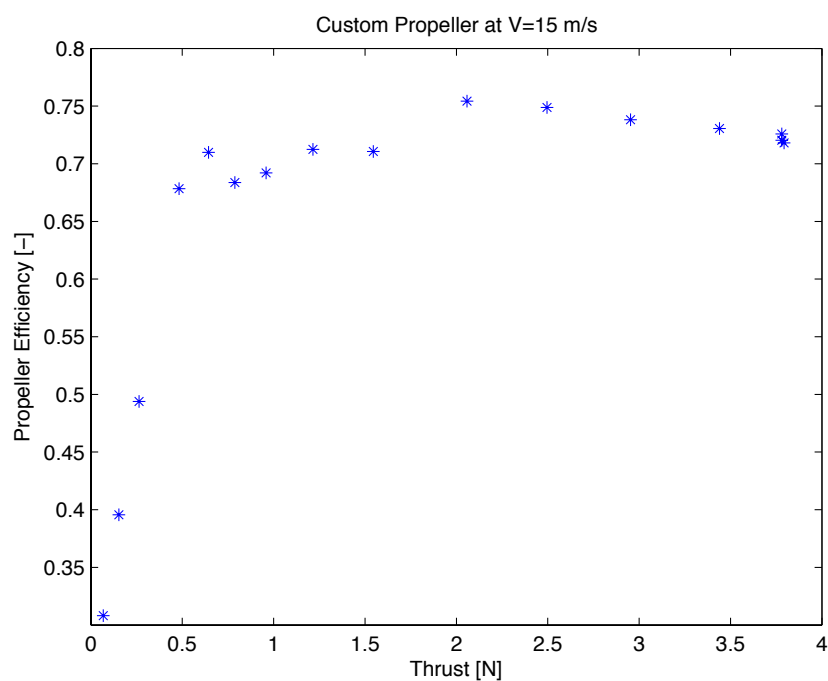


FIGURE B.9: The propeller efficiency versus Thrust [N] plot for the custom designed propeller at 15  $m/s$  speed.

# Appendix C

## Publications

# **Towards a Long Endurance MAV**

**Murat Bronz, Jean Marc Moschetta, Pascal Brisset, Michel Gorraz**

Reprinted from

## **International Journal of Micro Air Vehicles**

Volume 1 · Number 4 · December 2009



**Multi-Science Publishing**  
**ISSN 1756-8293**

# Towards a Long Endurance MAV

**Murat Bronz<sup>\*</sup>, Jean Marc Moschetta<sup>†</sup>, Pascal Brisset<sup>‡</sup>, Michel Gorraz<sup>§</sup>**

Institut Supérieur de l'Aéronautique et de l'Espace, University of Toulouse, France  
and Ecole Nationale de l'Aviation Civile, Toulouse, France

May 2009

## ABSTRACT

A conceptual design and performance analysis method (Long Endurance Conceptual Design Program) for long-endurance mini-micro UAVs is presented. Recent long endurance oriented results and achievements are looked through for possible usage for mini-micro scale. A real mission is also explained, whose objective is to accomplish a 200 km straight line flight autonomously with the smallest electric platform possible. Design phases of the platform by using the presented method, flight tests and comparison of the results are included. On the following section a design study for long-endurance MAVs using a hybrid energy system combining solar energy and Lithium batteries and the effect of size and cruise speed are investigated. We demonstrate that under a certain size, the use of solar energy becomes not useful at all. We conclude with the study of a candidate design for EMAV09 Endurance Mission in the light of the rules and scoring of the mission.

**Keywords:** Long Endurance, Solar Power, System Design and Optimization, Paparazzi Autopilot

## 1. INTRODUCTION

The number of the fields are increasing day by day which UAVs can take part in, but all of these fields have different and additional demands for their particular mission. These are pushing the limits of the UAVs to extremes by all means of disciplines such as structure, electronics, aerodynamics etc. Of course the operational costs are usually among the most important issues. By the help of miniaturization of the on-board electronics, it has become much more feasible to shrink the size of the UAVs which brings cost advantages and operational simplicity as well.

The biggest problem for small UAVs is the energy source which is not small enough to achieve the same endurance as the big ones. For sure, long endurance capability is needed and is a big advantage for any kind of mission. So we concentrate our effort on having a long-endurance mini-micro UAV.

This paper will present the initial approach for a Long-endurance mini-micro UAV conceptual design, by introducing the method and the Long Endurance Conceptual Design Program behind, some ideas for extracting energy which are planned for future work, candidate energy sources that are decided to be used, an example mission which was chosen for coefficient verification of the design program, and also the feasibility study of using the above techniques for MAV design. In the last part a candidate design for EMAV09 Endurance Mission will be studied with the rules and scoring in mind.

## 2. DESIGN STUDY FOR A LONG-ENDURANCE MINI-UAV

The Design process has several phases, like conceptual, preliminary and detailed design. Generally in the conceptual design phase of a UAV, a wide competitor-study according to the type of the mission can lead to quite close results for the geometrical specifications of the design, which will be frozen on the final design. However on a design like long-endurance mini-UAV, as the concept is novel, a competitor-study will either not be sufficient or not lead to an innovative design.

---

<sup>\*</sup>PhD Student, Murat.Bronz@isae.fr

<sup>†</sup>Professor in Aerodynamics, Jean-Marc.Moschetta@isae.fr

<sup>‡</sup>Lecturer in Computer Science, Pascal.Brisset@enac.fr

<sup>§</sup>Lecturer in Electronics, Michel.Gorraz@enac.fr

So the key points of the challenge for a long-endurance Mini-UAV have been investigated and a Long-Endurance Conceptual Design Program (LECDP) has been developed and is presented briefly below.

## 2.1. Energy Sources

At the scale of Mini and Micro UAVs, energy storage systems become even more problematic than the bigger UAVs since it can reach 40% of the total weight. Thus, a wide research of current state of the art for energy sources has been completed. The paper contains a brief survey of this research.

Battery technology keeps improving rapidly because of the huge demand of portable computers, cell phones and Radio Control models. Currently Lithium-Polymer batteries are the most dominant ones in the market. They have a specific energy of 150 to 200  $Wh/kg$ . After scanning the whole envelope for suitable battery technology (Table 1), Lithium-Polymer and Lithium-Sulfur<sup>1</sup> batteries were selected as the two candidates for the calculations.

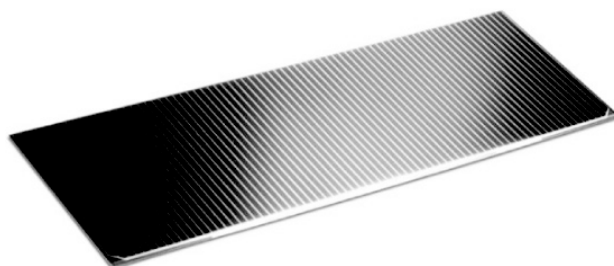
Most recent long-endurance world records for small UAVs, that are just using the energy stored on board, are broken with Fuel-cells[1, 2]. Fuel-cells have high specific energy around 1000  $Wh/kg$  which is a great advantage. However their minimum initial system weight is around 1.9  $kg^2$ . Although this system has sufficient energy for 10 hours of flight for a UAV that has 2.5  $m$  wing span<sup>3</sup>, it doesn't seem to be feasible to realise a long-endurance UAV smaller than 2  $m$  wing span utilising fuel-cells at this stage because of the total system weight. As we are dealing with a Mini-UAV whose maximum dimensions do not exceed 1 meter, we are obliged to wait and watch the new technology progress.

Benefiting from solar energy became very popular in the sense of green energy and also became feasible for small UAV activities since the solar-cell technology improved a lot. Recent Silicon solar cells are thin, flexible and very light while still having a reasonably good efficiency. These properties make them well suited for the small UAV activities. After a market search we obtained S-32 Silicon cells (Figure 1) which are the state of the art high efficiency, low weight silicon cells with an integrated by-pass diode (AzurSpace solar Power GMBH<sup>4</sup>).

There are several examples of applications about utilising solar energy in UAVs [3, 4] but recently the most remarkable one and the most closest one to Mini-UAV scale is for sure the SkySailor<sup>5</sup> [5] which has accomplished a 27 hours continuous flight. Although Noth et al.[5] resulted on 3.2  $m$  wing span for continuous flight (between certain place and time of the year), they also showed the feasibility of a solar powered Mini-UAV which has 0.77  $m$  wing span [6].

Table 1. Battery specifications from different sources. Numbers for Li-Po have been measured while the numbers for Li-S come from the manufacturer.

	Ni-Cd	Ni-Mh	Li-Po	Li-S
Specific Energy ( $Wh/kg$ )	40	80	180	350
Energy Density ( $Wh/l$ )	100	300	300	350
Specific Power ( $W/kg$ )	300	900	2800	600



Size (mm)	32 × 74
Weight (g)	0.757
Open circuit V (mV)	628
Open circuit I (mA/cm <sup>2</sup> )	45.8
Voltage @ Pmax (mV)	528
Current @ Pmax (mA/cm <sup>2</sup> )	43.4
Avg. Efficiency (%)	16.9

**Figure 1.** Azur Space S-32 solar cell and its specifications.

<sup>1</sup>www.sionpower.com

<sup>2</sup>www.protonex.com

<sup>3</sup>www.ns.umich.edu/htdocs/releases/story.php?id=6833

<sup>4</sup>www.azurspace.com

<sup>5</sup>sky-sailor.epfl.ch

## 2.2. Extracting Energy from Environment

On-board energy storage is always limited and additional capacity always brings additional weight. That's why calculations end up with an optimum total weight that corresponds to a certain storage capacity. This limits the energy that we can carry on-board. However extracting energy from the environment not always needs an additional system weight and can be continuous for some cases which will certainly make a huge improvement in endurance performance of the UAVs [7].

A good example for extracting energy from the environment is achieved by D.J. Edwards [8]. By actively searching out and having advantage of thermals, naturally occurring convective air updrafts, and using the initial potential energy from a 140 m launch, their autonomous SBXC glider achieved 48 km of distance while staying aloft 1.5 hour.

The challenge is to design a UAV that is optimised for extracting energy from the environment, utilising different energy sources if there is more than one and being capable of managing the required mission at the same time.

This part will not take place in the design method for now since there is already a lot of challenges with utilising the energy systems alone, but planned to be explored in the following months.

## 2.3. Long Endurance Conceptual Design Program "LECDP"

The objective of LECDP is to be able to see the variation of performance values such as endurance and range for different kinds of designs, and it also aims to fix the performance values and search for a feasible geometry for conceptual design. The most important philosophy behind LECDP is to keep it as simple as possible and still be very flexible to change and adapt it for the new technological improvements. So a simple block structure in Scilab<sup>6</sup> is used for writing the program. Figure 2 simply shows the main blocks that are working together in the program.

The program runs with the identified design variables such as wing geometry, mission requirements, cruise velocity etc. All of the assumptions made in the early design are included in the input such as propeller, motor, speed controller and battery efficiencies, parasite drag coefficient for fuselage, battery and motor weight constants to find the corresponding weight for a given voltage and power. First estimation of battery weight and capacity is made in the **Battery Weight Estimation Block**.

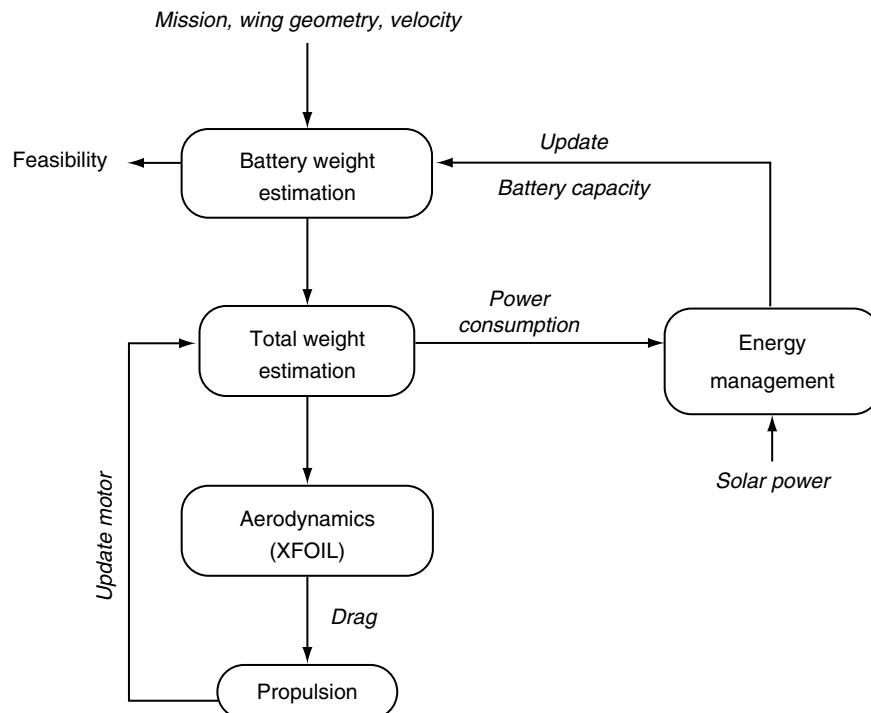


**Figure 2.** Brief Flow-Chart of the LECDP.

<sup>6</sup>www.scilab.org

All of the mass values are generated and summed in the **Total Weight Estimation** Block. Then iteration starts with updating the **Aerodynamics** Block with the new total weight, here the required lift coefficient is calculated by using the first given design variables. Traditional formulas are used to find the infinite 2-D airfoil lift coefficient then in order to have a better estimation of the drag, an external program **XFOIL**<sup>7</sup> is called[9]. This is much more convenient than having a constant value for skin friction and pressure drag coefficient of an airfoil since XFOIL also takes into account Reynolds variations, and also gives permission to change the airfoil used in the design program. After calculating the total drag of the plane, the **Propulsion** Block updates the motor weight in the **Total Weight Estimation** Block taking into account the required thrust and power until a fixed point is reached and then power consumption is calculated.

The **Energy Management** Block is responsible for utilising the existing energy source, and combining them together for an hybrid use or charging process. The **Solar Power** Block uses a sinusoidal model of the Sun Irradiation and calculates the power output and weight of the solar cells to be updated in **Energy Management** and **Total Weight Estimation** Blocks.

If a performance value is fixed, like the one which is going to be described in Section 2, then the **Battery Weight Estimation** Block will keep changing the capacity and updating the weight till the target value is reached if it is feasible otherwise program moves to the next input values.

The explained Block architecture allows the user to change the Blocks independently if needed. Of course coefficients and constants used in the early design are really important, since they can affect the performance dramatically. So as to verify the coefficients, the focus is on both theoretical and experimental studies.

## 2.4. Paparazzi Autopilot

There are several world records and record attempts in F5S FAI class<sup>8</sup> on which the pilots are in the loop all the time and flying the aircraft manually around 12 hours<sup>9</sup>. One of the main objective of this study is to have the aircraft flying autonomously without requiring a human pilot for stabilisation and navigation.

Paparazzi is an open-source autopilot system oriented toward inexpensive autonomous aircraft of all types. The project began in 2003 and has enjoyed constant growth and evolution ever since. The system has been used on dozens of airframes and implemented by several teams around the world. Hundreds of hours of autonomous flight have been successfully achieved with the Paparazzi system.

The Paparazzi system (Figure 3) is extensively described in [10, 11] and cooperatively documented in a the [paparazzi.enac.fr](http://paparazzi.enac.fr/wiki) wiki.

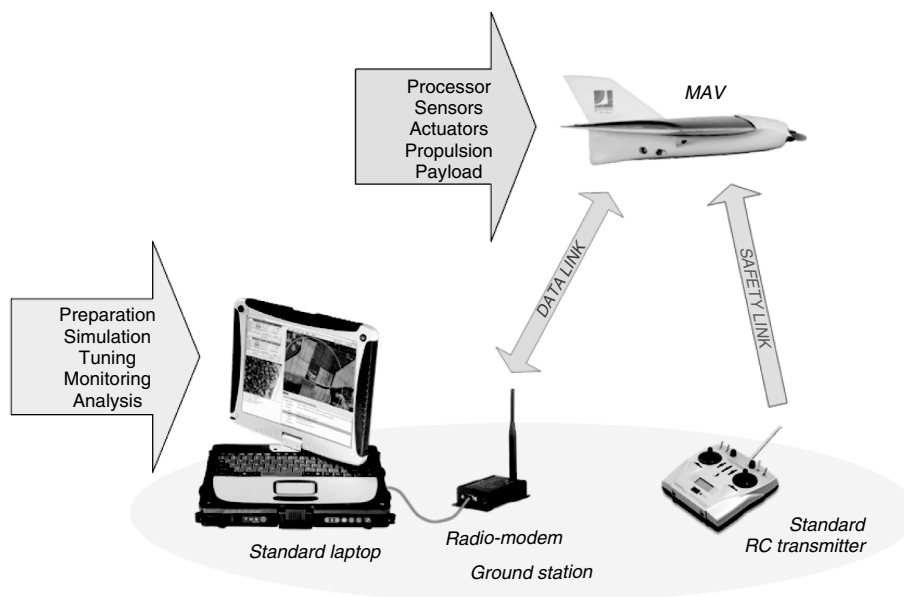


**Figure 3.** The Paparazzi system includes the airborne autopilot and the GCS.

<sup>7</sup>[raphael.mit.edu/xfoil/](http://raphael.mit.edu/xfoil/)

<sup>8</sup>[www.fai.org](http://www.fai.org)

<sup>9</sup>Oklahoma State University DragonFly Project, [osu.okstate.edu](http://osu.okstate.edu)

There are of course several pros and cons of using an autopilot versus a human pilot. A human pilot has hidden expertise, can examine the environment efficiently and take advantage of it immediately (like topology-wind interaction for slope flight, thermalling birds, dust devils).

However having an autopilot on-board ensures the ability to fly out of sight, and a much better stability of the aircraft even in a perturbed environment by the help of the on-board sensors. It is also able to control and fly at the exact attitude which is needed most of the time in order to get the best flight performance of the aircraft and to keep better track of the navigation for an efficient surveillance mission. The most important advantage is to control the propulsion system much more efficiently for a longer energy run. Having Paparazzi Autopilot on-board will sustain these benefits to achieve long-endurance flights with a mini-UAV.

### 3. CORSICA MISSION

#### 3.1. Mission Description

The Corsica Mission was just an idea that came out of a brainstorming session at first and later was started by two groups of students from ISAE ([www.isae.fr](http://www.isae.fr)) and ENAC ([www.enac.fr](http://www.enac.fr)) also with the contributions of the two Institute's advisors. It was a short term project that was to be fulfilled in 9 months. The main objective of the project is to design and build the smallest possible electric powered UAV that will have a capability to survey a 200 *km* line autonomously. To prove the feasibility of the project, the mission was chosen to be performed over the Mediterranean Sea across Nice and Calvi (Corsica), which also brings the originality of the project (Figure 4).

#### 3.2. Relevance of the Mission with Long Endurance

Although the project is not totally concentrated on the Long-Endurance objective, still 200 *km* of range requires a long-endurance capability for such a small electric UAV. So the project is a good candidate for the LECDP to be tested. Additionally, the flight test results gave us the opportunity to compare and verify the initial coefficients which have been chosen in the beginning.

#### 3.3. Prototype Design and Manufacture

As we have been trying to push the limits to extremes, we couldn't select the regular values for any of our coefficients and constraints such as wingloading, power to weight ratio, emptyweight fraction, etc.

In order to verify our first assumptions and coefficients we decided to build a prototype rapidly. First of all, we were in search for a suitable and meaningful cruise speed for the mission. As it is a kind of surveillance mission, it is decided that the cruise speed should not go higher than a certain value. The lower boundary of the speed envelope has no limitation because the stall speed of the designed aircraft will already limit it. After several analysis with LECDP, 20 *m/s* cruise speed was chosen to be appropriate for the mission taking into account for both the energy consumption not to be too high and the mission time not to be too long to be risky for the effect of cross-wind. The required battery capacity values for a span variation from 1 *m* to 1.8 *m* for 20 *m/s* cruise speed is presented in Figure 5. Here it can be seen that for an UAV with 1.8 *m* span and 0.2 *m*<sup>2</sup> wing area, 19 *Ah* of battery capacity (at 14.8 *V*) is needed

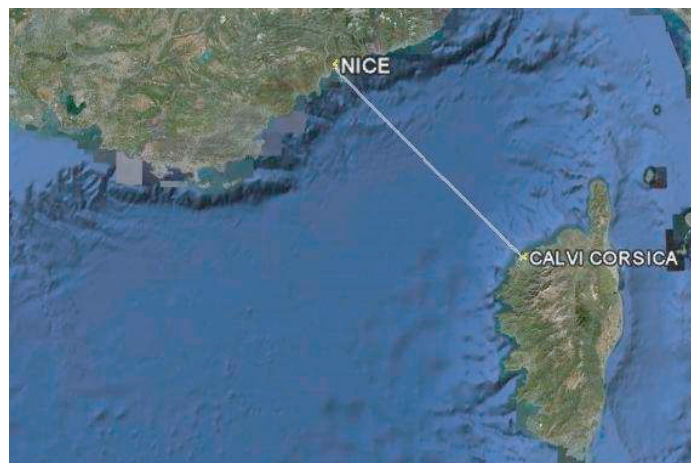


**Figure 4.** Planned Corsica mission flight path (200 *km*).

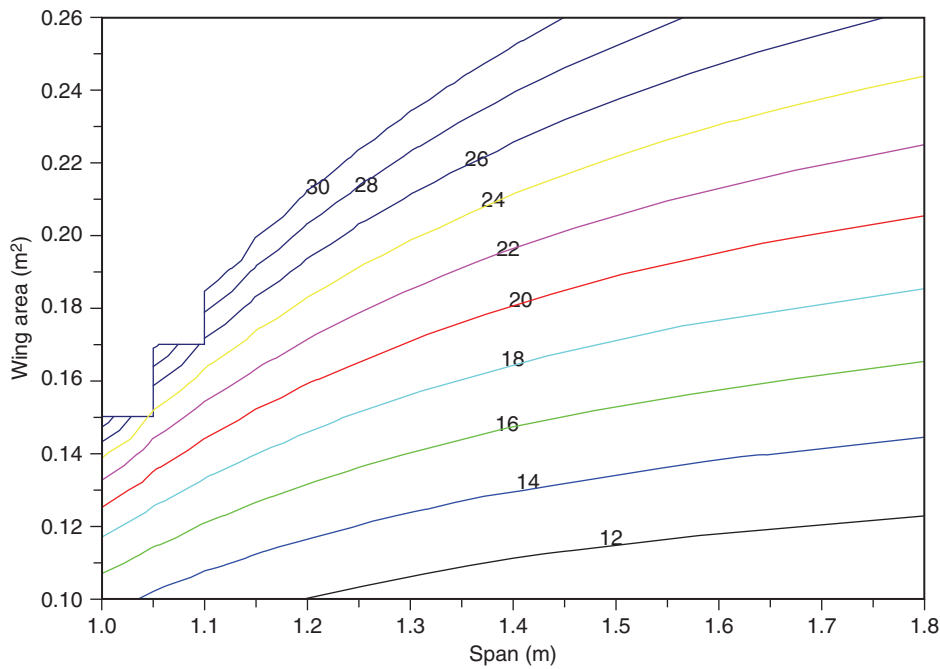


**Figure 5.** Required battery capacity in Ah for 20 m/s cruise speed (14.8 V, 200 km).

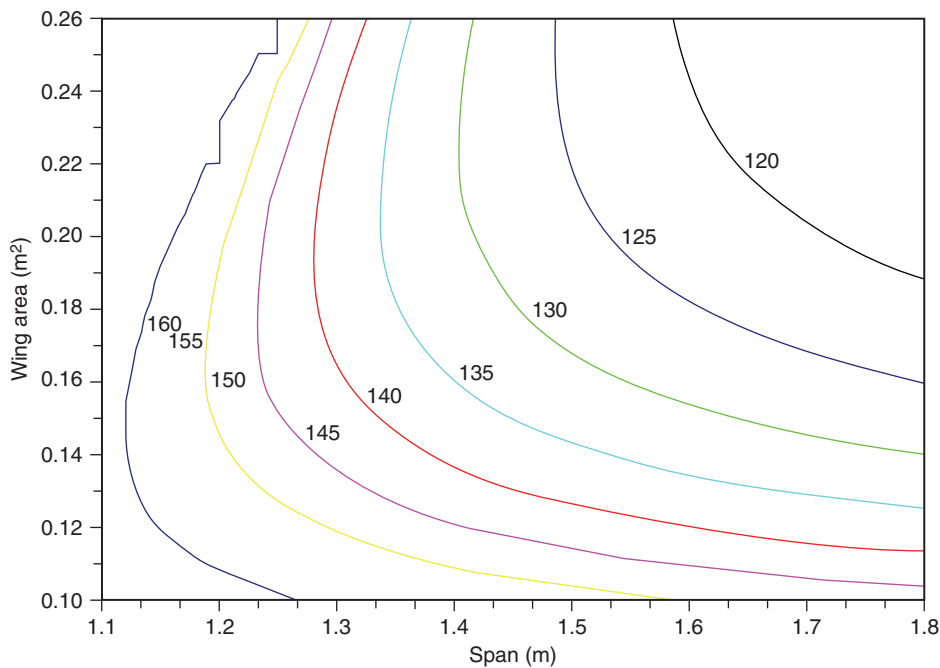


**Figure 6.** Wing-loading ( $N/m^2$ ) at 20 m/s cruise speed for a 200 km mission.

to cover 200 km of straight line where as for a 1.2 m span and the same wing area of 0.2  $m^2$  the required battery capacity becomes 28 Ah.

After the choice of cruise speed, LECDP analyses were examined again to see the variation of wing-loading and total weight for different wing spans and areas (Figure 6 and 7). As the objective is to be as small as possible, it is favourable to stay in the lower left end of the graphs but, as it is seen in Figure 6, the wing-loading value is getting too high compared to an radio-controlled electric model's wing-loading which is around 20 – 60  $N/m^2$ . Also as LECDP does not take construction and component

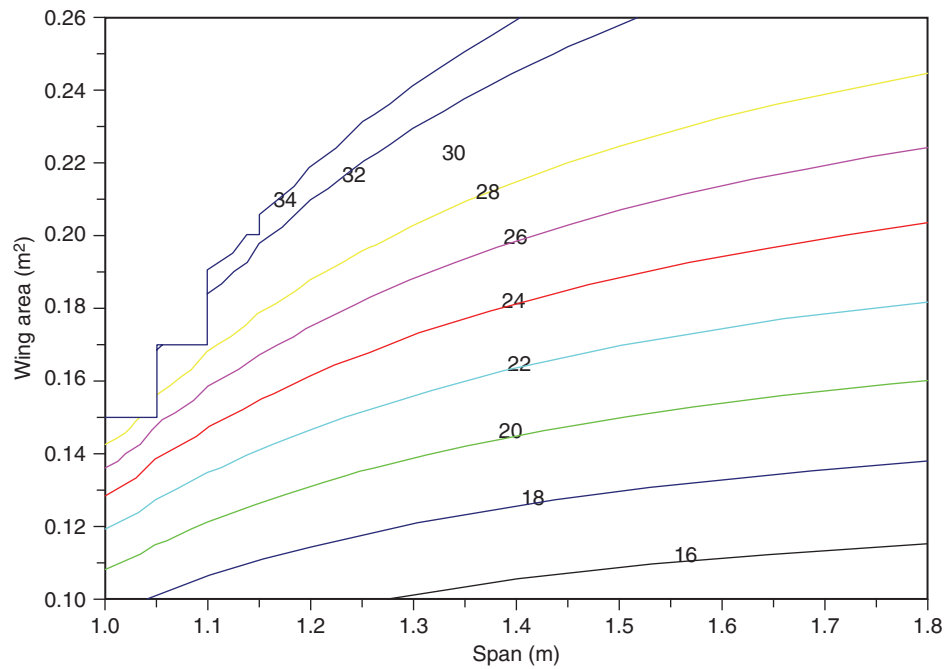


**Figure 7.** Total weight ( $N$ ) at 20  $m/s$  cruise speed for a 200  $km$  mission.

Table 2. Chosen values for the 200  $km$  mission prototype from the LECDP results.

Required Total Power	( $W$ )	126.44
Battery Capacity	( $Ah$ )	25.94
Structural Weight	( $N$ )	5.35
Total Weight	( $N$ )	29.45
Wing-Loading	( $N/m^2$ )	124.28
Lift Coefficient		0.5072
Span	( $m$ )	1.5
Chord	( $m$ )	0.158
Drag	( $N$ )	2.36

storage problems into account, a final decision of the human expert is needed. As an example, the batteries are decided to be placed all in the wing, which creates a constraint between the volume of the total batteries and the volume of the wing. And as the battery volumes are fixed with the shape, after some market search and analyses, chord of the wing is fixed according to the selected battery type. This makes it possible to represent the wing span by the number of batteries inside or by the capacity as well. While keeping the wing-loading in a safe region and optimising the wing span, corresponding battery capacity for 1.5  $m$  wing span ended with a little bit less than needed, but the difference was small enough to compensate it with a small battery pack in the fuselage.

The fuselage is constructed from aramid besides the small reinforcement parts around motor and wing mount which are made of carbon fiber. The wings are precisely cut by a CNC foam cutter machine in Composite Laboratory of ISAE and covered with aramid and carbon fiber. As the first prototype is designed for coefficient verification and proof of concept, it doesn't have the originally selected batteries (KOKAM 7.5  $Ah$ ) instead it has three housings for inserting steel rods to simulate the battery weight and inertia in the wing. This also allows us to progressively increase the weight of the Prototype to measure its flying characteristics and also power consumption for different weights.

### 3.4. Propulsion and Flight Tests

The prototype's wing design permits the testing of different weights. First to measure the flight characteristics of the plane, only carbon rods are inserted for joining the two wing-halves and as a result the first flights were made for only 1kg of total mass. At this weight, it was satisfactory enough to

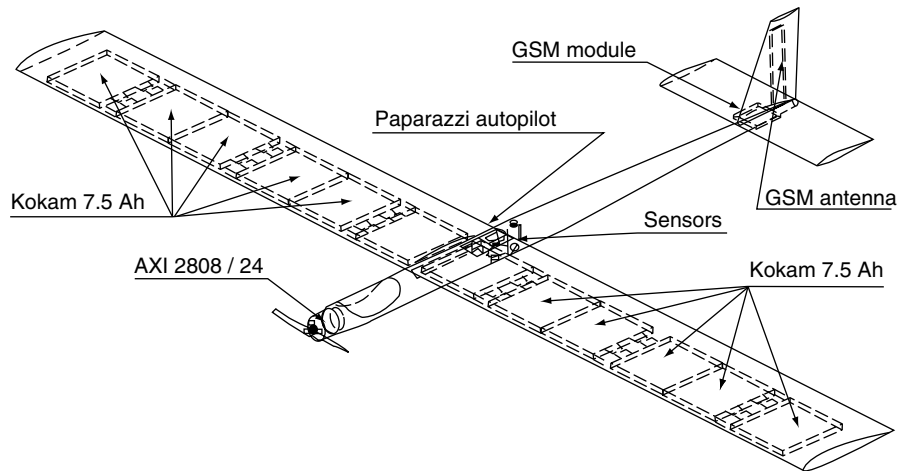


**Figure 8.** Sketch of the prototype for the 200 *km* mission.



**Figure 9.** The 200 *km* mission prototype ready for its first flight.

hand-launch the plane. After tuning the manual and autopilot settings, steel rods were inserted for progressively increasing the weight up to expected flying weight.

In order to obtain aerodynamic and propulsion efficiencies from the flight tests, two methods were planned. The first was to climb to a safe altitude, glide along a straight line without throttle at a certain velocity to obtain the lift to drag ratio of the whole plane [12, 13]. Lacking of a differential pressure sensor for speed measurements and just relying on GPS information for speed and altitude, environmental effects such as thermals and sinks, made it not possible to have satisfactory results in short term glide tests. So a long term test was decided upon, in which values were averaged in order to give better values. In Figure 11, which is the view of the flight test trajectories exported to Google Earth, fixed altitude circle and oval type flights can be seen. On those flights, altitude and cruise speed were kept as constant as possible and circles were flown for 160 seconds autonomously. The power consumption was also recorded. After averaging, it is seen that the cruise speed is 18.6 *m/s* instead of 20 *m/s*, which also affects the predicted design power consumption. Table 3 shows the previously designed values, the values obtained from flight tests and the updated values as the cruise speed



**Figure 10.** Surface quality and holes for steel rods simulating battery weight and inertia.

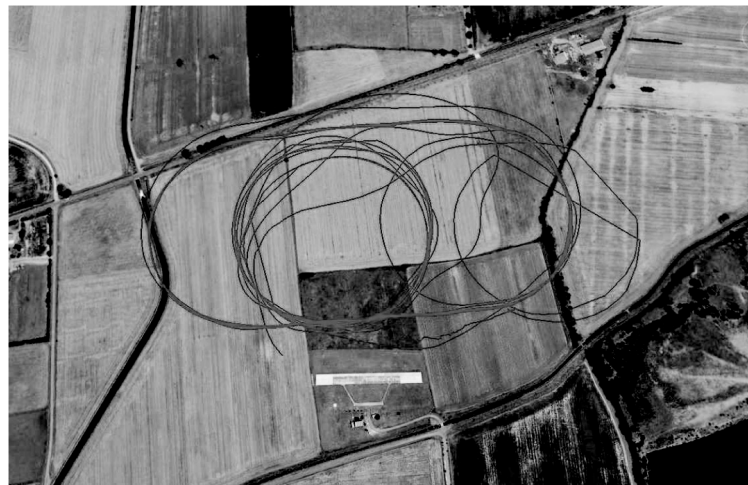


**Figure 11.** First autonomous flight test of the 200 *km* mission prototype.

Table 3. Variation of Designed, Tested and Updated values.

		Designed	Flight	Updated
Total Power	( <i>W</i> )	126.44	63.5	100.8
Cruise Speed	( <i>m/s</i> )	20	18.6	18.6

changed between the designed conditions and the flight conditions. It can be easily seen that the first coefficient assumptions were overly pessimistic.

After modifying the coefficients according to the obtained results from flight tests, it was obvious that the size of the plane can be decreased a little bit, but unfortunately the selected batteries can only allow a major difference as the pack sizes are fixed. However another option could be to change the battery type and brand but as it is a short term project, there was not enough time to do that.

#### 4. STUDY FOR A HYBRID SOLAR POWERED MAV

Although having verified the coefficients with the flight test of the prototype, the results that were obtained from LECDP for MAVs were not consistent. So we used previous flight data acquired from Slicer and Storm-1<sup>10</sup> and wind-tunnel results to recalibrate some of the coefficients in the LECDP for MAV scale. After this tuning, analyses were done for the hybrid system with the solar energy and Li-Po battery taken into account. The objective was to see the feasibility of using solar energy for MAVs to enhance the flight time.

Two different configuration were taken into account, 500 *mm* and 300 *mm* span. For each of the configurations, wing area and endurance have been optimised using LECDP for a given battery capacity on board (910 *mAh*).

<sup>10</sup>Previous MAVs that were designed and flew in competitions by our team

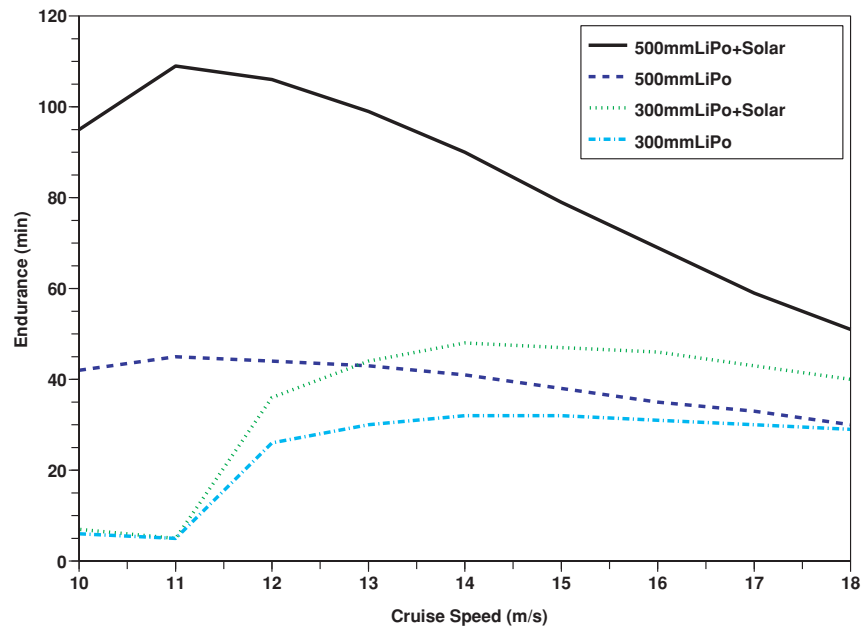


**Figure 12.** Endurance comparison of 500 mm and 300 mm MAVs using solar cells.

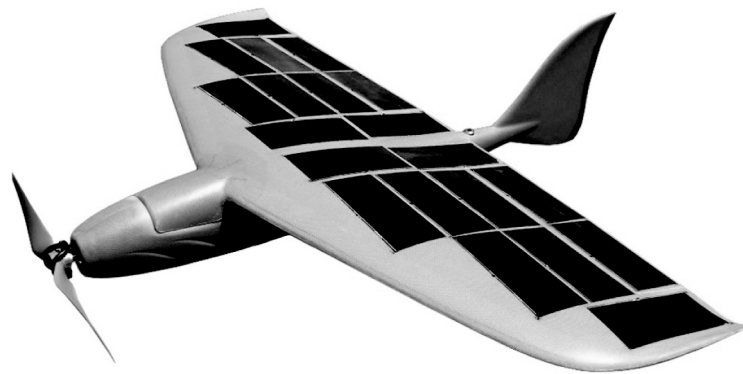


**Figure 13.** The 500 mm Solar-Storm prototype covered with 20 S-32 solar tiles.

In the analyses, the maximum sun irradiance is taken as  $900 \text{ W/m}^2$  and 70% of the wing is assumed to be covered with solar cells. The efficiency of the solar cells, 16.9%, is taken as it is given in the data sheet of the manufacturer.

Figure 12 shows the flight time versus the cruise speed of two different configurations with and without solar cells. Both have the same battery capacity on board. It can be seen that the benefit that is taken from solar cells for flight time is much higher for the bigger 500 mm MAV than the small 300 mm one. It can be shown that under a certain size, there is almost no benefit that can be taken from the solar cells. This is a result of the reduced wing surface area of the small sized MAV reducing the total solar cell area which is linearly proportional with energy extracted from the sun. Another important issue is the weight ratio of the solar cells and the required electronics to the weight of the MAV. This ratio is becoming larger when the MAV gets smaller in size, reducing the overall efficiency of the MAV. It should be noted that these conclusions are made taking into account the Paparazzi autopilot and electronics weights.

Figure 13 shows the hybrid solar powered MAV prototype. Twenty RWE Si-32 solar cells are bonded on the wing with silicon based glue<sup>11</sup>. The wing platform is optimised in order to place the

<sup>11</sup>With the collaboration of the [www.map-coatings.com/company](http://www.map-coatings.com/company)

maximum number of solar cells safely on the surface while keeping in mind the span efficiency, elliptical loading and the tip stall issues. This was especially important in order to reach the same percentage of solar cell area to wing area that we have assumed in the calculations.

The powerful XFOIL airfoil analysis and design program is used to design the airfoils. There are three different custom airfoils along the span, which are particularly designed according to their corresponding Reynolds number for the cruise speed while observing the stall behaviour and maximum lift coefficient. Spanwise transition and the design procedure will not be included here more deeply as it is not in the scope of this paper.

#### 4.1. Maximum Power Point Tracker

Although we have kept the efficiency of the solar cells constant and at maximum value (16.9%) in the calculations, this is not exactly true for all cases in real life. According to the angle of the solar cells with the sun rays, time of the day and year, geographic location, solar cells will have different output power.

When the pads of the solar cells are not connected, the voltage between the pads is  $V_{OC}$  the open circuit voltage and the current is null. When the pads are short circuited, the voltage becomes zero and the current is  $I_{SC}$ , the *short circuit current*. The maximum output power has to be found between these two points. This point is called maximum power point (*MPP*) and the voltage and the current at this particular point are  $V_{MPP}$  and  $I_{MPP}$ .

The search for the *MPP* requires an ad hoc electronics circuitry adapted in real time with a control loop. Figure 14 shows the schematics of this board. Note that it includes a micro-controller which can be linked to the autopilot to be monitored from the ground station.

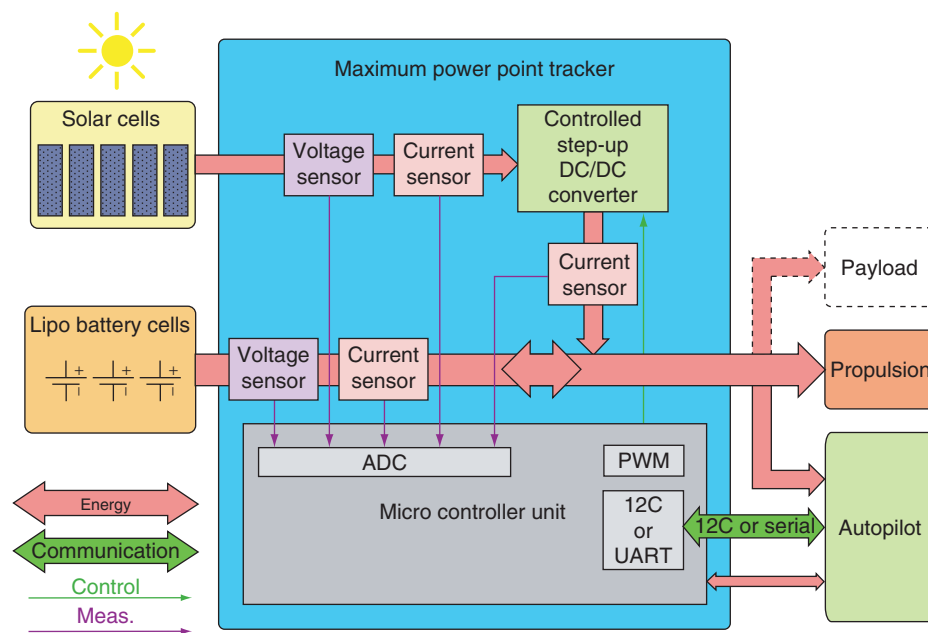


**Figure 14.** Maximum Power Point Tracker (MPPT) to optimize solar cells usage.

#### 4.2. Initial Flight Test Results

The second flight test with the Solar-Storm has resulted with an endurance of 90 minutes. Figure 15 displays the power management for a five minutes part of the flight. The variation of solar voltage can be seen between 7 V and 11 V due to clouds shadows.

The sinusoidal behaviour of the obtained solar power can be easily seen. This is due to the circular flight path: As the plane banks to the direction of where the solar rays comes, the solar power increases and when it banks to the other direction, the solar power decreases. As an average, 40% of the total power is obtained from the solar cells during the flight.

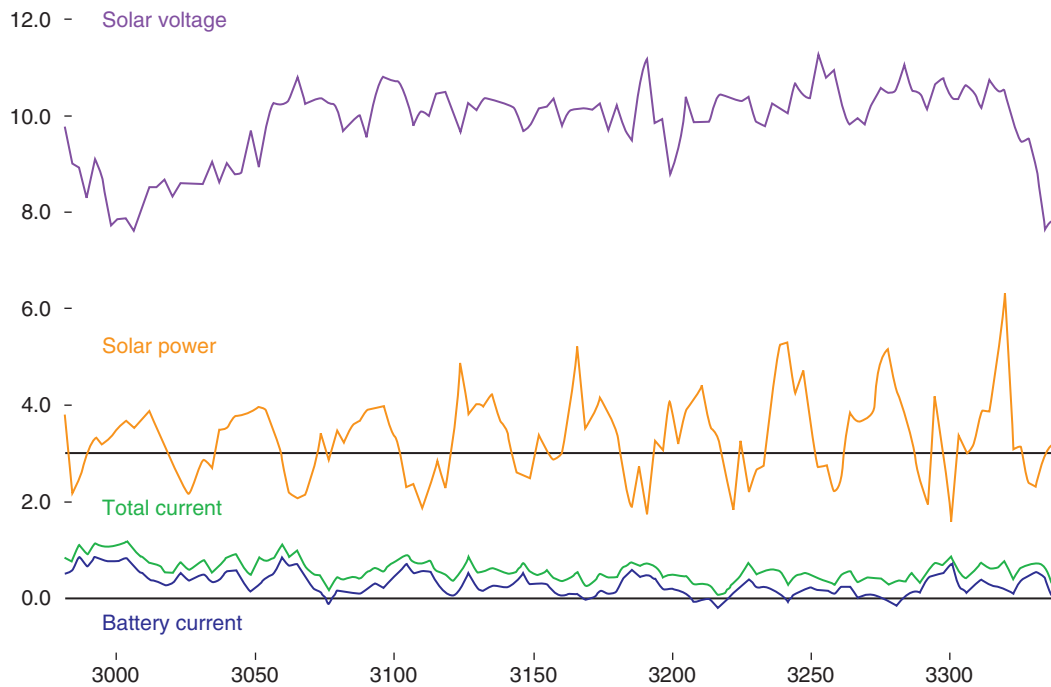


**Figure 15.** Solar Voltage (Volt), Solar Power (W), Total (solar+battery) and Battery Current (A) during 300s of flight. When the battery current is non positive, the battery is charged.

Attention should be pointed to the short periods where the Battery Current goes below zero, meaning that the on board battery is charged, an unexpected great achievement for such a small sized solar MAV.

## 5. CANDIDATE DESIGN FOR EMAV09 ENDURANCE MISSION

### 5.1. Mission Definition

The EMAV09 Outdoor Endurance Mission simulates a payload drop task where the target is far away from the launch zone. The distance between the launch zone and the target is simulated by flying a number of laps to the target, dropping a paintball on the target and then returning by flying the same number of laps before landing.

Although it has been shown in the previous sections results that a 300 mm MAV will not be able to achieve flight times as long as a 500 mm MAV does, still the rules of EMAV09 Endurance Mission promote being small by taking into account maximum dimension at the flight score calculation.

However, the mission is more focused on the range performance rather than the maximum airborne time. So, it is more important to fly at the “maximum lift to drag ratio speed” of the MAV rather than the “minimum power consumption speed” in order to get more points.

### 5.2. Computation Results

We have compared three candidates for the mission: the 300 mm Slicer, the solar powered 500 mm Solar-Storm and the 500 mm Fire-Storm. The Fire-Storm (Figure 16) has the same airframe as the Solar-Storm and is filled with as much battery capacity as possible. In order to stay in the optimum point of the designed airfoils while keeping an operable flight speed, it is powered with two 1320 mAh batteries (3 cells).

We compare here the expected scores for the three aircraft for different wind speeds. We make the hypothesis that, flying ovals, the average ground speed is  $(V^2 - W^2)/V$  where  $V$  is the airspeed and  $W$  the wind speed. The oval lap length is estimated to 1150 m.

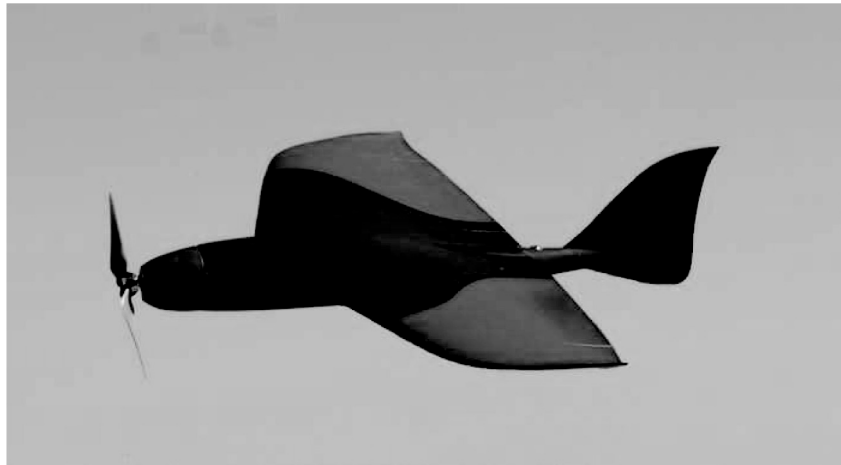


**Figure 16.** The 500 mm Fire-Storm designed for the EMAV09 Endurance mission.

Table 4 gives the number of laps and the corresponding expected score (autonomy set to 9, size  $S$  in mm, endurance  $T$  in mn):

Table 4. Scoring and lap numbers for the EMAV09 endurance mission for different wind speeds (0, 5 and 10 m/s).

	$S$ (mm)	$V$ (m/s)	$T$ (min)	$W = 0$	$W = 5$	$W = 10$
Slicer	300	12	35	22/388	18/317	6/105
Solar-Storm	500	12	145	<b>90/910</b>	<b>74/666</b>	26/234
Fire-Storm	500	16	90	74/666	68/612	<b>46/414</b>

The hypothesis for the Solar-Storm are highly optimistic: optimum hour in the day and sun irradiance about  $900 \text{ W/m}^2$ , something which probably never happen in Holland in September. So from these numbers and expected weather, the Fire-Storm seems more favourable.

## CONCLUSION

The so called LECDP (Long Endurance Conceptual Design Program) has been presented with the methodology behind it. A real mission has been described and design phase of the prototype for the mission is presented. Also the comparison of the calculated power consumption and the power consumption obtained from flight tests has been done. The results obtained from those comparisons are used for coefficient verification and calibration. Similar procedure is followed to calibrate the coefficients for MAV scale. Obtained results have been shown for possible long endurance MAVs utilising a hybrid solar energy and Lithium batteries. It is seen that there is a minimum size limit for the MAV to be able to use solar energy and below that limit it is no use to have solar cells and the required electronics on board for enhancing the flight time. In the last section, an initial study has been made to achieve a high score for the EMAV09 Outdoor Endurance mission. Future work will include updating the LECDP in the light of all obtained results, and implementing a more precise modelling of the aircraft.

## ACKNOWLEDGEMENTS

The present research has been partially supported by ENAC and ISAE under the aegis of the University of Toulouse. The authors would like to express their gratitude to Guy Mirabel and Xavier Foulquier from the composite laboratory of ISAE for their help to the fabrication of prototypes, M. Etienne Rapp from CNES for his advice regarding solar cell technology, M. Olivier Guillaumon and M. Yann Ollivier from the MAP coatings company for their helpful advice on solar cells bonding.

## REFERENCES

- [1] Thomas H. Bradley, Blake A. Moffitt, Dimitri N. Mavris, and David E. Parekh. Development and experimental characterization of a fuel cell powered aircraft. *Journal of Power Sources*, 2007.
- [2] Thomas H. Bradley, Blake A. Moffitt, Thomas F. Fuller, Dimitri Mavris, and David E. Parekh. Design studies for hydrogen fuel cell powered unmanned aerial vehicles. In *American Institute of Aeronautics and Astronautics*, Honolulu, Hawaii, August 2008.
- [3] Alan Cocconi. Solong UAV : Solar electric powered. Technical report, AC Propulsion, CA, 2005.
- [4] André Noth. History of solar flight. Technical report, Autonomous Systems Lab, Zürich, 2008.
- [5] A. Noth. *Design of Solar Powered Airplanes for Continuous Flight*. PhD thesis, ETH ZÜRICH, 2008.
- [6] N. Diepeveen. The sun surfer: Design and construction of a solar powered MAV. Master's thesis, Autonomous Systems Lab, ETHZ, Zürich, March 2007.
- [7] Ying Celia Qi and Yiyuan J. Zhao. Energy-efficient trajectories of unmanned aerial vehicles flying through thermals. *Journal of Aerospace Engineering*, April 2005.
- [8] D. J. Edwards. Implementation details and flight test results of an autonomous soaring controller. In *American Institute of Aeronautics and Astronautics*, 2008.
- [9] Harold Youngren Mark Drela. *XFOIL 6.94 User Guide*. MIT Aero and Astro, 2001.
- [10] P. Brisset and A. Drouin. PaparaDzIY: do-it-yourself UAV. In *Journées Micro Drones*, Toulouse, France, September 2004.
- [11] P. Brisset, A. Drouin, M. Gorraz, P.-S. Huard, and J. Tyler. The Paparazzi solution. In *MAV2006*, Sandestin, Florida, November 2006.
- [12] Helmut Reichman. *Cross-Country Soaring*. Soaring Society of America, Inc., 2005.
- [13] Dan Edwards. Performance testing of RNR's SBXC using a piccolo autopilot. Technical report, North Carolina State University, 2008.



# Towards a Long Endurance MAV

Murat Bronz\*, Jean Marc Moschetta†, Pascal Brisset‡, Michel Gorraz§  
Institut Supérieur de l'Aéronautique et de l'Espace, Toulouse, France  
and  
Ecole Nationale de l'Aviation Civile, Toulouse, France

## ABSTRACT

A conceptual design and performance analysis method (Long Endurance Conceptual Design Program) for long-endurance mini-micro UAVs is presented. Recent long endurance oriented results and achievements are looked through for possible usage for mini-micro scale. A real mission is also explained, whose objective is to accomplish a 200 km straight line flight autonomously with the smallest electric platform possible. Design phases of the platform by using the presented method, flight tests and comparison of the results are included. On the following section a design study for long-endurance MAVs using a hybrid energy system combining solar energy and Lithium batteries and the effect of size and cruise speed are investigated. We demonstrate that under a certain size, the use of solar energy becomes not useful at all. We conclude with the study of a candidate design for EMAV09 Endurance Mission in the light of the rules and scoring of the mission.

**Keywords:** Long Endurance, Solar Power, System Design and Optimization, Paparazzi Autopilot

## INTRODUCTION

The number of the fields are increasing day by day which UAVs can take part in, but all of these fields have different and additional demands for their particular mission. These are pushing the limits of the UAVs to extremes by all means of disciplines such as structure, electronics, aerodynamics etc. Of course the operational costs are usually among the most important issues. By the help of miniaturization of the on-board electronics, it has become much more feasible to shrink the size of the UAVs which brings the cost advantage and operational simplicity as well.

The biggest problem rise up for small UAVs is the energy sources which are not small enough to achieve the same endurance than the big ones. For sure long-endurance capability

is needed and a big advantage for any kind of mission. So we concentrate our effort on having a long-endurance mini-micro UAV.

This paper will present the initial approach for a Long-endurance mini-micro UAV conceptual design, by introducing the method and the Long Endurance Conceptual Design Program behind, some ideas for extracting energy which are planned for future work, candidate energy sources that are decided to be used, an example mission which has decided to be used for coefficient verification of the design program, and also the feasibility study of using the decided techniques for a MAV design. At the last part a candidate design for EMAV09 Endurance Mission will be studied with the rules and scoring in mind.

## 1 DESIGN STUDY FOR A LONG-ENDURANCE MINI-UAV

The Design process has several phases, like conceptual, preliminary and detailed design. Generally in the conceptual design phase of a UAV, a wide competitor-study according to the RFP of the mission can lead to quite close results for the geometrical specifications of the design, which will be frozen on the final design. However on a design like long-endurance mini-UAV, as the concept has been newborn, competitor-study will either not be sufficient or not lead to an innovative design.

So the key points of the challenge for a long-endurance Mini-UAV have been investigated and a Long-Endurance Conceptual Design Program (LECDP) has been developed and is presented briefly below.

### 1.1 Energy Sources

At the scale of Mini and Micro UAVs, energy storage systems become even more problematic than the bigger UAVs since it can reach 40 % of the total weight. Thus, a wide research of current state of the art for energy sources has been completed. However a brief look will be taken place in the paper.

Battery technology keeps improving rapidly because of the huge demand of portable computers, cell phones and Radio Control models. Currently Lithium-Polymer batteries are the most dominant ones in the market. They have a specific energy of 150 to 200 Wh/kg. After scanning the whole envelope for suitable battery technology (Table 1), Lithium-Polymer and Lithium-Sulfur <sup>1</sup> batteries were selected as the

\*PhD Student, Murat.Bronz@isae.fr

†Professor in Aerodynamics, Jean-Marc.Moschetta@isae.fr

‡Lecturer in Computer Science, Pascal.Brisset@enac.fr

§Lecturer in Electronics, Michel.Gorraz@enac.fr

<sup>1</sup>www.sionpower.com

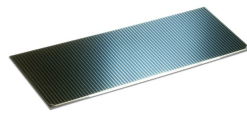
	Ni-Cd	Ni-Mh	Li-Po	Li-S
Specific Energy ( $Wh/kg$ )	40	80	180	350
Energy Density ( $Wh/l$ )	100	300	300	350
Specific Power ( $W/kg$ )	300	900	2800	600

Table 1: Battery specifications from different sources, numbers for Li-Po are already tested and the numbers for Li-S are rely on the manufacturer.

two candidates for the calculations.

Most recent long-endurance world records for small UAVs, that are just using the energy stored on board, are broken with Fuel-cells[1, 2]. Fuel-cells have high specific energy around  $1000 Wh/kg$  which is a great advantage. However their minimum initial system weight is around  $1.9 kg^2$ . Although this system has sufficient energy for 10 hours of flight for a UAV that has  $2.5 m$  wing span<sup>3</sup>, it doesn't seem to be feasible to realise a long-endurance UAV smaller than  $2m$  wing span utilising fuel-cells at this stage because of the total system weight. As we are dealing with a Mini-UAV whose maximum dimensions doesn't exceed 1 meter, we are obliged to wait and watch the new technology progress.

Benefiting from solar energy became very popular in the sense of green energy and also became feasible for small UAV activities since the solar-cell technology improved a lot. Recent Silicon solar cells are thin, flexible and very light while still having a reasonably good efficiency. These properties make them well suited for the small UAV activities. After a market search we obtained S-32 Silicon cells (Figure 1) which are the state of the art high efficiency, low weight silicon cells with an integrated by-pass diode (AzurSpace solar Power GMBH<sup>4</sup>).



	S-32
Open circuit V ( $mV$ )	628
Open circuit I ( $mA/cm^2$ )	45.8
Voltage @ Pmax ( $mV$ )	528
Current @ Pmax ( $mA/cm^2$ )	43.4
Avg. Efficiency (%)	16.9

Figure 1: Azur Space S-32 solar cell and its specifications.

There are several examples of applications about utilising solar energy in UAVs [3, 4] but recently most remarkable one and the most closest one to Mini-UAV scale is for sure the SkySailor<sup>5</sup> [5] which has accomplished a 27 hours continuous flight. Although Noth et al.[5] resulted on  $3.2 m$  wing span for continuous flight (between certain place and time of the year), they also showed the feasibility of a solar powered Mini-UAV which has  $0.77 m$  wing span [6].

<sup>2</sup>www.protonex.com

<sup>3</sup>www.ns.umich.edu/htdocs/releases/story.php?id=6833

<sup>4</sup>www.azurspace.com

<sup>5</sup>sky-sailor.epfl.ch

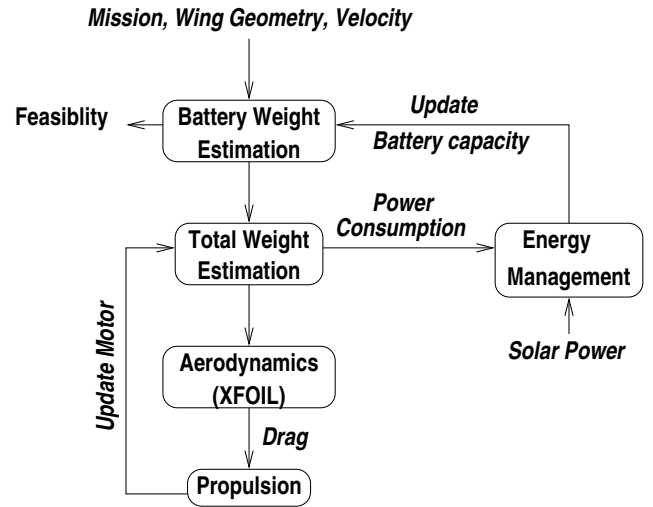


Figure 2: Brief Flow-Chart of the LECDP.

## 1.2 Extracting Energy from Environment

On-board energy storage is always limited and additional capacity always brings additional weight. That's why calculations end up with an optimum total weight that corresponds to certain storage capacity. This limits the energy that we can carry on-board. However extracting energy from environment not always needs an additional system weight and can be continuous for some cases which will certainly make a huge improvement in endurance performance of the UAVs [7].

A good example for extracting energy from environment is achieved by D.J. Edwards [8]. By actively searching out and having advantage of thermals, naturally occurred convective air updrafts, and using the initial potential energy from a  $140 m$  launch, their autonomous SBXC glider achieved  $48km$  of distance while staying aloft 1.5 hour.

The challenge is to design a UAV that is optimised both for extracting energy from environment, utilising different energy sources if there is more than one and also being capable of managing the required mission at the same time.

This part will not take place in the design method for now since there is already a lot of challenges with utilising the energy systems alone, but planned to be explored in the following months.

## 1.3 Long Endurance Conceptual Design Program "LECDP"

Objective of LECDP is to be able to see the variation of performance values such as endurance and range for different kinds of designs, and it also aims to fix the performance values and search for a feasible geometry for conceptual design. The most important philosophy behind LECDP is to keep it as simple as possible and still be very flexible to change and adapt it for the new technological improvements. So a sim-

ple block structure in Scilab<sup>6</sup> is used for writing the program. Figure 2 simply shows the main blocks that are working together in the program.

Program runs with the identified design variables such as wing geometry, mission requirements, cruise velocity etc. All of the assumptions made in the early design are included in the input such as propeller, motor, speed controller and battery efficiencies, parasite drag coefficient for fuselage, battery and motor weight constants to find the corresponding weight for a given voltage and power. First estimation of battery weight and capacity is made in the **Battery Weight Estimation** Block.

All of the mass values are generated and summed in the **Total Weight Estimation** Block. Then iteration starts with updating the **Aerodynamics** Block with the new total weight, here the required lift coefficient is calculated by using the first given design variables. Traditional formulas are used to find the infinite 2-D airfoil lift coefficient then in order to have a better estimation of the drag, an external program **XFOIL**<sup>7</sup> is called[9]. This is much more convenient than having a constant value for skin friction and pressure drag coefficient of an airfoil since XFOIL also takes into account Reynolds variations, and also gives permission to change the airfoil used in the design program. After calculating the total drag of the plane **Propulsion** Block updates the motor weight in the **Total Weight Estimation** Block taking into account the required thrust and power until a fixed point is reached and then power consumption is calculated.

The **Energy Management** Block is responsible for utilising the existing energy source, and combining them together for an hybrid use or charging process. The **Solar Power** Block uses a sinusoidal model of the Sun Irradiation and calculates the power output and weight of the solar cells to be updated in **Energy Management** and **Total Weight Estimation** Blocks.

If a performance value is fixed, like the one which is going to be described in Section 2, then the **Battery Weight Estimation** Block will keep changing the capacity and updating the weight till the target value is reached if it is feasible otherwise program moves to the next input values.

Explained Block architecture lets user to change the Blocks independently if needed. Of course coefficients and constants used in the early design is really important since it can effect the performance dramatically. So as to verify the coefficients, it is concentrated on both theoretical and experimental studies.

#### 1.4 Paparazzi Autopilot

There are several world records and record attempts in F5S FAI class<sup>8</sup> on which the pilots are in the loop all the time and flying the aircraft manually around 12 hours<sup>9</sup>. One of the

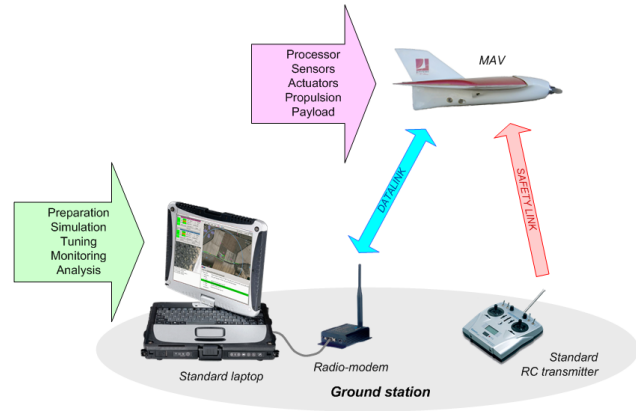


Figure 3: The Paparazzi system includes the airborne autopilot and the GCS.

main objective of this study is to have the aircraft flying autonomously without requiring a human pilot for stabilisation and navigation.

Paparazzi is an open-source autopilot system oriented toward inexpensive autonomous aircraft of all types. The project began in 2003 and has enjoyed constant growth and evolution ever since. The system has been used on dozens of airframes and implemented by several teams around the world. Hundreds of hours of autonomous flight have been successfully achieved with the Paparazzi system.

The Paparazzi system (Figure 3) is extensively described in [10, 11] and cooperatively documented in a the `paparazzi.enac.fr` wiki.

There are of course several pros and cons of using an autopilot versus a human pilot. A human pilot has hidden expertise, can examine the environment efficiently and take advantage of it immediately (like topology-wind interaction for slope flight, thermalling birds, dust devils).

However having an autopilot on-board ensures the ability to fly out of sight, and a much better stability of the aircraft even in a perturbed environment by the help of the on-board sensors. It is also able to control and fly at the exact attitude which is needed most of the time in order to get the best flight performance of the aircraft and to keep better track of the navigation for an efficient surveillance mission. The most important advantage is to control the propulsion system much more efficiently for a longer energy run. Having Paparazzi Autopilot on-board will sustain these benefits to achieve long-endurance flights with a mini-UAV.

## 2 CORSICA MISSION

### 2.1 Mission Description

Corsica Mission was just an idea that came out of a brainstorming session at first and later was started by two groups of students from ISAE (`www.isae.fr`) and ENAC (`www.enac.fr`) also with the contributions of the two Insti-

<sup>6</sup>[www.scilab.org](http://www.scilab.org)

<sup>7</sup>[raphael.mit.edu/xfoil/](http://raphael.mit.edu/xfoil/)

<sup>8</sup>[www.fai.org](http://www.fai.org)

<sup>9</sup>Oklahoma State University DragonFly Project, [osu.okstate.edu](http://osu.okstate.edu)

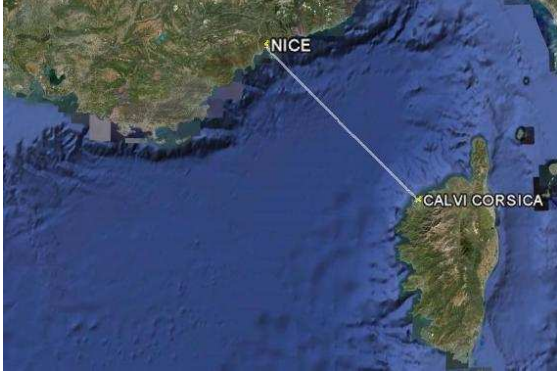


Figure 4: Planned Corsica mission flight path (200 km).

tute's advisors. It was a short term project that should be fulfilled in 9 months. Main objective of the project is to design and build the smallest possible electric powered UAV that will have a capability to survey 200 km line autonomously. To prove the reality of the project, the mission is chosen to be performed over the Mediterranean Sea across Nice and Calvi (Corsica) (Figure 4) which also brings the originality of the project.

## 2.2 Relevance of the Mission with Long Endurance

Although the project is not totally concentrated on the Long-Endurance objective, still 200 km of range requirement is demanding a long-endurance capability for such a small electric UAV. So that the project is a good candidate for the LECDP to be tested. Additionally, the flight test results gave us the opportunity to compare and verify the initial coefficients which has been chosen in the beginning.

## 2.3 Prototype Design and Manufacture

As we have been trying to push the limits to extremes, we couldn't select the regular values for any of our coefficients and constraints such as wingloading, power to weight ratio, emptyweight fraction, etc.

In order to verify our first assumptions and coefficients we decided to build a prototype rapidly. First of all, we were in search for a suitable and meaningful cruise speed for the mission. As it is a kind of surveillance mission, it is decided that the cruise speed should not go higher than a certain value. The lower boundary of the speed envelope has no limitation because the stall speed of the designed aircraft will already limit it. After several analysis with LECDP, 20 m/s cruise speed was chosen to be appropriate for the mission taking into account for both the energy consumption not to be too high and the mission time not to be too long to be risky for the effect of cross-wind. The required battery capacity values for a span variation from 1 m to 1.8 m for 20 m/s cruise speed is presented in Figure 5. Here it can be seen that for an UAV with 1.8 m span and 0.2 m<sup>2</sup> wing area, 19 Ah of battery

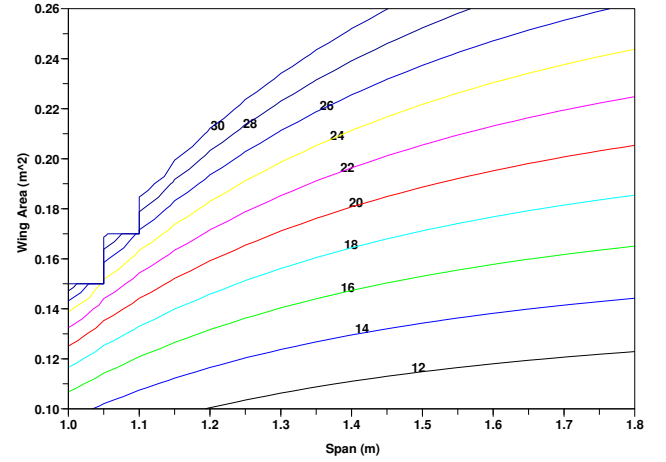


Figure 5: Required battery capacity in Ah for 20 m/s cruise speed (14.8 V, 200 km).

capacity (at 14.8 V) is needed to cover 200 km of straight line where as for a 1.2 m span and the same wing area of 0.2 m<sup>2</sup> the required battery capacity becomes 28 Ah.

After the choice of cruise speed, LECDP analyses examined again to see the variation of total weight and wing-loading for different wing spans and areas (Figure 7 and 6). As the objective is to be small as possible, it is favourable to stay in the lower left end of the graphs but, as it is seen in Figure 6, the wing-loading value is getting too high compared to an radio-controlled electric model's wing-loading which is around 20 – 60 N/m<sup>2</sup>. Also as LECDP does not take construction and component storage problems into account, a final decision of the designer is needed. As an example, the batteries are decided to be placed all in the wing, which creates a constraint between the volume of the total batteries and the volume of the wing. And as the battery volumes are fixed with the shape, after some market search and analyses, chord of the wing is fixed according to the selected battery type. This makes it possible to represent the wing span by the number of batteries inside or by the capacity as well. While keeping the wing-loading in a safe region and optimising the wing span, corresponding battery capacity for 1.5 m wing span ended with a little bit less than needed, but the difference was small enough to compensate it with a small battery pack in the fuselage.

The fuselage is constructed from aramid besides the small reinforcement parts around motor and wing mount which are carbon fiber. The wings are precisely cut by a CNC foam cutter machine in Composite Laboratory of ISAE and covered with aramid and carbon fiber. As the first prototype is designed for coefficient verification and proof of concept, it doesn't have the originally selected batteries (KOKAM 7.5 Ah) instead it has three housing for inserting steel rods to simulate the battery weight and inertia in the wing. This also let us to progressively increase the weight of the Prototype to

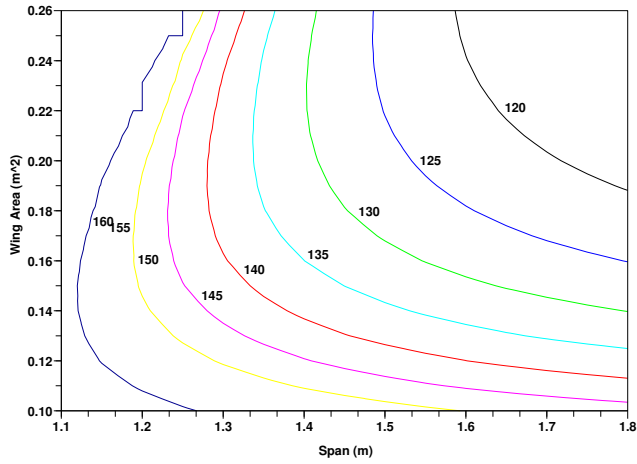


Figure 6: Wing-loading ( $N/m^2$ ) at 20  $m/s$  cruise speed.

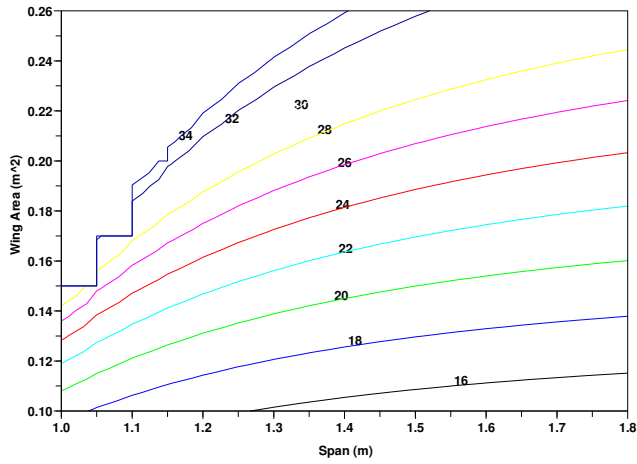


Figure 7: Total weight ( $N$ ) at 20  $m/s$  cruise speed.

		Prototype
Required Total Power	( $W$ )	126.44
Battery Capacity	( $Ah$ )	25.94
Structural Weight	( $N$ )	5.35
Total Weight	( $N$ )	29.45
Wing-Loading	( $N/m^2$ )	124.28
Lift Coefficient		0.5072
Span	( $m$ )	1.5
Chord	( $m$ )	0.158
Drag	( $N$ )	2.36

Table 2: Chosen values for the first prototype from the LECDP results.

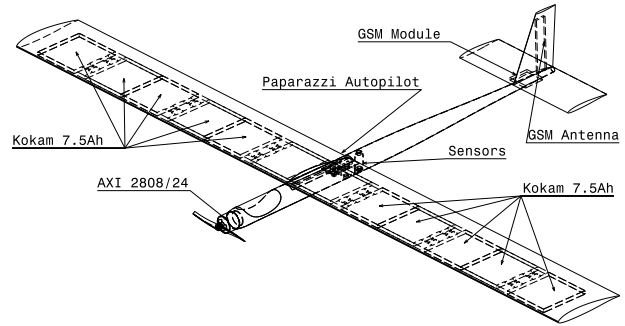


Figure 8: Sketch of the prototype with its components.



Figure 9: Prototype ready for its first flight.



Figure 10: Surface quality and holes for steel rods simulating battery weight and inertia.

measure its flying characteristics and also power consumption for different weights.

#### 2.4 Propulsion and Flight Tests

The prototype's wing design lets to be tested for different weights. First to measure the flight characteristics of the plane, only carbon rods are inserted for joining the two wing-halves and as a result the first flights were made for only 1kg of total mass. At this weight, it was satisfactory enough to hand-launch the plane. After tuning the manual and autopilot settings, steel rods were inserted for progressively increasing the weight up to expected flying weight.

In order to obtain aerodynamic and propulsion efficiencies from the flight tests, two methods are planned. First is to climb at a safe altitude, glide along a straight line without throttle at a certain velocity to obtain the lift to drag ratio of the whole plane [12, 13]. Lacking of a differential pressure sensor for speed measurements and just being relying on GPS information for speed and altitude, environmental effects such as thermals and sinks, made it not possible to have satisfactory results in a short term glide tests. So it is more concentrated on a long term test which will give better values when averaged. In Figure 11, which is the view of the flight test trajectories exported to Google Earth, fixed altitude circle and oval type flights can be seen. On those flights, altitude and cruise speed tried to be kept fixed and circles are flown for 160 seconds autonomously. Power consumption is also recorded. After averaging, it is seen that the cruise speed is  $18.6 \text{ m/s}$  instead of  $20 \text{ m/s}$ , which also effects the predicted design power consumption. Table 3 shows the previously designed values, the values obtained from flight tests and the updated values as the cruise speed changes between the designed conditions and the flight conditions. It can be easily seen that the first coefficient assumptions were overly pessimistic.

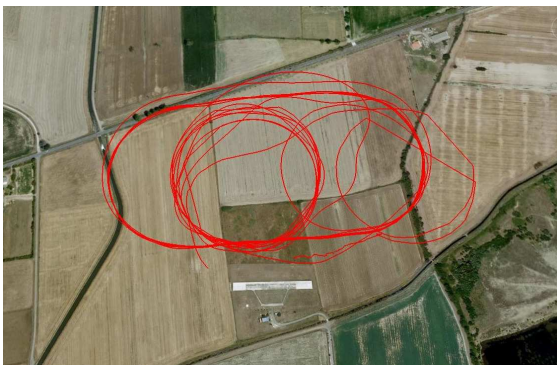


Figure 11: First autonomous flight test

After modifying the coefficients according to the obtained results from flight tests, it was obvious that the size of the plane can be decreased a little bit, but unfortunately the selected batteries can only allow a major difference as the pack

		Designed	Flight	Updated
Total Power	(W)	126.44	63.5	100.8
Cruise Speed	(m/s)	20	18.6	18.6
Battery Volts	(V)	14.4	13.35	14.4

Table 3: Variation of Designed, Tested and Updated values.

sizes are fixed. However another option could be to change the battery type and brand but as it is a short term project, there was not enough time to do that.

### 3 STUDY FOR A HYBRID SOLAR POWERED MAV

Although having verified the coefficients with the flight test of the prototype, the results that were obtained from LECDP for MAVs were not consistent. So we used previous flight data acquired from Slicer and Storm-1<sup>10</sup> and wind-tunnel results to recalibrate some of the coefficients in the LECDP for MAV scale. After this tuning, analyses were done for the hybrid system with the solar energy and Li-Po battery taken into account. The objective was to see the feasibility of using solar energy for MAVs to enhance the flight time.

Two different configuration were taken into account, 500 mm and 300 mm span. For each of the configurations, wing area and endurance have been optimised using LECDP for a given battery capacity on board (910 mAh).

In the analyses, the maximum sun irradiance is taken as  $900 \text{ W/m}^2$  and 70 % of the wing is assumed to be covered with solar cells. The efficiency of the solar cells, 16.9 %, is taken as it is given in the data sheet of the manufacturer.

Figure 12 shows the flight time versus the cruise speed of two different configurations with and without solar cells. Both have the same battery capacity on board. It can be seen that the benefit that is taken from solar cells for flight time is much higher for the bigger 500 mm MAV than the small 300 mm one. It can be shown that under a certain size, there is almost no benefit that can be taken from the solar cells. This is a result of the reduced wing surface area of the small sized MAV reducing the total solar cell area which is linearly proportional with energy extracted from sun. Another important issue is the weight ratio of the solar cells and the required electronics to the weight of the MAV. This ratio is becoming larger when the MAV gets smaller in size, then reducing the overall efficiency of the MAV. It should be noted that these conclusions are made taking into account the Paparazzi autopilot and electronics weights.

Figure 13 shows the hybrid solar powered MAV prototype. Twenty RWE Si-32 solar cells are bonded on the wing with silicon based glue<sup>11</sup>. The wing platform is optimised in order to place the maximum number of solar cells safely on the surface while keeping in mind the span efficiency, elliptical loading and the tip stall issues. This was especially

<sup>10</sup>Previous MAVs that were designed and flew in competitions by our team

<sup>11</sup>With the collaboration of the [www.map-coatings.com/](http://www.map-coatings.com/) company

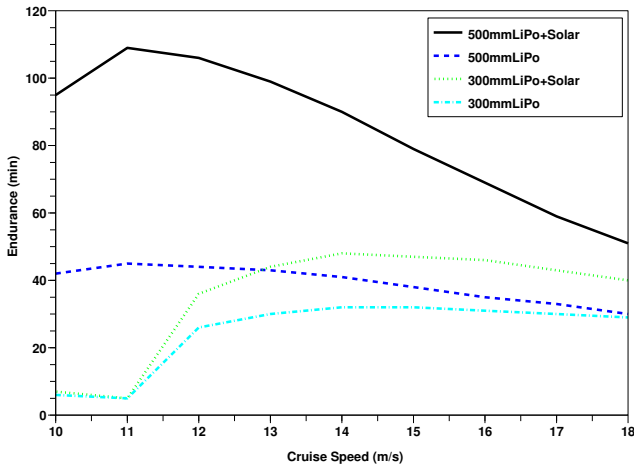


Figure 12: Endurance comparison of 500mm and 300mm MAVs using solar cells.

important in order to reach the same percentage of solar cell area to wing area that we have assumed in the calculations.

The powerful XFOIL airfoil analysis and design program is used to design the airfoils. There are three different custom airfoils along the span, which are particularly designed according to their corresponding Reynolds number for the cruise speed while observing the stall behaviour and maximum lift coefficient. Spanwise transition and the design procedure will not be included here more deeply as it is not in the scope of this paper.



Figure 13: Solar-Storm prototype

### 3.1 Maximum Power Point Tracker

Although we have kept the efficiency of the solar cells constant and at maximum value (16.9%) in the calculations, this is not exactly true for all cases in real life.

According to the angle of the solar cells with the sun rays, time of the day and year, geographic location, solar cells will have different output power.

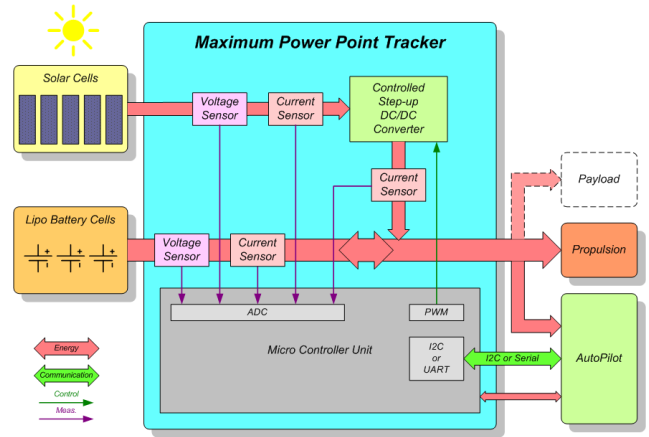


Figure 14: MPPT for solar cells.

When the pads of the solar cells are not connected, the voltage between the pads is  $V_{OC}$  the open circuit voltage and the current is null. When the pads are short circuited, the voltage becomes zero and the current is  $I_{SC}$ , the *short circuit current*. The maximum output power has to be found between these two points. This point is called maximum power point (*MPP*) and the voltage and the current at this particular point are  $V_{MPP}$  and  $I_{MPP}$ .

The search for the *MPP* requires an ad hoc electronics circuitry adapted in real time with a control loop. Figure 14 shows the schematics of this board. Note that it includes a micro-controller which can be linked to the autopilot to be monitored from the ground station.

## 4 CANDIDATE DESIGN FOR EMAV09 ENDURANCE MISSION

### 4.1 Mission Definition

EMAV09 Outdoor Endurance Mission simulates a payload drop task where the target is far away from the launch zone. The distance between the launch zone and the target is simulated by flying a number of laps to the target, dropping a paintball on the target and then returning by flying the same number of laps before landing.

Although it has been shown in the previous sections results that a 300 mm MAV will not be able to achieve flight times as long as a 500 mm MAV does, still the rules of EMAV09 Endurance Mission promote being small by taking into account maximum dimension at the flight score calculation.

However, the mission is more focused on the range performance rather than the maximum airborne time. So, it is more important to fly at the "maximum lift to drag ratio speed" of the MAV rather than the "minimum power consumption speed" in order to get more points.

#### 4.2 Computation Results

We have compared three candidates for the mission: the 300 mm Slicer, the solar powered 500 mm Solar-Storm and the 500 mm Fire-Storm. The Fire-Storm (Figure 15) has the same airframe than the Solar-Storm and is filled with as much battery capacity as possible. In order to stay in the optimum point of the designed airfoils while keeping a operable flight speed, it is powered with two 1320 mAh batteries (3 cells).

We compare here the expected scores for the three aircraft for different wind speeds. We make the hypothesis that, flying ovals, the average ground speed is  $(V^2 - W^2)/V$  where  $V$  is the airspeed and  $W$  the wind speed. The oval lap length is estimated to 1150 m.

The following table gives the number of laps and the corresponding expected score (autonomy set to 9, size  $S$  in mm, endurance  $T$  in mn):

	S	V	T	$W = 0$	$W = 5$	$W = 10$
Slicer	300	12	35	22/388	18/317	6/105
Solar-Storm	500	12	145	90/910	74/666	26/234
Fire-Storm	500	16	90	74/666	68/612	46/414

The hypothesis for the Solar-Storm are highly optimistic: optimum hour in the day and sun irradiance about  $900 W/m^2$ , something which probably never happen in Holland in September. So from these numbers and expected weather, the Fire-Storm seems more favourable.

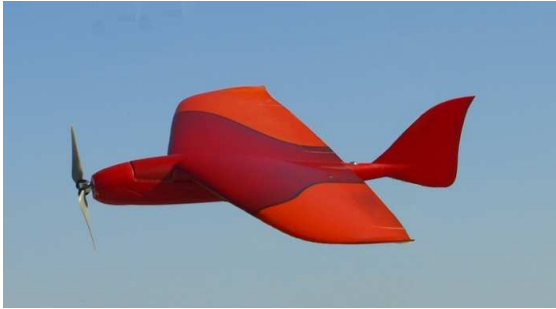


Figure 15: Fire-Storm designed for EMAV09 Endurance mission

#### CONCLUSION

The so called "LECDP" has been briefly explained with the methodology behind it. A real mission has been described and design phase of the prototype for the mission is presented. Also the comparison of the calculated power consumption and the power consumption obtained from flight tests has been done. The results obtained from those comparisons are used for coefficient verification and calibration. Similar procedure is followed to calibrate the coefficients for MAV scale. Obtained results have been shown for possible long endurance MAVs utilising a hybrid solar energy and Lithium batteries. It is seen that there is a minimum size limit for the MAV to be able to use solar energy and below that limit it

is no use to have solar cells and the required electronics on board for enhancing the flight time. In the last section, an initial study has been made to achieve a high score for the EMAV09 Outdoor Endurance mission.

#### REFERENCES

- [1] Thomas H. Bradley, Blake A. Moffitt, Dimitri N. Mavris, and David E. Parekh. Development and experimental characterization of a fuel cell powered aircraft. *Journal of Power Sources*, 2007.
- [2] Thomas H. Bradley, Blake A. Moffitt, Thomas F. Fuller, Dimitri Mavris, and David E. Parekh. Design studies for hydrogen fuel cell powered unmanned aerial vehicles. In *American Institute of Aeronautics and Astronautics*, Honolulu, Hawaii, August 2008.
- [3] Alan Cocconi. Solong UAV : Solar electric powered. Technical report, AC Propulsion, CA, 2005.
- [4] André Noth. History of solar flight. Technical report, Autonomous Systems Lab, Zürich, 2008.
- [5] A. Noth. *Design of Solar Powered Airplanes for Continuous Flight*. PhD thesis, ETH ZÜRICH, 2008.
- [6] N. Diepeveen. The sun surfer : Design and construction of a solar powered MAV. Master's thesis, Autonomous Systems Lab, ETHZ, Zürich, March 2007.
- [7] Ying Celia Qi and Yiyuan J. Zhao. Energy-efficient trajectories of unmanned aerial vehicles flying through thermals. *Journal of Aerospace Engineering*, April 2005.
- [8] D. J. Edwards. Implementation details and flight test results of an autonomous soaring controller. In *American Institute of Aeronautics and Astronautics*, 2008.
- [9] Harold Youngren Mark Drela. *XFOIL 6.94 User Guide*. MIT Aero and Astro, 2001.
- [10] P. Brisset and A. Drouin. PaparaziDY: do-it-yourself UAV. In *Journées Micro Drones*, Toulouse, France, September 2004.
- [11] P. Brisset, A. Drouin, M. Gorraz, P.-S. Huard, and J. Tyler. The Paparazzi solution. In *MAV2006*, Sandestin, Florida, November 2006.
- [12] Helmut Reichman. *Cross-Country Soaring*. Soaring Society of America, Inc., 2005.
- [13] Dan Edwards. Performance testing of RNR's SBXC using a piccolo autopilot. Technical report, North Carolina State University, 2008.



# Flying Autonomously to Corsica : A Long Endurance Mini-UAV System

Murat Bronz<sup>\*</sup>, Jean Marc Moschetta<sup>†</sup>, Pascal Brisset<sup>‡</sup>  
Institut Supérieur de l'Aéronautique et de l'Espace, Toulouse, France  
and

École Nationale de l'Aviation Civile, Toulouse, France



## ABSTRACT

The paper presents the whole design steps of a 1.5 m UAV so called *Spirit of Corsica 2 (SPOC-2)* which is designed to fly over the Mediterranean sea from Menton to Corsica. Conceptual design is described following the decision taking for the mission constraints. Aerodynamics and windtunnel results of the design has been presented. A specific, mission based propulsion system matching methodology has been described. A compact and lightweight proposal has been made for one of the biggest difficulties for long range communication by using a GSM module. Finally the mission attempt has been described.

## 1 INTRODUCTION

Long endurance UAVs generally require a large airframe and a significant infrastructure. Although limited in energy density, electrically powered UAVs offer flexibility and robustness and can be combined with solar cell power supply. The present paper addresses the technical dilemma between

endurance and size with the objective of investigating long endurance mini-UAV systems. As an example of this effort, a specific over-the-sea mission has been designed to assess the feasibility of a long-endurance mini-UAS.

## 2 PROJECT DESCRIPTION & HISTORY

*Fly to Corsica Project* has started as a collaborative student project between ISAE and ENAC in 2009. The objective of the project is to fly autonomously from Menton to Calvi (approximately 185 km, figure 1) with the smallest possible electrically powered UAV. Figure 2 illustrates two successive versions of the Corsica mini-UAVs with their specifications. In 2009, the first year of the project, three prototypes have been manufactured and, more than 90 minutes of test flights have been accomplished in total. Unfortunately the final plane was not ready at the time of mission attempt so it has been decided to extend the project to 2010. New version of the mini-UAV (*SPOC-2*) has been redesigned and fine tuned in the light of the experiences gained from the initial prototypes. Following sections will cover all of the design and development phases of *SPOC-2*.

## 3 CONCEPTUAL DESIGN AND AERODYNAMIC ANALYSES

### 3.1 Aircraft Conceptual Design

Conceptual design has been done using a homemade tool[1, 2], sweeping over a range of wing spans and wing

<sup>\*</sup>PhD Student, Murat.Bronz@isae.fr,  
Murat.Bronz@recherche.enac.fr

<sup>†</sup>Professor in Aerodynamics, Jean-Marc.Moschetta@isae.fr

<sup>‡</sup>Lecturer in Computer Science, Lost his life in an accident (22 May 2010)

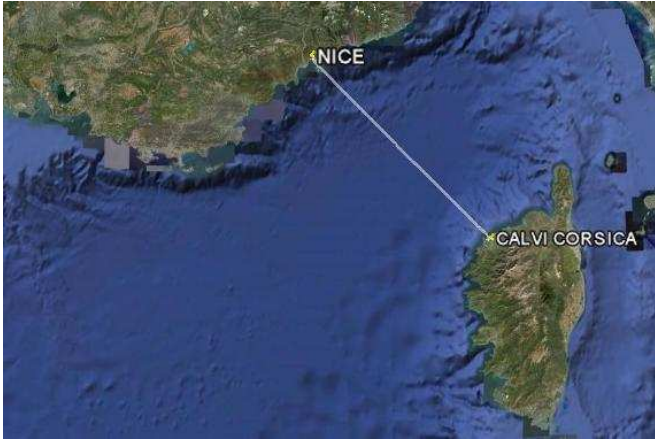


Figure 1: Planned mission map.

Design Restrictions			
Stall Speed	<11	( $m/s$ )	
Ground Distance	185	( $km$ )	
Head-Wind	2.5	( $m/s$ )	
Span	<2	( $m$ )	

Table 1: Constraints of the mission for the conceptual design.

surface areas in order to find the optimum design according to the mission definition.

The mission can be simply expressed as flying a straight line of 185  $km$  ground distance. Without any restrictions, constraints and safety margins, conceptual design program shows that the mission is feasible even with an 40  $cm$  sized plane. As it is known that there will never be perfect conditions and as the practical reasons should be taken into account such as safety piloting, landing approach, etc. more restrictions and constraints have been added to the mission definition. Table 1 shows the constraints.

Most of the constraints have been added in the light of last year's experience, especially the difficulties that have been seen while landing made us decide to have a limit on the wing loading. Also an average wind speed have been extracted from previous year's meteorological records which lead us to extend the distance in order to be able to deal with the additional head-wind.

Finally after all of these constraints, one final limitation is added with the selection of battery. As it is decided to place all of the batteries inside the wing instead of fuselage in order to have more sleek design, the wing geometry and the airfoil became dependent on the battery choice. The previous year's experiences showed us that using several individual battery cells in parallel creates a lot of troubles during the building and operating the plane. So in order to reduce the number of cells used in the design, 21  $Ah$  Lithium Polymer batteries



Version 2009		
Total Power	( $W$ )	100
Battery Capacity	( $Wh$ )	310
Structural Weight	( $N$ )	5.35
Total Weight	( $N$ )	29.45
Wing-Loading	( $N/m^2$ )	124
Lift Coefficient		0.50
Span	( $m$ )	1.5
Chord	( $m$ )	0.158
Drag	( $N$ )	2.36



Version 2010		
Total Power	( $W$ )	45
Battery Capacity	( $Wh$ )	210
Structural Weight	( $N$ )	4.50
Total Weight	( $N$ )	19
Wing-Loading	( $N/m^2$ )	91
Lift Coefficient		0.65
Span	( $m$ )	1.5
Chord	( $m$ )	0.140
Drag	( $N$ )	1.3

Figure 2: 2009 and 2010 versions of Corsica mini-UAV.

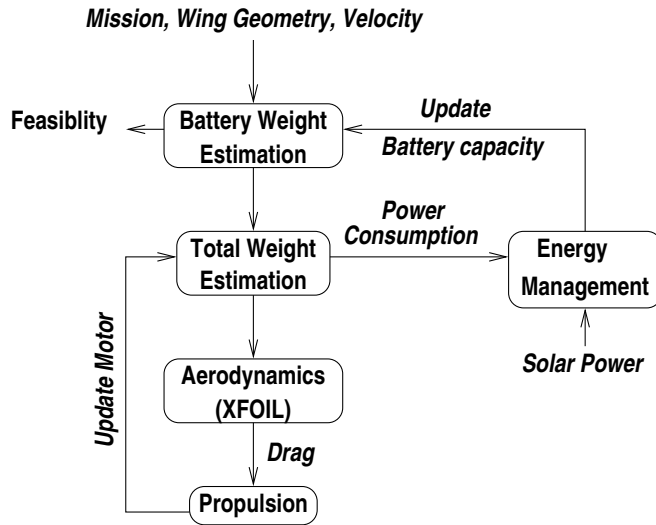


Figure 3: Flow chart of Conceptual Design program

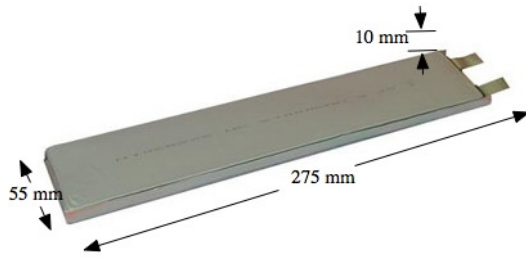


Figure 4: Selected 21 Ah Lithium Polymer Battery

have been selected (Figure 4). The decision of the battery has limited the chord length to 14 – 15 cm for a suitable airfoil for the mission. Analyses carried out on Xfoil<sup>1</sup> and finally a modified SB96 Airfoil (5) has been chosen for the plane mostly because of its advantageous volume and high  $Cl_{max}$ .

### 3.2 Aerodynamic Analyses

As a result from the conceptual design program, we obtain the wing area, span, airfoil, tail surfaces and the moment arm of the tail surfaces. After, preliminary sizing has been evaluated with analytical methods and numerical methods (AVL<sup>2</sup> and XFLR5<sup>3</sup>) using a classical vortex lattice method (Figure 5). The wing planform shape has been designed to have almost elliptical lift loading along the span so as to have a higher span efficiency. It has been also taking into account for the low Reynolds problems near the small tip chords, avoiding tip stalls for favourable flight characteristics and integration of the batteries. Figure 5 shows the lift and lift coefficient distribution along the span for total equi-

<sup>1</sup>[raphael.mit.edu/xfoil](http://raphael.mit.edu/xfoil)

<sup>2</sup>[raphael.mit.edu/avl](http://raphael.mit.edu/avl)

<sup>3</sup>[xflr5.sourceforge.net](http://xflr5.sourceforge.net)

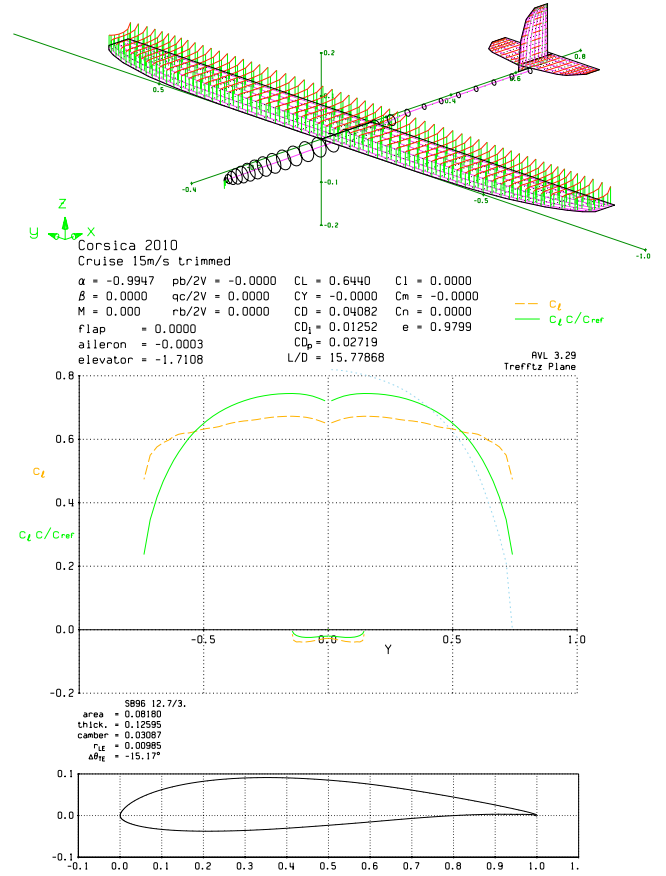


Figure 5: Analysis of SPOC-2 in AVL, with the wingloading visible on the top, lift force and lift coefficient visible along the span in the middle and the airfoil chosen on the bottom.

librium cruise condition at 15 m/s. Finally, the horizontal tail sizing have been done by using Naylor-Prandtl Theorem in order to calculate the downwash of the wing over horizontal tail. The horizontal tail has been designed as a zero lifting surface while satisfying %5 longitudinal static margin. In figure 5, it can be easily seen that the horizontal tail is almost at zero lift condition.

A specific wind tunnel campaign has been carried out as well in order to compare the theoretical and experimental results. Figure 7 shows the typical lift coefficient versus angle of attack and drag coefficient of SPOC-2 for different speeds. The effect of increased flight speed over lift to drag ratio is clearly visible in figure 8.

## 4 PROPULSION ANALYSIS

As expected, the importance of propulsion efficiency has been enlightened by the conceptual design program. Therefore, special effort has been given to experimentally and numerically analyse various electric motors and propellers. Both motors and propellers have been separately charac-

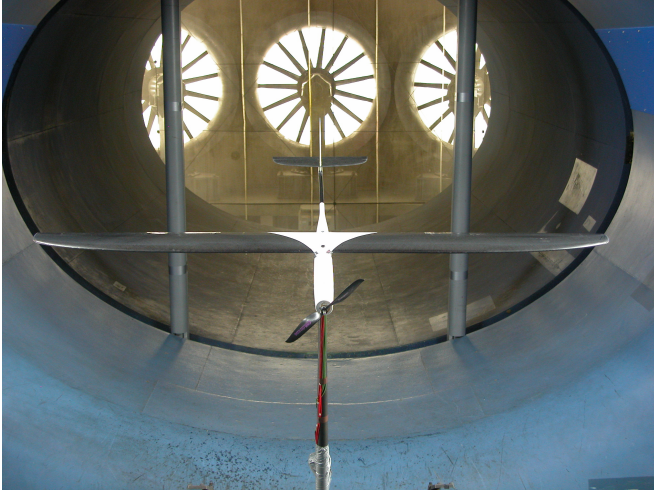


Figure 6: SPOC-2 in the S4 Windtunnel.

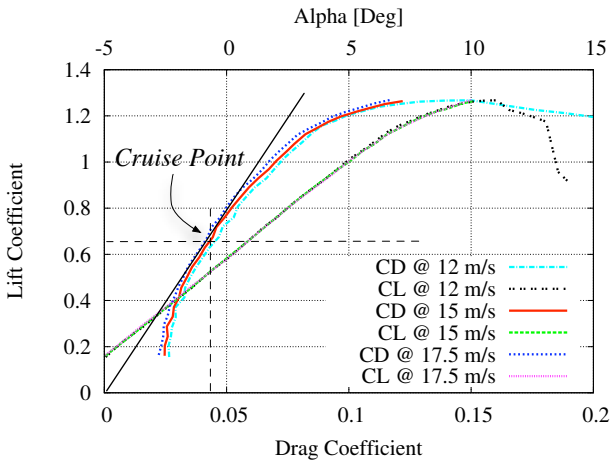


Figure 7: CL versus alpha and CL versus CD plots.

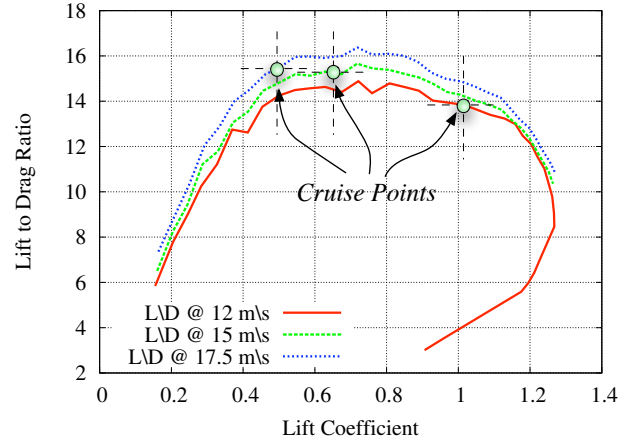


Figure 8: Lift to drag ratio of SPOC-2 for different flight speeds with the equilibrium points marked for each corresponding flight speed.

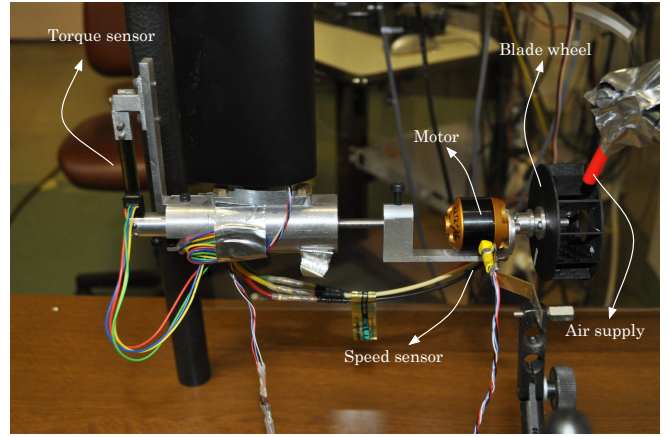


Figure 9: Characterisation of Motors

terised in order to determine the best matching couple for maximising performances.

#### 4.1 Motor, Propeller & Battery Characterisation

A custom designed specific test bench has been used to measure the torque, rpm, volt and current required while continuously changing the resistance applied to the motor (Figure 9). Pressurised air has been blown on to a small fan in order to change the resistance. By this method, it is possible to characterise the motor solely. The efficiency of the motor is simply given by the following formula :

$$\eta_{motor} = \frac{Q \cdot \omega}{U \cdot I}$$

where  $Q$  is the torque (Nm),  $\omega$  is the rotation speed (rad/s),  $U$  is the tension (V) and  $I$  the current consumed (A).

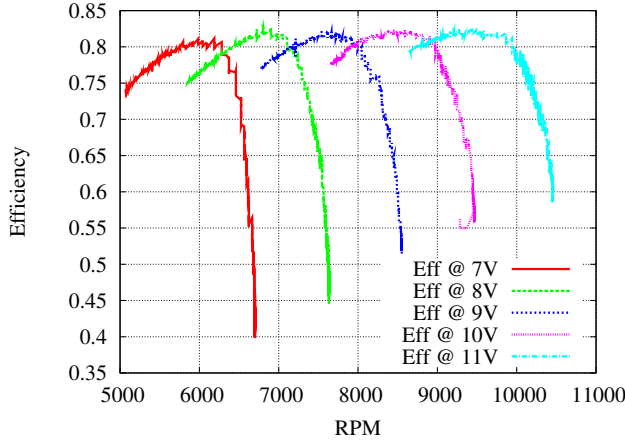


Figure 10: Efficiency graph of AXI 2212/26 brushless motor at various Voltages.

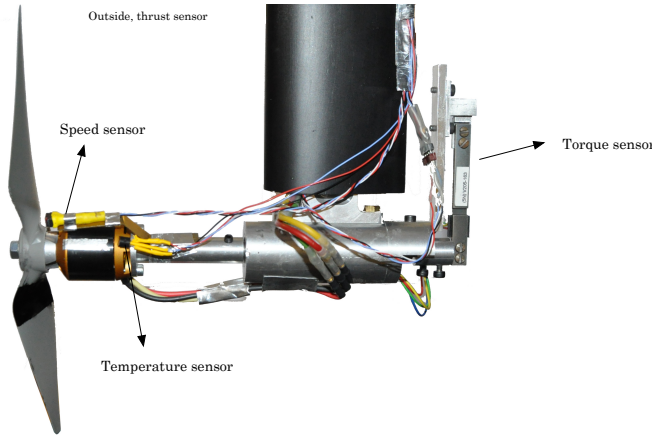


Figure 11: Characterisation of propellers

The same test bench (Figure 11) is placed into the S6 closed circuit wind tunnel of ISAE in order to characterise various propellers at different forward speed conditions. Mechanical input power of the propeller is measured with the built in torque and rpm sensor, and out put power is recorded from the thrust generated times the forward speed. The propeller efficiency given by:

$$\eta_{prop} = \frac{T \cdot V_w}{Q \cdot \omega},$$

where  $T$  is the thrust (N) and  $V_w$  is the forward wind speed (m/s).

Finally, as the batteries need to be characterised as well, they have been discharged at various power output conditions in order to see the real capacity corresponding to each discharge output and their efficiency.

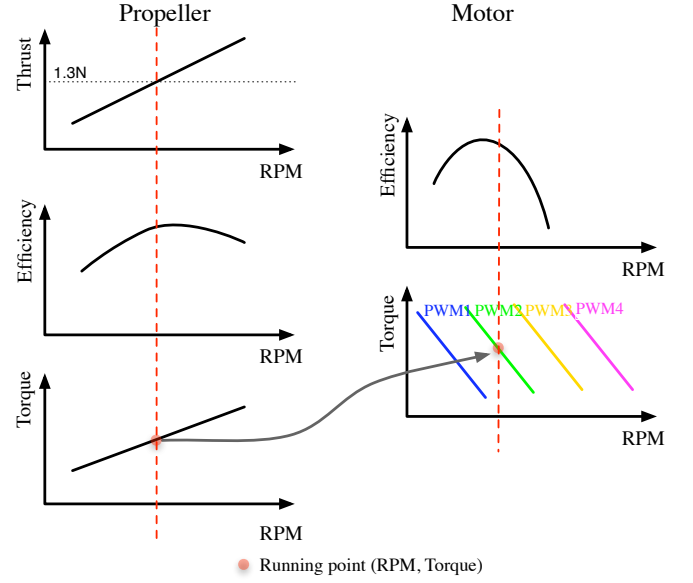


Figure 12: Motor and propeller matching methodology

#### 4.2 Matching of System

Knowing the real performance of the motors and propellers at our disposal, the best propeller-motor couple have been determined following the scheme pictured in figure 12[3].

Starting by finding the rotation speed of the propeller giving 1.3 N of thrust, the efficiency  $\eta_{prop}$  and torque for that point are also known (thanks to the data recorded during the tests). The [torque, RPM] point required for the cruise is then searched for the motor used and its efficiency  $\eta_{motor}$  is also obtained. Finally, the global efficiency is found by  $\eta = \eta_{prop} \cdot \eta_{motor}$ .

Finally, experiments showed that it is possible to achieve an efficiency as high as %83 for the motor and %74 for the propeller. With a proper matching of motor and propeller with in some additional practical constrains like a certain thrust at static condition or a certain thrust at a given forward speed, it is feasible to have a total efficiency of %50 for the propulsion system at cruise conditions.

#### 4.3 Endurance Tests

A crucial test before trying the actual mission was to ensure that the batteries actually held enough energy to allow such a long trip (185 km). For this experiment, the propeller test bench (placed in the S6 wind tunnel) has been used; unlike the propeller characterisation test, the power supply was the battery. The wind tunnel was set to have a 15 m/s wind while the propeller was providing 1.3 N of thrust which are the cruise condition values. As the voltage of the batteries decreased during the course of each test, the throttle command (PWM) had to be corrected. The cut-off voltage for each cell

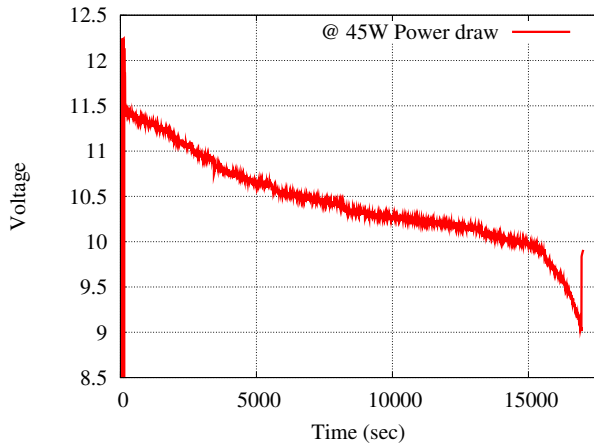


Figure 13: 4 hours and 40 minutes of discharge graph of the batteries.

has been set at 3 V to avoid any irreparable damage. Figure 13 shows the discharge graph of the batteries inside the wind tunnel at the cruise condition power consumption rate (45 W). Finally it was only possible to extract 18.6 Ah of capacity out of 21 Ah but as the batteries happened to be lighter than their specifications, they still satisfied their 191 Wh/kg specific energy.

Also a cooling test has been carried out in the wind tunnel. As the selected motor is very optimized for the cruise conditions, whenever more power is needed it gets extremely hot. Figure 14 shows the temperature of the motor while the cruise condition, while simulating a climb with maximum throttle at 15 m/s and while simulating a fast straight flight at maximum throttle at 20 m/s. The effect of additional speed on cooling can be easily seen.

## 5 EMBEDDED SYSTEMS & COMMUNICATION

### 5.1 Autopilot System

For the autonomous navigation and stabilisation system, the well proved and worldwide well known Paparazzi System<sup>4</sup> is integrated [4, 5]. Primary attitude stabilisation is established by the help of infrared thermopiles. Additionally, for the roll rate correction, the UAV is equipped with a gyro.

### 5.2 GSM Module

As expected, typical low power radio-modem ranges are not sufficient to keep contact during the whole flight (mid-point range is approximately 90 km from the two GCS). It was also not possible to use a high power radio-modem because of power emitting regulations in France. A GSM module was planned to be used for the telecommand and telecontrol communications. This would enable us to keep track of the extremely important information such as GPS location, power

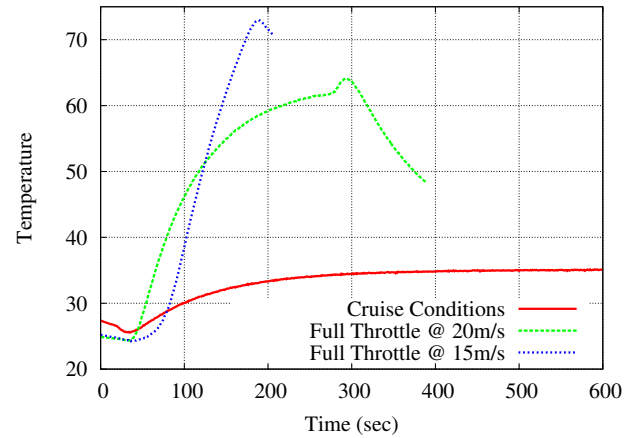


Figure 14: Motor temperature during three different conditions.

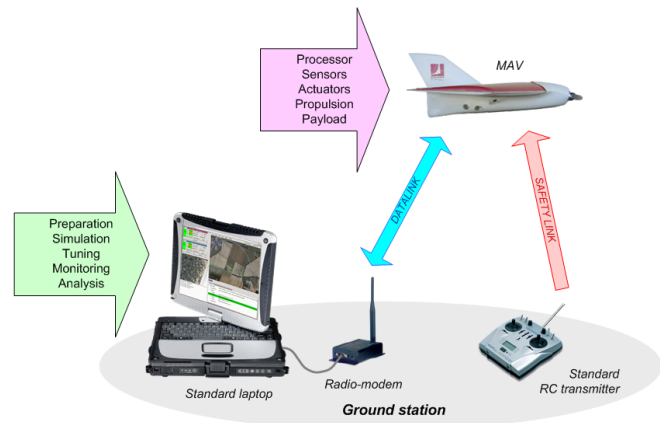


Figure 15: Paparazzi System overview and Autopilot board

<sup>4</sup>[paparazzi.enac.fr](http://paparazzi.enac.fr)

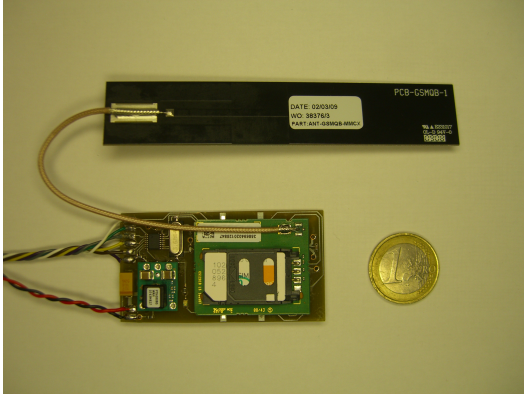


Figure 16: Telit GC864 GSM/GPRS Module with antenna

consumption and the remained energy on-board during the flight. It would also allow us to abort the flight if an unexpected and unrecoverable situation happens. These communications were also required for a periodic reporting of the position of the aircraft to the air traffic control.

Because of its small size and weight, Telit GC864 GSM/GPRS module is chosen. It requires an UART connection to exchange data, but as there were no UART connections left available on the Paparazzi module, the remaining SPI ports are used. And an all-in-one embedded GSM module is developed for Corsica mission, including a switching power supply (SMPS), a Maxim MAX3100 SPI/UART converter, and the GSM/GPRS module. The Telit GC864 is connected to a standard patch antenna which is located in the tail. For the ground stations, two of the same module is used one at Menton, one at Lozari/Calvi with an additional FTDI serial-to-USB cable which allows us to connect these ground stations directly to laptops.

With regard to the software, two additional pieces of code have been developed. The embedded code is designed to initialize the Telit GC864 settings, then to send a text message every minute. These messages contain the position of the plane, its altitude, its speed, the battery voltage and the strength of the GSM signal. The code for the ground stations reads messages as soon as they are received, and parse them in order to get the data in a readable form.

## 6 MANUFACTURING & INTEGRATION

In order to achieve the required surface quality and the accuracy in the integration, CNC-machined molds have been used in the manufacturing of the UAV (Figure 17).

Manufacturing process has been accomplished by the professionals of the composite laboratory of ISAE, which resulted in a high quality airframe as required. *SPOC2* is made out of fully composite materials with wet layup and vacuum bag technique. One of the particular property of the UAV is to carry large capacity of lithium polymer batteries, which are embedded inside the hollow molded wing. The integra-



Figure 17: Composite molds of SPOC-2.

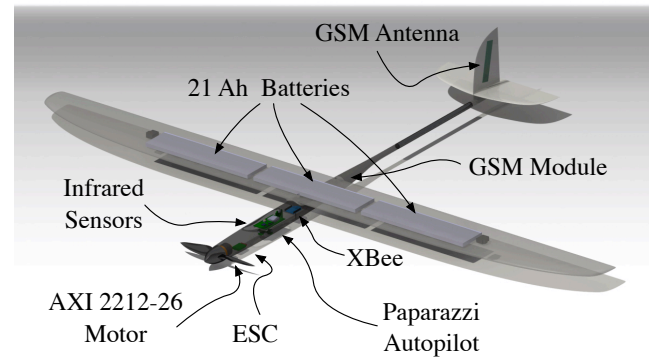


Figure 18: Integration of the components.

tion of the batteries is done in the mold before combining the top and bottom wing skins together. Through out the whole project in 2010, four wings, four tail group and six fuselages have been manufactured in five months. Figure 18 shows the final integration of main components.

## 7 FLIGHT TO CORSICA

### 7.1 Certification

In order to operate UAVs in a legal way, several authorizations from the DGAC (Direction Générale de l'Aviation Civile, French Civil Aviation Authority) needs to be obtained dealing with different aspects of the system. For the platform (plane or helicopter), it is needed to have a "Permit to Fly" which will allow to use the platform with in the conditions mentioned in the permit. The DSAC department of DGAC has been contacted in order to obtain Permit to Fly which is only given after a certification visit composed by a technological analysis and a flight demonstration.

When a "Laisser-passer" type permit to fly obtained, the restricted area in which the UAV will fly needs to be determined. Therefore, a file including all GPS coordinates which

describe the area and flight altitude, has been provided to DGAC. Then the DSR department has been contacted in order to "build" the area for the mission. Finally the last point to fly legally was to obtain the a matriculation number for SPOC-2 (*F-WZSC*) has been taken from DGAC in order to fly legally.

## 7.2 The Mission

A good knowledge of the weather conditions was a key parameter for the success of the mission. That's why AROME and ALADIN forecasts models from Meteo France were used, in order to choose the best day for the launching. A few minutes before the launching, the weather was checked one final time with the current data of the local Meteo France centers.

At 6.30 AM the 23<sup>rd</sup> June 2010 the weather conditions were favourable. Unfortunately, just after the take off, the pilot lost the RC link, probably due to a considerable electromagnetic pollution, and the mode of the plane changed to HOME (meaning that the plane should go directly to Calvi). The plane intended to climb to reach its cruise altitude too rapidly and a stall happened resulting with a crash on the rocks near the harbor. Immediately, preparations have been started for the next attempt, starting by finding the reason of failure.

- The HOME mode has been replaced by the AUTO2 mode with a low altitude reference, to avoid any stall in case of RC loss.
- After several tests in different environments, we concluded that there was too much electro-magnetic influence on the coast. We took the decision to pilot the plane directly through the Xbee (2.4GHz Datalink) with a remote control plugged on the ground station.
- In order to avoid the risk related to the proximity with the boats, we changed the take off place, using a large free beach.

On the second day of attempt, at 6.10 AM the 24<sup>th</sup> June 2010, the take off happened without any problems, final trimming and the tuning occurred quickly and without difficulties. After 6 minutes, it is decided to stop circling for testing and send the plane to Corsica for its real mission. Finally, when the plane was in direction to Calvi, the altitude, the speed, and the direction(19) were perfect during the first eight minutes. We have lost the contact with the plane after flying 5 km as expected. GSM module was not in operation as we had some problems in the first attempt. Finally, we couldnt have had any more information from SPOC-2. Without data, we are not able to give the real failure reason. Of course, some hypotheses can be imagined like path through low clouds (Figure 20), wind gust,... but without certitudes.

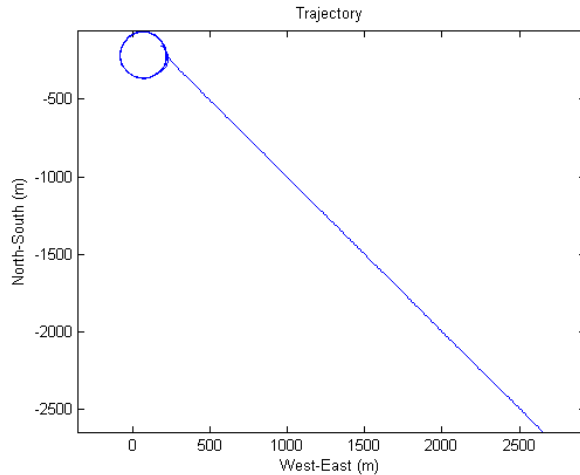


Figure 19: Trajectory of SPOC-2 before losing communication.

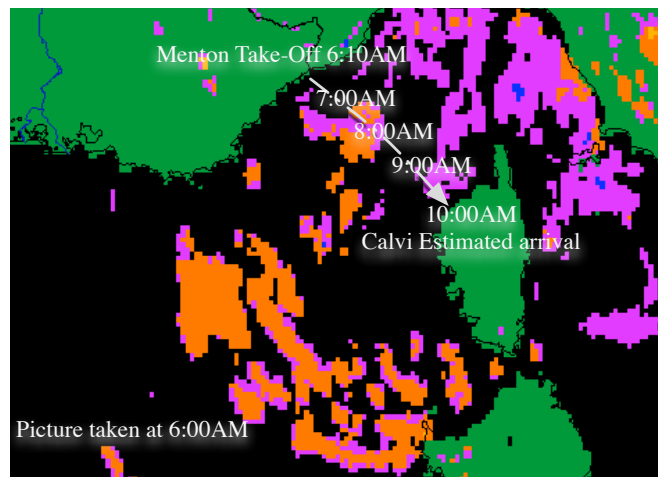


Figure 20: Satellite picture of the clouds taken at 6:00 AM, orange colour shows very low altitude clouds which could cause the failure of the infrared sensors.

## 8 CONCLUSION

The design of a long-range mini UAV so called *SPOC-2* has been described with all of its development phases. A specific wind tunnel campaign has been accomplished in order to verify the real specifications of the design. As a result of this wind tunnel campaign, it has been proven that for 1.5 m span UAV, a lift to drag ratio of 16 is feasible to obtain. A specific method for matching the propeller and motor according to the mission requirements has been briefly described, and shown that at least %50 of total efficiency for the propulsion system is feasible to achieve at this scale. Also a solution found for a lightweight long range communication by using a GSM modem. Although not being able to accomplish the mission, the attempt is done with a perfect take-off and start phase. *SPOC-2* has left the coast of Menton/Nice and flew towards Calvi/Corsica smoothly before disappearing in the sky. For the future of the project it has been decided to concentrate more on the test flights. Also some minor modifications to both hardware and autopilot software have been planned. As an additional to this year's attempt, it is planned to use an IMU and a pitot-static tube on the next year's plane.

## ACKNOWLEDGMENTS

The authors would like to point out that the present work has been a team work which contributors are gratefully acknowledged: D.Bernard, X.Foulquier, G.Mirabel, F.Dupont, L.Rion, C.Plachot, P.Toucas, M.Morere, P.Joachim, G.Soete, B.Fragniere, C.Ronfle-Nadaud, M.Gorraz, FX.Marmet, J.Scattolin, T.Lefez and G.Hattenberger.



We will never forget you Pascal...

## REFERENCES

- [1] Murat Bronz, Jean-Marc Moschetta, Pascal Brisset, and Michel Gorraz. Towards a Long Endurance MAV. In *EMAV2009*, Delft, Netherlands, September 2009.
- [2] Murat Bronz, Jean-Marc Moschetta, Pascal Brisset, and Michel Gorraz. Towards a Long Endurance MAV. *International Journal of Micro Air Vehicles*, 1(4):241–254, 2009.
- [3] MIT OpenCourseWare, Unified Engineering.
- [4] P. Brisset and A. Drouin. PaparaDzIY: do-it-yourself UAV. In *Journées Micro Drones*, Toulouse, France, September 2004.
- [5] P. Brisset, A. Drouin, M. Gorraz, P.-S. Huard, and J. Tyler. The Paparazzi solution. In *MAV2006*, Sandestin, Florida, November 2006.



# Multi-Point Optimisation of a Propulsion Set as Applied to a Multi-Tasking MAV

Murat Bronz<sup>\*</sup>, Jean Marc Moschetta<sup>†</sup>, Gautier Hattenberger<sup>‡</sup>  
Institut Supérieur de l'Aéronautique et de l'Espace, Toulouse, France  
and  
École Nationale de l'Aviation Civile, Toulouse, France

## ABSTRACT

This study focus on optimisation of electric propulsion system for a given mission with multiple working conditions. A program called *Qoptimizer* is developed and presented which can analyse and couple numerous motors and propellers from databases for a specific mission. It can also design a custom propeller by using the motor and airfoil databases. *Qoptimizer* uses *Qprop* and *Qmil* opensource propeller analyses and design programs from Mark Drela. Motor and propeller couples are simulated at each predefined working condition and given a score according to their total performance. This methodology ensures the optimisation of the selected motor and propeller couples to be valid and optimum not only for one working condition (for example: cruise condition) but for all of them (take-off, high speed, etc...). Theoretical models and experimental measurements are explained in order to generate the required databases for the existing motors, propellers and airfoils. Finally, an application of the *Qoptimizer* program on a real mission is also presented where a custom propeller is optimised according to the weighted mission working conditions.

## 1 INTRODUCTION

For an electric powered UAV, the motor consumes the biggest percentage of the total energy consumption. This clearly states the importance of optimisation of it. The system approach is the key point on propulsion system optimisation, that is, not only finding the best motor or the best propeller separately, but determining

the best motor plus propeller combination.

The mission requirements plays a big role on the selection and optimisation of the propulsion system. These usually consists more than one condition that needs to be satisfied such as take-off and cruise flight. Previous works from T.J. Mueller et al. presents a good example of motor and propeller selection for a MAV [1], but it lacks the identification of each motor and propeller combination's performance evaluation during different phases of the flight since this information can be used as a selection criteria. So in this work, the selection and the optimisation criteria will consider all of the prescribed flight phase (*working conditions*) requirements.

This paper focuses on the optimisation of the propulsion system selection process, for a specific mission with multiple conditions. The new developed *QOPTIMIZER* program will be presented, which is a motor and propeller coupling program for a large number of input motors and propellers. It uses a set of mission defined working conditions with weighted functions in order to select the best motor and propeller couple for the specific mission. Then the open source programs used in *QOPTIMIZER* will be explained. Following that, the matching process of motor and propeller couple will be explained including the basics of the electric motor, propeller theoretical models and experimental characterisation test processes.

## 2 PROBLEM DEFINITION

### 2.1 Elements of Propulsion System

Electric propulsion system mainly consists of four sub-elements, shown in figure 1; the battery, the motor controller (also called as electronic speed controller, ESC), electric motor and the propeller. A gear system can also be found between the motor and the propeller but mainly it is included in the motor sub-element. Modélisation of the motor and propeller will be explained further in section 4.

---

<sup>\*</sup>PhD Student, muratbronz@gmail.com, murat.bronz@isae.fr

<sup>†</sup>Professor in Aerodynamics, jean-marc.moschetta@isae.fr

<sup>‡</sup>Lecturer in Flight Dynamics, gautier.hattenberger@enac.fr

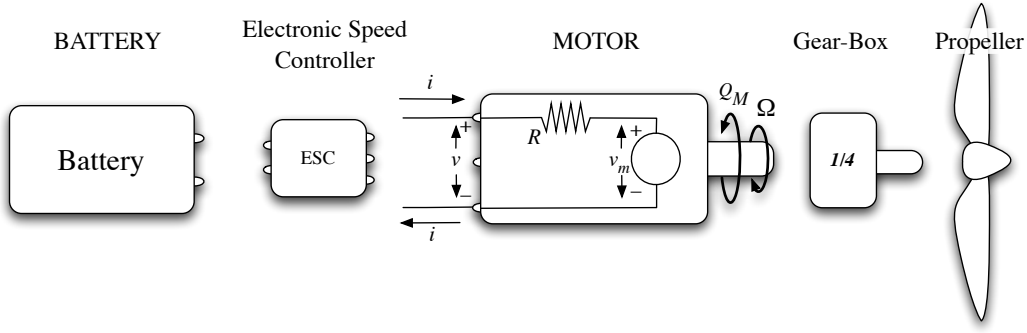


Figure 1: Elements of a generic electric propulsion system.

The electronic speed controller design is out of scope of this thesis, therefore its design will not be included into the optimisation routine, however an efficiency coefficient is included as there exists an effect coming from different brands and types of speed controllers. The same is true for the battery, it is not included in the optimisation routine as they do not have a direct effect on the propulsion system as long as an appropriate type is selected taking into account of its continuous discharge rate. The weight of each element is disregarded in this stage as this makes sense if only when the complete aircraft optimisation is done with the propulsion system included. A conceptual design program, as presented in [2, 3, 4], has to be used as it takes into account the weight of each element while calculating the performance of the aircraft. On this study, the main interest is going to be on the motor and propeller selection.

## 2.2 Mission Definition

The most important part in the optimisation of the propulsion system is the definition of the mission requirements. Generally it is only the cruise flight conditions which are taken into account while selecting and optimising the motor and propeller selections. In reality, there exists other phases of the flight which the propulsion system has to satisfy additional requirements.

Figure 2 shows several flight phases of an aircraft such as take-off, climb to an altitude, loiter at a constant altitude for surveillance and finally go from point A to B and return at a higher speed for an emergency situation. In each phase of the flight, the aircraft operates at different velocity ( $V$ ) and thrust ( $T$ ), the altitude can also be different so that the density will be different ( $\rho$ ) and the duration of the phase ( $t$ ) varies according to the mission definition.

Such a flight envelope clearly shows that optimising the propulsion system only for cruise conditions can not be optimum for the overall performance of the aircraft

for that given mission. Each phase (will be called as **Working Condition**) has to be taken into account in the optimisation with its specific variables ( $T_n, V_n, \rho_n, t_n$ ) in order to achieve an optimum selection for the propulsion system.

Finally, the *Mission Definition* will be described by the *Working Conditions* and their duration time ( $t$ ). The duration time is only taken as a weight factor here and can be modified if one of the working conditions needs more priority than its duration time compared to the whole mission time.

## 3 QOPTIMIZER PROGRAM

QOPTIMIZER Program is developed in order to select a motor and propeller couple for a given mission definition with multiple conditions as described previously. Numerous motors and propellers from databases can be numerically tested and given a score according to their performance on the defined mission. The mission definition is not only limited with one working conditions, the user can define several working conditions such as in table 1 as previously shown in the figure 2.

	Unit	WC#1	WC#2	WC#3	...	WC#n
Thrust	[N]	1.2	1.8	4.5	...	...
Power	[W]	0	0	0	...	...
Speed	[m/s]	15.0	20.0	3.5	...	...
$\rho$	[kg/m <sup>3</sup> ]	1.225	1.225	1.225	...	...
WeightFactor	[-]	900	150	30	...	...

Table 1: Example of mission working conditions.

These *Working Conditions* mainly act as an objective and also as a constraint in the optimisation process. One can define a **WC** with a weight factor of only 1, relatively low compared to a working condition representing cruise flight with 900 weight factors, so that the program makes sure that the propulsion system satisfies the **WC** but does not give a big score for its performance.

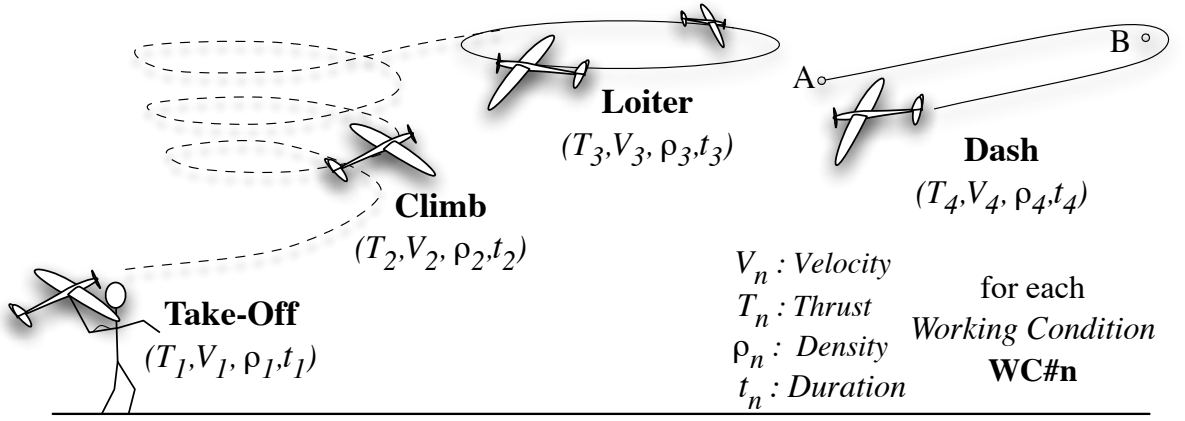


Figure 2: A generic mission definition with multiple flight phases which are called *Working Conditions (WC)*.

The program uses QPROP and QMIL as its main analyser core and gather their outputs in order to define a score for each motor and propeller couple. This score represents the performance of each motor and propeller couple for the selected mission.

### 3.1 QPROP and QMIL

QPROP is an open source analysis program for predicting the performance of propeller-motor or windmill-generator combinations. QMIL is the companion propeller and windmill design program which is also open source. Both programs are written by Mark Drela from MIT.

The theoretical aerodynamic formulation is explained in [5]. There, the author remarks that QPROP and QMIL use an extension of the classical blade-element / vortex formulation, developed originally by Betz[6], Goldstein[7], and Theodorsen[8], and reformulated by Larrabee[9]. The extensions include

- Radially varying self-induction velocity which gives consistency with the heavily-loaded actuator disk limit
- Perfect consistency of the analysis and design formulations
- Solution of the overall system by a global Newton method, which includes the self-induction effects and powerplant model
- Formulation and implementation of the Maximum Total Power (MTP) design condition for windmills

QPROP uses three motor specification coefficients ( $K_v$ ,  $\mathcal{R}$ ,  $i_0$ ) as an input in order to model the electric motor. For modelling the propeller, it requires the geometry of the propeller which is defined by chord length

( $c_n$ ) and the pitch angle ( $\beta_n$ ) of each spanwise location ( $r_n$ ) and the airfoil properties which is approximated by a polynomial curve fit as shown in figure 3. This method results with an extremely rapid analyses of motor propeller couples for various conditions.

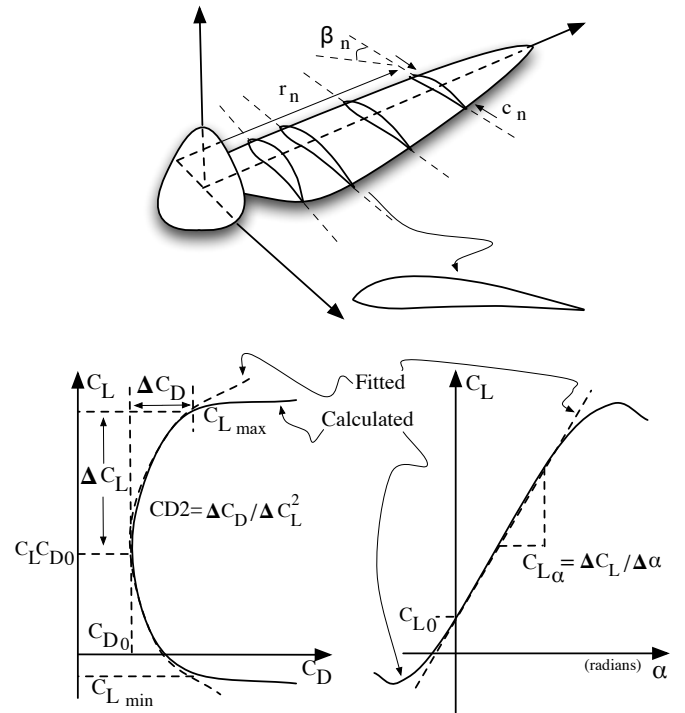


Figure 3: Propeller airfoil coefficients used in QPROP program.

Likewise QMIL requires the working conditions of the propeller that is going to be designed and optimised for. These information include the aerodynamic properties of the airfoil ( $C_{D0}$ ,  $C_L C_{D0}$ ,  $C_{Lmin}$ ,  $C_{Lmax}$ ,  $C_{L\alpha}$ ,  $C_{L0}$ ,  $C_{D2upper}$ ,  $C_{D2bottom}$ ) that is planned to be used,

lift distribution along the span, operating flight speed, desired RPM, diameter and the desired thrust or power generated.

### 3.2 QOPTIMIZER Program Flow

QOPTIMIZER program has two main capabilities. First is to match the most appropriate motor and propeller combination among the motor and propeller databases according to the defined mission requirements. Second is to design the best probable propeller while matching it to the motors from the database. In both cases the final selection is done while taking into account the working conditions and their weight factors. Figure 4 shows the main flow of the program.

The existing motors and propellers are defined with their characteristic coefficients in the corresponding databases. If a custom propeller is going to be designed, then the possible geometry (min and max radius) and RPM envelope has to be defined by the minimum and maximum values that they can get. The mission is mainly defined in the *INPUT* with the working conditions. These working conditions are both used while determining the propeller design conditions and also in the *SIMULATION* phase.

In the *DESIGN* phase, the input file for QMIL is generated according to the mission definition, required working condition specifications and the design envelope which was defined by possible geometry and the RPM minimum and maximum limits. Then QMIL outputs the custom propeller specifications with optimised chord and twisting law.

The *MATCH* phase simply generates different cases for each possible combination of motor and propeller out of the given propeller and motor databases.

Most important phase is the *SIMULATION* phase, where each of the motor propeller combination is analysed by QPROP for each of the defined working conditions. After the analyses, each working condition's result is multiplied with its weight factor and finally by summing out all of the working conditions score, a total weighted score is obtained for the motor propeller couple.

An additional *FILTER* is also defined in order to cancel certain candidates, such as propellers with too low or too high aspect ratios (limited between 3 and 15 as a default) or a maximum weight limit can also be defined (which has to be defined in the *INPUT* otherwise there is no limitation as a default) for the motor and propeller couple.

An example use of QOPTIMIZER is explained in section 6 including all the design, manufacturing and

test phases. As a brief information, the efficiency of the custom designed propeller was %71 at the defined cruise conditions ( $V_{cruise} = 15 \text{ m/s}$  and  $T_{cruise} = 1.3 \text{ N}$ ) while matching the electric motor's high efficiency working regime ( $> \%75$ ). The total propulsion system efficiency resulted as %50 including the electronic speed controller and the miscellaneous losses (such as cables, connectors...).

## 4 MODELLING ELECTRIC MOTOR AND PROPELLER

### 4.1 Electric Motor

Basically, electric motors are electromechanical machines that converts electrical input power into mechanical output power. The general power supply used in the UAVs is DC (Direct Current) so DC motors will be investigated in this chapter. Most common types are brushed and brushless motors. Brushed motors use mechanical and brushless motors use electronic commutation in order to change the direction of electric current and generate a pulling magnetic force between the stator and the magnets. Brushless motors have numerous advantages such as having a higher efficiency than brushed motors, longer lifetime, generating less noise, having higher power to weight ratio. Therefore they are more reliable for the UAV applications. And also they have become more available with the increased interest on radio controlled model aircraft world. Two types of brushless motors exists, In-runner and Out-runner. In the in-runner configuration, the magnets are placed on the shaft of the motor and the windings are at the outer part of the motor. Whereas the out-runner configuration has the magnets turning around the stator. The low inertia of in-runner motor shaft makes them reach to higher rotation speeds compared to out-runner motors. However the out-runner motors commonly preferred for their cooler running and high torque specifications which eliminates the use of additional gear-box.

The important task is to choose the suitable motor for the specified mission requirements. In order to be able to select the correct motor, the characterisation is a must.

First order simplified model using three motor constants, and experimentally obtained characteristics of DC motors will be explained in this section. Figure 5 shows an equivalent circuit model of an electric motor.

As described in [10], the resistance  $\mathcal{R}$  of the motor is assumed to be constant and the motor shaft torque  $Q_m$  is proportional to the current  $i$  according to motor torque constant  $K_Q$ . The friction based losses can be

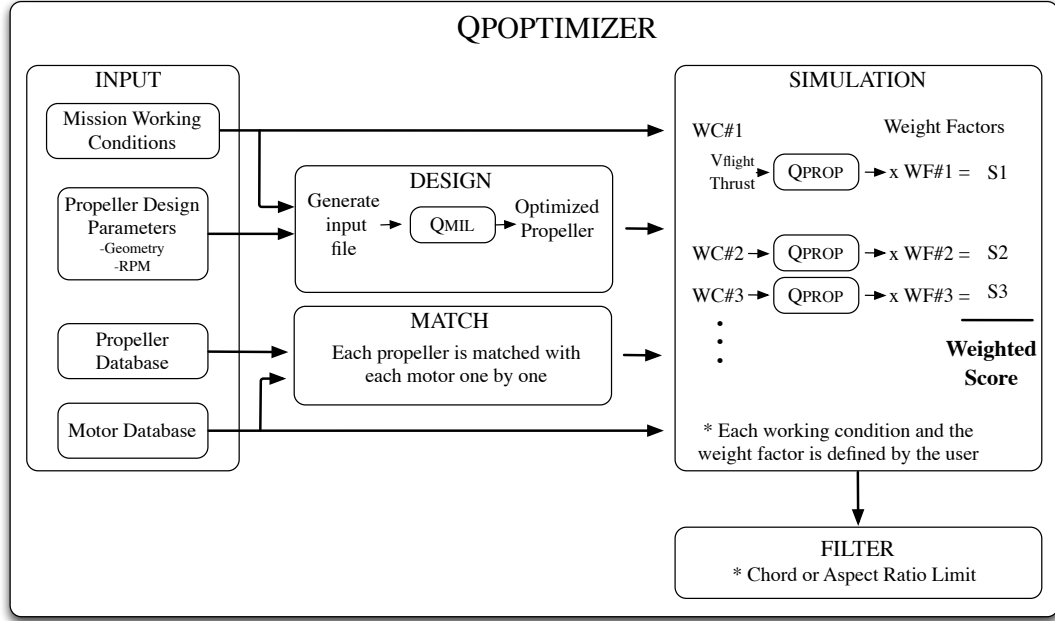


Figure 4: Main flow chart of the QOPTIMIZER program.

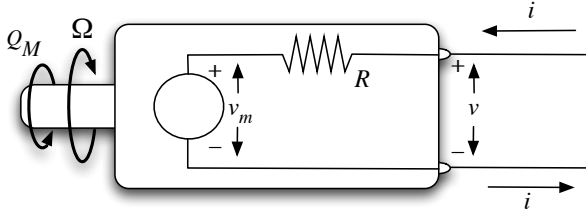


Figure 5: Equivalent circuit for a DC electric motor[10].

represented by the no load current  $i_0$  as a subtraction.

$$Q_m(i) = (i - i_0)/K_Q \quad (1)$$

Internal voltage  $v_m$  is assumed to be proportional to the rotation rate  $\Omega$  according to the speed constant  $K_v$  of the motor.

$$v_m(\Omega) = \Omega/K_v \quad (2)$$

Then the motor terminal voltage can be obtained by adding the internal voltage and the resistive voltage drop.

$$v(i, \Omega) = v_m(\Omega) + i\mathcal{R} = \Omega/K_v + i\mathcal{R} \quad (3)$$

The above model equations can be rewritten in order to give power, torque, current and efficiency as a function of terminal voltage and rotation rate of the motor. Firstly, the current function is obtained from equation 3.

$$i(\Omega, v) = \left(v - \frac{\Omega}{K_v}\right) \frac{1}{\mathcal{R}} \quad (4)$$

Then the others follow ;

$$Q_m(\Omega, v) = [i(\Omega, v) - i_0] \frac{1}{K_Q} = \left[\left(v - \frac{\Omega}{K_v}\right) \frac{1}{\mathcal{R}} - i_0\right] \frac{1}{K_Q} \quad (5)$$

$$P_{shaft}(\Omega, v) = Q_m \Omega \quad (6)$$

$$\eta_m(\Omega, v) = \frac{P_{shaft}}{iv} = \left(1 - \frac{i_0}{i}\right) \frac{K_v}{K_Q} \frac{1}{1 + i\mathcal{R}K_v/\Omega} \quad (7)$$

As a reminder,  $K_v$  is usually given in RPM/Volt in motor specifications, however here it is taken as rad/s/Volt and  $K_Q$  is taken in Amp/Nm. It should be also noted that  $K_Q \approx K_v$ .

By knowing the first order motor constants ( $K_v, K_Q, i_0, \mathcal{R}$ ) of any off the shelf motor, the theoretical characteristic plots can be obtained by using above equations. General view of the motor outputs are shown in figure 6.

#### 4.2 Experimental Motor Characterisation

In order to characterise the electric motors experimentally, the test bench which is shown in figure 7 is used. The motor is fixed on a free turning axle supported with ball bearings, and a torque sensor limits the turning of this axle in order to measure the torque generated by the motor while running. The calibration of the thrust

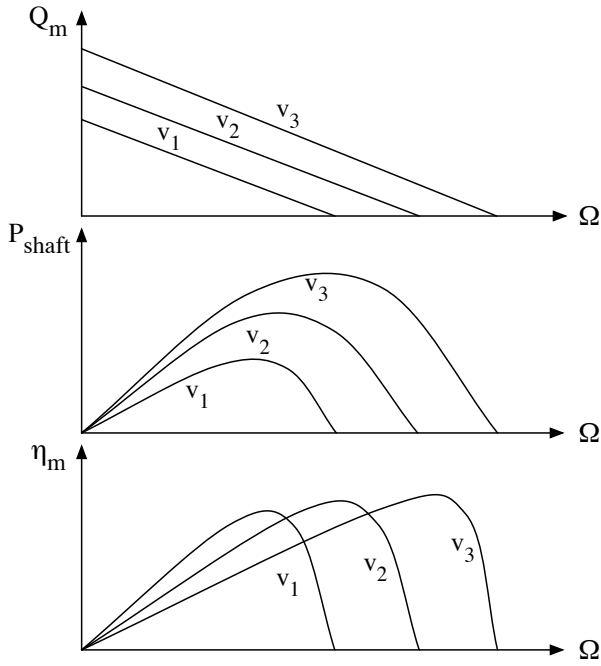


Figure 6: Theoretical motor outputs versus motor rotation rate for different input voltages.

and torque load-cells are done by using traditional pulleys with known loads attached on to them with thin rigid ropes. The load sensor (V018-113) that is used for the torque measurements was limited to  $0.5\text{ N}$  where the load arm was applied from  $8\text{ cm}$  from the centre of the rotation axis of the motor resulting with a  $4\text{ Ncm}$  limit. The thrust axis uses a  $20\text{ N}$  limited load cell and calibrated by using  $50\text{ gr}$  increments with the pulley. An optical speed sensor located near the motor measures the rotation speed. The power supply that is connected can directly record the voltage and the current consumed by the motor. Finally, all these sensors are integrated in a synchronised way in *Labview*<sup>1</sup> program.

The key point is to generate variable resistance for the motor while running on a *constant voltage*. Figure 8 shows the wheel that is used for this purpose. Simply, an air supply is used in order to generate a breaking force on the motor and the flow rate of the air supply is increased in order to cover all of the working envelope of the motor. By this way the whole characteristics of the motor for a given voltage input can be viewed. The procedure is repeated for different voltages and the whole performance characteristics are extracted.

The characterisation of the motor can also be done by other methods such as using a second motor connected to the shaft of the first one in order to generate and vary

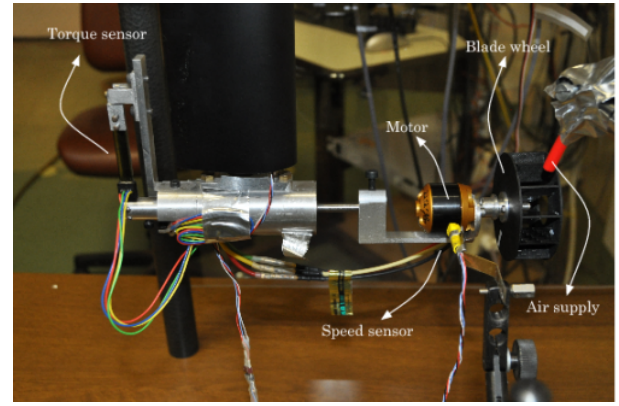


Figure 7: Motor test bench.

the resistance load or a magnetic breaking system can be implied which will result with a higher precision on the resistance change. However the simplicity of using an air break at the moment of the tests outweighed all of the possible disadvantages.

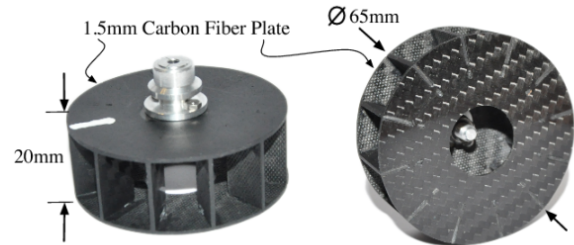


Figure 8: The wheel that is used in motor characterisation.

Figure 9 and 10 shows the comparison of performance curves that are measured experimentally and calculated with the previously explained theoretical model for AXI 2212-20 motor.

It can be seen that the simple model has an error of approximately 5% on average. As a conclusion, this theoretical and experimental match shows that in the absence of experimental testing of the electric motors, the characteristic specifications which are given by the manufacturer can be used for the initial selection of the motor.

<sup>1</sup><http://www.ni.com/labview/>

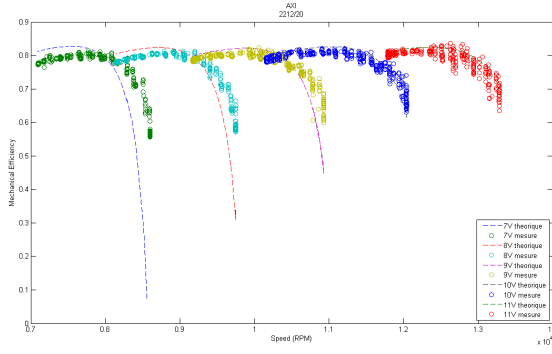


Figure 9: AXI 2212-20 Theoretical and experimental mechanical efficiency curves versus rotation rate for various input voltages.

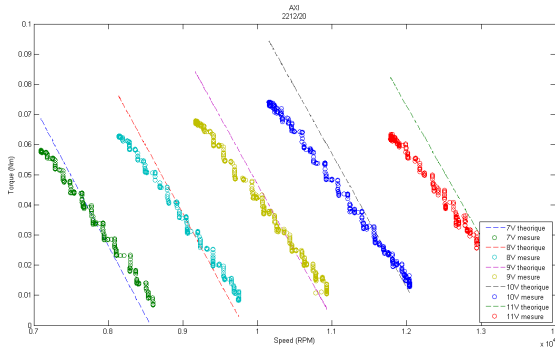


Figure 10: AXI 2212-20 Theoretical and experimental shaft torque curves versus rotation rate for various input voltages.

### 4.3 Propeller

The propeller is a rotating wing which utilises the mechanical power input in order to accelerate the air particles to generate thrust.

The basics of characterisation of the propeller is going to be explained here, however a deeper explanation can be found in [11]. The thrust and power coefficients are used to characterise a propeller, which depend on the advance ratio  $\lambda$ , the average blade Reynolds number  $Re$ , and the geometry of the propeller.

$$C_T = C_T(\lambda, Re, geometry) \quad (8)$$

$$C_P = C_P(\lambda, Re, geometry) \quad (9)$$

Reynolds number of the propeller is defined according to its average chord length  $c_{ave}$

$$Re = \frac{\rho \Omega R c_{ave}}{\mu} \quad (10)$$

Advance ratio  $\lambda$  is also well known as  $J$  in most of the literature.

$$\lambda(\Omega, V) = \frac{V}{\Omega R} \quad (11)$$

$$\lambda(\Omega, V) = J(\Omega, V) = \frac{V}{nD} \quad (12)$$

where  $n$  is,

$$n = \frac{\Omega}{2\pi} \quad (13)$$

Thrust and torque of the propeller as a function of rotation speed and the velocity,

$$T(\Omega, V) = \frac{1}{2} \rho (\Omega R)^2 \pi R^2 C_T = \frac{1}{2} \rho V^2 \pi R^2 \frac{C_T(\lambda, Re)}{\lambda^2} \quad (14)$$

$$Q(\Omega, V) = \frac{1}{2} \rho (\Omega R)^2 \pi R^3 C_P = \frac{1}{2} \rho V^2 \pi R^3 \frac{C_P(\lambda, Re)}{\lambda^2} \quad (15)$$

Finally, the efficiency of the propeller is,

$$\eta_{propeller}(\Omega, V) = \frac{T(\Omega, V)V}{Q(\Omega, V)\Omega} = \frac{C_T}{C_P} \lambda \quad (16)$$

### 4.4 Typical Propeller Performance Curves

Typical propeller performance plots  $\eta$ ,  $C_T$  and  $C_P$  versus advance ratio are shown in figures 11, 12 and 13 [12]. The curves in the figures are for the same chord distribution and twisting law but with various root pitch angle, which is commonly seen on variable pitch propellers.

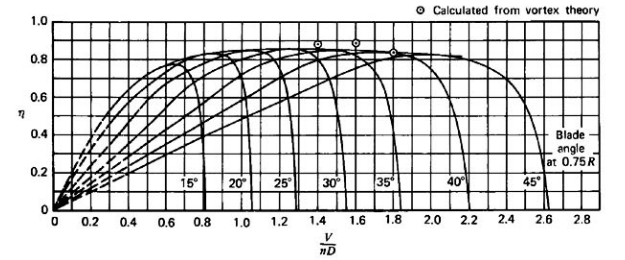


Figure 11: Typical propeller efficiency curves as a function of advance ratio  $J$ .

### 4.5 Experimental Propeller Characterisation

The same test bench which has been shown in section 4.2 is also used for the experimental characterisation of the propellers. Instead of the resistance generating wheel, the propellers that are going to be tested, are mounted to the test bench. Rotational speed, torque and the thrust of the propeller is measured at different wind tunnel speeds. Test bench is shown in figure 14.

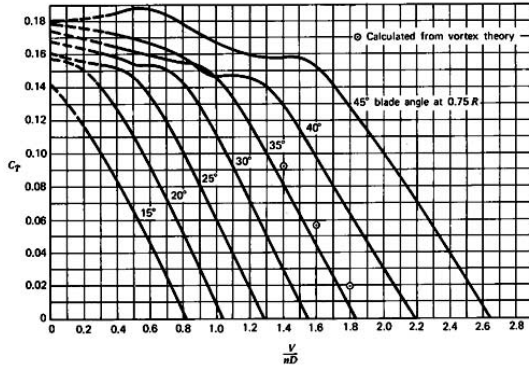


Figure 12: Typical propeller thrust curves as a function of advance ratio  $J$ .

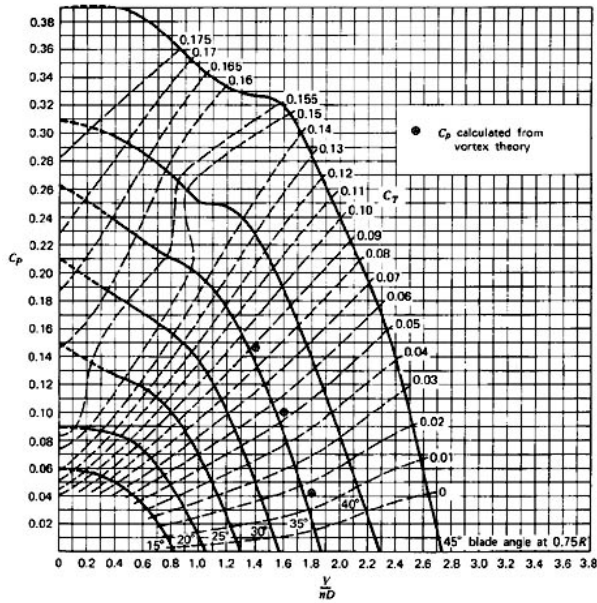


Figure 13: Typical propeller power curves as a function of advance ratio  $J$ .

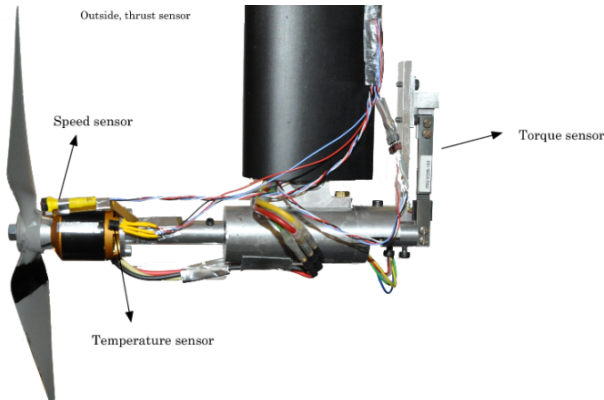


Figure 14: Propeller test bench.

## 5 MOTOR AND PROPELLER MATCHING

Regardless of its maximum efficiency of an electric motor or a propeller, if they are not matched correctly for the given mission specifications, the resultant total efficiency will be poor. The theoretical and the experimental characterisation of the electric motors and the propellers have to be used in order to match the motor and propeller couples. Figure 15 explains the matching process with steps.

The mission requirements states the *Thrust* ( $T_p$ ) (Step 1) needed at a certain flight speed  $V$  for the propeller, according to propeller's thrust versus rotation speed characteristic curve, the corresponding rotation speed ( $\Omega$ ) is found (Step 2). The rotation speed at the given flight speed  $V$  will determine the efficiency of the propeller ( $\eta_p$ ) (Step 3). In optimal case, the efficiency peak of the propeller should roughly correspond to the given rotation speed. Then the torque of the propeller  $Q_p$  defined for the given flight speed is plotted and the torque value corresponding to the rotation speed ( $\Omega$ ) is found (Step 4). In order to match the motor and the propeller's torques ( $Q_m = Q_p$ ), the required voltage of the motor is calculated ( $v$ ) (Step 5). The resultant voltage and the rotation speed of the motor gives the efficiency point,  $\eta_m$ , where the motor works (Step 6). Finally, the multiplication of the motor and the propeller efficiencies gives the total propulsion set efficiency (speed controller efficiency has to be added separately). If the motor's efficiency is on the peak region, then the matching can be defined as good. Otherwise, a gear can be used to shift the peak efficiency region of the motor in order to match with the propeller's rotation speed. The explained method has already been built-in the QPROP program.

## 6 APPLICATION OF QOPTIMIZER

As explained in section 3.2 the most important input is the working conditions which is defined by the mission itself. The final performance criteria is also going to be evaluated according to these working conditions and their weight factor which implies the importance of each working condition.

### 6.1 Working Conditions

The first calculations and later the wind tunnel test of the aircraft, *SPOC*, that is designed for the long range mini UAV project showed that the thrust needed at cruise speed is around  $1.3\text{ N}$ . This condition created the first working condition and as the main flight is going to

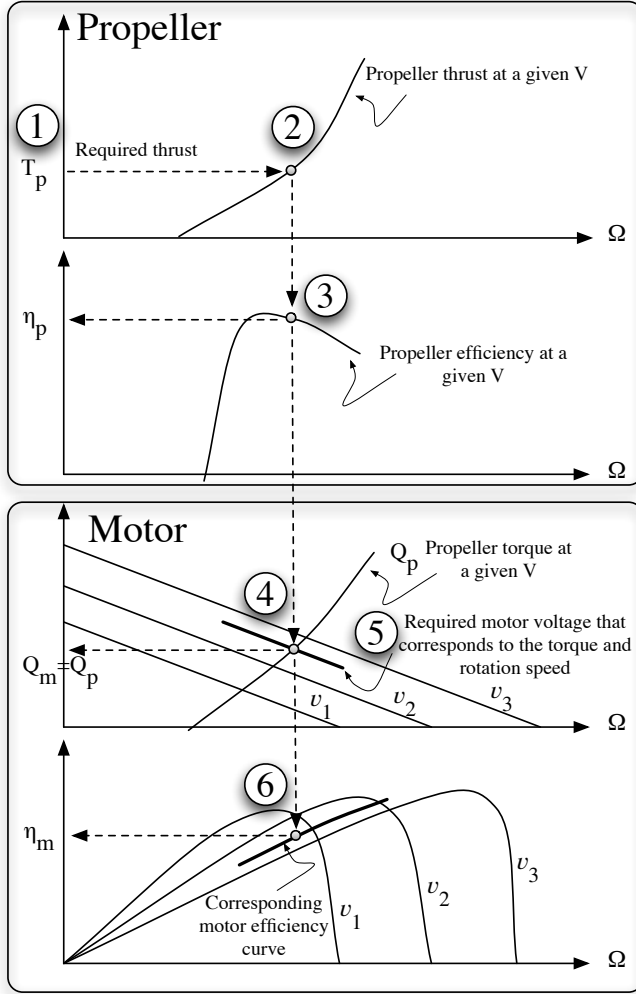


Figure 15: Motor and propeller matching procedure as explained in [11].

be almost flown in this condition, the weight factor has been selected to be 70 for it. In the time of this custom propeller design phase, the first flight tests of the *SPOC* was already accomplished. There, the need of an instant climbing ability has seen to be required. Constant climb with  $2\text{ m/s}$  vertical speed requires  $3\text{ N}$  of thrust at  $15\text{ m/s}$  flight speed for *SPOC*, this condition created the second working condition. The weight factor is selected to be 10 as it is not that much significant for the final mission performance, the important thing is to be able to achieve that condition. As the last condition, the stall phase has been selected, from the wind tunnel tests, it is known that the stall speed for *SPOC* is around  $11\text{ m/s}$  and the required equilibrium thrust is  $1.4\text{ N}$ , given with a really small weight factor of 5, the third working condition has been created. The sum of the weight factors do not necessarily need to be 100, they are normalised

within the program. The table 2 show all of the selected working conditions for QPOPTIMIZER.

	Unit	WC#1	WC#2	WC#3
Thrust	$[N]$	1.3	3.0	1.4
Speed	$[m/s]$	15.0	15.0	11.5
WeightFactor	$[-]$	70	10	5

Table 2: Mission working conditions of the *SPOC* UAV.

## 6.2 Motor Database

The ability of using a big motor database in QPOPTIMIZER gives a big freedom on choosing motors but in the content of the project there was only two motors to be used while designing the optimised propeller. These motors are selected according to their experimental bench test results and finally the fuselage of the *SPOC* is optimised according to the use of these motors. They are AXI 2212-26 and AXI 2217-12. Another important reason why these motors were chosen for the project is the rapid availability of them for the school.

## 6.3 Airfoil Selection

The airfoils that are going to be used in the propeller design needs to be defined in the inputs for QPOPTIMIZER. The definition is simply done by a polynomial curve fit to the aerodynamic characteristics plot of the airfoil, which are drag coefficient versus lift coefficient and lift coefficient versus angle of attack plots.

Some off the shelf propellers were already experimentally tested previously at the cruise speed and required thrust. These tests gave an approximate value about the average chord reynolds number of the propeller which is around 60000. Additionally, the dominance of thin cambered airfoils in the low reynolds conditions is shown in several work [?]. Firstly, some existing thin airfoils have been searched through the internet databases <sup>2</sup> and M.Selig's books [13, 14, 15]. The comparison is made between 60000 and 100000 reynolds number regime, also a smooth stall and consistent drag change versus lift is considered as selection criterias. After some investigation, five airfoils are selected as candidates, BE-50, GOE-417a, BW-3, CR-001 and GM-15.

One of the most important criteria while airfoil selection was the manufacturability. As we already selected a computer assisted numerically driven CNC milling machine manufacturing with moulds, controlled variation of thickness along the chord was achievable. This gives the opportunity of selecting better performing airfoils

<sup>2</sup>UIUC, <http://www.ae.illinois.edu/m-selig/ads.html>

rather than curved constant thickness (plate like) airfoils. As a next step, a custom airfoil is designed fulfilling a wider range of lift regime. The five candidate airfoils and the designed MBP-006 airfoil geometries and their aerodynamic characteristics are shown in figure 16.

For our application, the best suited airfoil among the first five selected candidates was BE-50, because of its smoother behaviour around  $Cl = 1.0 - 1.2$  and lower drag value at corresponding smaller lift coefficients than 1.0. All the other airfoils have a sudden peak of change in drag coefficient, and also have higher drag coefficient at lift coefficients that are lower than 1.0.

BE-50 is taken as the reference airfoil to start the design with XFOIL. The objective was to improve the already existing good characteristics and work on the lower lift coefficient part. In order to smooth the high lift coefficient regime a little bit more and reduce drag coefficient around  $Cl = 0.2 - 1.0$  lift coefficient regime, maximum lift coefficient is compromised.

The resultant MBP-006 airfoil has %10 less maximum lift coefficient but performs smoother in overall. Ideally, the required thrust should stay almost constant over the entire flight, but it is already known from the previous tests that there will be fluctuations on the required thrust while controlling the aircraft. Obtained reduced drag around  $Cl = 0.2 - 1.0$  regime becomes very important for the airfoil performance of the propeller and makes it more optimised in a practical way.

## 7 RUN CASES

The two motors which are selected for the project previously, were AXI2217-12 and AXI2212-26. The bench test results showed that there is a significant difference between the expected theoretical performance and the experimental performance of AXI2217-12, the theoretical performances are almost %10 overestimated than the experimental ones. The performance plots are shown in figure 17 and 18. As an additional to this, there is an 13g of weight penalty for AXI2217-12 as it is a bigger motor than AXI2212-26. Being a bigger motor also means that the throttle percentage is going to be low while cruise flight conditions, so that the speed controller efficiency will be lower than expected for this case as well. The only advantage is going to be the additional maximum thrust value for safety reasons. Taking into account all these facts, the design of the new propeller is selected to be made primarily for the small AXI2212-26 motor and try to have the bigger AXI2217-12 motor for some critical test flight where

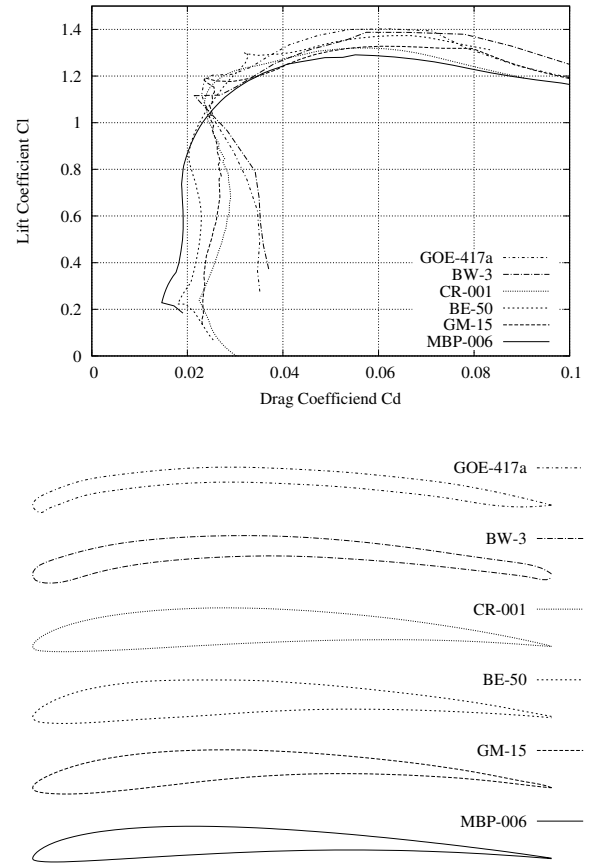


Figure 16: Selected airfoils and their lift versus drag coefficient plot calculated by XFOIL for 60000 Reynolds number.

the additional power can be necessary.

As an input, the RPM and propeller tip radius ranges must be defined in order to run the simulations. The precision of the optimisation is defined by the step of both parameters. Table 3 shows the selected envelope for the design.

Spanwise location	Minimum	Maximum	Step
RPM	2000	12000	50
Tip radius [mm]	10	200	1

Table 3: Parameters used for the optimization

Additionally, the desired spanwise lift coefficient distribution required to be defined for QOPTIMIZER (QMIL program needs this information). Two spanwise  $C_L$  distributions were tested and are shown in table 4.

Previously selected working conditions, shown in

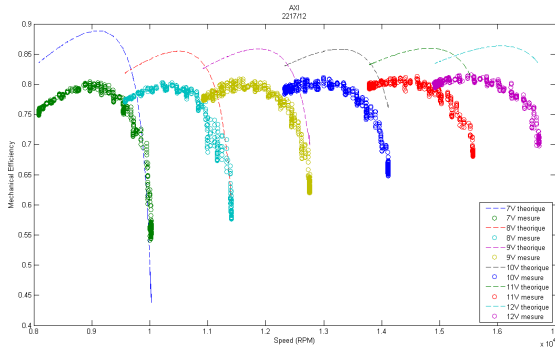


Figure 17: AXI 2217-12 theoretical and experimental mechanical efficiency curves versus rotation rate for various input voltages, showing the significant difference between the theoretical and experimental test results.

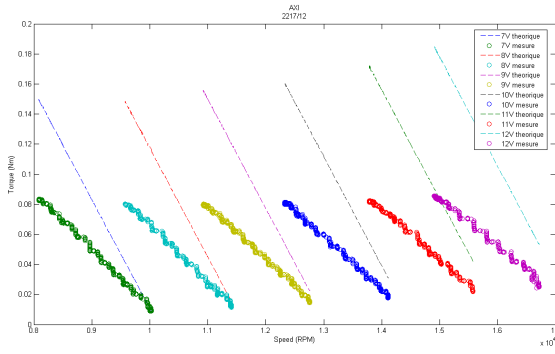


Figure 18: AXI 2217-12 theoretical and experimental shaft torque curves versus rotation rate for various input voltages, showing the significant difference between the theoretical and experimental test results.

table 2, used for every run case. As a common result in every run case, the higher  $C_L$  distribution gave better performances. The table 5 shows the best results of all the run cases.  $C_{L1}$  distribution is selected to be used for the final design.

The resultant global efficiency is higher using the bigger AXI2217-12 motor as expected. As it is already known that the AXI2217-12 is over estimated for the efficiency and also heavier, the small AXI2212-26 motor fits more appropriately for our application.

A monoblade propeller was also designed using the same approach. Demanding the same thrust with only one blade created a propeller with wider chords. This improved the overall airfoil efficiencies along the span because of increased Reynolds number. The best estimated overall efficiency for the motor and monoblade

Spanwise location	0.10	0.50	1.00
$C_L$ distribution 1	0.75	0.65	0.40
$C_L$ distribution 2	0.60	0.45	0.40

Table 4: Lift coefficients distributions

		Cruise efficiency	RPM	Tip radius [cm]
AXI2212-26	$C_{L1}$	59.5%	5800	11
AXI2212-26	$C_{L2}$	58.9%	5700	11.5
AXI2217-12	$C_{L1}$	63%	5000	12.5
AXI2217-12	$C_{L2}$	61.9%	5000	12

Table 5: Best global efficiencies of the motor and propeller couples for the cruise conditions are shown (note that the speed controller losses are not included).

propeller couple is calculated as 62.6% by QOPTIMIZER. Unfortunately, because of the limited time span of the project and the expected possible problems that could come with a monoblade propeller cancelled the investigation of the monoblade concept and the manufacturing continued with the bi-blade propeller design.

## 8 MANUFACTURING

The manufacturing of the propeller is decided to be done in house, in composite laboratory of ISAE. Thinking about each landing phase of the tests flights and having no landing gear on the SPOC plane, the propeller was in danger of breaking while landing. In order to prevent this, the hub of the propeller is designed for a folding root, and finally a custom spinner is also build in the exact needs of SPOC plane. Figure 19 shows the integration of the folding blade with the spinner.

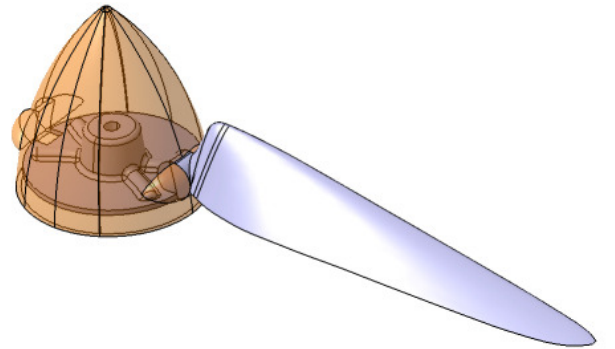


Figure 19: Designed propeller and its spinner's CATIA drawing.

Moulds are designed in Catia V5 and manufactured with CNC milling machines in order to achieve the necessary precision. Each blade is build out of three piece of moulds, top, bottom and the folding axis pin. The

spinner cone is build by using six pieces of moulds, two sides, two folding axe pins and two prop blade root inserts. Finally the base of the cone is build by using three moulds, top bottom and the rotation axis pin. The spinner cone and the base moulds are designed to fit each other in order to maintain the base to the cone in the same rotation axis perfectly to prevent any possible balance problems.

The propeller was made of carbon fibre. The material was chosen because of its low weigh and its high strength. The required pieces are first cut into shape and then wet lay-up is done by hand into the moulds. Different orientations ( $45^\circ$  and  $90^\circ$ ) of carbon fibre woven were used on the skin for the torsional strength of the propeller. Additionally, unidirectional carbon fibre mesh were placed in order to sustain the bending forces of the blade. As the propeller blade has a specific airfoil, a certain amount of material should have filled the thickness. The exact required material quantity is found by trial and error as the weight of each blade was only 1.5 g. There was no need to use vacuum bagging process as the two mould halves completely fits onto each other.

The spinner cone is also build by wet lay-up by hand, in order to achieve a smooth surface and fix the layer on the skin of the cone, a balloon is inflated inside the cone. A silicon insert should have given better results but this method is used because of the time restrictions. The figure 20 shows the resulting cone and its molds.

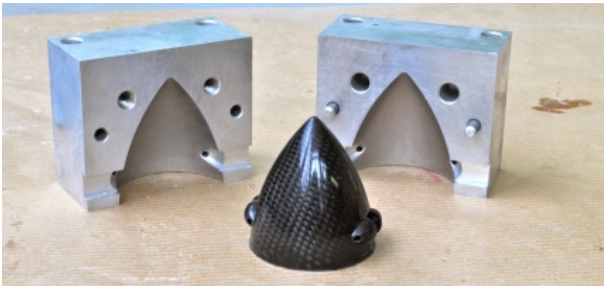


Figure 20: The cone and its molds

Finally after manufacturing two blades, spinner cone and the base, they are integrated into each other to form the custom designed propeller. The figure 21 shows the resulting propeller. The fixation of the spinner to the motor shaft is done internally. First the two blades should have removed and then the inner fixation screws that are placed on the spinner base plate can be reached. This method makes the fixation a little bit complex but

once it is fixed there will not be any gap between the spinner and the nose of the plane or any protruding screws that can create additional drag.



Figure 21: The resulting custom propeller

## 9 TEST RESULTS

The propeller test bench which is shown in section 4.3 figure 14 is used for the tests. The main point of interest was to measure the performance at cruise conditions which are 15 m/s of flight speed and 1.3 N of thrust generation. Additionally, as expected from the theoretical calculations, the propeller has to have more than 4 N of thrust at this flight speed at full throttle. Figures 22 and 23 show the global efficiency (speed controller + motor + propeller) and propeller efficiency alone versus thrust generated at 15 m/s flight speed condition. It can be seen that the propeller efficiency is around 71% at cruise condition thrust, and the final global efficiency is around 50% which includes the speed controller, motor and the propeller. The maximum thrust measured at full throttle was 4.25 N at 15 m/s speed.

Expected global efficiency was 59.5% however, the measured efficiency was only 50%. The assumptions and the simplifications that is done in theoretical calculations will cause a difference between the real world and the calculations, but there are also several reasons that cause difference. First of all the theoretically assumed 59.5% efficiency does not take into account the speed controller, which usually have around 95% of maximum efficiency. Additionally, the designed spinner could not have used in the wind tunnel tests because of the additional pressure drag that it generates without having the real fuselage behind it. Instead of spinner, an aluminium piece is manufactured in order to hold the two folding propeller blades together in the wind tunnel, there is additional drag coming from this piece resulting with lower efficiency. Finally the manufactured airfoil shape and the propeller geometry could have differ from the designed and analysed one which results normally reduction on the expected efficiency as well.

## 10 CONCLUSION

A multi-point optimisation methodology and a devoted program called QOPTIMIZER is introduced for matching and designing electric propulsion system. The importance of the mission definition and optimisation of the propulsion system according to multiple working conditions is highlighted. The modelling of the motor and propeller is described stating the importance of the accuracy of the models. The motor and propeller matching procedure is explained deeply.

Finally, the proposed program is used in designing a custom propeller for a real life application for a mini-UAV that has to fly a long range mission. The results showed that the program correctly matches the motor and propeller's individual peak efficiency regions optimised while taking into account every working conditions. This leads to an optimum selection of the propulsion system. However, the resultant performance values are a little bit optimistic (%5 – 10 for the complete propulsion system) compared to the experimental measurements which has been previously expected.

## ACKNOWLEDGEMENT

The authors would like to thank Prof. Mark Drela for sharing his great work QPROP and QMIL within the GNU v2 licence which makes it possible to use them as the core aerodynamic analyser programs of the QOPTIMIZER. Also we would like to thank a lot Xavier Foulquier and Guy Mirabel for their precious helps and advices for the composite manufacturing.

The realisation of the custom propeller would not be possible without the work that has been done by Miguel Morere Y Van Begin, Guillaume Soete, Pierre Joachim and Benjamin Fragnière (aka. The Belgium Beatles). Finally, this study has been co-funded by the European Union. Europe is involved in Midi-Pyrénées with European Fund for regional development.

## REFERENCES

- [1] Thomas J. Mueller, James C. Kellogg, Peter G. Ifju, and Sergey V. Shkarayev. *Introduction to the Design of Fixed-Wing Micro Air Vehicles*. American Institute of Aeronautics and Astronautics, Inc., Virginia, VA, 2007.
- [2] Murat Bronz, Jean-Marc Moschetta, Pascal Brisset, and Michel Gorraz. Towards a Long Endurance MAV. In *EMAV2009*, Delft, Netherlands, September 2009.

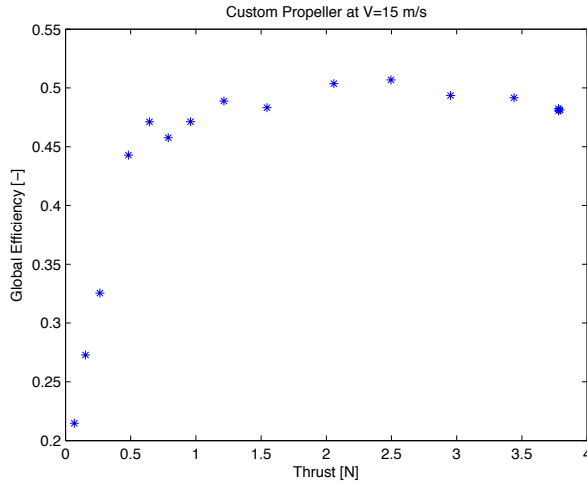


Figure 22: The global efficiency versus Thrust [N] plot for the custom designed propeller at 15 m/s speed.

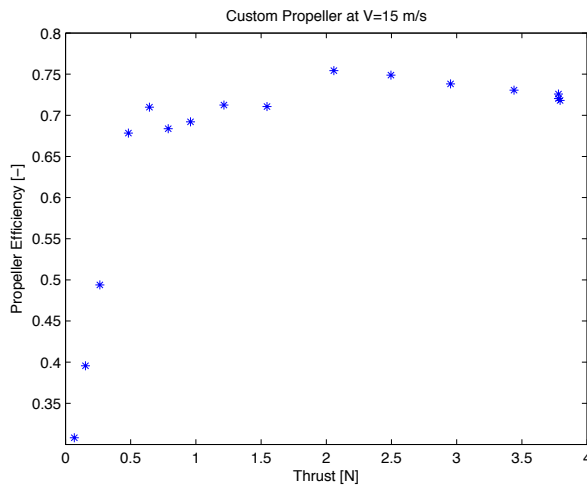


Figure 23: The propeller efficiency versus Thrust [N] plot for the custom designed propeller at 15 m/s speed.

- [3] Murat Bronz, Jean-Marc Moschetta, Pascal Brisset, and Michel Gorraz. Towards a Long Endurance MAV. *International Journal of Micro Air Vehicles*, 1(4):241–254, 2009.
- [4] Murat Bronz, Jean-Marc Moschetta, and Pascal Brisset. Flying Autonomously to Corsica : A Long Endurance Mini-UAV System. In *IMAV2010*, Braunschweig, Germany, July 2010.
- [5] Mark Drela. *QPROP Formulation*. MIT Aero and Astro, June 2006.
- [6] A.Betz. Airscrews with minimum energy loss. Technical report, Kaiser Wilhelm Institute of Flow Research, 1919.
- [7] S.Goldstein. On the vortex theory of screw propellers. In *Proceedings of the Royal Society*, volume 123, 1929.
- [8] Theodore Theodorsen. *Theory of Propellers*. McGraw-Hill, New York, 1948.
- [9] E.E Larrabee and S.E. French. Minimum induced loss windmills and propellers. *Journal of Wind Engineering and Industrial Aerodynamics*, 15:317-327:317–327, 1983.
- [10] Mark Drela. First-order dc electric motor model. Technical report, MIT, Aero and Astro, February 2007.
- [11] Mark Drela. Dc motor and propeller matching , lab 5 lecture notes. Technical report, MIT, March 2005.
- [12] McCormick B.W. *Aerodynamics, Aeronautics & Flight Mechanics*. John Wiley & Sons, Inc., 1979.
- [13] Michael Selig. *Summary of Low-Speed Airfoil Data*, volume 1. SoarTech Publications, Virginia Beach, VA, 1995.
- [14] Michael Selig. *Summary of Low-Speed Airfoil Data*, volume 2. SoarTech Publications, Virginia Beach, VA, 1996.
- [15] Michael Selig. *Summary of Low-Speed Airfoil Data*, volume 3. SoarTech Publications, Virginia Beach, VA, 1997.

# Bibliography

- [1] F. W. SCHMITZ. *Aerodynamik des Flugmodells*. C. J. E. Volckmann Nachf. E. Wette, Berlin-Charlottenburg, 1942.
- [2] Solar irradiance on a horizontal surface at the 22nd of september 1994 in rio de janeiro (clear day), . URL <http://www.solar.coppe.ufrj.br/solar.html>.
- [3] Mark Drela. First-order dc electric motor model. Technical report, MIT, Aero and Astro, February 2007.
- [4] Mark Drela. Dc motor and propeller matching , lab 5 lecture notes. Technical report, MIT, March 2005.
- [5] Amit industries ltd. URL <http://www.amicell.co.il>.
- [6] Nrel, national center for photovoltaics, . URL <http://www.nrel.gov/ncpv/>.
- [7] Sion power, the rechargeable battery company. URL [www.sionpower.com](http://www.sionpower.com).
- [8] Daniel P. Raymer. *Aircraft Design : A Conceptual Approach*. American Institute of Aeronautics and Astronautics,Inc., Virginia,VA, 2006.
- [9] Thomas J. Mueller, James C. Kellogg, Peter G. Ifju, and Sergey V. Shkarayev. *Introduction to the Design of Fixed-Wing Micro Air Vehicles*. American Institute of Aeronautics and Astronautics,Inc., Virginia,VA, 2007.
- [10] Murat Bronz, Jean-Marc Moschetta, Pascal Brisset, and Michel Gorraz. Towards a Long Endurance MAV. *International Journal of Micro Air Vehicles*, 1(4):241–254, 2009.
- [11] Murat Bronz, Jean-Marc Moschetta, Pascal Brisset, and Michel Gorraz. Towards a Long Endurance MAV. In *EMAV2009*, Delft, Netherlands, September 2009. URL <http://www.emav09.org/>.

- [12] Murat Bronz, Jean-Marc Moschetta, and Pascal Brisset. Flying Autonomously to Corsica : A Long Endurance Mini-UAV System. In *IMAV2010*, Braunschweig, Germany, July 2010. URL <http://imav2010.org/>.
- [13] Murat Bronz. Multi-point optimization of a propulsion set as applied to a multi-tasking mav. In *International Micro Aerial Vehicle Conference and Competition*, July 2012.
- [14] Condor long endurance uav from boeing. URL <http://www.boeing.com/history/boeing/condor.html>.
- [15] URL [www.avinc.com](http://www.avinc.com).
- [16] A. Noth. *Design of Solar Powered Airplanes for Continuous Flight*. PhD thesis, ETH ZÜRICH, 2008.
- [17] N. Diepeveen. The sun surfer : Design and construction of a solar powered MAV. Master's thesis, Autonomous Systems Lab, ETHZ, Zürich, March 2007.
- [18] Dr.-Ing. S. F. HOERNER. *Fluid-Dynamic Drag*. 1965.
- [19] Martin Simons. *Model Aircraft Aerodynamics*. Special Interest Model Books Ltd., 1999.
- [20] Donald W. Srull Thomas J. Mueller, Gabriel E. Torres. *Elements of Aerodynamics, Propulsion, and Design*, chapter 2, pages 39–107. American Institute of Aeronautics and Astronautics, Inc., 2006.
- [21] M.D. Maughmer D.M. Somers. Theoretical aerodynamic analyses of six airfoils for use on small wind turbines. Technical Report NREL/SR-500-33295, NREL, June 2003.
- [22] Mark Drela. Low-reynolds number airfoil design for the mit daedalus prototype: A case study. *Journal of Aircraft*, 25(8):724–732, August 1988.
- [23] Harold Youngren Mark Drela. *XFOIL 6.94 User Guide*. MIT Aero and Astro, 2001.
- [24] Mark Drela. An analysis and design system for low reynolds number airfoils. In University of Notre Dame, editor, *Conference on Low Reynolds Number Airfoil Aerodynamics*, June 1989.

- [25] Mark Drela. Integral boundary layer formulation for blunt trailing edges. In *Paper AIAA-89-2200*, August 1989.
- [26] Mark Drela. Vortex lattice method summary. Technical report, 1999. URL <http://groups.yahoo.com/group/xfoil/files/vlm.pdf>.
- [27] Murat Bronz. Experimental comparison of 1-meter conventional, pusher and tractor flying wing aircraft configurations in s4 wind-tunnel. Technical report, ISAE, 2009.
- [28] Mark Drela. *QPROP Formulation*. MIT Aero and Astro, June 2006.
- [29] A.Betz. Airscrews with minimum energy loss. Technical report, Kaiser Wilhelm Institute of Flow Research, 1919.
- [30] S.Goldstein. On the vortex theory of screw propellers. In *Proceedings of the Royal Society*, volume 123, 1929.
- [31] Theodore Theodorsen. *Theory of Propellers*. McGraw-Hill, New York, 1948.
- [32] E.E Larrabee and S.E. French. Minimum induced loss windmills and propellers. *Journal of Wind Engineering and Industrial Aerodynamics*, 15:317-327:317–327, 1983.
- [33] McCormick B.W. *Aerodynamics, Aeronautics & Flight Mechanics*. John Wiley & Sons, Inc., 1979.
- [34] Energy storage, . URL [http://en.wikipedia.org/wiki/Energy\\_storage](http://en.wikipedia.org/wiki/Energy_storage).
- [35] Electrochemical cell : Batteries, . URL [http://en.wikipedia.org/wiki/Battery\\_\(electricity\)](http://en.wikipedia.org/wiki/Battery_(electricity)).
- [36] Thunder power batteries. URL [www.thunderpowerrc.com](http://www.thunderpowerrc.com).
- [37] F.Mitlitsky A.H.Myers Weisberg and Blake. Vehicular hydrogen storage using lightweight tanks. In *U.S. DOE Hydrogen Program 1999 Annual Review Meeting, Lakewood, Colorado*, May 1999.
- [38] C.P.Garcia B.J.Chang D.W.Johnson D.J.Bents V.J.Scullin I.J.Jakupca. Round trip energy efficiency of nasa glenn regenerative fuel cell system. In *NHA Annual Hydrogen Conference 2006*, Long Beach, California, March 12-16 2006.

- [39] F.Barbir T.Molter D.Luke. Regenerative fuel cells for energy storage : Efficiency and weight trade-offs. Number AIAA-2003-5937, August 2003.
- [40] Horizon energy systems, . URL <http://www.hes.sg/>.
- [41] Protonex fuel cell, . URL <http://www.protonex.com/defense/index.aspx>.
- [42] Arrêté du 21 mars 2007 relatif aux aéronefs non habités qui évoluent en vue directe de leurs opérateurs, May 2010.
- [43] Thomas H. Bradley, Blake A. Moffitt, Dimitri N. Mavris, and David E. Parekh. Development and experimental characterization of a fuel cell powered aircraft. *Journal of Power Sources*, 2007. URL [www.elsevier.com/locate/jpowsour](http://www.elsevier.com/locate/jpowsour).
- [44] Thomas H. Bradley, Blake A. Moffitt, Thomas F. Fuller, Dimitri Mavris, and David E. Parekh. Design studies for hydrogen fuel cell powered unmanned aerial vehicles. In *American Institute of Aeronautics and Astronautics*, Honolulu, Hawaii, August 2008. URL <http://www>.
- [45] Michael J. Allen. Guidance and control of an autonomous soaring uav. Technical Memorandum NASA/TM-2007-214611 , NASA, February 2007. URL [http://cafefoundation.org/v2/pdf\\_tech/eCFI.Flight.Deck/NASA.eCFI.UAV.ThermalSoar.pdf](http://cafefoundation.org/v2/pdf_tech/eCFI.Flight.Deck/NASA.eCFI.UAV.ThermalSoar.pdf).
- [46] Michael J. Allen. Updraft model for development of autonomous soaring uninhabited air vehicles. American Institute of Aeronautics and Astronautics, Inc., 2006. URL [http://ntrs.nasa.gov/archive/nasa/casi.ntrs.nasa.gov/20060004052\\_2006002817.pdf](http://ntrs.nasa.gov/archive/nasa/casi.ntrs.nasa.gov/20060004052_2006002817.pdf).
- [47] D. J. Edwards. Implementation details and flight test results of an autonomous soaring controller. In *American Institute of Aeronautics and Astronautics*, 2008.
- [48] P. Brisset and A. Drouin. PaparadziY: do-it-yourself UAV. In *Journées Micro Drones*, Toulouse, France, September 2004. URL [http://www.recherche.enac.fr/paparazzi/papers\\_2004/paparadziy.pdf](http://www.recherche.enac.fr/paparazzi/papers_2004/paparadziy.pdf).
- [49] Michael Selig. *Summary of Low-Speed Airfoil Data*, volume 1. SoarTech Publications, Virginia Beach, VA, 1995.

- 
- [50] Michael Selig. *Summary of Low-Speed Airfoil Data*, volume 2. SoarTech Publications, Virginia Beach, VA, 1996.
- [51] Michael Selig. *Summary of Low-Speed Airfoil Data*, volume 3. SoarTech Publications, Virginia Beach, VA, 1997.